Exploring the Physics of 3D Magnetic Nanowires and 3D Artificial Spin-Ice Lattices

Arjen van den Berg

A thesis submitted to Cardiff University in in partial fulfilment of the requirements for the degree of Doctor of Philosophy.

May, 2023

Author: Arjen van den Berg
Title: Exploring the physics of 3D magnetic nanowires and 3D artificial spin-ice lattices
Date of first submission: January 2022

Significant Contributions

The work presented in this thesis is part of a collective effort among the members of the research group and our collaborators. As such, this thesis contains significant contributions from Andrew May & Matthew Hunt formerly from Cardiff University, Michael Saccone from Los Alamos National Laboratories, and Myléne Carouel.

Initial optical magnetometry of the 3D artificial spin-ice lattices presented in Figure 5-15 was performed by Matthew Hunt, and magnetic force microscopy measurements shown in chapter 4 were performed by Andrew May along with the simulations for domain wall potential presented in Figure 5-19 and Figure 5-20. Analysis was performed by the author. Michael Saccone contributed with Monte Carlo simulations presented in Figure 5-25. Myléne Carouel contributed to Chapter 5 by performing the initial exploration of Poly(acrylic acid) as a sacrificial layer and the AFM measurements for characterizing laser ablation of the PAA layer. Analysis of measurements was performed by the author. Finally, EDX measurements in chapter 5 were performed with the support of Duncan Muir of Cardiff University. All other presented work was performed by the author.

Training for two-photon lithography, MOKE magnetometry, and AFM/MFM were provided by Matthew Hunt and Andrew May. Training for thermal evaporation and SEM were provided by Robert Lang of Cardiff University.

Micromagnetic simulations presented in this thesis were performed using the Raven and Hawk supercomputing clusters at Advanced Research Computing at Cardiff (ARCCA) and we gratefully acknowledge Christine Kitchen for her support.

We gratefully acknowledge funding from the Engineering and Physical Sciences Research Council (EP/R009147/1 and EP/N509449/1)

Publications

A. May, M. Hunt, **A. Van Den Berg**, A. Hejazi, and S. Ladak, "Realisation of a frustrated 3D magnetic nanowire lattice," Communications Physics, vol. 2, no. 1, p. 13, 2019/02/01 2019, doi: 10.1038/s42005-018-0104-6.

M. Hunt, M. Taverne, J. Askey, A. May, **A. van den Berg**, Y-LD. Ho, J. Rarity, and S. Ladak, "Harnessing Multi-Photon Absorption to Produce Three-Dimensional Magnetic Structures at the Nanoscale," Materials, vol. 13, no. 3, 2020, doi: 10.3390/ma13030761.

A. May, M. Saccone, **A. van den Berg**, J. Askey, M. Hunt, and S. Ladak, "Magnetic charge propagation upon a 3D artificial spin-ice," Nature Communications, vol. 12, no. 1, p. 3217, 2021/05/28 2021, doi: 10.1038/s41467-021-23480-7.

A. van den Berg, M. Caruel, M. Hunt, and S. Ladak, "Combining two-photon lithography with laser ablation of sacrificial layers: A route to isolated 3D magnetic nanostructures," Nano Research, 2022/07/30 2022, doi: 10.1007/s12274-022-4649-z.

O. V. Dobrovolskiy, O. V. Pylypovskyi, L. Skoric, A. Fernández-Pacheco, **A. Van Den Berg**, S. Ladak, M. Huth, “Complex-shaped 3D nano-architectures for magnetism and superconductivity” (Book chapter) in Curvilinear Micromagnetism: From Fundamentals to Applications, D. Makarov and D. D. Sheka Eds. Cham: Springer International Publishing, 2022, pp. 215-268.

Index

List of Figures

Chapter 5

List of Tables

List of Symbols and Acronyms

Symbol	Definition
a	Lattice parameter
α	Phenomenological Gilbert Damping Coefficient
$A, \mathbf{A}$	Area
A_{ex}	Exchange Stiffness
$B, \mathbf{B}$	Magnetic induction
d_v	Voxel Diameter
D	Coupling constant
e	Electron charge
$\hat{\boldsymbol{e}}_{\boldsymbol{ij}}$	Ising axis unit vector
$\hat{\boldsymbol{e}}_{\parallel}$	Unit vector along long axis
$\hat{\boldsymbol{e}}_{\perp}$	Unit vector normal to surface
$\hat{\boldsymbol{e}}_{\dashv}$	Binormal unit vector.
$\mathbf{E}$	Electric field
ε_0	Permittivity of free space
$\underline{\boldsymbol{\varepsilon}}$	Dielectric tensor
ε	Dielectric constant
$\boldsymbol{\mathcal{E}}$	Energy density
E	Energy
E_{anis}	Anisotropy Energy
$\mathcal{E}_{anis}$	Anisotropy Energy Density
E_{demag}, E_d	Demagnetization Energy
$\mathcal{E}_{demag}, \mathcal{E}_d$	Demagnetization Energy Density
E_{ex}, E_{exch}	Exchange Energy
$\mathcal{E}_{ex}, \mathcal{E}_{exch}$	Exchange Energy Density

Symbol	Definition
E_F	Fermi Energy
E_{zeeman}	Zeeman Energy
$\mathcal{E}_{zeeman}$	Zeeman Energy Density
E_0	Ground State energy
E_*	Excited State energy
f_γ	Laser Pulse repetition Frequency
$\mathbf{F}$	Force
$\mathbf{F_l}$	Lorentz Force
$g(E)$	Density of states
γ_L	Orbital Gyromagnetic Ratio
γ_S	Spin Gyromagnetic Ratio
h	Planck's Constant
$\hbar$	Reduced Planck's Constant
$\mathbf{H}$	Magnetic field
H_c	Coercive field
$\mathbf{H_d}$	Demagnetizing field
$\mathbf{H_{ex}}$	Effective field due to exchange interactions
$\mathbf{H_{eff}}$	Effective field due to all energy terms
$\mathbf{H_{anis}}$	Effective field due to Magnetocrystalline anisotropy
$\mathbf{I}$	Current
I	Intensity
I_{focal}	Intensity in the focal plane
$\mathbf{J}$	Electron total angular momentum
J_1, J_2	Interaction strengths between adjacent nanowires
$\mathcal{J}_{12}$	Exchange integral
k	Spring constant
k_B	Boltzmann constant
K_n	Magnetocrystalline anisotropy constant of the nth order.
K_S	Shape Anisotropy Constant
l	Length
ℓ	Orbital quantum number
l_v	Voxel length
$\mathbf{L}$	Orbital angular momentum
λ	Anisotropy constant

Symbol	Definition
$\mathbf{m}$	Magnetic moment
$m, \mathcal{m}$	Mass, effective mass
m_e	Electron Mass
$\mathcal{m}_l$	Magnetic quantum number
$\mathcal{m}_s$	Spin magnetic quantum number
μ	Chemical potential
μ^*	Effective Chemical potential
μ_0	Permeability of free space
μ_B	Bohr Magneton
μ_L	Orbital magnetic moment
μ_s	Spin magnetic moment
$\mathbf{M}$	Magnetization
M_c	Madelung constant
M_R	Magnetization at remanence
M_S	Saturation magnetization
n	Refractive index
$\mathcal{n}$	Principal quantum number
N	Number
NA	Numerical aperture
$\underline{\boldsymbol{N}}$	Demagnetizing tensor
N_x, N_y, N_z	Diagonal components of demagnetizing tensor
$\mathbf{P}$	Polarization vector
P	Laser power
ψ	Spatial component of wavefunction
Ψ	Complete wavefunction
ρ	Density
ρ_{init}	Photoinitiator density
ρ_{rad}	Free radical density
$Q, \mathcal{Q}, q$	Charge
$\mathbf{Q}$	Voigt Vector
$\mathbf{r}, r$	Position vector, distance/radius
$\mathbf{S}$	Spin vector

Symbol	Definition
S	Entropy
S_R	Residual entropy
σ^-, σ^+	Left- and right-handed circular polarization
σ_{1PA}	Single photon absorption cross-section
σ_{2PA}	Two photon absorption cross-section
t	Time
t_0	Attempt time
t_m	Observation time
T	Temperature
T_B	Blocking temperature
θ	Angle
$\boldsymbol{\tau}$	Torque
τ	Pulse length
ω	Optical beam width
ω_0	Optical beam waist
U	Potential energy
V	Volume
χ	Susceptibility
$\chi(1,2)$	Spin component of two-electron wavefunction

Acronym	Definition
2D	2 Dimensional / 2 Dimensions
3D	3 Dimensional / 3 Dimensions
3DNL	3D nanowire Lattice
ABMO	Antibonding Molecular Orbital
AFM	Atomic Force Microscopy
AOM	Acousto-Optic Modulator
AR	Aspect Ratio
ARCCA	Advanced Research Computing at Cardiff
ASI	Artificial Spin Ice
ATDW	Asymmetric Transverse Domain Wall
BCC	Body Centered Cubic
BMO	Bonding Molecular Orbital
BPW	Bloch Point Wall
CAD	Computer Aided Design
DMI	Dzyaloshinskii Moriya Interaction
EDX	Electron Dispersive X-ray
FCC	Face Centered Cubic
FD	Finite Difference
FDM	Finite Difference Method
FE	Finite Element
FEM	Finite Element Method
HDD	Hard Disk Drive
HH	Head-to-Head
IPA	Isopropyl Alcohol
LASP	Long axis substrate projection
LLG	Landau-Lifshitz-Gilbert
LOS	Line-of-sight
MAP	Monopole-Antimonopole Pair
MFM	Magnetic Force Microscopy

Acronym	Definition
MOKE	Magneto Optical Kerr Effect
MRM	Magnetic Racetrack Memory
OPP	One-Photon Polymerisation
PAA	Poly(Acrylic Acid)
PEEM	Photoemission Electron Microscopy
PGMEA	Propylene Glycol Methyl Ether Acetate
PMMA	Poly(Methyl Methacrylate)
QCM	Quartz Crystal Monitor
RMS	Root Mean Square
SEM	Scanning Electron Microscope/Microscopy
SNR	Signal to Noise Ratio
SPM	Scanning Probe Microscopy
TDW	Transverse Domain Wall
TPA	Two-Photon Absorption
TPL	Two-Photon Lithography
TPP	Two-Photon Polymerisation
TT	Tail-to-Tail
UV	Ultraviolet
VDW	Vortex Domain Wall
XMCD	X-ray Magnetic Circular Dichroism

Dedication

Firstly, I would like to thank my supervisor, Sam Ladak, for his invaluable help, guidance, and infectious excitement for the subject. And of course, I would be nowhere without my fellow team members Matthew Hunt, Andrew May, Alaa Hejazi, Joseph Askey, and Edward Harding. I would like to thank you all for sharing your knowledge and helping me get to grips with all the equipment. I would also like to thank our annual summer students Jacquelyn Sharpe, Félix Gayot, Eloise Rahier, and David Evans, who were fantastic fun to work with. And of course, Myléne Carouel, the summer student who played a crucial role in the development of our fabrication methods.

I want to thank my family for always encouraging me not just to achieve as highly as possible, but to do so in something that brings joy and I can be passionate about.

Finally, I would like to thank my partner, Amy Paine, for always being there for me. For her understanding and compassion during the difficult times and making the good times even better.

Summary

Recent studies demonstrate the use of two-photon lithography (TPL) combined with line-of-sight (LOS) deposition to fabricate 3D artificial spin-ice (3DASI) systems comprising magnetic nanowires arranged in a diamond-bond lattice geometry. This thesis explores the micromagnetic studies performed for the initial lattice characterisation and later work demonstrating magnetic charge propagation within these lattices.

The fabrication method yields nanowires with a novel crescent-shaped cross-section; we explore the impact of this geometry on domain wall (DW) structure and magnetic reversal. We show that the wires are Ising-like: a single domain with a sharp transition between two well-defined states.

We computed spin textures, energies and surface charge associated with conventional artificial spin-ice vertex types. The ice-rule states are almost degenerate, and singly charged monopole excitations are stable. Computed surface charge densities aid the identification of magnetic charges and their propagation through the lattice.

We find that the energy associated with excitations upon surface coordination-two vertices is a factor ~3 larger than their counterparts upon coordination-four vertices in the bulk. The computed energies inform Monte-Carlo simulations performed by collaborators to reproduce experimental results.

Despite the success of TPL as a tool for magnetic nanostructure fabrication, LOS deposition yields thin substrate film interacting with functional components and producing spurious signals during measurements. Chapter 5 explores a poly(acrylic acid) sacrificial layer compatible with TPL and laser ablation to remove substrate film. The method produces isolated magnetic nanowires with no detectable film upon the substrate, and we introduce a nucleation pad to control DW injection. An out-of-plane perturbation is explored to control DW motion. The validity of the result is discussed.

The sacrificial layer procedure is applied to fabricating 3DASI lattices to show that previously detected low-field features due to background film in MOKE measurements are eliminated. We show that careful consideration of polariser and analyser angle in MOKE can be exploited to obtain depth-dependent switching information elucidating switching in the different sublattices.

Abstract

Three-dimensional magnetic nanostructures have become subject to recent intense interest due to the availability of new fabrication techniques. 3D nanostructured materials provide access to a host of new phenomena such as novel spin textures established by exotic 3D geometries and curvature, ultrafast domain walls beating the Walker limit, controlled spin-wave emission, and a plethora of technological applications.

Two-photon lithography (TPL) is a powerful tool facilitating the fabrication of 3D magnetic nanostructures, as has been demonstrated in recent work realizing a 3D lattice of nanowires arranged in a diamond bond structure. Initial experimental work has shown that this technique, when combined with thermal evaporation, can be used to produce 3D artificial spin-ice (3DASI) systems.

After providing a background to the relevant physics and experimental techniques, chapter 4 outlines a detailed micromagnetic study of key geometries that make up the experimental 3DASI lattice. This study provides a detailed understanding of switching in individual wires, coordination-two bipod structures present on the surface and coordination-four tetrapod structures present within the bulk. These studies provide a deeper understanding of measurements performed upon the system. TPL with line-of-sight (LOS) deposition results in magnetic nanowires with a crescent-shaped cross-section where non-uniform thickness and curvature leads to novel switching mechanisms and perturbs domain wall structure. Simulations show that the individual wires in the lattice

are Ising-like, single domain with sharp reversals between two well-defined states. The crescent-shaped cross-section perturbs domain wall structure and introduces novel edge states impacting switching. The Ising-like condition continues to hold in more complex geometries comprising these wires. Simulations exploring the switching in single wires, bipod systems, and tetrapod systems are explored and compared to experimental optical magnetometry.

Every permutation of magnetization within coordination-two and coordination-four vertices are simulated to obtain spin textures, energies, and magnetic surface charge density of conventional artificial spin-ice vertex types. The energies of ice-rule states are found to be almost degenerate, and high energy singly charged monopole states are shown to be stable. Doubly charged monopole states are not stable within the simulation geometries.

Computed magnetic surface charge density aids the identification of vertex types measured using magnetic force microscopy, enabling the identification of magnetic charges propagating through the lattice. The energy associated with a monopole excitation upon the surface coordination-two vertices of the 3DASI is shown to be a factor of ~3 higher than an excitation in the coordination-four vertices of the bulk. The utilisation of the calculated energies within Monte Carlo simulations performed by collaborators allowed a reasonable agreement to be obtained with experimental results.

Despite the success of TPL and LOS deposition as a tool for magnetic nanostructure fabrication, a limitation in the methodology comes from a thin film of the functional material being deposited on the substrate. In the case of magnetic materials, the substrate film may interact with the functional components and unwanted signals in measurements

using MOKE or other techniques where relatively large spot sizes capture background film. The presence of substrate film is then a limiting factor in the types of structures that may be fabricated using TPL and studied. Chapter 5 explores a modification to the TPL fabrication procedure to include a poly(acrylic acid) sacrificial layer compatible with TPL and laser ablation to create a process that removes the substrate film. The novel sacrificial layer process is used to produce isolated magnetic nanowires with no detectable material upon the substrate. MOKE measurements upon a simple nanowire show hysteresis loops with a sharp transition at 9.9 mT, the introduction of a large nucleation pad reduces the wire switching field to 1.63 mT, demonstrating controlled domain wall injection into the nanowire. We present a proof-of-principle of using 3D nanostructuring to introduce out-of-plane perturbations to control domain wall motion in the wires. Finite difference simulations elucidate the pinning mechanism at the proposed perturbation, and MOKE magnetometry suggests a 3mT pinning field. The validity of the pinning measurements is discussed. MOKE measurements performed on 3DASI lattices fabricated using the sacrificial layer approach show that previously detected low-field features due to background film were eliminated; this shows potential for MOKE as a technique to obtain depth-dependent switching information from our lattice. In particular, it is shown that the experimental parameters associated with MOKE, such as polarization and analyzer angle, can be used to help elucidate switching taking place upon the different sublattices.

The successful implementation of a sacrificial layer enables the use of TPL with line-of-sight deposition to produce a wide variety of interesting 3D geometries that have been explored within the literature. Examples include gaussian surfaces, which stabilize skyrmions and other topological spin textures. Experimental feasibility of domain wall

injection into a 3D nanowire system opens the possibility of realizing more complex domain wall circuits, approaching racetrack like devices. Finally, the work upon sacrificial layers and depth-dependent switching also has important implications for the study of 3DASI systems. Soon the group intends to study thermal systems. Here the removal of the sheet film will eliminate possible spurious signals from the substrate, whilst depth-dependent switching will allow the dynamic route to ground state to be studied.

1. Introduction

In the current generation of commercially available magnetic storage devices, we exploit magnetic domains on a 2D surface that can be magnetized either “up” or “down” out of the plane representing binary information. The most ubiquitous example of this is the hard disk drive (HDD) comprising a spinning disk and read/write head used to manipulate and measure the surface magnetization [1]. This technology has the advantage of being cheap, reliable, and offering high storage capacities. However, increasing demand for data storage capacity and higher read/write speeds presents increasing challenges for the technology. Storage capacity may be improved by increasing the density of the magnetic domains on the device; however, the commensurate reduction in magnetic domain size will ultimately result in domains small enough to switch between “up” and “down” due to random thermal fluctuations in this superparamagnetic limit [2]. An alternative is to increase the disk size; however, the rotation speeds must reduce to ensure mechanical stability, affecting read/write speeds. The latter challenge is primarily addressed by cloud computing, where the data is stored in high-efficiency data centres where additional storage requirements are easily addressed by adding more devices at minimal cost and effort. In these dedicated environments, the challenge becomes the management of heat generated by computing process. Strict climate control is then required in datacenters to ensure reliable operation of data storage devices [3] and is currently estimated to account

for 50% of a datacenter's energy consumption [4]. With global internet usage accounting for 10% of energy consumption [5], the case for more energy-efficient devices becomes clear.

An example of a proposed device capable of addressing these challenges is the magnetic racetrack memory proposed by Parkin et al. [6], comprising magnetic nanowires arranged in 3D space where magnetic domains along the wire length encode binary information (Figure 1-1). Spin-polarized currents passed through the wire move the magnetic domains across a set of read and write heads to measure and alter the state of the domains.

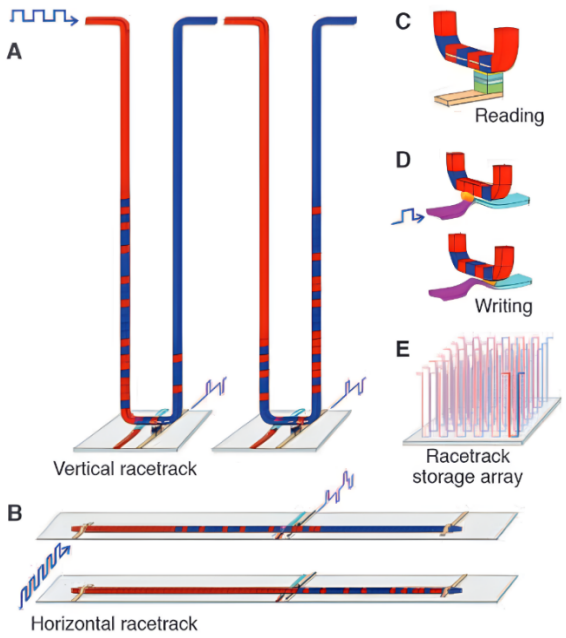

Figure 1-1 Magnetic racetrack memory device concept as proposed by Parkin et al. [6]. (a) U-shaped magnetic nanowires arranged vertically to ensure maximum storage density. Magnetic domains along the wire are used to encode binary information. The domains may be moved through the racetrack through the application of a spin-polarised current. (b) horizontal racetrack where the wire is parallel to the substrate. (c) using a magnetic tunnel junction, the orientation of the domain above the read-head may be measured. (d) The magnetisation of a domain may be manipulated using a local fields or spin-momentum transfer torque through spin-polarised currents perpendicular to the wire. (e) vertically arranged U-shaped wires may be placed in an array to scale the capacity of the device.

The proposed magnetic racetrack memory device has the advantage of being solid-state as the most common cause of defects in current generation HDDs is mechanical failure. Extending the storage capacity to a 3D volume improves current capacities, given the amount of unused space in current devices. The first 2D magnetic racetrack memory device realised by Parkin et al. comprised a set of planar permalloy magnetic nanowires with a set of notches along the wire acting as pinning sites for the magnetic domain walls (DW) [6]. This proof of concept demonstrated a device offering significant advantages over extant technologies with faster read/write speeds compared to HDD and orders of magnitude reduction in write energy per bit compared to flash memory. Furthermore, extending the technology to a 3D device allows the utilisation of empty space above a silicon wafer. However, the work outlines clear challenges with limitations in domain wall velocity and control over domain wall motion.

To offer competitive read and write speeds with current devices, one must be able to move domain walls through the wires at high velocities. Domain walls may be moved along a wire using external magnetic fields or spin-polarised currents with domain wall velocity increasing linearly with applied field and current. However, domain wall velocity is subject to the stability of the domain wall structure for planar wires, which breaks down at a critical value of an applied field or current, and the associated velocity is known as the Walker limit [7]. The walker limit arises due to deformation in the domain wall structure, yielding an increase in energy proportional to the square of the domain wall velocity akin to kinetic energy with an associated effective mass [8]. From this perspective, the walker limit represents the energy at which a single well-defined domain wall is no longer favourable, and Walker breakdown occurs.

As further detailed in section 3.2.7, the Walker limit in an idealised system shows a strong dependence on the nanowire geometry-dependent demagnetising tensor [9]; the domain wall's effective mass may be tuned or eliminated by varying nanowire geometry. Indeed, micromagnetic studies of low dimensional cylindrical nanowires and nanotubes reveal domain walls with zero effective mass beating the Walker limit and giving rise to exotic physics such as the spin-Cherenkov effect [10, 11] and new domain wall types [12]. Cylindrical nanowires fabricated using porous alumina templates with electrodeposition techniques allow the physics of domain walls in these systems to be studied [13-16], but techniques to cast these into arbitrary 3D geometries remain limited. Combining positive-tone photoresists structured using two-photon lithography with electrodeposition has shown promise to yield arbitrary 3D geometries [17]. However, dark erosion during photoresist development limits the feature size. A suggested alternative uses negative-tone photoresists for two-photon lithography not subject to dark erosion to produce templates for electrodeposition [18], enabling 3D nanostructuring of cylindrical nanowires in the ultrafast domain wall regime.

Parallel research efforts focus on controllable domain wall motion: functional domain wall devices require the ability to move domain walls reliably between well-defined positions and prevent any undesirable domain wall transport. There has been extensive work to control domain wall motion by introducing "pinning" via locally perturbing the domain wall potential through the introduction of notches [6, 19-23], curvature [24, 25], breaks [26], exchange bias [27], width modulation [28, 29], and local magnetostatic fields [30-32]. Despite the intense research effort into various pinning mechanisms, there is a paucity of research applying these to 3D systems. Furthermore, 3D geometries will

inherently contain some of these geometric features such as width modulation and curvature affecting domain wall motion and structure. The final challenge of realising functional 3D domain wall devices is the nanostructuring itself. As methods for producing 3D polymer and metallic structures are reaching maturity, intense research is needed to cast high-purity magnetic materials into complex 3D geometries.

Beyond the direct technological applications of 3D nanostructuring, there is also significant promise for fundamental research. Particularly pertinent to this thesis is the study of artificial spin-ice, which acts as a model system to study the physics of geometric frustration occurring when not all pairwise interactions within a system may be satisfied simultaneously. Geometric frustration has been shown to play an important role in molecular bonding in water ice [33], protein folding [34], and the production of solar flare phenomena [35]. In spin-ice, geometric frustration gives rise to emergent magnetic monopoles in the vector fields **M** and **H** [36] with its mesoscopic analogue, artificial spin-ice, being able to reproduce the essential physics of these systems [37]. Until recently, artificial spin-ice systems were only realized as two-dimensional and quasi-3D systems (2.5D) that do not fully capture the energetics required to realise a true mesoscopic analogue of bulk spin-ice.

Chapter 3 of this thesis explores the pertinent principles in magnetism from first principles, gives an outline of domain wall behaviour in magnetic nanowires, and an overview of the physics of spin-ice and artificial spin ice along with the challenges faced in this subject area. Chapter 4 outlines the experimental methods used to fabricate 3D magnetic nanostructures and the methods used for characterization and experimentation. The first empirical chapter (chapter 5) details micromagnetic studies performed to

contextualize and elucidate experimental results in our work to characterize a 3D artificial spin-ice system [38] and demonstrate magnetic charge propagation therein [39]. Our fabrication methodology utilizes two-photon lithography in combination with line-of-sight deposition through thermal evaporation of functional materials. This method has been shown to be a versatile approach to producing 3D magnetic nanostructures but suffers from background sheet film as the functional material is uniformly deposited on the samples. Traditional lithography techniques have used sacrificial layers to shield the substrate; Chapter 6 discusses the development of a method exploiting similar principles applied to two-photon lithography. Two-photon lithography is combined with a sacrificial layer and laser ablation to fabricate magnetic nanowires and show a proof of principle for domain wall injection in 3D magnetic nanowires. We explore the possibility of controlled domain wall motion via the introduction of a novel out-of-plane perturbation functioning as a pinning site in the wires. Finally, the chapter explores MOKE measurements of a 3DASI to demonstrate the ability to obtain depth-dependent switching information in the magnetic nanowire lattices.

2. 3D magnetic nanostructuring: the current state of the art.

Recent years have seen increasing interest in 3D magnetic nanostructures made accessible through the development of novel fabrication methods such as Focused Electron Beam Induced Deposition (FEBID) [40-43] and Two-Photon Lithography (TPL) [38, 39, 44].

FEBID is a direct-write method for nanostructure fabrication capable of achieving feature sizes similar to electron-beam lithography [45], with the additional benefit of enabling the fabrication of 3D nanostructures as shown in [43]. The process uses the injection of a precursor gas which adsorbs onto a surface, and a focussed electron beam provided by a scanning electron microscope (SEM) yields electron-induced dissociation at the focal spot. Electron-induced dissociation of precursor gases such as iron pentacarbonyl ($Fe(CO)_5$) and cobalt carbonyl ($Co_2(CO)_8$) yields volatile carbonyls whilst the metallic elements remain on the surface. FEBID uses modified SEM systems such that stage rotation, translation, and tilt may be exploited to create complex 3D geometries [42] (Figure 2-1). A wide range of available precursors offers great flexibility in materials, enabling the fabrication of 3D nanostructured metals, alloys, and superconductors.

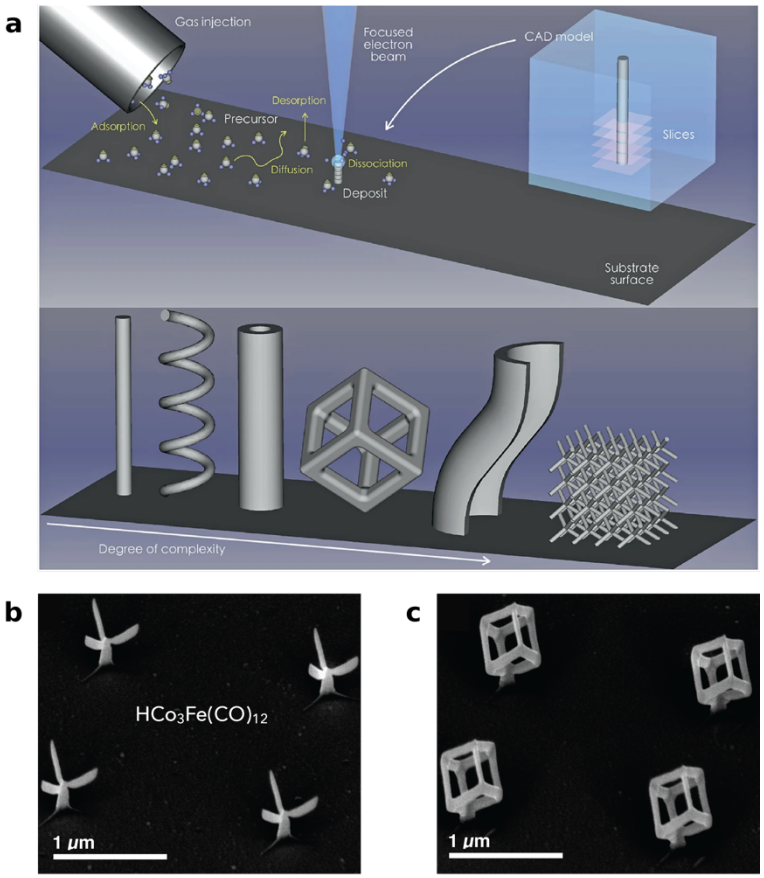

Figure 2-1 (a) outline of FEBID fabrication process. Precursor gases are injected to the target region where the gas adsorbs onto the surface. A focused electron beam at the target volume results in electron-induced dissociation yielding volatile gases and the metallic elements remain on the surface. Using stage translation, rotation, and tilt, FEBID enables the fabrication of complex 3D nanostructures. Figure adapted from [46]. (b&c) example magnetic nanostructures fabricated using FEBID [47, 48].

Despite the impressive feature sizes and relative ease of use, there remains a significant limitation for FEBID; the electron-dissociation process is not selective to the metal-carbon bonds in precursors used for magnetic materials, and volatile products may recombine with the deposited metal. These factors result in high levels of impurities which have a significant impact on the magnetic properties of the deposited material [49-51].

One area of interest regarding FEBID is the effort to improve nanostructure purity with particular gains made using in-situ local heating producing cobalt deposits with up to 80% purity [52], and 95% purity being achieved using ex-situ annealing during post-

processing [53]. These methods applied to metal carbonyl offer promising results, with the exception of nickel's principal carbonyl, nickel tetracarbonyl, being unfavourable due to its extreme toxicity [54]. Other nickel precursors are available, but the aforementioned processing techniques have thus far not resulted in high-purity deposits [54, 55]. Given the importance of Permalloy ($Ni_{81}Fe_{19}$) as a material in magnetism with vanishingly small magnetocrystalline anisotropy and low coercivity, this presents a significant challenge to the community.

Thermal evaporation is a simple method by which high-purity materials may be deposited, Sans-Hernandez et al used FEBID to produce platinum scaffolds upon which permalloy could be deposited using thermal evaporation [56]. By growing the nanowire at an angle to the substrate, the group was able to use a novel dark-field MOKE technique to characterise the wires. Despite the success of this work, its applicability is restricted to a limited set of geometries; in any optical magnetometry upon nanostructures orders of magnitude smaller than the focal spot, there must be careful consideration of signal from the substrate overwhelming signal from the region of interest.

One final limitation to FEBID pertinent to this thesis is the speed of the process with deposition rates well below 1 μm per second [57, 58]. Despite its impressive feature size, the technique is currently unsuitable for larger structures. Although unable to offer feature sizes competing with FEBID, two-photon lithography offers write speeds orders of magnitude larger (up to 10 mm s^{-1}) than FEBID. TPL harnesses two-photon absorption to induce polymerisation in a photoresist at a diffraction-limited focal spot of a femtosecond pulsed laser [59], with the relevant physics discussed in section 3.4 and methods in section 4.1 To produce 3D magnetic nanostructures, one may write channels in a positive-tone

photoresist which are back-filled with the desired functional materials using electrodeposition (Figure 2-2 a&b) [17]. However, dark erosion places significant limits on the achievable lateral feature size (>400 nm) and producing single-domain magnetic nanowires using this method remains a challenge. Recent focus on using TPL to realise 3D magnetic nanostructures uses a negative-tone resist to produce a scaffold upon which functional materials are cast (Figure 2-2 c) using thermal evaporation [38, 39], high-vacuum sputtering [60], electroless deposition [18, 61], or magnetron sputtering [62]. The focus of this work is magnetic nanostructures fabricated using a negative-tone resist in combination with thermal evaporation.

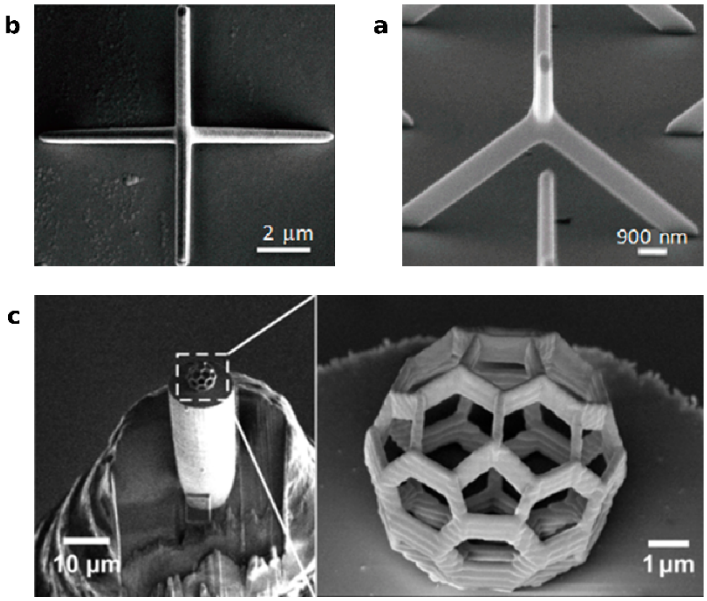

Figure 2-2 example structures fabricated using two-photon lithography. (a) tilted SEM of a tetrapod structure created using a positive tone resist and electrodeposition. After electrodeposition, the resist is stripped to leave an isolated metallic nanostructure. (b) top-down SEM of the structure shown in (a) revealing a ~400nm lateral feature size [17]. (c) SEM of buckyball nanostructure fabricated using a negative tone photoresist upon which a 30nm Cobalt layer was sputtered [60]

Standard commercial TPL systems offer a minimum feature size of ~160 nm for IPL-780 negative-tone photoresists which can be reduced using post-processing techniques

such as pyrolysis, oxygen plasma etching, or a combination of the two [63] as shown in Figure 2-3a.

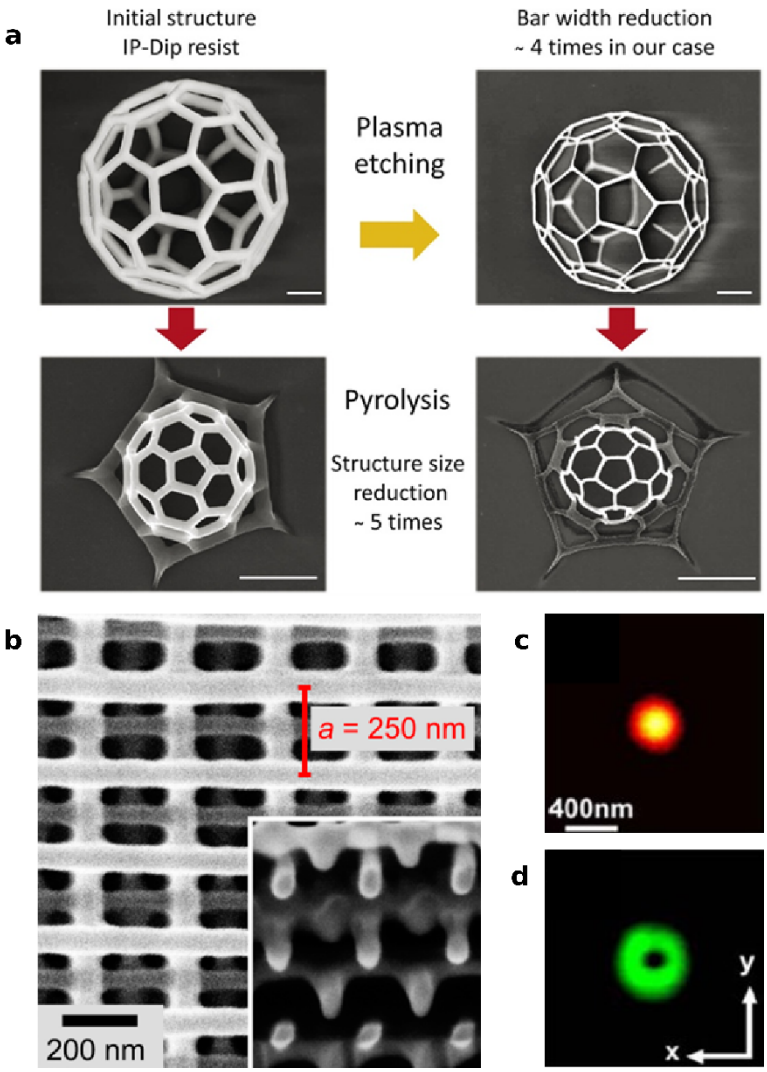

Figure 2-3 (a) SEM of buckyball nanostructure fabricated using TPL showing the reduction in feature size after plasma etching, pyrolysis, and a combination of the two [63]. (b) SEM of woodpile structure fabricated using TPL with a 405nm laser yielding a lateral feature size of 65 nm [64]. Measured lateral point spread function of lasers in STED TPL system at the focal spot (c) PSF of 780 nm stimulation laser (d) PSF of 532 nm depletion laser with phase mask applied yielding a ring-like focal spot [65].

Alternatively, modifications to standard systems have shown great progress in feature size reduction with feature sizes well below 100 nm. The most straightforward method is to replace the standard 780 nm laser with a 405 nm laser to reduce the focal spot size yielding the smallest reported lateral feature size of 65 nm in a woodpile structure

(Figure 2-3 b) [64]. Another approach known as stimulated emission depletion (STED) TPL uses a 780 nm laser with an additional 532 nm laser passed through a phase mask to generate a Laguerre-Gaussian mode at the focal spot. Figure 2-3 c & d show the point spread function of the primary activation laser and the depletion laser (respectively) in the focal plane. This ring-like intensity profile inhibits polymerisation to yield reported lateral feature sizes of 55 nm [65].

With promising advances in feature size for TPL using negative-tone photoresists and its high write speed, there is an exciting promise for 3D nanomagnetism when combined with thermal evaporation. There remains a key challenge as these deposition techniques are not selective; functional material is deposited on both the desired components and the substrate, which may result in undesirable interactions between the two. Using FEBID, Sans-Hernandez et al. grew platinum nanowires angled away from the substrate and cast permalloy upon the structures using thermal evaporation [56]. By placing the wire at an angle, the wire and film response could be measured with separate detectors (Figure 2-4 a), whilst adding a bridge to shadow the wire-substrate interface from the evaporation source, resulting in wires independent of the substrate film (Figure 2-4 b). This dark field MOKE method is reliant on the signal of the substrate and the nanostructure being reflected at separate and well-defined angles and is thus limited to simple geometries.

A later attempt at selectively depositing materials employed a sacrificial stencil mask written on the structure using TPL [66]. Spin-coating an SU8 (negative tone) photoresist onto a glass slide provides a sacrificial layer which is briefly exposed to UV light before IPL photoresist is drop-cast upon the sacrificial layer. The UV flashing polymerises the SU8 and provides a barrier preventing diffusion of layers. The desired nanostructure may then be

written in the same step as the sacrificial stencil mask, where the stencil mask is anchored only to the SU8 layer and not the substrate. After development in IPA which removes residual IPL whilst the SU8 remains unaffected, metals may be deposited using thermal evaporation exposing only the selected areas to the evaporation source. Finally, the sacrificial structure is removed in the standard SU8 developer.

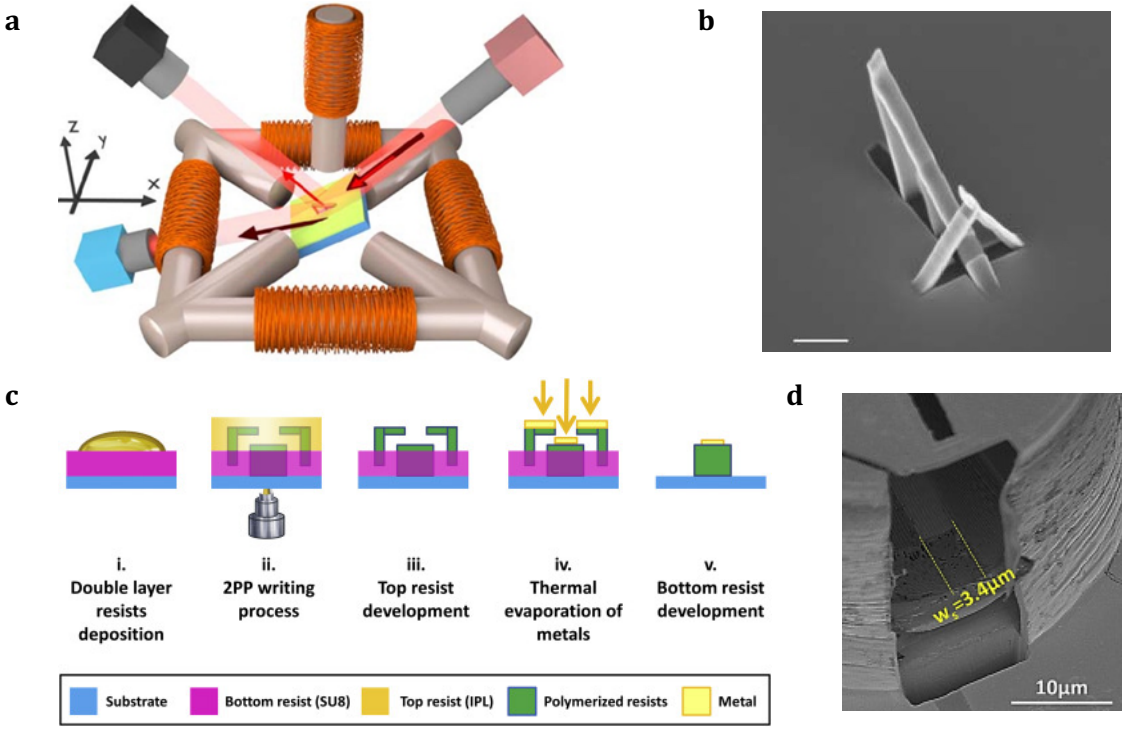

Figure 2-4 (a) dark-field MOKE configuration for measuring magnetic nanowires grown at an angle from the substrate. With different incident angles for the substrate and the nanowire, reflections off the substrate and the wire may be measured separately. (b) SEM of magnetic nanowire grown at an angle from the substrate using FEBID. A bridge structure shadows a section of the nanowire near the base to ensure the wire is disconnected from the substrate. Scale bar indicates **1 µm**. Panel a&b adapted from [56]. (c) outline of TPL fabrication method using sacrificial stencils enabling selective deposition of metals. (d) tilted SEM showing inside of sacrificial structure after evaporation indicating the position of a metallic nanowire deposited upon a pedestal. Panel c&d adapted from [66].

The process is outlined in (Figure 2-4 c)with an SEM image of the structure showing the sacrificial stencil and the deposited material underneath in Figure 2-4 d. These sacrificial stencils show promise for selective deposition upon 2D surfaces but are limited to 2D structures. At the very least, applying this method to 3D nanostructuring would be

prohibitively difficult. The intuitive next step to selective deposition is to remove the sacrificial stencil; with the material deposited on the polymerised SU8 film, one could directly deposit on the sample and perform a lift-off procedure. Unfortunately, lifting off the polymerised film requires an ultrasonic bath which can easily damage delicate 3D nanostructures.

The work presented in chapter 6 explores a novel method for fabricating 3D magnetic nanostructures using polyacrylic acid (PAA) as a sacrificial layer. PAA may be ablated using a femtosecond pulsed laser like those in TPL systems and remains unaffected by standard developer chemicals used in TPL whilst swelling in water. We show a proof-of-principle by fabricating a complex magnetic domain wall conduit without functional materials upon the substrate and demonstrate the feasibility of the method for the fabrication of 3D magnetic nanostructures.

3. Background

This chapter concerns the theoretical basis of the concepts pertinent to this work to establish a description of ferromagnetic materials, artificial spin ice, and magnetic domain wall structure. In addition, we explore the principles governing the fabrication techniques used for this work.

3.1. Basic Concepts

3.1.1. Magnetic Moments

The basic building block in any description of magnetism is the magnetic moment, and its response to external magnetic fields is essential in understanding dynamic processes. There exist two useful classical definitions of a magnetic moment. The first comprises a dipole moment between two hypothetical charges separated by some distance **d** as an analogy to an electric dipole, as shown in Figure 3-1a. The other definition is associated with the magnetic field generated by a closed loop of current, as shown in Figure 3-1b.

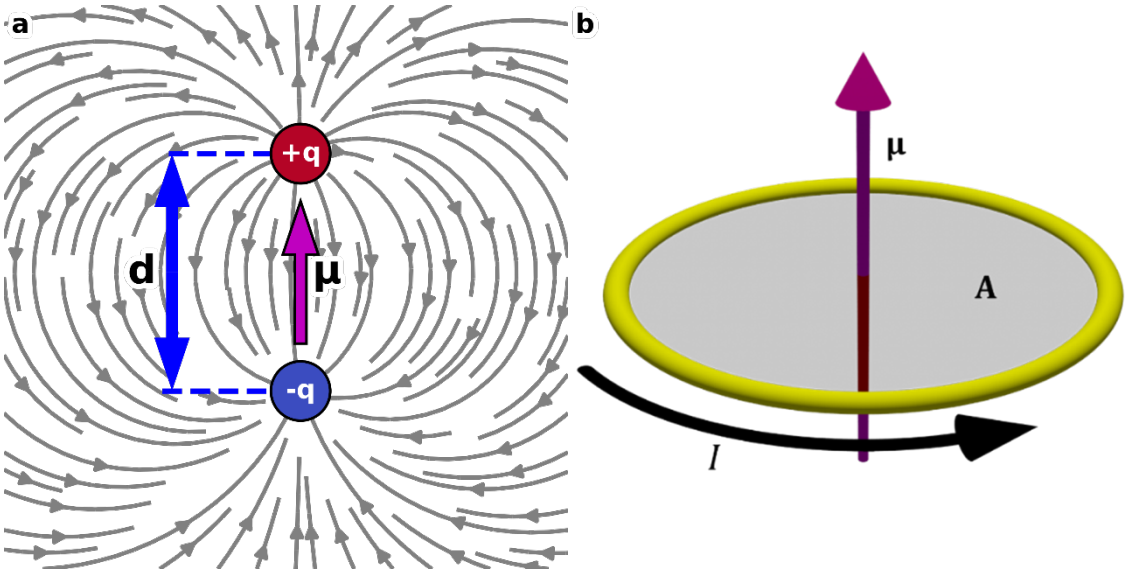

Figure 3-1 Depiction of definitions of magnetic moments. (a) Dipole model with two charges -q and q separated by a finite distance d. (b) Current flowing in a loop enclosing an area A.

In the case of the current loop, the magnetic moment is defined as the product of the magnitude of the current through the loop (I) and the normal vector of the area enclosed by the current loop ($\mathbf{A}$) [67]

$$\boldsymbol{\mu} = I\mathbf{A} \tag{3.1}$$

To determine the magnetic field ($\mathbf{B}$) at position $\mathbf{r}$ due to the current loop, we consider Ampère's circuital law in the steady-state which equates the curl of the magnetic field to the product of the permeability of free space (μ_0) and the current density ($\mathbf{j}$) at position ($\mathbf{r}'$):

$$\nabla \times \mathbf{B}(\mathbf{r}) = \mu_0 \mathbf{J}(\mathbf{r}') \tag{3.2}$$

And we choose the Coulomb gauge ($\mathbf{B} = \nabla \times \mathbf{A}$ and $\nabla \cdot \mathbf{A} = 0$) such that:

$$\nabla \times \mathbf{B} = \nabla \times (\nabla \times \mathbf{A}) = \nabla(\nabla \cdot \mathbf{A}) - \nabla^2 \mathbf{A} = -\nabla^2 \mathbf{A} \tag{3.3}$$

The vector **A** indicates the magnetic vector potential 3.1. Substituting 3.3 into 3.2 then yields:

$$\nabla^2 \mathbf{A} = -\mu_0 \mathbf{J}(\mathbf{r}') \tag{3.4}$$

Which is the Poisson Equation with the solution

$$\mathbf{A}(\mathbf{r}) = \frac{\mu_0}{4\pi} \int \frac{\mathbf{J}(\mathbf{r}')}{|\boldsymbol{r} - \boldsymbol{r}'|} d^3\mathbf{r}' \tag{3.5}$$

Given that $\mathbf{B} = \nabla \times \mathbf{A}$ and:

$$\nabla \times \frac{\mathbf{J}(\mathbf{r}')}{|\boldsymbol{r} - \boldsymbol{r}'|} = \frac{\mathbf{J}(\mathbf{r}') \times (\boldsymbol{r} - \boldsymbol{r}')}{|\boldsymbol{r} - \boldsymbol{r}'|^3} \tag{3.6}$$

It follows that

$$\mathbf{B}(\mathbf{r}) = \frac{\mu_0}{4\pi} \int \frac{\mathbf{J}(\mathbf{r}') \times (\boldsymbol{r} - \boldsymbol{r}')}{|\boldsymbol{r} - \boldsymbol{r}'|^3} d^3\mathbf{r}' \tag{3.7}$$

In differential form and taking that for a thin wire $\mathbf{j}(\mathbf{r}')\mathrm{d}^3\boldsymbol{r}' = Id\boldsymbol{\ell}$ and taking the limit where $\mathbf{r} = \mathbf{r}'$, we arrive at the familiar form of the Biot-Savart law:

$$d\mathbf{B}(\mathbf{r}) = \frac{\mu_0 I}{4\pi} \frac{d\boldsymbol{\ell} \times \boldsymbol{r}}{r^3} \tag{3.8}$$

It then follows that the magnetic field outside of the current loop is given by:

$$\mathbf{B} = \mu_0 \mathbf{H} = \frac{\mu_0}{4\pi}\left[\frac{3\mathbf{r}(\boldsymbol{\mu}\cdot\mathbf{r})}{r^5} - \frac{\boldsymbol{\mu}}{r^3}\right] \quad 3.9$$

The potential energy of a magnetic moment in a magnetic field is given by:

$$U = -\boldsymbol{\mu}\cdot\mathbf{B} \quad 3.10$$

Therefore, it follows that the force acting upon the magnetic moment is given by:

$$\mathbf{F} = -\nabla U = \nabla(\boldsymbol{\mu}\cdot\mathbf{B}) \quad 3.11$$

If we take the magnetic field due to one moment and introduce a second moment into the field, we find the dipole interaction energy due to the interaction between the moments through substitution of 3.9 into 3.10:

$$U = -(\boldsymbol{\mu}\cdot\mathbf{B}) = -\frac{\mu_0}{4\pi r^3}[3(\boldsymbol{\mu_1}\cdot\hat{\mathbf{r}})(\boldsymbol{\mu_2}\cdot\hat{\mathbf{r}}) - \boldsymbol{\mu_1}\cdot\boldsymbol{\mu_2}] \quad 3.12$$

3.1.2. Atomic Moments

3.1.2.1. Orbital Magnetic Moment

We may refer to the Rutherford model of the atom to establish an intuitive understanding of orbital magnetic moment. The Rutherford model posits electrons moving in circular orbits about the nucleus, which establishes small current loops. In this model, the current (I) of each orbit with radius r is given by the charge (e) of an electron divided by the orbital period $I = ev/2\pi r$. The moment of an electron in the simple case of a hydrogen atom is then found with the product of current and the area enclosed by the orbit as per equation 3.1:

$$\mu_L = IA = \frac{ev}{2\pi r}\, 2\pi r^2 = \frac{evr}{2} \tag{3.13}$$

This may also be expressed in terms of orbital angular momentum $L = mvr$ and the orbital gyromagnetic ratio $\gamma_L = e/2m_e$.

$$\mu_L = \frac{evr}{2} = \frac{e}{2m_e} L = \gamma_L L \tag{3.14}$$

This result does not account for the quantization of angular momentum (L), which is described in terms of a positive integer value known as the orbital quantum number ℓ (or, azimuthal quantum number) in the expression:

$$L^2 = \hbar^2 \ell(\ell + 1) \tag{3.15}$$

The azimuthal quantum number may take a non-negative integer value. Measuring a principal component of the angular momentum vector yields the result

$$L_{\hat{e}} = \hbar m_l \tag{3.16}$$

Where m_l is the magnetic quantum number and may take non-zero integer values from $-\ell$ to ℓ. In the simple case of the hydrogen atom with a single electron such that $L = \hbar$, the orbital magnetic moment is given by

$$\mu_L = \mu_B = \frac{e\hbar}{2m} = 9.27 \times 10^{-24} \text{A m}^2 \tag{3.17}$$

This value (μ_B) is known as the Bohr magneton, the most fundamental unit of magnetic moment.

3.1.2.2. Spin

The Stern-Gerlach experiment performed in 1922 used a collimated beam of silver atoms passed through a non-uniform magnetic field perpendicular to the beam[68]. The contemporarily dominant Bohr-Sommerfeld theory of quantum mechanics predicted the observed beam splitting along the magnetic field direction due to the quantization of orbital angular momentum. Gerlach used silver in his experiments to yield sufficient signal and was thought to have non-zero angular momentum due to a single valence electron. Later developments in quantum mechanics showed that this is incorrect with the single valence electron in the 5s orbital with an azimuthal quantum number $\ell = 0$ and, therefore, zero angular momentum. It follows that there must exist another source of angular momentum.

Wolfgang Pauli postulated an additional degree of freedom to explain hyperfine splitting in spectroscopic data in 1924. George Uhlenbeck and Samuel Goudsmit identified this as angular momentum intrinsic to the electron, or electron spin [69].

Spin angular momentum follows similar rules as those for orbital angular momentum outlined in equations 3.15 and 3.16 with the magnitude of the spin vector (S) in terms of the spin quantum number s:

$$S^2 = \hbar^2 s(s+1) \tag{3.18}$$

And the component of spin along any principal axis in a cartesian framework is given by:

$$S_{\hat{e}} = \hbar m_s \tag{3.19}$$

Where the subscript $\hat{e}$ indicates the unit vector associated with a cartesian axis, m_s gives the spin magnetic quantum number which may take values of $\mathcal{s}$ or $-\mathcal{s}$ where $\mathcal{s} = 1/2$ for all fermions. The magnetic moment of an electron is given by the expression

$$\mu_s = \gamma_s S = \pm\frac{\gamma_s \hbar}{2} \tag{3.20}$$

Where γ_s is the spin gyromagnetic ratio given by the ratio of electron charge and electron mass. The spin gyromagnetic ratio is related to the orbital gyromagnetic ratio according to:

$$\gamma_s = g\frac{e}{2m_e} = 2\gamma_L \tag{3.21}$$

Where g denotes the electron g-factor, a dimensionless constant with an experimentally determined value of $g \approx -2$. Substituting 3.21 into 3.20 gives the result that the electron's magnetic moment due to its intrinsic angular momentum is equal to the Bohr magneton at the aforementioned value of 9.27×10^{-24}A m^{-2}

$$\mu_s = \pm\gamma_s\frac{\hbar}{2} = \pm\gamma_L\hbar = \pm\frac{e\hbar}{2m_e} = \pm\mu_B \tag{3.22}$$

3.1.3. Spin-orbit coupling.

Orbital magnetic moment and spin magnetic moment were discussed in the previous sections; however, we must consider the interaction between the two. The most straightforward description can be found in the semiclassical Bohr-Sommerfeld description of the atom when considering a reference frame at rest with respect to the electron. In this picture, we observe the positively charged nucleus orbiting the electron.

Following the Biot-Savart 3.8, the magnetic field at the centre of a loop with radius r carrying a current I is given by:

$$\mathbf{B} = \frac{\mu_0}{4\pi r^3}\,\mathbf{I} \times \mathbf{r} \tag{3.23}$$

Which can be written in terms of the current being the product of charge (-*Ze*) and velocity (**v**) divided by the circumference of the current loop

$$\mathbf{B} = \frac{\mu_0}{4\pi}\frac{Ze}{r^3}\,\mathbf{v} \times \hat{\mathbf{r}} \tag{3.24}$$

Taking angular momentum as $\mathbf{L} = m\mathbf{r} \times \mathbf{v} = -m\mathbf{v} \times \mathbf{r}$

$$\mathbf{B} = -\frac{\mu_0}{4\pi}\frac{Ze}{mr^3}\mathbf{L} \tag{3.25}$$

Substitution into 3.10 then yields:

$$U = \frac{\mu_0}{4\pi}\frac{Ze}{mr^3}\mathbf{L} \cdot \mathbf{S} \tag{3.26}$$

Where S is the angular momentum which may take values of $\pm\,\hbar/2$ corresponding to spin-up $(+\,\hbar/2)$ and spin-down $(-\,\hbar/2)$ and implies an interaction between an electron's orbital angular momentum and its spin resulting in degeneracy lifting of electron orbitals with a single electron. The result also allows the definition of a useful quantity representing the total angular momentum as the sum of orbital angular momentum and spin angular momentum.

$$\mathbf{J} = \mathbf{L} + \mathbf{S} \tag{3.27}$$

3.1.3.1. Hund's first rule

Hund's first rule states that the term with the highest spin multiplicity has the lowest energy for a given electron configuration, implying that singly occupied orbitals are favoured over mixed states.

For a two-electron system, there exist four spin states α representing spin-"up" and β representing spin-"down". The wave function's spin component may then be written as:

i. $\chi(1,2) = \alpha(1)\alpha(2)$ ii. $\chi(1,2) = \beta(1)\beta(2)$
iii. $\chi(1,2) = \frac{1}{\sqrt{2}}\{\alpha(1)\beta(2) + \alpha(2)\beta(1)\}$ iv. $\chi(1,2) = \frac{1}{\sqrt{2}}\{\alpha(1)\beta(2) - \alpha(2)\beta(1)\}$

Expressions i, ii, and iii are symmetric under the exchange operator ($\hat{P}\psi = \psi$), whereas iv is antisymmetric under the exchange operator ($\hat{P}\psi = -\psi$). The wave function's spatial component, describing the electrons in state a or b, is given by the determinants of the 2×2 matrices:

$$\psi_{sym} = \frac{1}{\sqrt{2}}\begin{vmatrix}\psi_a(1) & -\psi_a(2)\\ \psi_b(1) & \psi_b(2)\end{vmatrix}, \qquad \psi_{asym} = \frac{1}{\sqrt{2}}\begin{vmatrix}\psi_a(1) & \psi_a(2)\\ \psi_b(1) & \psi_b(2)\end{vmatrix} \tag{3.28}$$

If we allow $\psi_b \rightarrow \psi_a$,

$$\psi_{sym} = \sqrt{2}\psi_a(1)\psi_a(2), \qquad \psi_{asym} = 0 \tag{3.29}$$

This indicates that allowing the two electrons to occupy the same state for the antisymmetric spatial component results in an unphysical zero-valued function for all space.

The complete wave functions are given by the product of the spin and spatial components, $\Psi = \chi\psi$ with the condition that the wave function must be antisymmetric for fermions ($\hat{P}\Psi = -\Psi$). Only one of the wave function components may be antisymmetric, adding the constraint that a wave function with spin components i, ii, or iii must have an antisymmetric spatial component. The function allowing these three spin states is the triplet state with $S = 1$ and multiplicity of 3. The function allowing only spin state iv has a multiplicity of 1 ($S = 0$) and is referred to as the singlet state.

The above is a simple proof of the Pauli exclusion principle stating that no two fermions may have the same quantum numbers: for $\alpha(1)\alpha(2)$ and $\beta(1)\beta(2)$, the electrons have the same spin quantum number and given that $\psi_b \rightarrow \psi_a$ yields an unphysical result for antisymmetric spatial components, the quantum numbers for the spatial component are necessarily different. Another key result is that the antisymmetric spatial component must be $\Psi = 0$ for $r = 0$, which is not required for the symmetric spatial component. This implies a larger separation between the electrons in a triplet state and reduces potential energy due to Coulomb interactions. Triplet states are lower energy and therefore favoured, as described by Hund's first rule.

3.1.3.2. Hund's Second Rule

Hund's second rule states that the state with the highest orbital angular momentum is the lowest energy state for a given multiplicity. A classical picture provides the intuitive explanation that the state with the highest orbital angular momentum is when electrons orbit in the same direction. The potential energy of a two-electron system is inversely proportional to their separation. Electron separation is maximized if their orbits are in the same direction (their orbital angular momenta are collinear), resulting in lower energy.

3.1.3.3. Hund's Third Rule

Finally, the third rule states that the state with the lowest value for the total angular momentum (J) is the lowest in energy for a less than half-filled outermost subshell. The state with the highest total angular momentum is the lowest energy state if the outermost subshell is more than half-filled. Equation 3.26 describes the energy of an electron with given orbital and spin angular momenta, and we defined the total angular momentum J in 3.27. It follows that:

$$\mathbf{J^2} = \mathbf{L}^2 + \boldsymbol{S}^2 + 2\mathbf{L}\cdot\mathbf{S} \rightarrow \mathbf{L}\cdot\mathbf{S} = \frac{1}{2}\left(\mathbf{J^2} - \mathbf{L^2} - \mathbf{S^2}\right) \quad 3.30$$

Replacing the RHS vectors with the eigenvalues of their corresponding operators :

$$\mathbf{L}\cdot\mathbf{S} = \frac{1}{2}(j(j+1) - \ell(\ell+1) - s(s+1)) \quad 3.31$$

Considering the energy expression given by 3.26, it is clear that the energy is lowest when **L** and **S** are collinear. It follows that orbitals fill with like spins before mixing of spin states. Orbital filling order gives rise to many important phenomena, ferromagnetism being the most pertinent for this work.

3.1.4. Spin coupling and the Exchange interaction

As discussed in section 3.1.3.1, no two electrons may be in a state described by the same quantum numbers; the result is that two electrons with like spin may not occupy the same spatial state. This gives rise to a series of interactions known as the exchange interactions, which are key to ferromagnetism. The antisymmetric spatial component of the wave function also results in the probability of electrons being close to each other, reducing

the electrostatic energy. Assuming the wave functions are normalized, the energy of the triplet (Ψ_T) and singlet (Ψ_S) states are given by:

$$E_T = \int \Psi_T^* \hat{\mathcal{H}} \Psi_T \, d\mathbf{r}_1 d\mathbf{r}_2$$

$$E_S = \int \Psi_S^* \hat{\mathcal{H}} \Psi_S \, d\mathbf{r}_1 d\mathbf{r}_2 \qquad 3.32$$

The difference in energy is then:

$$E_s - E_T = 2 \int \psi_a^*(\mathbf{r_1}) \psi_b^*(\mathbf{r_2}) \, \hat{\mathcal{H}} \psi_a(\boldsymbol{r_1}) \psi_b(\boldsymbol{r_2}) d\mathbf{r}_1 d\mathbf{r}_2 \qquad 3.33$$

The difference between triplet and single states may be parameterized in terms of $\boldsymbol{S_1} \cdot \boldsymbol{S_2}$ such that their interaction may be described with the spin component of the Hamiltonian:

$$\hat{\mathcal{H}} = \hat{\mathbf{S}}_\mathbf{1} \cdot \hat{\mathbf{S}}_\mathbf{2} \qquad 3.34$$

The $\hat{\boldsymbol{S}}_\mathbf{1}$ and $\hat{\boldsymbol{S}}_\mathbf{2}$ operators are Pauli matrices representing electron spin, and can be represented by a total spin operator $\hat{\mathbf{S}} = \hat{\mathbf{S}}_\mathbf{1} + \hat{\mathbf{S}}_\mathbf{2}$ to give:

$$\hat{\mathbf{S}}^\mathbf{2} = \hat{\mathbf{S}}_\mathbf{1}^\mathbf{2} + \hat{\mathbf{S}}_\mathbf{2}^\mathbf{2} + \mathbf{2}\hat{\mathbf{S}}_\mathbf{1} \cdot \hat{\mathbf{S}}_\mathbf{2} \rightarrow \hat{\boldsymbol{S}}_\mathbf{1} \cdot \hat{\boldsymbol{S}}_\mathbf{2} = \frac{\mathbf{1}}{\mathbf{2}} \left(\hat{\boldsymbol{S}}^\mathbf{2} - \hat{\boldsymbol{S}}_\mathbf{1}^\mathbf{2} - \hat{\boldsymbol{S}}_\mathbf{2}^\mathbf{2} \right) \qquad 3.35$$

The total spin of a two-electron system may be either s=1 or s=0, and the eigenvalue for $\hat{\mathbf{S}}^\mathbf{2}$ is $s(s+1)$ and therefore 0 for s=0 and 2 for s=1

$$\hat{\mathbf{S}}_1 \cdot \hat{\mathbf{S}}_2 = \begin{cases} \frac{1}{4}, & \text{for s} = 1 \\ -\frac{3}{4}, & \text{for s} = 0 \end{cases} \tag{3.36}$$

The Hamiltonian in 3.33 may then be written as

$$\widehat{\boldsymbol{\mathcal{H}}} = \frac{1}{4}(E_s + 3E_T) - (E_s - E_T)\hat{\mathbf{S}}_1 \cdot \hat{\boldsymbol{S}}_2 \tag{3.37}$$

The first term is a constant, which may be included in other constant terms of the Hamiltonian. We can define an exchange constant representing the energy difference between the singlet and triplet state.

$$J = \frac{E_s - E_T}{2} = \int \psi_a^*(\mathbf{r_1})\psi_b^*(\mathbf{r_2})\,\widehat{\mathcal{H}}\psi_a(\boldsymbol{r_1})\psi_b(\boldsymbol{r_2})d\mathbf{r}_1 d\mathbf{r}_2 \tag{3.38}$$

And we rewrite the second spin-dependent term of 3.37

$$\widehat{\mathcal{H}}_{spin} = -2J\hat{\mathbf{S}}_1 \cdot \hat{\mathbf{S}}_2 \tag{3.39}$$

Summation over all spins gives the Hamiltonian of the Heisenberg exchange model:

$$\mathcal{H} = -\sum_{ij} J_{ij}\hat{\mathbf{S}}_\mathbf{i} \cdot \hat{\mathbf{S}}_\mathbf{j} \tag{3.40}$$

The dimensionality of the Heisenberg exchange model is D=3, such that the spins may lie in any direction in 3D space. Another useful related model is the Ising model, where the direction of the spin may only lie along one axis.

$$\mathcal{H} = -\sum_{ij} J_{ij} \hat{\mathbf{S}}^{\mathbf{z}}_{\mathbf{i}} \cdot \hat{\mathbf{S}}^{\mathbf{z}}_{\mathbf{j}} \qquad 3.41$$

3.1.4.1. Direct Exchange

Thus far, we have only considered the exchange interaction in terms of single atoms; however, its significance for ferromagnetism arises when considering overlapping orbitals from adjacent atoms forming molecular orbitals.

Contrary to the single atom system, singlet states are energetically favourable in Bonding Molecular Orbitals (BMO), increasing electron densities between nuclei such that the electrostatic interactions between nuclei are shielded. Antibonding Molecular Orbitals (ABMO) are triplet states, and as such, the spatial component of the wave function is zero between the nuclei. Lower electron density between adjacent nuclei reduces shielding and results in greater electrostatic interactions between nuclei. ABMO probability envelopes are also smaller, resulting in greater kinetic energy due to confinement.

As the singlet state is lower in energy than the triplet state, the exchange integral 3.38 is negative. It follows that the first five transition metals in the 3d band are antiferromagnetic as atoms bond only via BMO. Iron, cobalt, and nickel bonding via ABMOs and are therefore ferromagnetic. We refer to this interaction as 'direct exchange'. However, it becomes clear that this reasoning is incomplete: copper and zinc bond via ABMO but are not ferromagnetic. The interaction requires an overlap of electron orbits, and 4f electrons are highly localized, yet elemental gadolinium, terbium, and dysprosium are ferromagnetic at low temperatures.

The exchange integral can be expressed as a function of the distance between atomic cores (r_{ab}), the distance between electrons (r_{12}) and the distance between the electrons and their respective nuclei (r_{a2}, r_{b1}) [70]:

$$\mathcal{J}_{12} = \iint \Psi_a^*(r_1)\Psi_b^*(r_2)\left[\frac{1}{r_{ab}} - \frac{1}{r_{a2}} - \frac{1}{r_{b1}} - \frac{1}{r_{12}}\right]\Psi_a^*(r_1)\Psi_b^*(r_2)\mathrm{dV} \qquad 3.42$$

Giving rise to the Bethe Slater curve (Figure 3-2) describing the exchange integral as a function of the ratio of the interatomic spacing (r_{ab}) and the d-orbital radius r_d.

The Bethe Slater curve correctly predicts antiferromagnetism at small interatomic distances, ferromagnetism at intermediate interatomic distances, and a lack of magnetic ordering at larger distances. In addition, the curve predicts ferromagnetic properties in materials such as Heusler alloys (Cu_2MnSn, CU_2MnAl).

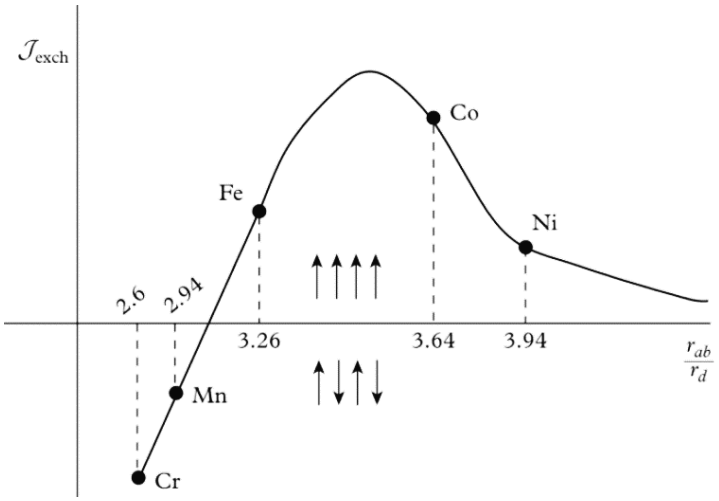

Figure 3-2 Bethe Slater curve illustrating that a favourable ratio between interatomic spacing and orbital radius is required for ferromagnetism [70]

3.1.4.2. Stoner Condition

There remains one part of the puzzle that is not explained by the aforementioned concepts. The magnetic moment per atom of iron is 2.2 μ_B, considering moments localized

to an atom, we would expect integer multiples of a Bohr magneton. A non-integer value suggests magnetization arising due to spin-split electronic bands.

We take spin-down electrons at the Fermi surface from the spin-down band and place these into the spin-up band as shown in Figure 3-3. The initial energies of these electrons range from $E_F - \delta E$ to E_F and the final energies range from E_F to $E_F + \delta E$, the average change is then δE. The number of electrons moved is $g(E)\,\delta E/2$ such that the total change in kinetic energy is then:

$$\Delta \mathrm{T} = \frac{1}{2} g(E)(\delta E)^2 \qquad 3.43$$

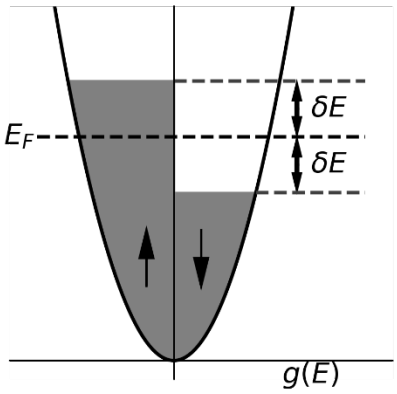

Figure 3-3 Density of states for spin-up and spin-down bands with electrons moved from the spin-down to the spin-up band.

The number densities of up spins ($n_\uparrow$) and down spins ($n_\downarrow$) is then:

$$\mathrm{n}_\uparrow = \frac{1}{2}(n + g(E_F)\delta E\,, \qquad n_\downarrow = \frac{1}{2}(n - g(E_F)\delta E) \qquad 3.44$$

With the electron magnetic moment equal to a Bohr magneton, the magnetization is given by:

$$\mathrm{M} = \mu_{\mathrm{B}}(n_{\uparrow} - n_{\downarrow}) \tag{3.45}$$

and the spin-orbit coupling constant λ, the change in potential energy due to the molecular field is then given by

$$\Delta\mathrm{U} = -\int_0^{\mathrm{M}} \mu_0(\lambda M')\, dM' = -\frac{1}{2}\mu_0\mu_B^2\lambda(n_{\uparrow} - n_{\downarrow}) = -\frac{1}{2}\mu_0\mu_B^2\lambda(g(E_F)\delta E)^2 \tag{3.46}$$

Adding equation 3.43 to 3.46 gives the total energy change:

$$\Delta\mathrm{E} = \Delta\mathrm{T} + \Delta\mathrm{U} = \frac{1}{2}g(E)(\delta E)^2[1 - \mu_0\mu_B^2\lambda g(E_F)] \tag{3.47}$$

Spontaneous magnetization is then possible if $\Delta E < 0$ and implies that

$$\mu_0\mu_B^2\lambda g(E_F) \geq 1 \tag{3.48}$$

This is known as the Stoner condition; spontaneous magnetization is energetically favourable for a high density of states at the Fermi level and strong coulomb effects seen in direct exchange.

3.1.5. Magnetocrystalline Anisotropy

For most ferromagnetic materials, the energy required to magnetize a sample is direction-dependent due to an intrinsic anisotropy attributed to the crystal structure and composition. The primary source of this magnetocrystalline anisotropy (MCA) is the spin-orbit interaction as electrons couple with the crystal electric field. A smaller contribution is

then found from spin coupling in the crystal. We can then define the magnetocrystalline energy as the work required to rotate the magnetic moment from the easy axis (lowest energy) to the hard axis (highest energy).

For uniaxial anisotropy, where there is one hard axis, the energy density is given by the power series:

$$\mathcal{E}_{anis} = \sum_{n} K_{u_n} \sin^{2n} \theta \tag{3.49}$$

Where θ is the angle between the moment and the easy axis, K_{u_n} is the nth anisotropy constant where magnetization-orientation curves show this to become vanishingly small beyond the second term such that the series can be expanded to:

$$\mathcal{E}_{anis} = K_{u_0} + K_{u_1} \sin^2 \theta + K_{u_2} \sin^4 \theta \tag{3.50}$$

As the K_{u_0} term has no dependence on direction, and it is often neglected.

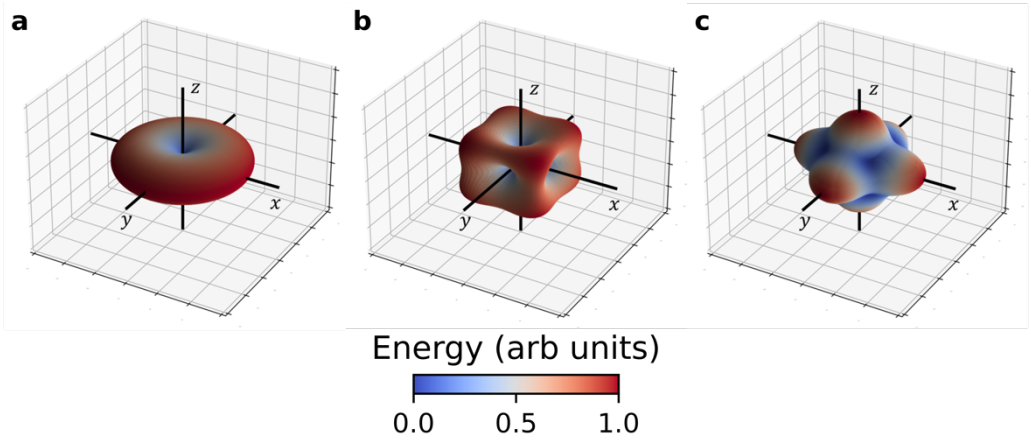

Figure 3-4 First order anisotropy energy surfaces for (a) cobalt, (b) iron, (c) nickel. The radial coordinate of each point on the surface is highlighted using the colourmap and indicates the energy associated with the given direction. Surface were computed using eq 3.50 and values shown in Table 3-1.

Figure 3-4 shows energy surfaces for the ferromagnetic transition metals where cobalt (Figure 3-4a) has a uniaxial anisotropy term due to the hexagonal close-packed (hcp) crystal structure. The body-centred cubic (bcc) structure of iron (Figure 3-4b) results in a cubic anisotropy with easy axes along the principal axes. The face-centred cubic (fcc) of nickel (Figure 3-4c) results in a cubic anisotropy with the hard axes along the principal axes. Typical values for the anisotropy constants of Iron and Nickel are shown in Table 3-1.

Material	$\boldsymbol{K_1}\ (\mathbf{J\,m^{-3}})$	$\boldsymbol{K_2}\ (\mathbf{J\,m^{-3}})$
Fe	4.8×10^4	5.0×10^3
Ni	-4.5×10^3	-2.3×10^3

Table 3-1 Typical room temperature values of anisotropy constants for Iron and Nickel [70].

The expressions given for these simple elemental materials are approximations derived using perturbative methods and are therefore approximations. Computing the anisotropy energy terms for alloys becomes prohibitively challenging, and a phenomenological approach is therefore favoured. Experimental characterisation of Nickel-Iron alloys show that the magnetocrystalline anisotropy constants approach zero for Permalloy $Ni_{81}Fe_{19}$ rendering the material ideal for a range of engineering applications and studying phenomena emergent due to the other energy terms [71].

3.2. Continuum Approximation

Thus far, this chapter has only considered individual moments and interactions at ranges shorter than the exchange length λ_E. At this juncture, it is more practical to consider scales large enough such that the continuum condition holds. In the mesoscopic range, the total magnetic moment per unit volume is given by the magnetization defined by:

$$\mathbf{M} = \frac{1}{V}\sum \boldsymbol{\mu} \tag{3.51}$$

Analogous to equation 3.10, the potential energy of a magnetized volume in an external magnetic field, known as the Zeeman energy, is then given by:

$$E_{zeeman} = -\mu_0 \int_V \mathbf{M} \cdot \mathbf{H}_{ext}\, dV \tag{3.52}$$

The other energy terms discussed in prior sections may also be described in terms of magnetization using Brown's equations. The exchange energy is given by:

$$E_{ex} = A \int_V \left[(\nabla m_x)^2 + \left(\nabla m_y\right)^2 + (\nabla m_z)^2 \right] dV \tag{3.53}$$

Where A_{ex} is the exchange stiffness as a function of the exchange constant J, the magnitude of the spin magnetic moment S, the lattice parameter a, and a lattice structure-dependent constant C in the expression:

$$A_{ex} = \frac{JS^2}{a} C \tag{3.54}$$

Finally, the magnetocrystalline anisotropy energy is then the volume integral of the anisotropy energy density function $\mathcal{E}_{anis}(\mathbf{m})$.

$$E_{anis} = \int_V \mathcal{E}_{anis}(\mathbf{m})\ dV \tag{3.55}$$

3.2.1. Demagnetizing Energy

The magnetic field due to a magnetic moment is given by equation 3.9; we can extend this to the field associated with the magnetization **M** by considering Ampère's law [72]

$$\nabla \times \mathbf{H} = 0 \tag{3.56}$$

Gauss's law for magnetism

$$\nabla \cdot \mathbf{B} = 0 \tag{3.57}$$

And the relationship between flux density (**B**), the applied field, and the magnetization

$$\mathbf{B} = \mu_0(\mathbf{M} + \mathbf{H}) \tag{3.58}$$

3.56 can be expressed in terms of the scalar potential

$$\mathbf{H} = -\nabla U \tag{3.59}$$

Substituting 3.59 and 3.58 into 3.57 yields

$$\nabla^2 U = \nabla \cdot \mathbf{M} \tag{3.60}$$

Where $\nabla \cdot \mathbf{M}$ is also referred to as the magnetic charge. At the surface of a magnet, there exist the boundary conditions that the component of **H** parallel to the surface and the component of **B** perpendicular to the surface must both be continuous. With consideration that $\mathbf{M} = 0$ outside the magnet, leading to the boundary conditions at the interface:

$$U_{int} = U_{ext} \tag{3.61}$$

$$\partial_n U_{int} = \partial_n U_{ext} + \mathbf{M} \cdot \mathbf{n} \tag{3.62}$$

Where $\mathbf{n}$ is the surface normal, and ∂_n gives the derivative with respect to distance from the surface. The magnetostatic potential is the unique potential that satisfies these conditions, and the gradient of the potential yields the stray field outside the magnet and the demagnetization field inside the magnet. The demagnetization energy is the energy associated with the magnetization of the magnet in the demagnetization field ($\mathbf{H}_d$) and takes the form:

$$E_d = -\frac{\mu_0}{2} \int_V \mathbf{M} \cdot \mathbf{H}_\mathrm{d} \, dV \tag{3.63}$$

For specific idealized geometries such as thin-films, cylinders, and ellipsoids, determining the demagnetization field is straightforward using the negative product of the demagnetization tensor and the magnetization.

$$\mathbf{H}_d = -\boldsymbol{N}\mathbf{M} \tag{3.64}$$

For magnetization along one of the principal axes, the demagnetization tensor may be diagonalized with a trace equal to 1.

$$\underline{\boldsymbol{N}} = \begin{pmatrix} N_x & 0 & 0 \\ 0 & N_y & 0 \\ 0 & 0 & N_z \end{pmatrix}, \qquad \mathrm{Tr}\left(\underline{\boldsymbol{N}}\right) = N_x + N_y + N_z = 1 \tag{3.65}$$

A commonly used special case is the ellipsoid, where the dimensions may be scaled to approximate infinite cylinders or thin films. Taking the axes, a, b, and c as being collinear

with the principal axes x, y, and z respectively, symmetry indicates that $\mathrm{N}_x = \mathrm{N}_y = \mathrm{N}_z = 1/3$ for a sphere as $a = b = c$. Figure 3-5a shows numerical calculations for the demagnetizing factor as a function of the aspect ratio a/b with $b = c$. As a/b approaches infinity, the geometry approximates a cylinder with $\mathrm{N}_x = 0\,, \mathrm{N}_y = \mathrm{N}_z = 1/2$. Similarly, Figure 3-5b shows numerical calculations for the demagnetizing factor as a function of the ratio b/c with $a = \infty$ such that the geometry is a cylinder. With $b \to \infty$, the geometry approximates a thin film with $\mathrm{N}_x = \mathrm{N}_y = 0$, and $\mathrm{N}_z = 1$.

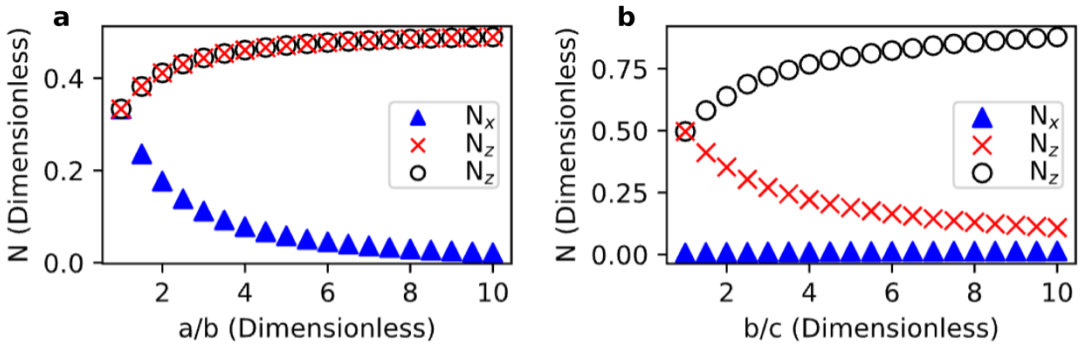

Figure 3-5 Micromagnetic computations of Demagnetizing factor of ellipsoids (a) as a function of the ratio between semi-major axis a and b. (b) infinite cylinders with aspect ratio given by b/c

Osborn [73] developed analytical derivations of the demagnetizing factor for these special cases. However, the complexity of the computations for other geometries renders the exercise impractical and numerical methods are favoured. Equation 3.62 indicates that magnetization parallel to the surface is energetically favourable. Considering the results for the demagnetizing factor, equations 3.63 and 3.64 show that the demagnetization energy is lowest with a magnetization along the longest axis of the geometry.

3.2.2. Curvature driven energy terms

Moments lie parallel to the surface to minimize demagnetization energy, and exchange energy is minimized by moments aligning. An important consideration in this work is the effect of a curved surface where both cannot be satisfied; magnetic moments tangent to the surface minimize demagnetization energy, but at the cost of exchange energy. Alternatively, aligning moments results in minimum exchange energy at the cost of demagnetization energy.

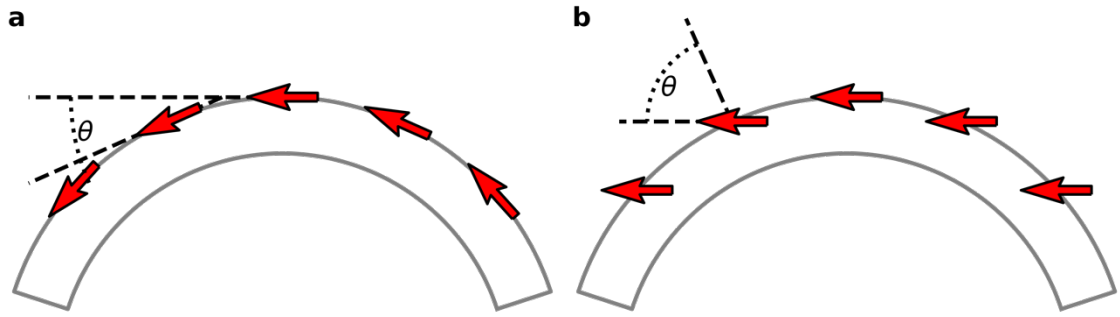

Figure 3-6 Magnetic moments on a curved surface. (a) moments are tangent to the surface such that $\mathbf{n} \cdot \mathbf{M} = 0$ thus minimizing demagnetization energy at the cost of exchange energy. (b) Moments are aligned to minimize exchange energy, leading to non-zero demagnetization energy as $\mathbf{n} \cdot \mathbf{M} \neq 0$.

Recent literature describes this trade-off as additional terms for the exchange energy [74]. The authors use a general Ginzburg-Landau vector model with the energy functional applied to Heisenberg magnets:

$$E = \int [\ell^2 \mathcal{E}_{ex} + \lambda(\mathbf{m} \cdot \mathbf{n})^2 \,] dV \qquad 3.66$$

The first term refers to the exchange energy density, whereas the second term describes the demagnetization energy density in terms of some anisotropy constant λ and the unit vector $\mathbf{n}$ denoting the anisotropy axis. When considering curved surfaces, the

Frenet-Serret frame provides a more intuitive set of basis vectors describing directions tangent ($\mathbf{e_1}$), normal ($\mathbf{e_2}$), and binormal ($\mathbf{e_3}$) to a curve parameterised in terms of arclength s: $\boldsymbol{\gamma} = \boldsymbol{\gamma}(s)$. We define the basis vectors as:

$$\mathbf{e_1} = \boldsymbol{\gamma}' , \qquad \mathbf{e_2} = \frac{\mathbf{e_1'}}{\left|\mathbf{e_1'}\right|} , \qquad \mathbf{e_2} = \mathbf{e_1} \times \mathbf{e_2} \tag{3.67}$$

Where the prime indicates the derivative with respect to arclength s where $|\gamma'| = 1$. Following the source, we use Latin indices to indicate the cartesian frame and Greek indices to indicate the Frenet-Serret frame such that $\hat{\mathbf{x}}_\mathbf{i}$ indicate cartesian basis vectors and $\hat{\mathbf{e}}_\boldsymbol{\alpha}$ indicate curvilinear basis vectors. The exchange energy term in 3.66 is given in the cartesian frame as:

$$E_{ex} = (\nabla \mathbf{m_i})(\nabla \mathbf{m_i}) \tag{3.68}$$

And the cartesian magnetization vector can be expressed in terms of the Frenet-Serret basis

$$m_i = m_\alpha (\boldsymbol{e_\alpha} \cdot \hat{\boldsymbol{x}}_\boldsymbol{i}) \tag{3.69}$$

Substituting into 3.68 and applying the curvilinear form of the del operator yields

$$E_{ex} = (m_\alpha e_\alpha)' \left(m_\beta e_\beta\right)' \tag{3.70}$$

Considering the differential properties of the curve in the Frenet-Serret frame

$$e_\alpha' = F_{\alpha\beta} e_\beta , \qquad \left|\left|F_{\alpha\beta}\right|\right| = \begin{pmatrix} 0 & \kappa & 0 \\ -\kappa & 0 & \tau \\ 0 & -\tau & 0 \end{pmatrix} \tag{3.71}$$

Where κ and τ represent curvature and torsion, 3.70 gives the sum of three terms:

$$E_{ex}^{0} = m'_{\alpha} m'_{\alpha} = |\mathbf{m}'|^2 \tag{3.72}$$

$$E_{ex}^{A} = K_{\alpha\beta} m_{\alpha} m_{\beta} \,, \qquad \left|\left|K_{\alpha\beta}\right|\right| = \begin{pmatrix} \kappa^2 & 0 & -\kappa\tau \\ 0 & \kappa^2 + \tau^2 & 0 \\ -\kappa\tau & 0 & \tau^2 \end{pmatrix} \tag{3.73}$$

$$E_{ex}^{D} = F_{\alpha\beta}\left(m_{\alpha} m'_{\beta} - m'_{\alpha} m_{\beta}\right) \tag{3.74}$$

The first term E_{Ex}^{0} is the familiar expression for the exchange energy density in simple planar wires. E_{ex}^{A} and E_{ex}^{D} represent curvature and torsion induced Anisotropy-like and Dzyaloshinskii-Moriya-like interactions, respectively.

These results demonstrate the introduction of a geometric potential due to curvature, which may impact domain wall structure and dynamics. The fabrication methods used for this work result in wires with a crescent-shaped cross-section, and curvature must therefore be considered to interpret the results.

3.2.3. Magnetic Domains

To minimize exchange energy, moments in a ferromagnetic material tend to align. However, aligned moments result in a large stray field and the associated magnetostatic energy. The total energy is minimised by forming magnetic domains: small regions in a material where moments are aligned to minimize exchange energy, but each region's net magnetization orients minimize the stray field. There exists a region between each domain known as a domain wall. These are the structures primarily of interest in this work, and one of the key focuses of research in the magnetism community.

3.2.4. Magnetic Domain Walls

If we consider an infinitesimally thin transition between two magnetic domains with opposing magnetization, we see from equation 3.39 that the exchange energy associated with two moments on either side of the transition is $\mathcal{E}_{ex} = -2JS^2 \cos\pi = 2JS^2$. It is therefore energetically favourable for a wider transition to form as the angle between adjacent moments is reduced to π/N such that $\mathcal{E}_{ex} \approx -2JS^2(\pi/N)^2$ for a sufficiently large N. This relation favours large N, as the energy is minimum as N approaches infinity. However, a wide domain wall comes at the cost of demagnetization and magnetocrystalline energy as moments in the transition region deviate from their easy axis. Common 180-degree domain wall types in thin films are Néel and Bloch walls where the magnetization rotates about the axis perpendicular to the surface in Néel walls and about the axis perpendicular to the wall in the case of Bloch Walls as shown in Figure 3-7.

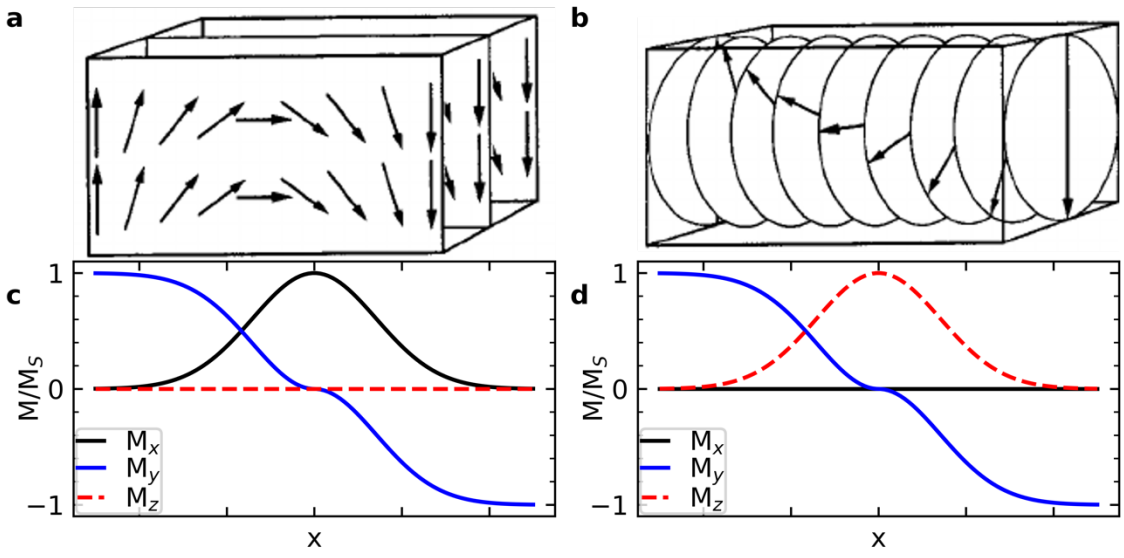

Figure 3-7 Schematic of the magnetization across a side-to-side Néel wall with the transition along x and the wall in the y-z plane. (b) Schematic of the magnetization across a Bloch wall with the transition along x and the wall in the y-z plane [75]. (c) line profile of magnetization in panel a. (d) line profile of the magnetization in panel b.

In thin films, the demagnetization tensor in equation 3.65 has the components $Nx = Ny = 0, Nz = 1$ indicating that tlarge demagnetization energy is associated with an out-of-plane magnetization; a Néel wall is energetically favourable. The two types become degenerate in bulk materials, with their widths determined by exchange energy and magnetocrystalline anisotropy energy. The theoretical width (W_L) of a 180° domain wall for the case of a uniaxial crystal is given by the expression:

$$W_L = \pi \sqrt{\frac{A}{K}} \qquad 3.75$$

Where A is the exchange stiffness constant, and K is the uniaxial anisotropy constant. This work is concerned with high aspect ratio permalloy ($Ni_{81}Fe_{19}$) nanowires. The anisotropy constant of $Ni_{81}Fe_{19}$ is vanishingly small, and as such, our concern is with exchange energy and magnetostatic energy when describing domain wall structure.

3.2.5. Domain Walls in Magnetic Nanowires

The trace of the demagnetization tensor must be equal to 1, as shown in equation 3.65, however, $N_x \approx 0$ for infinite magnetic nanowires with their long axis along x (which is the convention that is used unless otherwise stated in this work). For a thin rectangular nanostrip with no magnetocrystalline anisotropy, it is clear that a Néel wall (Figure 3-8a) is favourable. However, at the centre of the wall, the moment is perpendicular to the surface, increasing demagnetization energy (Figure 3-8b). The exchange energy density of the wall is shown in Figure 3-8c. Increasing the wall width decreases the exchange energy density but increase the demagnetization energy. In magnetic nanowires, the Néel wall is more commonly referred to as a transverse domain wall (TDW).

An increase in the wire thickness and width increases the demagnetization energy of the wall with increasing moment perpendicular to the surface. Beyond a certain width or thickness, a vortex domain wall (VDW) (Figure 3-8d) becomes energetically favourable. With very few moments perpendicular to a surface, the demagnetization energy of VDWs is lower than a TDW in the same wire. The demagnetization energy density is shown in Figure 3-8e. The vortex structure results in the angle between adjacent moments being larger than the case of TDWs; as such, the savings in the demagnetization energy come at the cost of exchange energy.

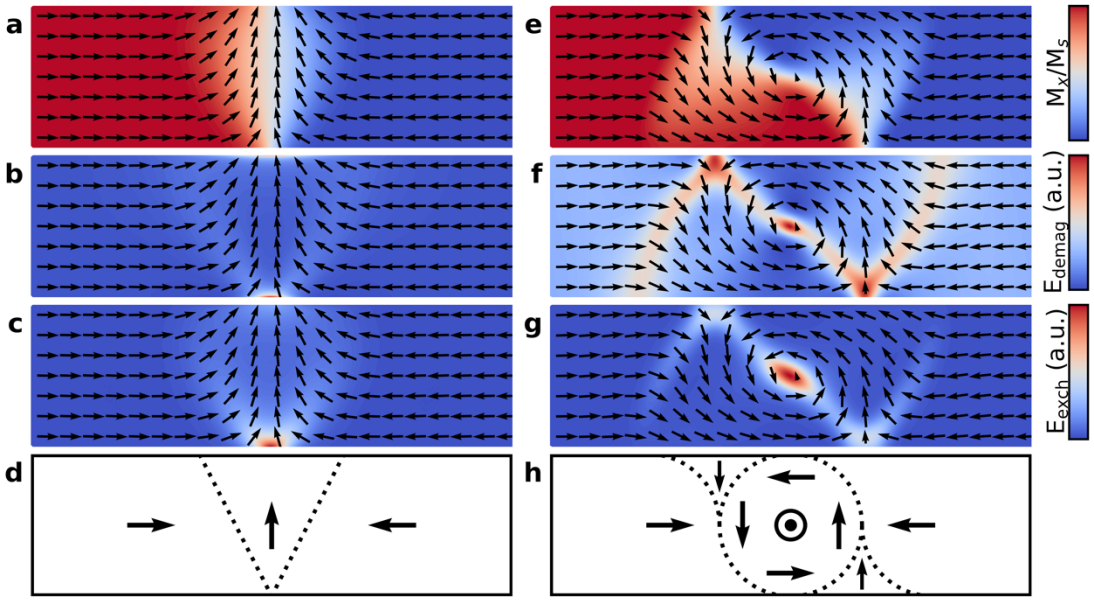

Figure 3-8 (a) Magnetization, (b) Demagnetization energy density, and (c) Exchange energy density of a transverse domain wall in a thin magnetic nanowire. (d) Diagram of magnetization of the transverse domain wall. (e) Magnetization, (f) Demagnetization energy density, and (g) Exchange energy density of a vortex domain wall in a thin magnetic nanowire. (h) Diagram of magnetization of the vortex domain wall. Glyphs indicate magnetization in all panels.

These results allow us to construct a phase diagram of domain wall type as a function of wire width and thickness. Prior work in micromagnetic simulations reveals a well-defined transition boundary between TDW and VDW with additional types of domain walls

such as asymmetric transverse domain walls (ATDW)[76] and Bloch Point walls (BPW)[77].

Figure 3-9 shows the phase portrait as computed for Permalloy $Ni_{80}Fe_{20}$ nanowires by Jamet et al. [77]. The key feature is a transition boundary at $wt \approx 61\lambda_E^2$ where λ_E represents the exchange length. On the lower right of the phase portrait, there exists a second transition indicating ATDW as an intermediate state between TDW and VDW[76]. Along the diagonal, transverse walls form for while $w = t < 7\lambda_E$, Bloch point walls are favourable in the region enclosed by the solid blue line and metastable in the region enclosed by the dashed blue lines. The blue lines intersect the diagonal at $w = t = 7\lambda_E$

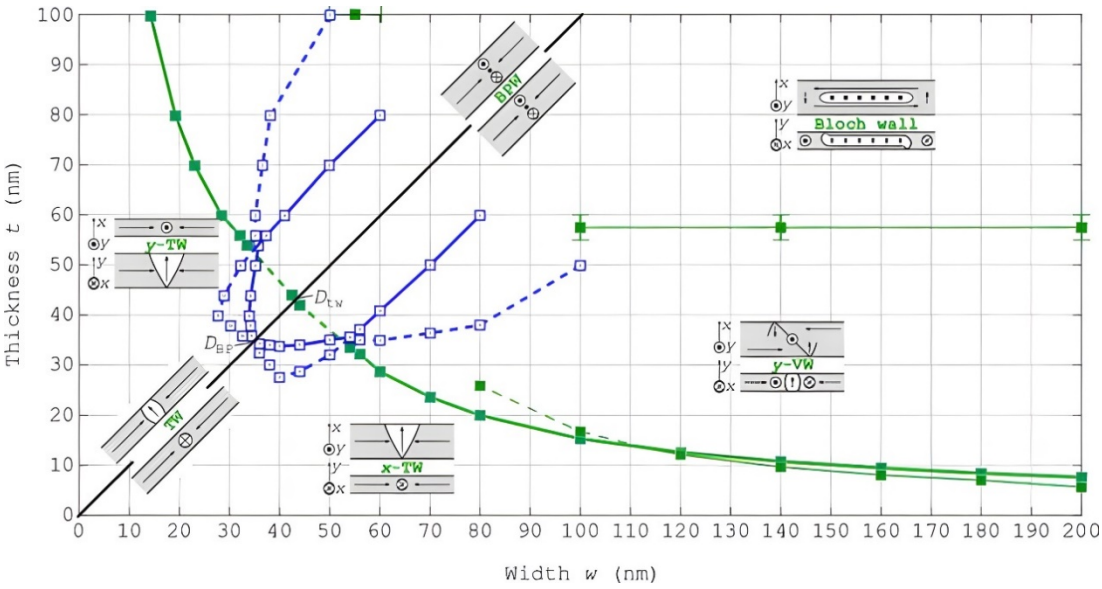

Figure 3-9 Phase portrait for soft ferromagnetic nanowires as computed by Jamet et al. [77]. Showing a distinct transition boundary between transverse domain walls and vortex domain walls at $\boldsymbol{wt \approx 61\lambda_E^2}$. Bloch walls appear for wires with large width and thickness as indicated by the transition boundary at $w > 100$ nm and $t \approx 58$ nm, asymmetric domain walls blur the boundary between TDW and VDW for thin wires with large widths. Along the diagonal, transvers walls appear where $w = t < 7\lambda_E$ and Bloch point walls (BPW) form in the region enclosed by the solid blue line. BPW are metastable in the region enclosed by the dashed blue line.

Asymmetric transverse domain walls are best understood as "tilted" transverse domain walls; the magnetization at the centre of a TDW is perpendicular to the

magnetization of the domains (Figure 3-10a-c). In ATDW, the central magnetization is somewhat tilted to increase the angle between the magnetization and the surface normal to reduce magnetostatic energy (Figure 3-10d). This configuration comes at a small cost in exchange energy (Figure 3-10e).

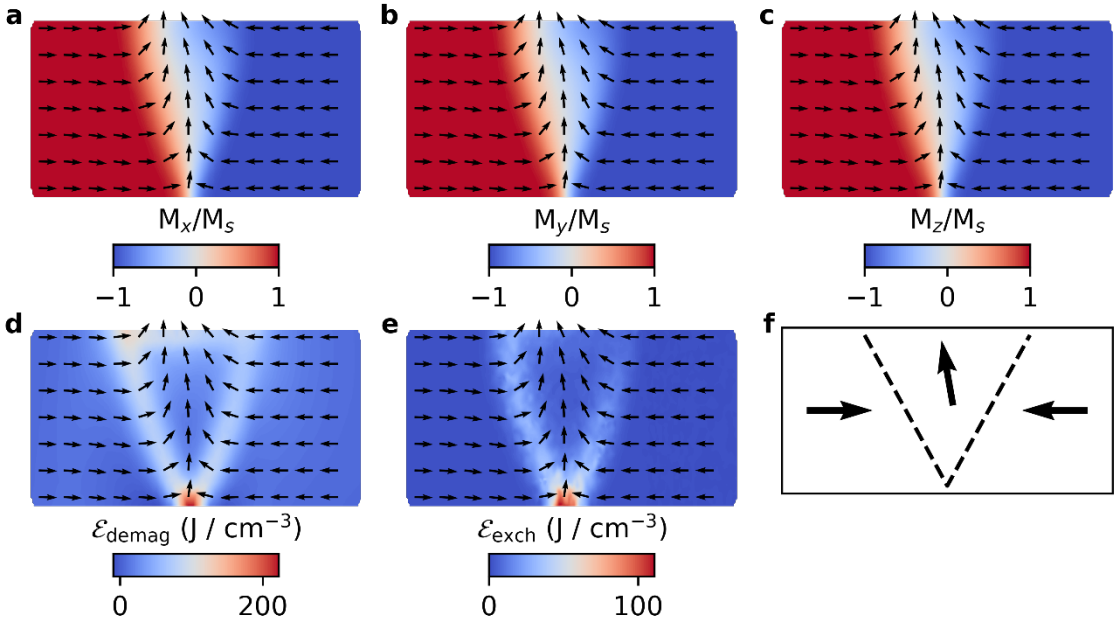

Figure 3-10 Finite difference simulations for asymmetric transverse domain wall. (a) magnetization with contrast according to $\boldsymbol{M_x}$. (b) magnetization with contrast according to $\boldsymbol{M_y}$. (c) magnetization with contrast according to $\boldsymbol{M_z}$. (d) Demagnetization energy density. (e) Exchange energy density. (f) diagram of magnetization.

We can consider domain wall structure in terms of topological defects. Mainly, vortices with a winding number of $n = +1$ (Figure 3-11a), antivortices with a winding number of $n = -1$ (Figure 3-11b), half vortices with winding number $n = +1/2$ (Figure 3-11c), and half-antivortices with winding number $n = -1/2$ (Figure 3-11d). In terms of topological defects, TDWs consist of two edge defects classified as a half-vortex and half-antivortex with $n = 0$ (Figure 3-11e). VDWs comprise a vortex with two half-antivortices on the edges, the total winding number is also $n = 0$ (Figure 3-11e).

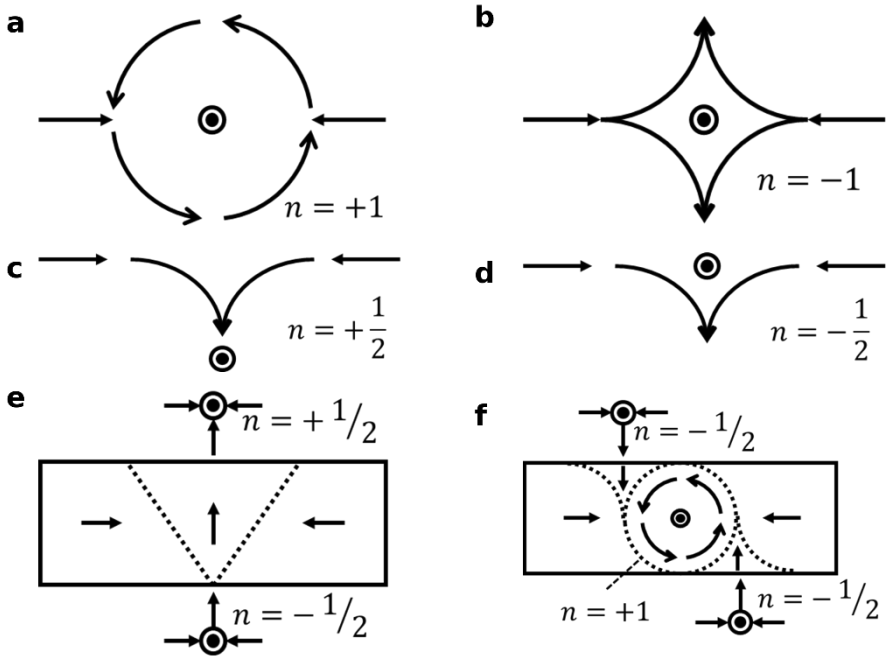

Figure 3-11 Topological defects pertinent to domain wall structure. (a) Vortex with winding number $n = +1$. (b) Antivortex with winding number $n = -1$. (c) Half-vortex with winding number $n = +1/2$. (d) Half-anitvortex with winding number $n = -1/2$. (e) Diagram of TDW with consideration of topological charge. (f) Diagram of VDW with considerations of topological charge.

Bloch Point walls minimize surface charge and, therefore, magnetostatic energy; in cylindrical nanowires with infinite rotational symmetry, BPW have negligible surface charge and therefore present the idealized case. We consider a cylindrical nanowire with a head-to-head BPW at $x = 0$, as shown in Figure 3-12. The magnetization of the domains is in the positive x direction for $x < 0$ and negative x direction for $x > 0$. When approaching the domain wall from $x < 0$ to $x = 0$, we observe a gradual transition from the uniform magnetization along x to a vortex with the vorticity vector along x and a chirality of ± 1. When approaching the domain wall from $x > 0$ to $x = 0$, we observe the gradual transition to a vortex with vorticity along $x = -1$ and chirality of ∓ 1. The opposing vorticities of the two vortices result in a singularity at the core of the domain wall where $M = 0$, this is referred to as the Bloch point. We can see this in Figure 3-12b-d, where each principal component of the magnetization tends to zero at the Bloch Point.

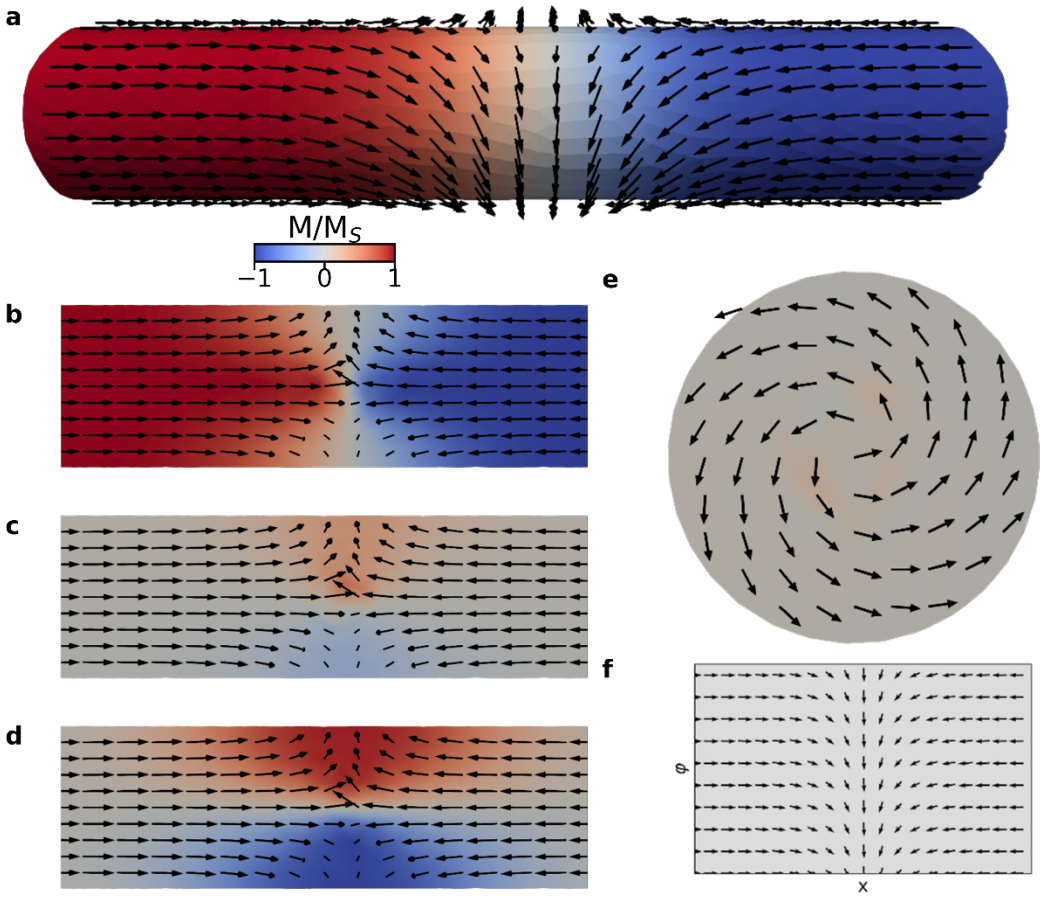

Figure 3-12 Bloch Point domain wall in cylindrical nanowire coloured according to the $\boldsymbol{x}$ component of the magnetization. (b,c,d) Magnetization of Bloch point domain wall on a slice along the long axis in the xy plane. Contrast according to M_x (b), M_y (c), M_z (d). (e) Magnetization at the domain wall plane. (f) Surface Magnetization in curvilinear basis with contrast according to surface normal component of magnetization which is negligible.

Similar to the transition boundary between TDW and VDW in rectangular nanowires, there exists a transition boundary between TDW and BPW in cylindrical nanowires. Ferguson et al. [78] described the energy terms of domain walls in cylindrical nanowires along with an additional metastable domain wall at larger diameters. Also, in wires with rectangular cross-sections, this transition is visible along the diagonal of the phase portrait in Figure 3-9.

3.2.6. Landau-Lifshitz-Gilbert Equation

Central to micromagnetics is the Landau-Lifshitz-Gilbert (LLG) equation[79], which is the equation of motion for magnetization in an effective magnetic field

$$\frac{d\mathbf{M}}{dt} = -\gamma \mathbf{M} \times \mathbf{H_{eff}} + \frac{\alpha}{M_s} \mathbf{M} \times \frac{d\mathbf{M}}{dt} \qquad 3.76$$

Where γ is the electron gyromagnetic ratio, M_s and α are material dependent values for the saturation magnetization and phenomenological damping constant, respectively. The first term yields precession of magnetization about the effective field, whereas the second term is a damping term that aligns the magnetization with the external field. The combined terms describe the magnetization vector precessing about the effective field vector where the enclosed angle decays exponentially as shown in Figure 3-13.

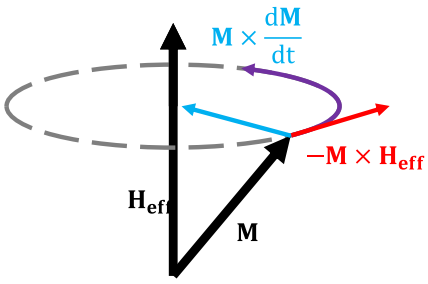

Figure 3-13 The different terms in the Landau-Lifshitz-Gilbert equation

The sum of the fields gives the effective field is given by the sum of fields due to the energy terms described previously:

$$\mathbf{H_{eff}} = \mathbf{H_{ext}} + \mathbf{H_d} + \mathbf{H_{ex}} + \mathbf{H_{anis}} \qquad 3.77$$

We see that the equation exhibits highly non-linear behaviour, which can be used to describe ferromagnets, spin waves, solitons, and numerous other phenomena not limited

to magnetism[80]. From equation 3.10, we see that the LLG equation describes the energy minimization of a moment in a magnetic field. Any stable solution to the LLG equation then represents a local energy minimum for the system. Furthermore, time-dependent magnetic behaviour can be obtained by numerical integration of the LLG equation with a well-defined time-step.

3.2.7. Domain Wall Motion

Domain wall motion in magnetic nanowires is of great interest in current research as the proposed key mechanism for the operation of spintronic devices. Under the application of an external magnetic field, energy is first minimised through domain wall motion such that domains aligned with the field grow at the expense of antialigned domains. Salhi and Berger showed domain wall propagation along a magnetic nanowire when a magnetic field or spin-polarised current is applied[81, 82]. The latter is out of the scope for this thesis.

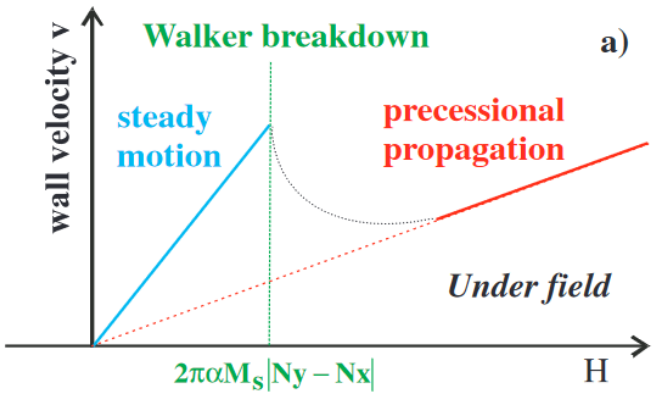

Figure 3-14 Domain wall velocity as a function of external field strength showing Walker breakdown reproduced from Mougin et al. [9]. Note that Mougin et al. used a convention with the wire's long axis along $\boldsymbol{y}$

Domain wall velocity is linearly proportional to the applied field below the Walker limit. Domain wall structure breaks down at the walker limit, and the velocity greatly

decreases [7]. This process is referred to as Walker breakdown with the walker limit given by the expression for a thin wire [9]:

$$H_w = 2\pi\alpha M_s|N_x - N_y| \tag{3.78}$$

Where α is the Gilbert damping factor, M_s is the saturation magnetization, N_x and N_y are the corresponding components of the demagnetization tensor with the wire long axis along x. Mougin et al.[9] derived Equation 3.78 by separately considering the damping term in the LLG equation and expanding the precessional term into components due to the external field and the demagnetizing field. For $H_{ext} < H_w$, the torque due to the demagnetizing field dominates, and domain wall structure remains stable in the steady motion regime shown in Figure 3-14. When $H_{ext} > H_w$, precession about the external field dominates leading to instability in domain wall structure.

In 1948, Döring showed an energy term proportional to the square of the domain wall velocity v due to deformation in domain wall structure. This additional term allows the formal definition of a kinetic energy term and, therefore, an effective mass m [8]:

$$E = E_0 + \frac{m}{2}v^2 \tag{3.79}$$

Walker breakdown occurs when the kinetic energy term of the domain wall increases to some critical value where a more complex structure with low velocity is favourable. This description provides a hint towards a way to beat the walker limit: is there a domain wall with zero effective mass that is therefore not subject to walker breakdown? Indeed, micromagnetic simulations of low-dimensional cylindrical nanowires and nanotubes have shown domain walls beating the walker limit [10, 11].

3.2.8. Hysteresis

Magnetic hysteresis loops are useful to characterize magnetic materials and are used throughout this work. Hysteresis refers to a change in an observable not only dependent on the current conditions but also the prior state of the observable, leading to a non-linear response as shown in Figure 3-15. In the initial magnetization curve from position i to position ii, the material moves from a demagnetized state (position i) where there is no net magnetization to the saturated state where all moments in the material are aligned.

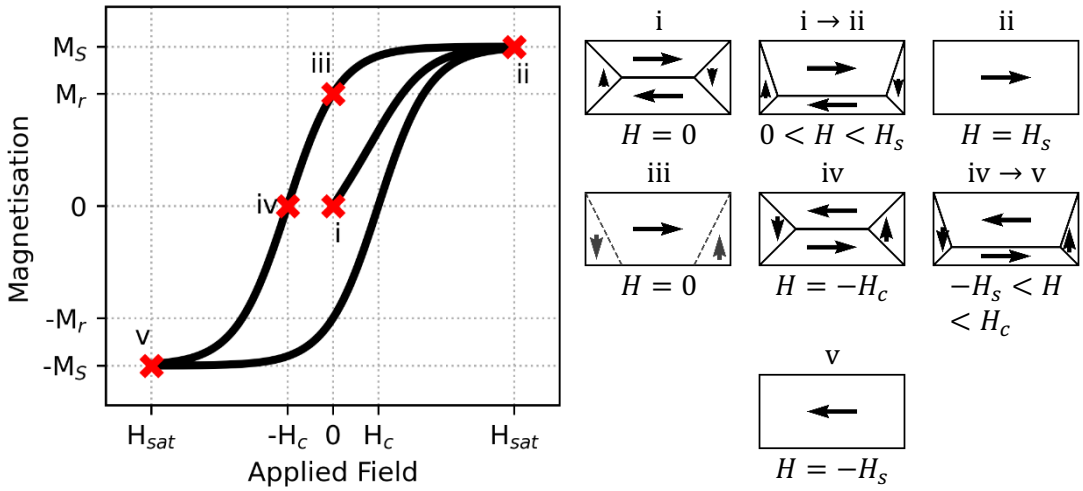

Figure 3-15 Representative hysteresis loop with initial magnetization curve and schematics of the magnetization at key points on the loop. (i) demagnetized state. (ii) saturated state. (iii) remanent state. (iv) demagnetized state at the coercive field. (v) saturated state in the opposite direction.

At position i, a multi-domain state is configured to ensure flux closure, the state with minimum magnetostatic energy. When a magnetic field is applied, Zeeman energy dominates and this is minimized by aligning the moments with the applied field. We see domain wall motion due to domains aligned with the magnetic field growing at the cost of domains not aligned with the magnetic field until the saturated state, where the entire sample is in a single domain state.

After reaching saturation (position ii), removing the external field relaxes the material into the remanent state (iii) We note that this state is different to the initial ground state at position i; the material remains in a single-domain state; however, there exists some curling in the magnetization at the edges to minimize magnetostatic energy. The amount of curling depends on the saturation magnetization, exchange stiffness, and the magnitude and direction of magnetocrystalline energy terms. "Soft" materials tend to curl more, and this reduces the net magnetization at remanence.

There is an energy barrier to returning to the ground state as this requires the nucleation of domain walls that occur at the edges. DW nucleation results in an increase in exchange energy but initially offers little reduction in magnetostatic energy as the bulk of the magnetization is still aligned. The magnetization may return to the ground state after applying an external field opposing the magnetization; the magnitude of this field is referred to as the coercivity. At the coercive field, the net magnetization is zero (position iv)

Increasing the field beyond the coercive field results in a similar response in the magnetization as the initial magnetization curve. Domains aligned with the external field grow at the expense of others to minimize Zeeman energy.

3.2.9. Hysteresis in magnetic nanowires

Unlike bulk materials, the ground state of an idealized magnetic nanowire is saturated, the demagnetization energy of a uniformly magnetized nanowire is sufficiently small such that a multi-domain state is not energetically favourable. In this case, hysteresis loops are more straightforward compared to bulk systems. Figure 3-16a shows the output

of a simple finite difference simulation of a hysteresis loop for a rectangular permalloy nano strip with length 1μm, width 100 nm, and thickness of 10nm. At remanence (ii), some curling at the edges is visible, and this curling increases as the system approaches the coercive field (iii). The increased curling results in the injection of two domain walls at the edges, and the domain walls propagate towards the centre (iv), where these annihilate to leave the wire saturated in the opposite direction (v).

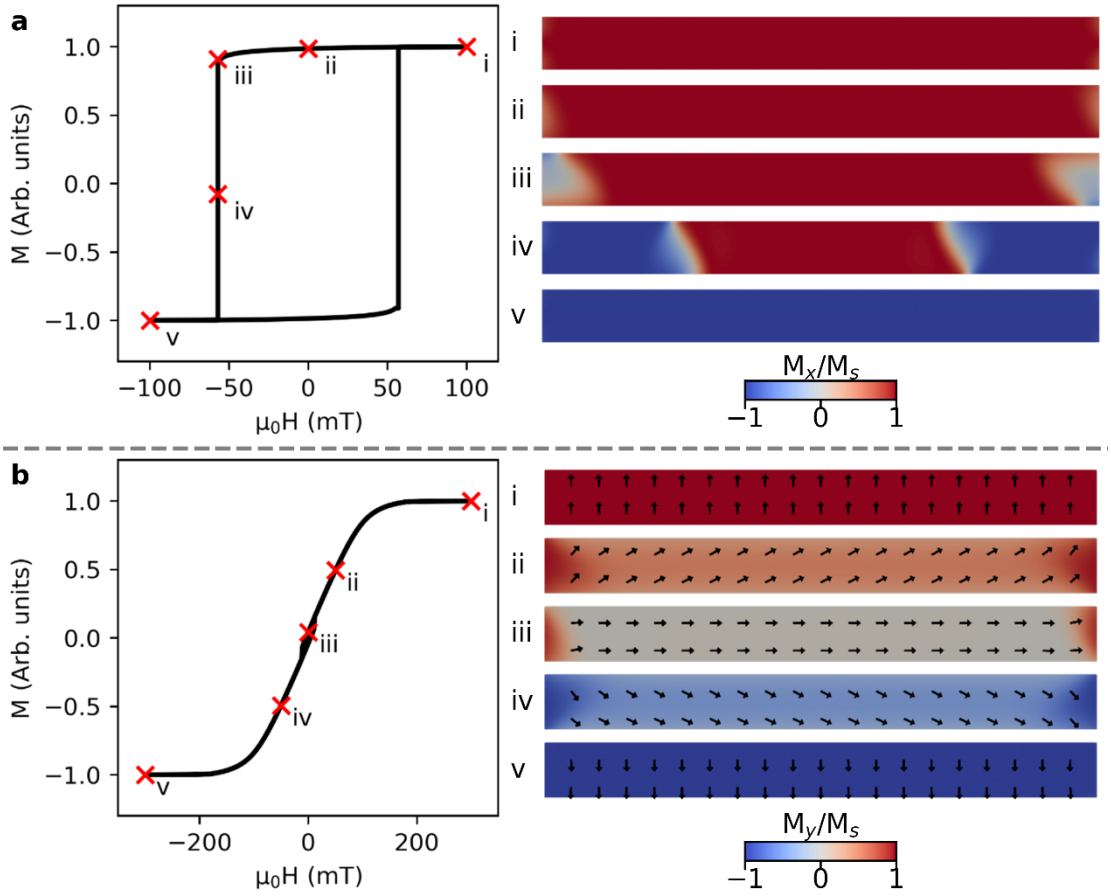

Figure 3-16 (a) Finite element simulation of hysteresis loop along the long axis of a Permalloy nanowire length 1μm, width 100 nm and thickness 10nm with snapshots at marked points showing: (i) saturation in a positive direction. (ii) remanence. (iii) state before switching. (iv) snapshot of the switch. (v) state after switching, saturation in the negative direction. (b) Hard axis hysteresis loop of permalloy nanowire with snapshots of the magnetization at selected loop stages.

Reversal via domain wall motion results in a sharp transition in the hysteresis loop. An alternative reversal mechanism arises through coherent rotation where the magnetization gradually rotates to align with the applied field. Figure 3-16b shows a hard-axis hysteresis loop of the permalloy nanowire with the smooth transition indicating reversal via coherent rotation.

3.2.10. Domain Wall Pinning

Applications using domain walls for logic operations and data storage require precise control over DW motion, a difficult task considering the propagation velocities of domain walls requiring picosecond pulses to move domain walls by a small distance. Another challenge is fine control over the position of domain walls in devices as the state and position of a domain wall must be reproducible for any functional device. A third challenge arises as materials are structured at increasingly smaller scales where the roughness and grain structure result in pinning sites where the potential landscape presents an energy barrier impeding domain wall motion.

However, domain wall pinning can also be exploited to address the challenge of controlled domain wall motion as pinning sites may be engineered such that domain wall states and positions become reproducible. There exist various methods to induce pinning. The first is to introduce defects such as triangular notches or rectangular notches [19-21] into the magnetic nanowire to modulate the width or thickness of the wire and tailor the local demagnetization field. An example is illustrated in Figure 3-17, showing a finite element simulation to illustrate domain wall pinning.

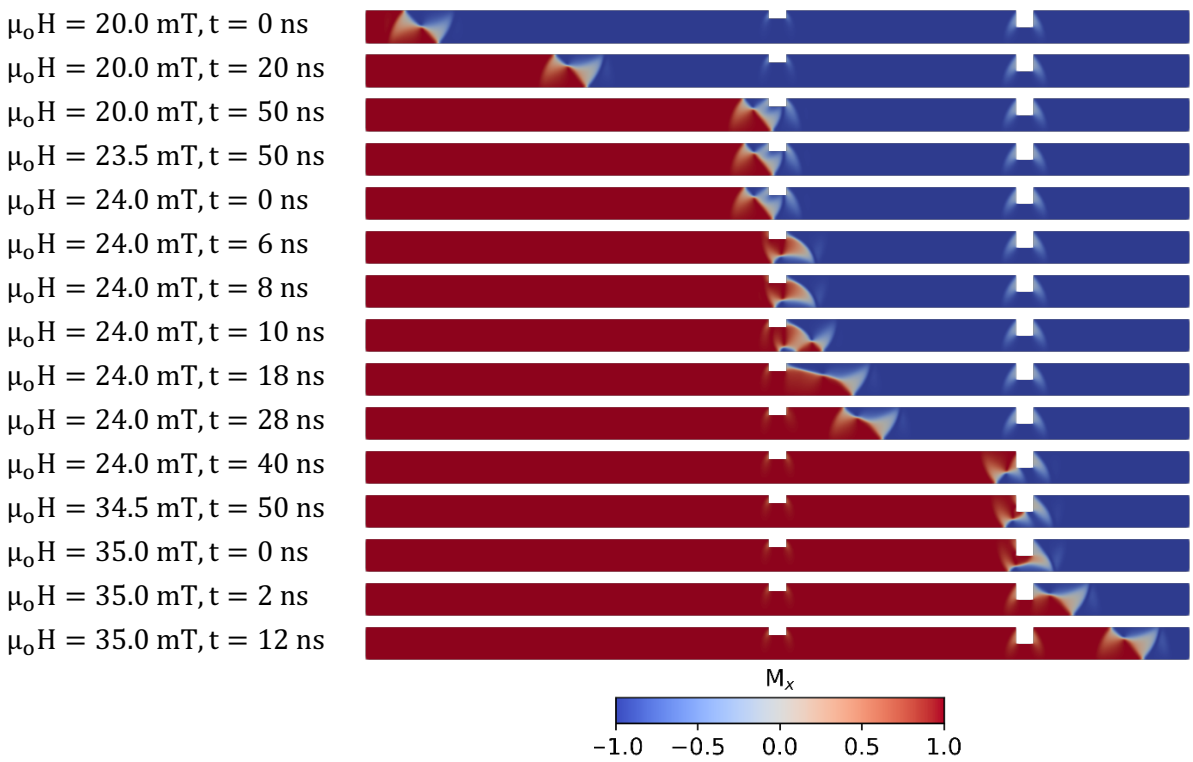

Figure 3-17 Finite element simulation of a domain wall moving through a magnetic nanowire at various field steps and times after application of the field.

A vortex domain wall is relaxed into the system, an external field is then applied and allowed to relax for 50ns before increasing the field by 0.5mT. At 20mT, the domain wall moves through the wire and is hindered by the first notch and pinned. The domain wall remains at this position until a 24 mT depinning field is applied, and the domain wall moves past the defect until it reaches the second. The dimensions of the second defect result in a greater potential barrier and, as such, requires a greater field (35 mT) for the domain wall to pass through. From Figure 3-17, we surmise that pinning introduces plateaus in the hysteresis loop provided that the depinning field is larger than the domain wall nucleation field. In the example given, the nanowire defects affect the domain wall's potential landscape as its lowest energy configuration is perturbed, requiring either significant deformation or transformation for the domain wall to progress. This method of pinning was

the first to be explored in racetrack memory devices, as demonstrated by Parkin et al. [22, 83].

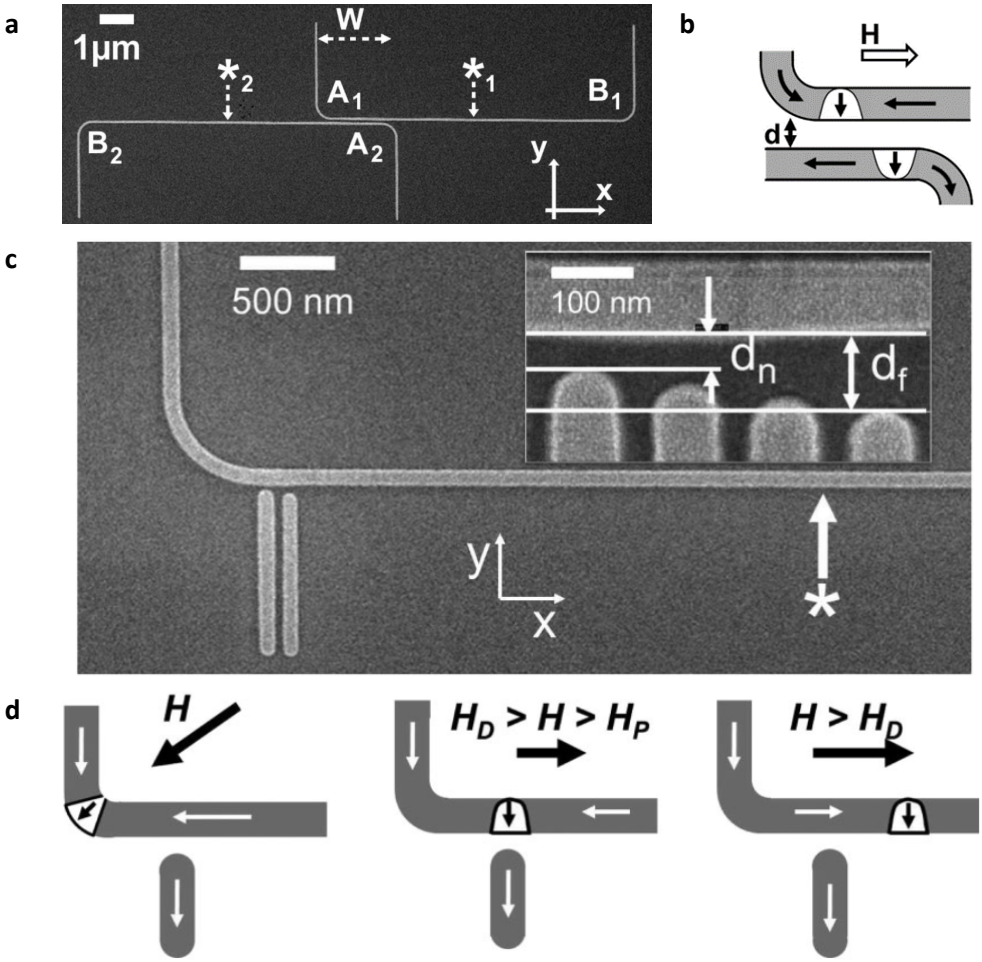

Figure 3-18 (a) SEM of two "U"-shaped nanowires separated by an edge distance of d=100nm. (b) schematic of a pair of TDWs created at corners "A" moving under an external field H. [30] (c) SEM of the experimental system in [31] where the stray field due to magnetized stubs at some distance d from the conduit perturbs the potential. (d) schematic of TDW moving through the potential in [31].

Non-deforming pinning potentials have been explored using magnetostatic interactions between two structures to achieve remote pinning. Notable examples involve two conduits with segments in close proximity (Figure 3-18a&b) such that domain walls in wires interact via a coulomb-like potential [30]. The work highlights these interactions as a potential limiting factor in the realization of domain wall devices with closely spaced wires as the potential may yield crosstalk. However, the work opens the possibility of using

a magnetized stub (Figure 3-18c) where the stray field perturbs the domain wall potential [31].

Lewis et al. [24] explored curvature in a conduit to introduce a pinning potential for a transverse domain wall, where the curvature introduces additional terms in the exchange energy (see section 3.2.2) and surface charge (Figure 3-19), resulting in pinning fields proportional to curvature. The type of potential is dependent on the chirality of the domain wall where the curved segment presents a potential well for a HH TDW with the core directed away from the centre of curvature and a potential barrier when the core is directed towards the centre of curvature.

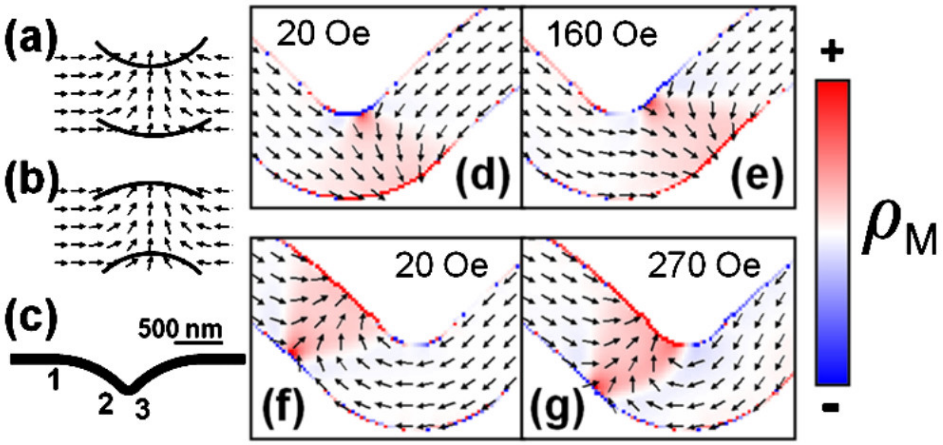

Figure 3-19 Micromagnetic simulations of domain wall pinning due to curvature in a magnetic nanowire [24]. [(a) and (b)] Schematic showing an increase in surface charge when HH TDW core is directed towards the centre of curvature (a) and a decrease in surface charge when directed away from the centre of curvature (b). (c) Schematic of simulated conduit, the bend at 2 has a radius of R=150nm. [(d)-(g)] stable configurations at indicated fields, contrast according to surface charge density computed as $\rho_m = -\mu_0 \nabla \cdot \vec{M}$. Glyphs indicate M

3.3. Frustration

Geometric frustration is defined as a situation where not all pairwise interactions can be satisfied simultaneously. A straightforward example is a system of three magnetic

moments subject to antiferromagnetic minimization on the vertices of an equilateral triangle, as shown in Figure 3-20. Moments μ_1 and μ_2 are antialigned as is favoured in antiferromagnetic systems. However, there is no clear indication of a favoured orientation for moment μ_3.

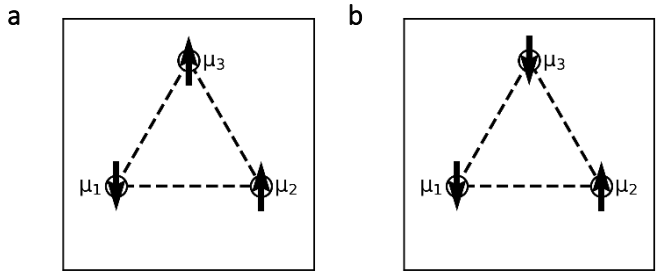

Figure 3-20 Antiferromagnetic moments placed on vertices of an equilateral triangle. $\boldsymbol{\mu_1}$ and $\boldsymbol{\mu_2}$ are antiferromagnetically coupled, $\boldsymbol{\mu_3}$ cannot minimise both interactions with $\boldsymbol{\mu_1}$ and $\boldsymbol{\mu_2}$.

Minimising the energy term due to the exchange interaction between μ_1 and μ_3 maximises the energy due to the exchange interaction between μ_2 and μ_3 and vice versa. The configurations shown in Figure 3-20(a) and (b) are then degenerate.

3.3.1. Frustration in bulk materials

Linus Pauling showed that at 0K, the entropy of water ice is non-zero due to bonding between oxygen and hydrogen atoms [33]. Oxygen can bond tetrahedrally with four hydrogen atoms; two via covalent bonding with a bond length of 0.95Å, and two via hydrogen bonding with a bond length of 1.81Å. It follows that each hydrogen atom bonds to two oxygen atoms, one covalently bonded and the other via hydrogen bonding. The different bond lengths result in the oxygen atom being closely bonded with two hydrogen atoms and distantly bonded with another two hydrogen atoms. This 2-near/2-far regime,

known as the ice rule, results in 6 permutations for the atoms to be arranged, as shown in Figure 3-21.

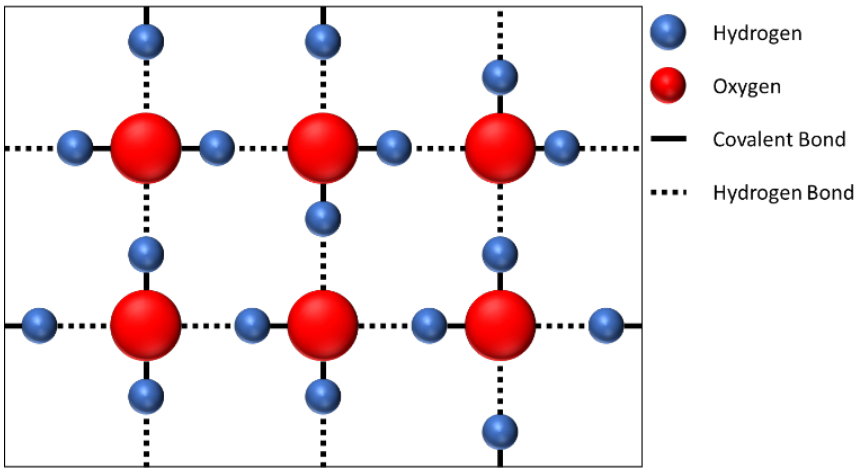

Figure 3-21 Possible configurations of atoms in a water-ice lattice at 0K

With six permutations for each oxygen atom in a crystal with N oxygen atoms, $\Omega = 6^N$ gives the multiplicity of the ground state, leading to a non-zero entropy at 0K as described by Boltzmann's entropy formula

$$S = k_b \log_{10}(\Omega) \tag{3.80}$$

This is referred to as the residual entropy S_R.

3.3.2. Spin ice

As demonstrated by Harris et al. [36], $Ho_2Ti_2O_7$ crystals show geometric frustration due to holmium atoms on the corner-sharing tetrahedra in the pyrochlore lattice. At low temperatures ($T < 10\ K$), the magnetic moment of the holmium atoms act as Ising spins limited in their direction either towards or away from the centre of the tetrahedron. Similar to the example of water ice where there are two possibilities for a hydrogen-oxygen bond,

there exist two possibilities for the direction of the magnetic moment; the 2-far/2-near regime is then analogous to the 2-in/2-out regime known as the Ice rule and giving these materials the name "spin ice".

The Hamiltonian of these systems describes the sum of the exchange energy 3.40 and the dipolar interaction 3.12 [84]:

$$\mathcal{H} = \frac{\mathcal{J}_{ij}}{3}\sum_{ij} S_i S_j + Da^3 \sum_{ij}\left[\frac{\hat{\mathbf{e}}_i \cdot \hat{\mathbf{e}}_j}{\left|\mathbf{r}_{ij}\right|^3} - \frac{3\left(\hat{\mathbf{e}}_i \cdot \mathbf{r}_{ij}\right)\left(\hat{\mathbf{e}}_j \cdot \mathbf{r}_{ij}\right)}{\left|\mathbf{r}_{ij}\right|^5}\right] S_i S_j \qquad 3.81$$

$\boldsymbol{S}$ describes the spin orientation, which may take values of $\pm\mathbf{1}$ on the axis indicated by the unit vector for the Ising axis $\hat{\mathbf{e}}$. D is a coupling constant given by $\boldsymbol{D = \mu_0 \mu^2 / 4\pi a^3}$. $\boldsymbol{a}$ gives the distance between spins. The ice rule can be violated in spin-ice materials as one of the spins can flip to create a 3-in/1-out state or 3-out/1-in state. In 2010, Castelnovo and Moessner showed that these ice-rule violating defects behave like magnetic monopoles, as shown in Figure 3-22.

In Figure 3-22a, the spin configuration follows the ice rule with a 2-in/2-out state for both corner-sharing tetrahedra. Excitation results in a shared spin flipping such that one tetrahedron attains a 1-in/3-out state and the other a 3-in/1-out state. Treating each spin as a pair of opposite magnetic charges on a dumbbell as shown in Figure 3-22 (c&d), we find that the net charge enclosed by the tetrahedra in the 2-in/2-out state is zero and ± 2 for the excited state. The excited states form emergent particles with non-zero magnetic charge acting as effective magnetic monopoles. In this instance, Gauss's law for magnetism retains validity as $\nabla \cdot \mathbf{H} = -\nabla \cdot \mathbf{M}$.

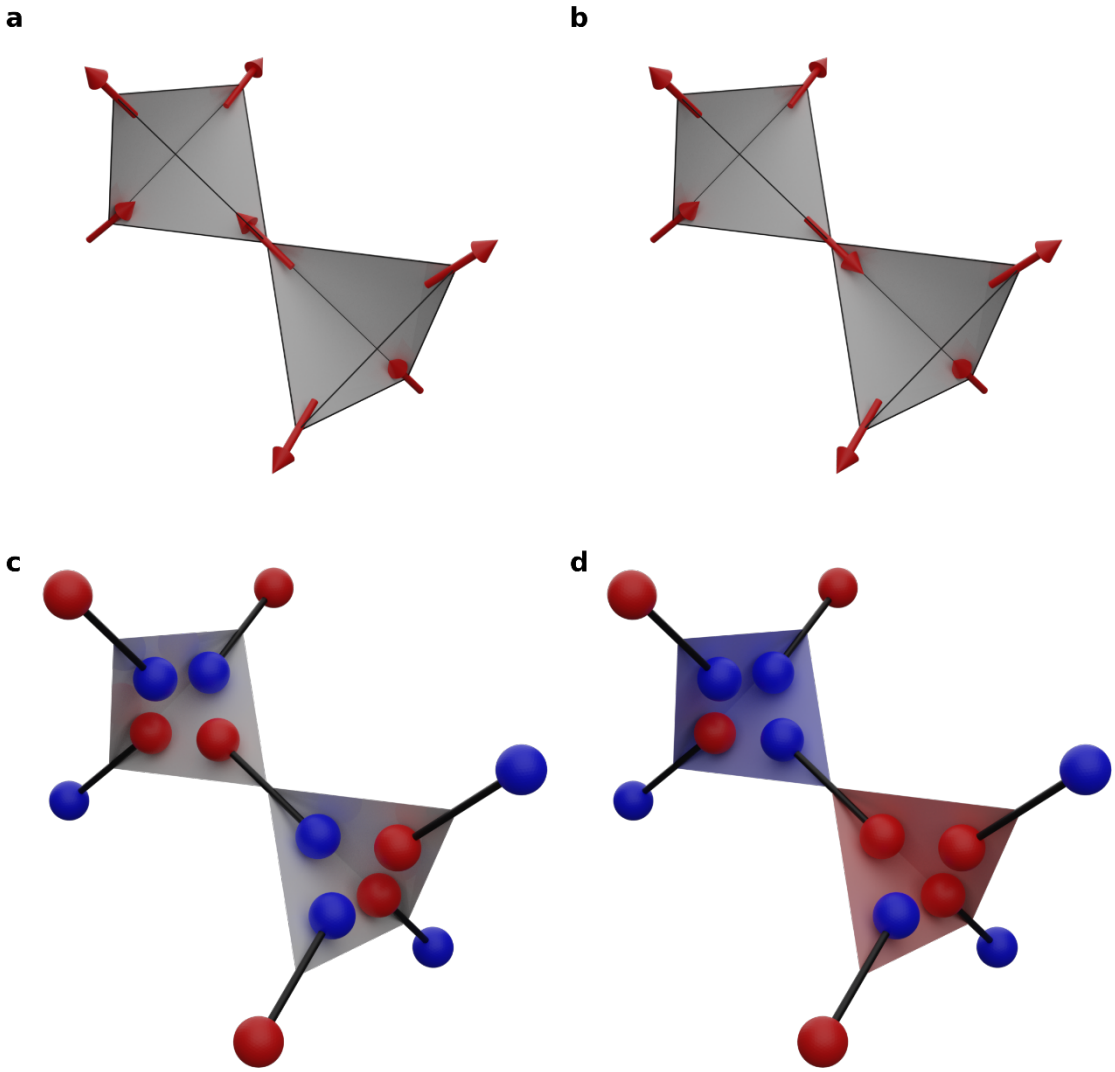

Figure 3-22 Illustration of excitation from 2-in/2-out state to 3-in/1-out state. (a) two corner-sharing tetrahedra with a magnetic moment on each corner. Two of the moments are directed towards their respective centres in both tetrahedra, and two are directed away. (b) the shared moment is flipped to result in a 1-in/3-out state in the first tetrahedron and a 3-in/1-out state in the second. (c) representation of (a) using a dumbbell model to indicate magnetic charge. The tetrahedron encloses no net charge. (d) representation of (b) using the dumbbell model showing a net enclosed charge of -2 in the first tetrahedron and a net enclosed charge of +2 in the second.

Additional spin flips in neighbouring tetrahedra result in the effective monopoles separating (Figure 3-23). Crucially, there exists an interaction between the monopole-antimonopole pair that follows a magnetic analogue of Coulomb's law, replacing ε_0 with μ_0 and electric charge with magnetic charge.

$$U(r) = \frac{\mu_0}{4\pi}\frac{Q_1 Q_2}{r} \qquad 3.82$$

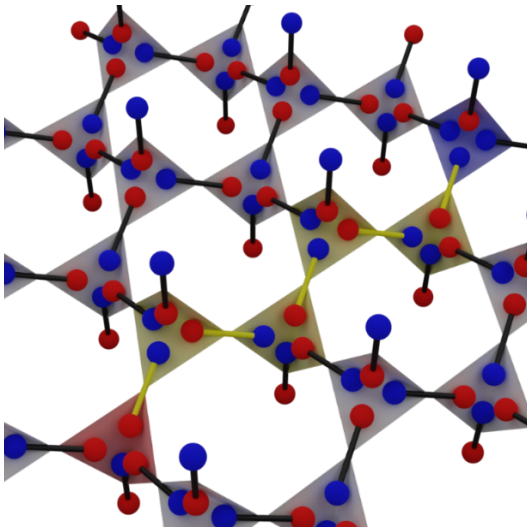

Figure 3-23 Schematic of separated monopole-like defects with the path of the Dirac string indicated in yellow.

Dirac's prediction of magnetic monopoles introduced an unobservable 1-dimensional solenoid-like string to conserve Maxwell's equations[85]. The excitations in spin-ice are created only via spin reversal, and as such, a monopole excitation is always paired with an anti-monopole excitation connected via a string of reversed spins. Upon a disordered background, this string is indistinguishable from the background and referred to as a Dirac string. These monopoles and their associated currents have now been experimentally observed in bulk spin-ice materials [86, 87].

3.3.3. Ising model and Ising-like magnetic nanowires

In an attempt to describe ferromagnetism using local forces only, Whilhelm Lenz developed a simple model which became the subject of Ernst Ising's 1925 doctoral thesis[88]. This simple model places spins in a 1-dimensional lattice with the spin's

direction restricted to either ‘up’ or ‘down’, and considers nearest-neighbour interactions only, with the energy of the system described with the Hamiltonian:

$$H = -\sum_{\langle i,j \rangle} \mathcal{J}_{ij}\sigma_i\sigma_j - \mu\sum_j h_j\sigma_j \qquad 3.83$$

Where $\mathcal{J}_{ij}$ is the nearest-neighbour interaction between adjacent spins, μ is the spin magnetic moment, and h_j is the external field at spin j. The direction of each spin is represented by the non-dimensional spin variable $\sigma = \pm 1$.

Although developed as a simplified model of ferromagnetism, the Ising model itself is not intrinsically a representation of any physical system. Extending the model to two dimensional systems reveals a transition between ordered and disordered phases, as shown by Peierls in 1936 with an analytical proof by Onsanger in 1944 [89]. Ising models may be extended to an arbitrary dimensionality and have shown utility in a wide range of topics such as phases of spin glasses [90], lattice structures of binary alloys [91], and neural networks [92].

Lieb applied the Ising model to 2D representations of Pauling’s Ice-type model, Slater’s KDP model, and the Rys-F model to find the first exactly solved vertex models in statistical mechanics [93-96]. The Ising model may be applied to the vertex types seen in spin ice materials where the spin variable $\sigma = \pm 1$ represents a spin pointing towards, or away from, a vertex.

The demagnetising field inside high aspect-ratio magnetic nanowires restricts the wire magnetisation to be parallel or antiparallel to the long axis. A sufficiently short wire, such that its ground state is single-domain and there exists no stable intermediate or multi-

domain state, may be parameterised using the Ising variable. Using these Ising-like magnetic nanowires, one can create mesoscopic analogues of spin ice materials as demonstrated by Wang et al [37].

3.3.4. Artificial Spin Ice

Studying spin ice materials presents many challenges due to low-temperature requirements and the inherent difficulty of visualizing atomic magnetic moments. Wang et al. [37] proposed a model system comprising single-domain magnetic nanowires arranged in a regular lattice (Figure 3-24 (a) Schematic of the artificial spin-ice system proposed by Wang et al. Reproduced from[37]. (b) possible vertex types in 2D square artificial spin ice lattices. (c) Excess percentage of each vertex type in a square lattice as shown by Wang et al. [37].a). Using high aspect ratio permalloy nanowires with zero magnetocrystalline anisotropy, the magnetization of the magnetic nanowires may lie parallel or antiparallel to the nanowire long-axis as an analogue to an Ising spin in bulk spin ice. Dipole interactions between the nanowires result in the frustration characteristic of spin-ice systems. The simplest way to capture the four-spin arrangement in two dimensions is by arranging the spins in a square lattice.

In an artificial spin ice system, individual nanowires are Ising-like such that they are single domain at remanence and reverse via a sharp transition as an analogue to spin reversals in spin ice materials. In the thermal regime where the temperature is above the blocking temperature T_B such that the nanoislands are superparamagnetic, small temperature fluctuations activate magnetization reversals. The blocking temperature is a function of the shape anisotropy constant K_s and the nanoisland volume V given by the expression [97]

$$T_B = \frac{K_s V}{k_B \ln\left(\frac{t_m}{t_0}\right)} \tag{3.84}$$

Where t_m is the observation time and t_0 is the attempt time. The anisotropy constant is given by:

$$K_s = \frac{1}{2}\mu_0 M_s^2 \, \Delta N \tag{3.85}$$

Where ΔN is the difference between the long axis and in-plane short-axis components of the demagnetization tensor, additional reversals in the magnetization may result in excitations moving around the lattice, and we continue the analogue to spin ice materials by considering the excitations as connected via a Dirac string. However, calculations have shown additional terms in the potential [98] such that the total energy of a monopole-antimonopole pair in artificial spin ice becomes:

$$U(r) = \frac{\mu_0}{4\pi}\frac{Q_1 Q_2}{r} + bX(r) + C \tag{3.86}$$

Where $X(r)$ is the string length, b is the string tension, and c is a constant associated with pair creation. Before discussing the origin of this term, we must explore degeneracy in artificial spin-ice systems.

Wang et al. immediately demonstrated the advantages of artificial spin ice by fabricating permalloy nanoislands large enough such that the magnetization is frozen with a blocking temperature well above room temperature. The frozen system is easily characterized using magnetic force microscopy, which was performed on devices with varying lattice spacings. The group reproduced the different vertex types shown in Figure

3-24 (a) Schematic of the artificial spin-ice system proposed by Wang et al. Reproduced from[37]. (b) possible vertex types in 2D square artificial spin ice lattices. (c) Excess percentage of each vertex type in a square lattice as shown by Wang et al. [37].b with population fractions of each type significantly different from random chance, indicating interactions between the nanowires. Increasing the lattice spacing resulted in the vertex populations approaching a random distribution as expected with decreasing interaction strengths. Vertices of each type are degenerate; however, it is noted that ice-rule states, unlike in bulk spin-ice, are separated in topologically separate vertex types I and II with different energies associated with these vertex types.

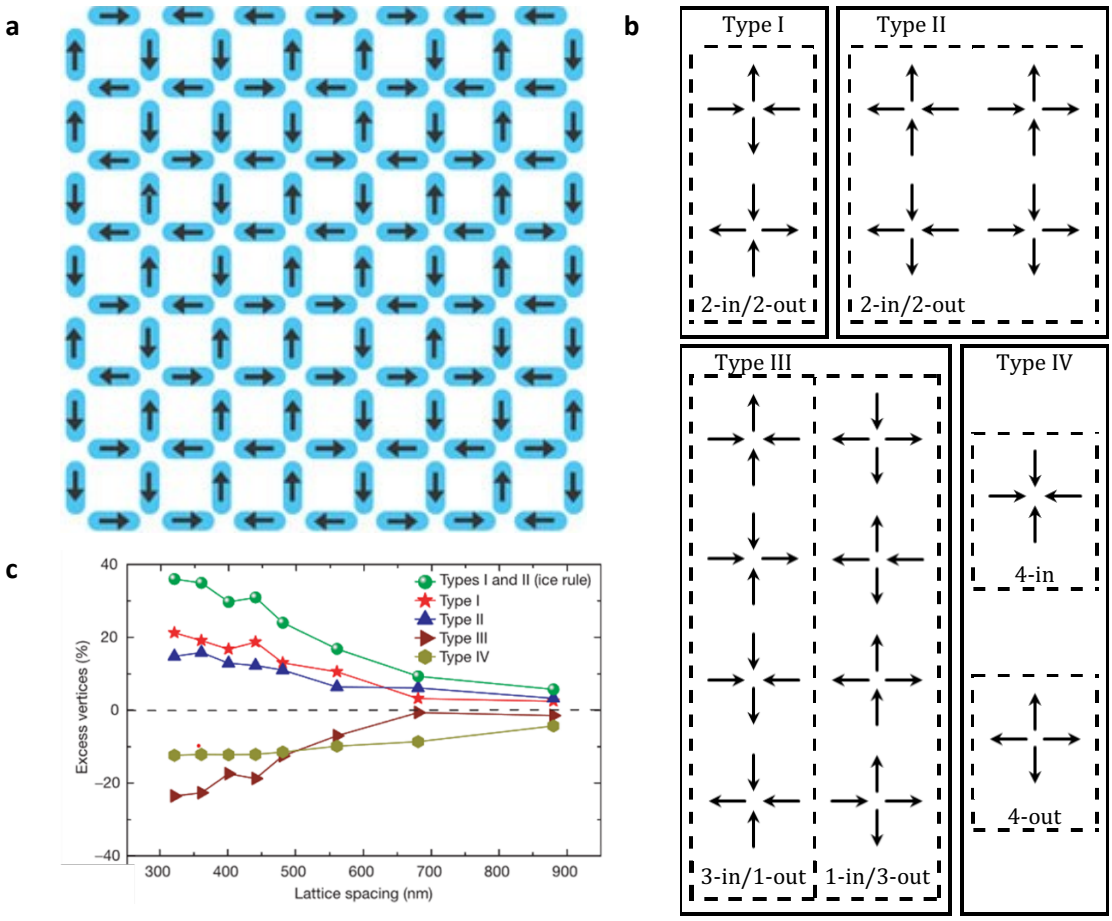

Figure 3-24 (a) Schematic of the artificial spin-ice system proposed by Wang et al. Reproduced from[37]. (b) possible vertex types in 2D square artificial spin ice lattices. (c) Excess percentage of each vertex type in a square lattice as shown by Wang et al. [37].

This non-degeneracy highlights a limitation of 2D artificial spin-ice systems if using it as a platform to study bulk spin-ice behaviour. As indicated in Figure 3-25a, the distance between opposite wires in the vertex is greater than adjacent wires resulting in the favouring of dipolar interactions between adjacent wires and an excess of type I vertices at smaller lattice spacings. Overall, this yields an antiferromagnetic ground state, unlike the disordered state seen in bulk systems. Kagome lattices comprising three nanowires at each vertex overcome this issue as all three wires are equidistant (Figure 3-25b). Such systems are interesting in their own right due to their complex phase diagram, which consists of states with dipolar order, charge order and loop states [99]. However, without a fourth moment, such systems can only be compared to spin-ice in a limited scenario such as Kagome ice, where a single spin is pinned via an external magnetic field.

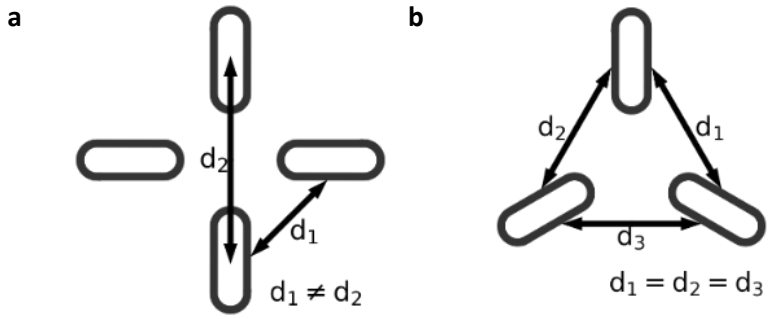

Figure 3-25 (a) A disconnected square lattice vertex with the distance between islands annotated. (b) disconnected Kagome lattice vertex with distances annotated.

The degeneracy lifting between the ice-rule states gives rise to ordering in the system such that the chain of reversals connecting a monopole-antimonopole pair is measurable. A trivial example is an instance of a background comprising type-I states where the excitations are connected via a path of type-II states (Figure 3-26a), or a background of Type-II states where the excitations are connected via a path of type-I states (Figure 3-26b).

The intrinsic energy difference between the type-I and type-II states then contributes to the additional energy term $bX(r)$ in equation 3.86.

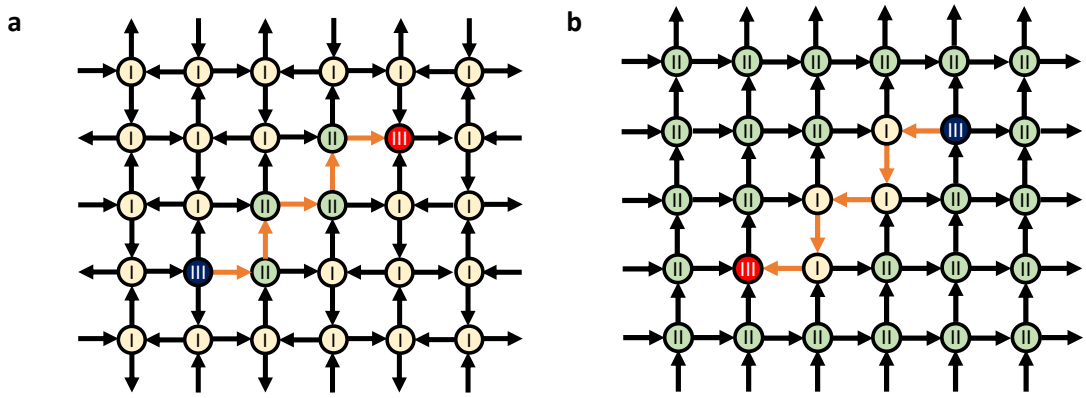

Figure 3-26 Dirac string upon a square 2D artificial spin ice lattice with (a) Type-I background, (b) Type-II background

Möller and Moessner predicted that degeneracy could be recovered in square systems by offsetting one of the sub-lattices by some height h, such that dipolar interactions between any pair are equivalent [99]. This was then experimentally demonstrated by Perrin et al. [100] (Figure 3-27a). An offset such that $\mathcal{J}_1 > \mathcal{J}_2$, reproduces the regime studied by Wang et al. with mainly type I vertices (Figure 3-27b). For $\mathcal{J}_1 < \mathcal{J}_2$, the sublattices become disconnected and ferromagnetic ordering dominates resulting in type II vertices (Figure 3-27c). At a critical separation between the sub-lattices ($h \approx h_c$), the interaction between opposite wires and adjacent wires becomes roughly equal ($\mathcal{J}_1 \approx \mathcal{J}_2$) and degeneracy is nearly recovered. Despite their success in recovering degeneracy, an earlier analysis showed that the moments in these types of lattices lie along the x or y direction in the lattice (Figure 3-27e), which results in some residual ordering and subsequent residual tension [101].

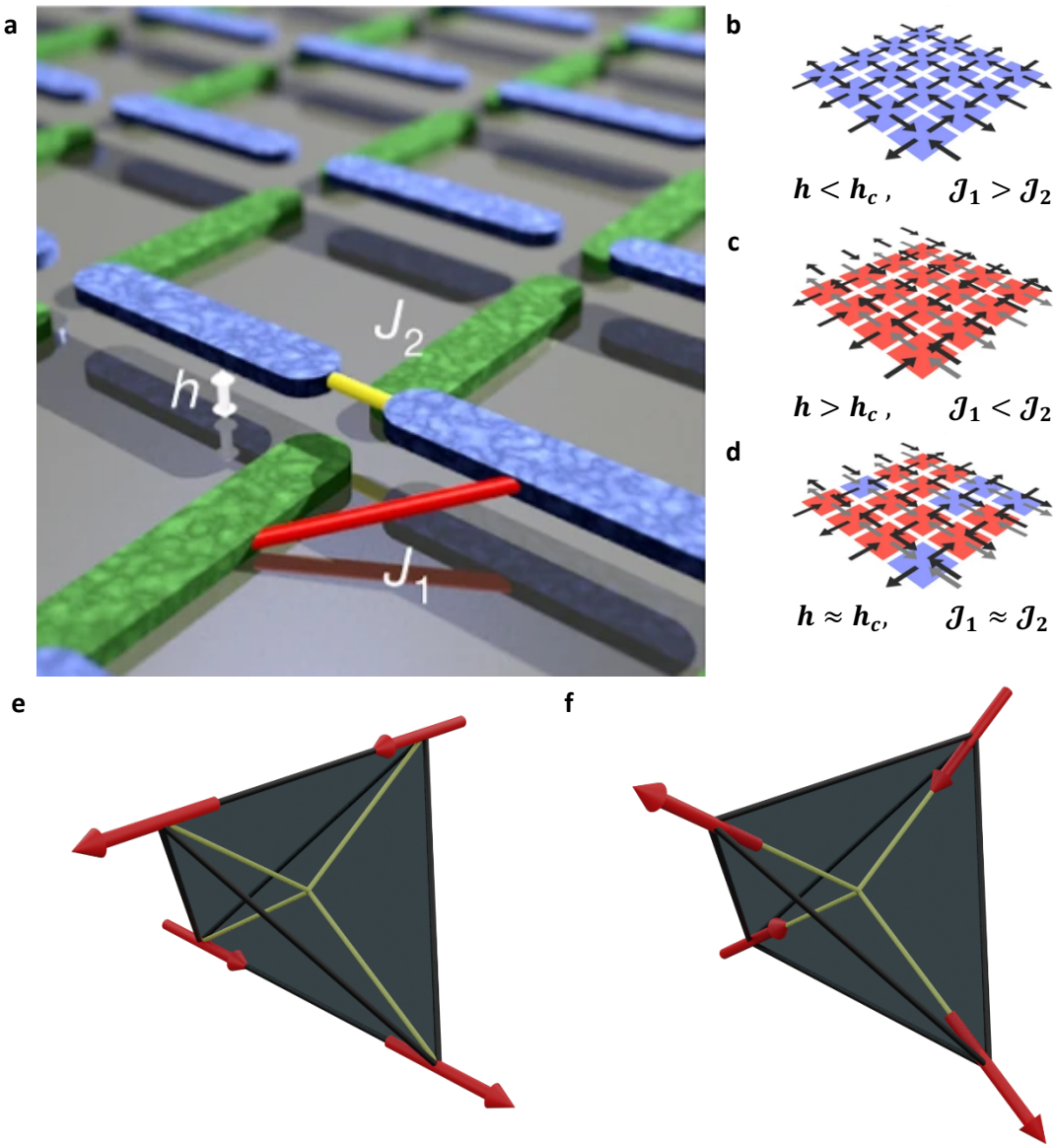

Figure 3-27 (a) schematic of square artificial spin ice with z-offset in one of the sublattices. (b-d) observed vertex types for $\boldsymbol{h < h_c}$, $\boldsymbol{h > h_c}$, and $\boldsymbol{h \approx h_c}$ respectively. Blue indicates type I vertex, red indicates type II vertex. Edited figure from [100]. (e) the direction of moments in the lattice described in refs [99-101] where moments lie in the x-y plane. (f) optimal orientation of magnetic moments aligned to their local $\langle \mathbf{1}, \mathbf{1}, \mathbf{1} \rangle$ axis.

Fine control over the energies of the vertex types presents an interesting opportunity to explore the exactly solved six-vertex models known as the Rys-F and the KDP models [93]. Applied to square artificial spin ice, where the ground state of a system is either described by a type-I (Rys-F [102]) or type-II (KDP [103]) background. The Rys-F model describes type-II vertices as excitations upon a type-I background. Since type-II vertices carry net magnetisation and divergence-full vertex types are prohibited, topological

restriction results in system-spanning strings or closed loops of type-II vertices separating domains of type-I vertices with opposite parity [104-106]. These flux lines, named Faraday loops, carry the system's energy, and due to the closed loops yield zero magnetisation and magnetic susceptibility leading to an infinite-order phase transition tied to the topological properties of the system.

2D and 2.5D artificial spin ice systems present an exciting opportunity for exploring exotic physical phenomena, but there exist limitations that motivate attempts to produce a true 3DASI. Firstly, 2DASI cannot capture true degenerate ice-rule states, which are essential to achieving deconfined monopole pairs. 2.5D systems recover degeneracy, but next-nearest neighbour interactions still yield residual ordering and subsequent residual string tension. 3DASI promises degenerate ice-rule states where moments lie along their local ⟨1,1,1⟩ axis and deconfined monopoles are achievable. Finally, the 2D and 2.5D systems are inherently limited to a single layer, and one cannot explore the impact of symmetry breaking upon the surface. The 2D square ASI systems discussed are composed entirely of coordination-four vertices comprising four nanowires. However, a surface termination in ASI consists of two wires not captured in 2DASI.

3.4. Two Photon Polymerisation

Methods such as photolithography and electron beam lithography are well established in nanostructure fabrication , currently achieving sub-10nm feature sizes [107, 108]. However, these methods lack variability along the incident beam path and are therefore unsuited to 3D nanostructure fabrication. Recent advances in laser technologies such as femtosecond lasers with pulse lengths $< 10^{-12}$ s provide access to non-linear

optical effects which may be exploited in photolithography. Key to this work is two-photon absorption (TPA); a third-order non-linear optical process that may be exploited to trigger polymerisation in a photoresist. This section covers the fundamentals of TPA and two-photon polymerisation (TPP), the practical application is discussed in section 4.1.

The photochemical processes in photolithography are initiated by the absorption of a photon ($h\nu$) by a photoinitiator (PI). The excited photoinitiator (PI^*) decays into a pair of free radicals ($R\cdot$), which bond with a monomer (M) to generate monomer radicals ($RM\cdot$). Monomer radicals may bond with further monomers to create monomer radicals of arbitrary length ($RMM\cdot \rightarrow RM_n\cdot$) until the monomer radical combines with another, terminating the reaction. The process is outlined in Table 3-2.

Stage	**Chemical process**
Initiation	$PI \xrightarrow{h\nu} PI^* \rightarrow R\cdot + R\cdot$
Propagation	$R\cdot + M \rightarrow RM\cdot \xrightarrow{M} RMM\cdot \rightarrow \cdots \rightarrow RM_n\cdot$
Termination	$RM_n\cdot + RM_m\cdot \rightarrow RM_{m+n}R$

Table 3-2 Outline of the photochemistry associated with photolithography.

This is a linear process where the material polarization (**P**) response induced by an applied electric field (**E**) with frequency (ω) is given by [59]

$$\mathbf{P}(\omega) = \varepsilon_0 \chi(\omega)\mathbf{E}(\omega) \qquad 3.87$$

Where ε_0 is the permittivity of free space, and χ denotes the linear susceptibility.

Standard UV sources used in photolithography are isotropic such that all unmasked regions are uniformly exposed. These factors limit the technique to 2D structures. Although

additive and subtractive techniques may be combined in sequence to stack 2D layers, realizing a complex 3D structure is prohibitively challenging.

In contrast to single-photon lithography initiated by the absorption of a single photon (Figure 3-28a), two-photon lithography relies on the near-simultaneous absorption of two photons by a molecule in the photoresist where the sum of the photon energies is equal to the bandgap (Figure 3-28b). The first absorption leads to an electron in a virtual state which must relax down to the ground state within the timeframe dictated by the time-energy uncertainty relation. The absorption of a second photon within this time interval (< 1 fs) allows the electron into the excited state. Sufficiently high electric fields result in additional non-linear terms to equation 3.87:

$$\mathbf{P} = \sum_{\mathbf{n}} \mathbf{P^n}$$

$$\mathbf{P^1} = \varepsilon_0 \chi^1 \mathbf{E} \qquad 3.88$$

$$\mathbf{P^2} = \varepsilon_0 \chi^2 \mathbf{E} \cdot \mathbf{E}$$

$$\mathbf{P^3} = \varepsilon_0 \chi^3 \mathbf{E} \cdot \mathbf{E} \cdot \mathbf{E}$$

Where the superscript indicates index rather than exponent. The rate of absorption for an n-photon process is typically proportional to $\mathbf{E} \cdot \mathbf{P^{2n-1}}$. For a single-photon process, the absorption rate is then proportional to $\mathbf{E} \cdot \mathbf{P^1} = \varepsilon_0 \chi^1 \mathbf{E} \cdot \mathbf{E}$, or, light intensity. It then follows that the rate of two-photon absorption is proportional to $\mathbf{E} \cdot \mathbf{P^3} = \varepsilon_0 \chi^3 \mathbf{E} \cdot \mathbf{E} \cdot \mathbf{E} \cdot \mathbf{E}$, or the square of the light intensity.

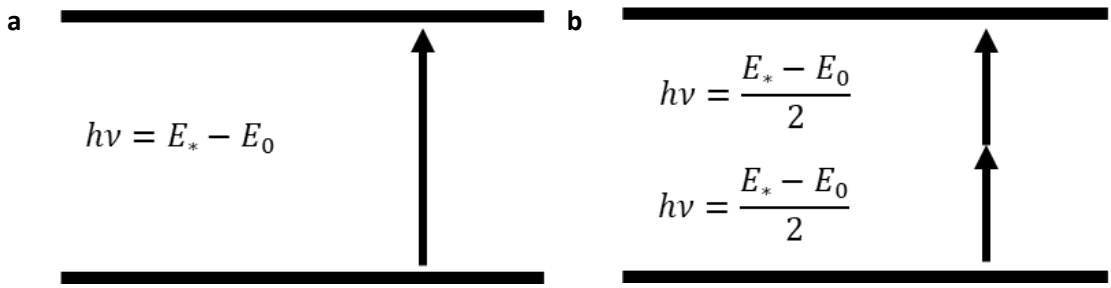

Figure 3-28 Electron excitation through (a) single-photon absorption and (b) two-photon absorption.

Intuitively, one would expect to be able to address the challenge of uniform exposure in single-photon lithography by employing a focused laser. For a plane wave, the attenuation via single-photon absorption is given by:

$$\frac{dI}{dz} = -\sigma_{1PA} N I(z) \tag{3.89}$$

Where the I represents the intensity, z the distance along the direction of light propagation, σ_{1PA} is the linear absorption cross-section of the photoinitiator molecule, and N represents the number of photoinitiator molecules per unit volume. The solution to 3.89 then yields the familiar Beer-Lambert law:

$$I(z) = I_0 e^{-\sigma_{1PA} N z} \tag{3.90}$$

For a Gaussian beam entering a high optical density medium, however, this yields the dose distribution shown in Figure 3-29a, where most absorption is at the surface. Reducing the photoinitiator concentration yields a focal spot in the x-y plane. However, we find a uniform dose distribution along the z-axis (Figure 3-29b). In contrast to the single-photon case, the attenuation via two-photon absorption is given by

$$\frac{dI}{dz} = -\sigma_{2PA} N \big(I(z)\big)^2 \qquad 3.91$$

Yielding dose deposition according to a Gaussian function in 3D space (Figure 3-29c) centred at the laser focal spot. The well-defined focal spot may then be moved with respect to the substrate, allowing for a 3D geometry of arbitrary design to be traced in the photoresist.

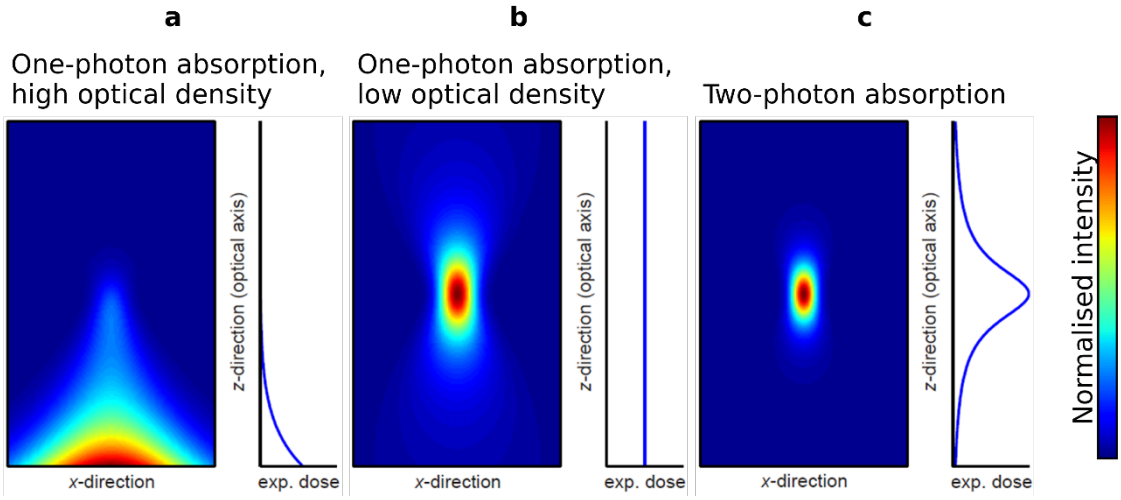

Figure 3-29 Dose distributions for a gaussian beam from below into a photoresist volume. (a) single-photon absorption where the photoresist has a high photoinitiator concentration. (b) single-photon absorption where the photoresist has a low photoinitiator concentration. (c) two-photon absorption. [109]

As two-photon absorption is a third-order non-linear process, two-photon lithography uses a femtosecond pulsed laser to create high-intensity exposures and the focal spot. Setting the photoinitiator molecule density (N) to the initial density (ρ_i) less the already radicalized molecules (ρ_r), the rate of free radical production is given by

$$\frac{d\rho_r}{dt} = (\rho_i - \rho_r)\sigma_{2PA} I^2 \qquad 3.92$$

Which has the solution

$$\rho_r = \rho_i[1 - \exp(-\sigma_{2PA} I^2 t)] \quad 3.93$$

The laser intensity for a gaussian beam is given by

$$I(r,z) = I_0 \left[\frac{\omega_0^2}{\omega(z)^2}\right] \exp\left[-\frac{2r^2}{\omega(z)^2}\right] \quad 3.94$$

Where ω_0 and I_0 represent the beam waist (radius) and intensity at the focal point where $r = z = 0$. At the focal point, ω_0 in immersion oil is given by:

$$\omega_0 = \frac{\lambda}{\pi NA}\sqrt{n_{oil}^2 - \mathrm{NA}^2} \quad 3.95$$

Where λ denotes the laser wavelength, n_{oil} the refractive index of immersion oil, and NA is the objective numerical aperture. The photon flux intensity at the focal plane can be expressed as a function of mean laser power (P), beam waist at the focal point (ω_0), pulse length (τ), pulse repetition frequency (f_γ), Planck's constant (h), and the photon frequency (ν)

$$I_{focal} = \frac{P}{\pi\omega_0^2 \tau f_\gamma h\nu} \quad 3.96$$

Which is related to I_0 according to

$$I_0 = \frac{2e^2}{e^2 - 1} I_{focal} \approx 2.3 I_{focal} \quad 3.97$$

Photon intensity is highest at the focal plane ($z = 0$), and 3.94 becomes:

$$I(r, z = 0) = I_0 \exp\left[-\frac{2r^2}{\omega_0^2}\right] \quad 3.98$$

And combining the prior equations then yields an expression for the TPL voxel diameter d_v in the focal plane.

$$d_v = \omega_0 \left[\ln \frac{\sigma_{2PA} I_0^2 n_p \tau}{C_\rho}\right]^{\frac{1}{2}} \quad 3.99$$

Where n_p is the number of pulses $n_p = ft$ and C_ρ is a function of the initial photoinitiator concentration and the threshold concentration ρ_t

$$C_\rho = \ln \frac{\rho_i}{\rho_i - \rho_t} \quad 3.100$$

We can apply a similar process to determine the voxel diameter along the beam axis (voxel length) by setting $r = 0$ in equation 3.94:

$$I(r = 0, z) = \frac{I_0 \omega_0^2}{\omega(z)^2} \quad 3.101$$

Which becomes:

$$l_v = 2z_R \left[\left(\frac{\sigma_{2PA} I_0^2 n_p \tau}{C\rho}\right)^{\frac{1}{2}} - 1\right]^{\frac{1}{2}} \quad 3.102$$

Where z_R is the Rayleigh wavelength $z_R = \pi\omega_0^2/\lambda$.

4. Experimental methods

4.1. Two-Photon Lithography

Photolithography is a well-established technique for realizing complex 2D structures upon a substrate. Typically, a photoresist is cast upon the substrate and selectively exposed to a UV light source with a stencil mask such that the solubility of the exposed region is altered to facilitate selective removal using specific solvents. In the case of positive tone resists, exposure results in an increase in the material's solubility in the solvent such that the exposed regions are removed in a subtractive process. In contrast, negative tone photoresists decrease the solubility such that unexposed regions are removed during development.

This work uses negative-tone photoresists only for nanofabrication using two-photon lithography. Specifically, we use a proprietary IPL-780 photoresist from NanoScribe GmbH with the NanoScribe photonic professional GT. We use a 780nm pulsed laser with ~100 fs pulse length, an 80MHz repetition rate, and 25kW peak power. Figure 4-1 shows a schematic of the NanoScribe system where the laser passes through an acousto-optic modulator (AOM) modulating the laser power. The beam is expanded and collimated before passing through a high numerical aperture (NA $= 1.4$) objective in immersion oil ($n_{oil} =$

1.518) to focus upon a point in the photoresist. Based on equation 3.95, this yields a beam waist of 104nm at focus.

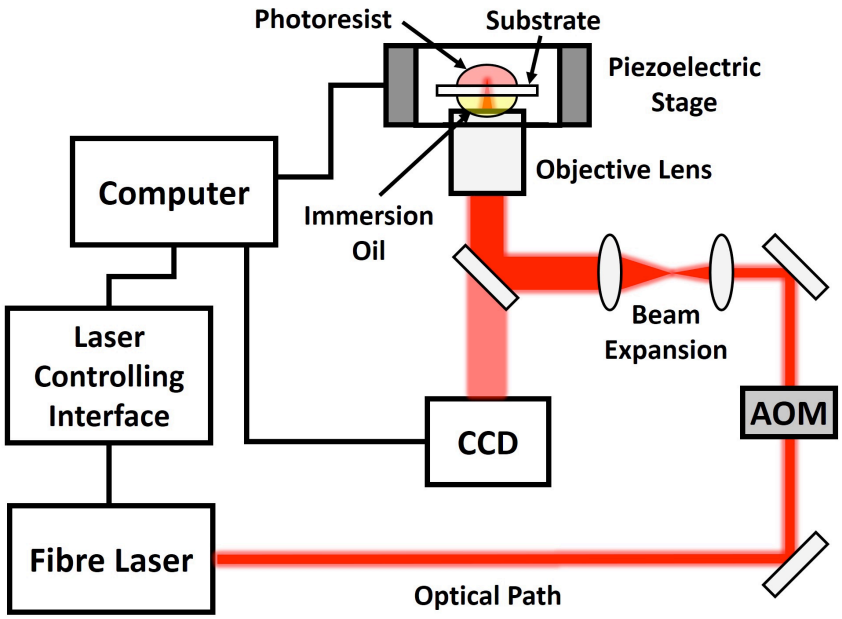

Figure 4-1 Schematic of TPL system. An optoacoustic modulator (AOM) modulates the beam intensity before the beam is expanded and then focussed down by the objective lens to diffraction limited spot in the photoresist. The piezoelectric stage translates the sample with respect to the focal spot to trace 3D geometries. A galvo mirror may be placed in the beam path to increase scan speeds in the xy plane.

Substrates are typically glass coverslips or ITO coated glass coverslips prepared with a 20-minute ultrasonic acetone bath, followed by a 20-minute ultrasonic isopropyl alcohol (IPA) bath, and subsequently dried using compressed air. Immersion oil (Immersol 518F with refractive index 1.518) is cast on the lower substrate surface, and negative-tone photoresist (NanoScribe IPL-780) is drop-cast on the upper side (Figure 4-2a), and the sample mount is inserted into the Nanoscribe with the immersion oil towards the objective lens. The objective lens is raised to be immersed in the immersion oil (Figure 4-2b), and the glass-resist interface is found before writing commences.

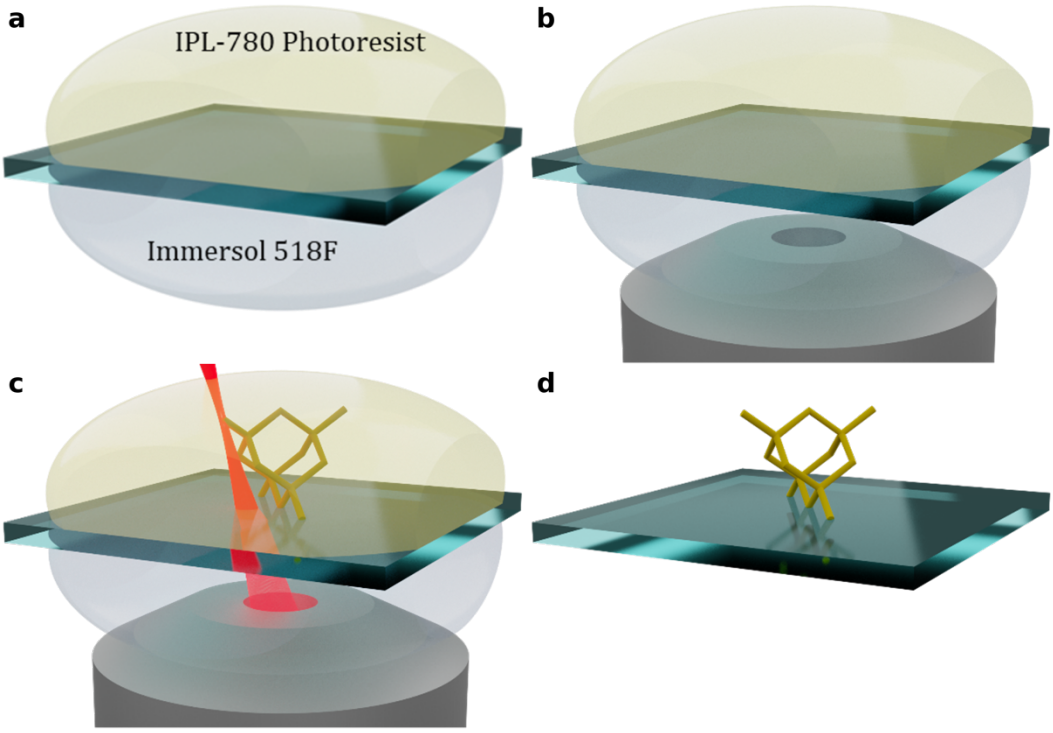

Figure 4-2 outline of two-photon lithography fabrication process using negative resist. (a) index-matched immersol 518F is drop-cast upon the bottom of the substrate and IPL-780 negative-tone photoresist is drop cast on top of the substrate. (b) Objective lens is immersed in the immersol. (c) Laser is focused with the focal spot in the photoresist to induce polymerisation. The focal spot is translated in 3D space to trace arbitrary 3D geometry. (d) After writing, the photoresist is removed with a PGMEA developer bath, followed by an IPA bath to remove remnant PGMEA and immersol.

The laser focal spot is translated in 3D space with respect to the substrate during the writing process, enabling the user to write arbitrary 3D geometries (Figure 4-2c). The objective lens is lowered after writing, and the samples may be removed to be placed in a 20-minute propylene glycol methyl ether acetate (PGMEA) developer bath, removing the unexposed resist. Finally, the samples are transferred to an IPA bath to remove PGMEA residue, and the samples are carefully dried using compressed air leaving a 3D polymer structure upon the substrate (Figure 4-2d).

Focal spot translation may be achieved in one of two scanning modes: The first mode fixes the focal position and uses the piezoelectric stage to translate the substrate along the x, y, and z axes, allowing the scan to follow a 3D path (Figure 4-3a). The second mode uses

a galvo mirror to translate the focal spot in the xy-plane where a z-slice of the desired geometry is written before using the piezoelectric stage to translate the substrate along z to write the next layer (Figure 4-3b). Piezo scan mode and Galvo scan mode offer advantages and disadvantages. Piezo scan mode may freely scan in 3D, but scan speeds are limited to 300 μm s^{-1} whereas galvo scan mode can operate at scan speeds up to 20 cm s^{-1} within the xy plane.

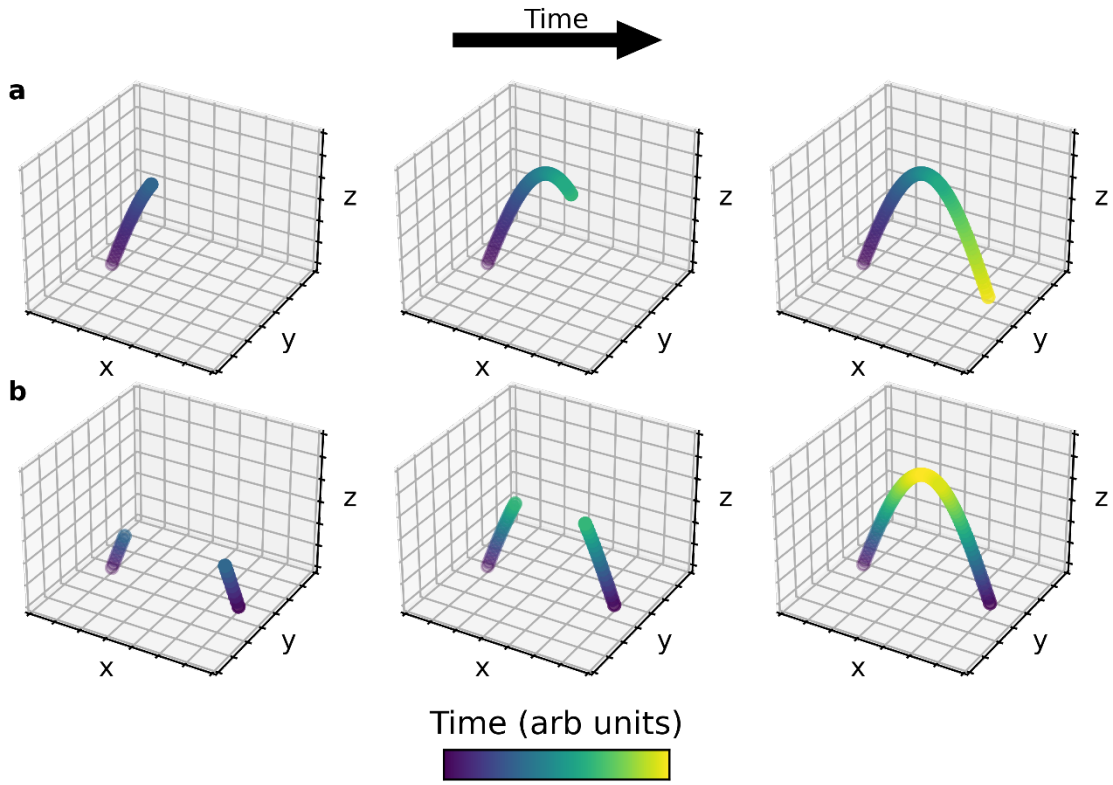

Figure 4-3 Schematic illustrating how a simple arch is written over time in (a) piezo mode, (b) galvo mode. In piezo mode, the path of the arch may be followed. In galvo scan mode, one can take advantage of the higher scan speeds in the xy plane by discretising the geometry along z

The user can define the desired geometry using either manually defined coordinates or a standard triangle language (STL) file generated using any Computer Assisted Design (CAD) software which is converted into a set of coordinates to be exposed. In the former case, the user may either specify a set of coordinates with the associated laser power and

exposure time at the coordinate in “pulsed mode” (Figure 4-4a) or invoke “continuous mode”, where two coordinates define a line along which the voxel travels at the specified scan speed and laser power (Figure 4-4b). The latter may also be achieved in pulsed mode by setting the “connectpoints” parameter to “on” such that the path between two coordinates is discretized and each point along the path is exposed in pulsed mode.

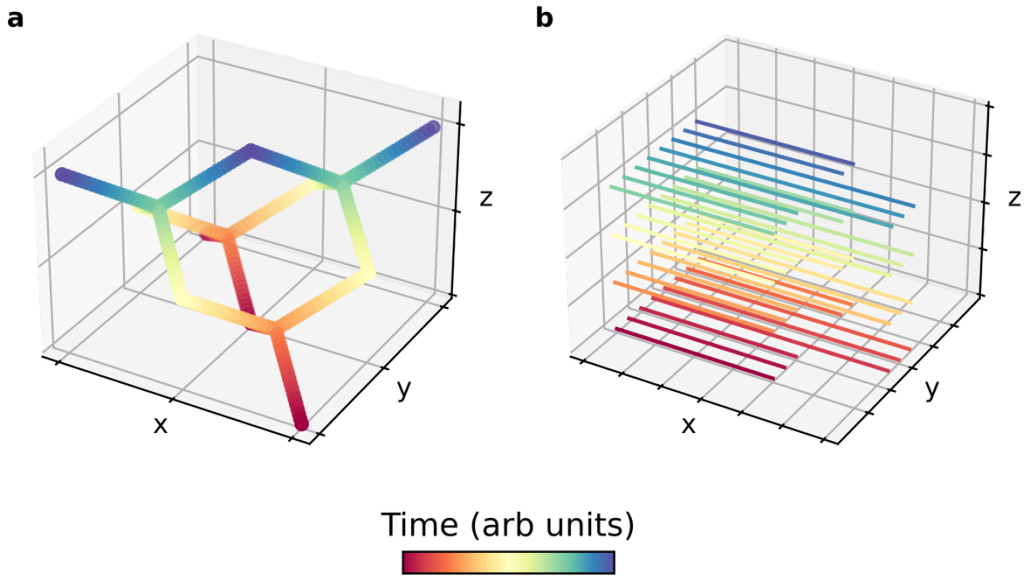

Figure 4-4 Schematic of how structures are written over time with NanoScribe using (a) pulsed mode, (b) continuous mode. Coordinates shaded in temporal order.

Exposure time and laser power affect the nanostructure feature size, where an increase in these parameters yields an increase in feature size. It is then desirable to minimize laser power and exposure to improve the feature size and resolution of the system; however, polymerization will not occur should these parameters fall below the threshold value. Conversely, should these parameters be too high, exposure results in “micro explosions” where there is a runaway propagation (Table 3-2) due to a high concentration of free radicals. The high level of automation available in TPL allows the user to empirically determine the optimum dose parameters by writing a large number of

structures and systematically varying the dose parameters. The key parameters are laser power, and exposure time in pulsed mode or scan speed in continuous mode.

4.2. Laser Ablation

Laser ablation is a top-down process that focuses a high-intensity laser beam at a substrate surface and removes material through either photochemical processes or localized heating, resulting in a phase change [110]. In the latter thermal regime, the process is initiated by the absorption of photons resulting in local heating during the laser pulse, whereas scission depolymerizes the material in the photochemical regime [110].

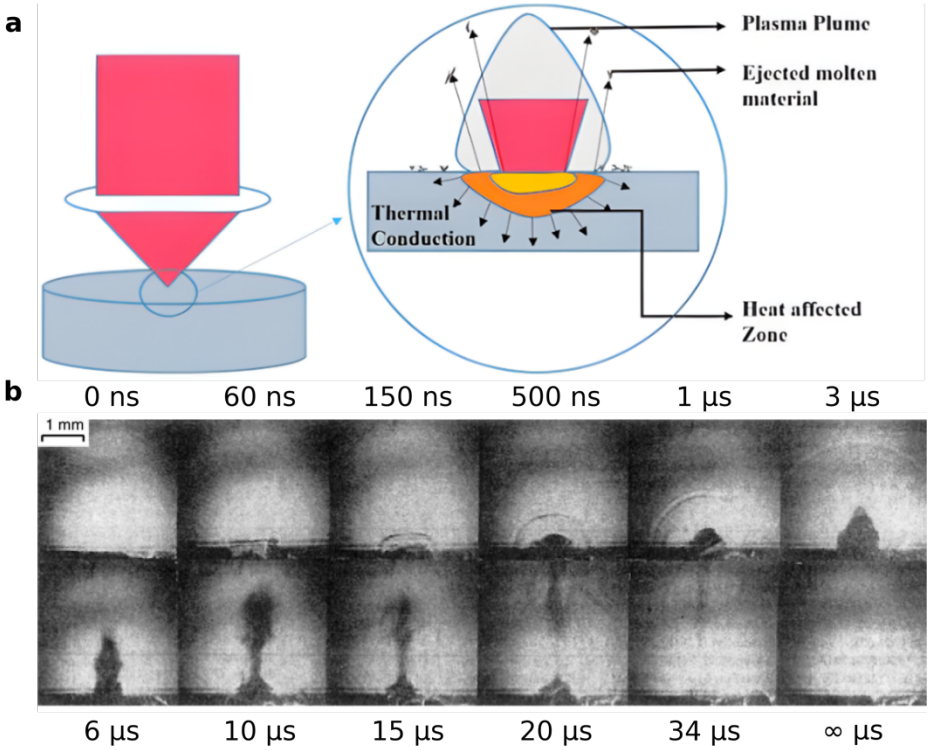

Figure 4-5 (a) schematic of laser ablation [110] (b) ultrafast imaging of laser ablation performed upon PMMA substrate [111]. From 150ns – 3µs, we observe the plasma plume and the ejection of the molten material until 34 µs.

Upon further exposure, material in the melt pool reaches the vaporization state resulting in a plasma plume around the target region, and recoil pressure ejects the

remaining molten material from the melt pool to be redeposited near the target site [112]. This process was captured in striking detail using ultrafast imaging of PMMA exposed to a single 20ns UV (248 nm) pulse in [111], and shown in Figure 4-5b.

We perform ablation using the standard 780nm wavelength laser in the Nanoscribe GT with ~100 femtosecond pulse duration, and an 80 MHz repetition rate, Idealized models of laser ablation assume only photochemical or photothermal reactions; however, both approaches yield mathematically nearly indistinguishable models [113, 114]. Of primary interest in this work is the dependence of etch depth per pulse (d) upon fluence (f) [115]:

$$d = \frac{1}{\alpha}\ln\left(\frac{f}{f_{th}}\right) \tag{4.1}$$

Where α is the material effective absorption coefficient, and f_{th} is the ablation threshold fluence. Extensive reviews regarding the laser ablation of polymers can be found at [110, 116] and subsequent references.

The work presented in chapter 5 explores the fabrication of 3D magnetic nanostructures using a polyacrylic acid sacrificial layer ablated to selectively expose the substrate and provide anchors for the nanostructures. The advantage of using ablation is that the laser power available in TPL systems is sufficient to ablate PAA and the user can define the geometries to ablate using the same scripting language using slower scan speeds and higher laser powers compared to a typical TPL script. After ablation, negative tone photoresists may be drop-cast onto the sample without the need to remove samples from their holder and alignment may be preserved.

4.3. Line of sight deposition

After fabricating the scaffolds using TPL, thermal evaporation is used to cast highly pure uniform thin films of Permalloy upon the scaffolds. A typical setup for thermal evaporation is shown in Figure 4-6a. A small amount of solid metal (evaporant) is cleaned in a 5-minute ultrasonic bath, dried using compressed air, and mounted on an alumina-coated molybdenum crucible connected to two electrodes. The samples are mounted to an aluminium sample mount and placed ~30cm above the crucible. Once the components are in place, a bell jar is placed over the setup, and the chamber is evacuated to pressures of approximately 2×10^{-2}mbar using the roughing pump. The chamber is then further evacuated to pressures below 10^{-6}mbar (our system typically reaches pressures of 5×10^{-7}mbar).

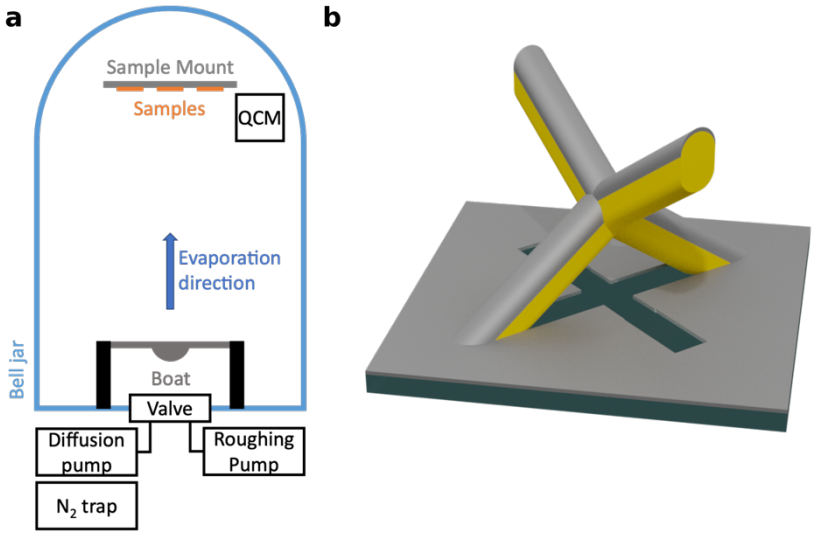

Figure 4-6 (a) schematic of typical thermal evaporation setup. The chamber is evacuated to ~10^{-3} mbar using the roughing pump, and further evacuated to pressures below 10^{-6} mbar. Joule heating in the crucible results in evaporation of the desired material which moves radially outwards. The distance between the source and the target samples is large such that the samples subtend a small angle resulting in effective top-down deposition. (b) schematic of 3d nanostructure upon which a material is deposited showing clear shadowing on the substrate due to the nanostructure.

Once a satisfactory vacuum has been achieved, current (60-90A) is passed through the crucible to heat the evaporant using Joule heating in the crucible. The current is gradually ramped to prevent thermal shock. A shutter above the crucible remains shut until the evaporant forms a melt pool and sufficient temperature is reached to evaporate the permalloy, and a quartz-crystal monitor (QCM) measures the deposition thickness. The shutter is not closed again until the evaporant has entirely evaporated, and the current is gradually ramped down to prevent thermal shock to the crucible.

The mean free path (λ) of a particle with diameter d may be approximated using the expression [67]:

$$\lambda = \frac{kT}{\sqrt{2}\pi p d^2} \tag{4.2}$$

Where p is the chamber pressure, and k is the Boltzmann constant.

Taking a worst-case scenario of a chamber pressure of 10^{-6} mbar, the mean free path for iron with $d = 250$ pm and Nickel with $d = 163$ pm [117] are orders of magnitude larger than the 30cm source-sample distance (~145 m and ~89 m respectively), resulting in the evaporant travelling in unimpeded straight lines. Given the small angle subtended by our samples, thermal evaporation can then be assumed to yield uniform thickness in z. This has important implications for nanostructured materials fabricated using TPL. Notably, only the top of the structures is exposed (Figure 4-6b), leading to a crescent cross-section of single-voxel nanostructures[38, 118]. Micromagnetic simulations outlined in chapter 5 explore the impact of this cross-section in magnetic nanowires and magnetic nanowire lattices.

4.4. MOKE magnetometry

The magneto-optical Kerr effect (MOKE) describes changes in polarization and intensity of reflected light after interacting with a magnetized surface. The oscillations of the electric field (**E**) result in the oscillation of electrons in the material, producing a time-dependent displacement vector (**d**) given by [70]:

$$\mathbf{d} = \underline{\boldsymbol{\mathcal{E}}}\mathbf{E} \tag{4.3}$$

Where $\underline{\boldsymbol{\mathcal{E}}}$ is a rank-2 tensor:

$$\underline{\boldsymbol{\mathcal{E}}} = \begin{pmatrix} 1 & -iQ_z & iQ_y \\ iQ_z & 1 & -iQ_x \\ -iQ_y & iQ_x & 1 \end{pmatrix} \tag{4.4}$$

The Voigt vector ($\boldsymbol{Q}$) describes the rotation of the polarization plane for an optical path due to magneto-optical interactions. Notably, the Voigt vector is parallel to the magnetization, and the magnitude is material dependent. For linearly polarized light, the tensor describes circularly polarized modes with dielectric constants:

$$\begin{aligned} \varepsilon^{+} &= \varepsilon(1 + \boldsymbol{Q} \cdot \mathbf{k}) \\ \varepsilon^{-} &= \varepsilon(1 - \boldsymbol{Q} \cdot \mathbf{k}) \end{aligned} \tag{4.5}$$

Linearly polarized light can be considered as a coherent superposition of left (σ^{-}) and right (σ^{+}) handed polarization, which introduces counter clockwise and clockwise (respectively) rotation in charges in a material and introduces a change in orbital angular momentum. Spin-orbit coupling in ferromagnetic materials result in small energy

contributions of opposite sign for σ^+ and σ^- such that the two propagate differently in the material and emerge with different amplitude and phases. The emerging light is then elliptically polarized with the major axis rotated by some angle θ_K in the case of reflected light (Kerr effect) or θ_F in the case of transmitted light (Faraday effect). The Kerr rotation (θ_K) may then be exploited for measuring hysteresis or magneto-optical imaging.

The dependence of the Kerr effect on the magnetization can be understood intuitively using the Lorentz force. The electric field causes oscillations in the charges, in the absence of magnetization, this results in the standard reflection amplitude R_{NM} with Fresnel reflection coefficients $R_{\parallel}$ and $R_{\perp}$ referring to the reflection coefficients for light polarized parallel and perpendicular (respectively) to the plane of incidence. The oscillations of the charges are in the direction of the electric field such that charges move in the induced magnetic field; as such, there exists a small oscillatory component ($\mathbf{V_l}$) perpendicular to both the local magnetization and the electric field [70].

$$\mathbf{V}_L \propto -\mathbf{M} \times \mathbf{E} \tag{4.6}$$

These oscillations result in a second amplitude R_K superimposed upon R_{NM}. Using simple geometric arguments for MOKE on a 2D sample plane, we find three well-defined geometries for MOKE measurements defined in terms of the incident plane, magnetization, and direction of the reflected light. Each of these geometries is sensitive to different components of the magnetization vector. First is polar MOKE (Figure 4-7a) with near-normal incidence such that the electric field causes in-plane oscillations, and equation 4.6 then yields in-plane oscillations perpendicular to **E** proportional to M_z resulting in a rotation in the polarization. At smaller angles of incidence, longitudinal and transverse

MOKE become more significant. Longitudinal MOKE (Figure 4-7b) is sensitive to the magnetization component parallel to both the incident and the surface, where equation 4.6 yields a rotation in the polarization. The induced oscillations in both polar and longitudinal MOKE are independent of polarization type, whereas transverse MOKE is polarisation-dependent.

Transverse MOKE (Figure 4-7c) is sensitive to the magnetization component perpendicular to the plane of incidence and parallel to the surface. S-polarization is defined as being perpendicular to the plane of incidence; it then follows that the transverse magnetization is parallel to the electric field such that $-\mathbf{M} \times \mathbf{E} = 0$ and s-polarization suppresses transverse MOKE. P-polarisation is parallel to the plane of incidence, and we find that induced oscillations are coplanar to the electric field. As a result, transverse MOKE yields a change in reflection intensity rather than a change in polarization.

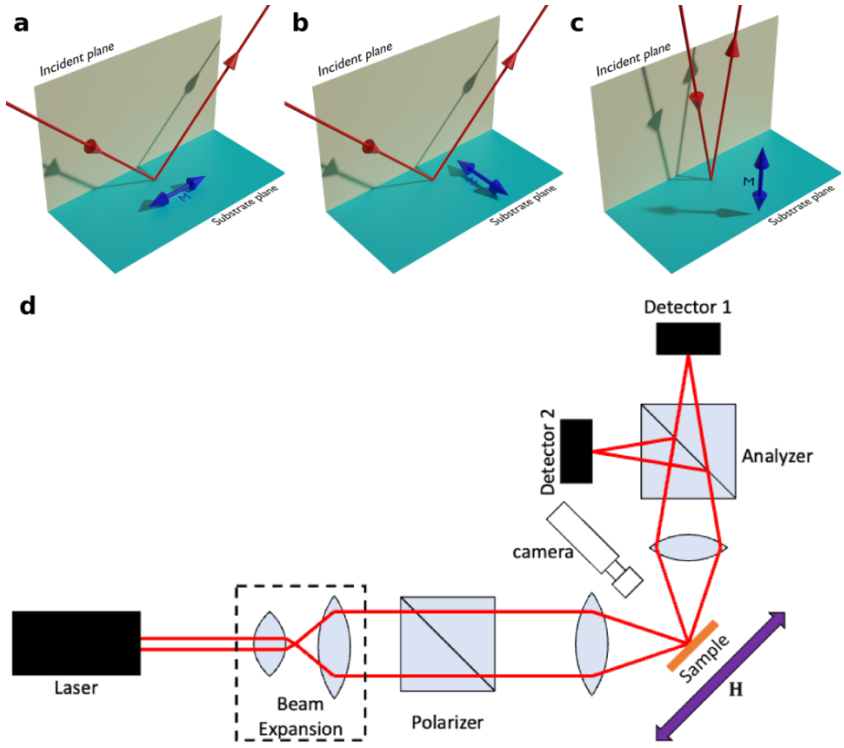

Figure 4-7 Schematic of (a) polar MOKE, (b) longitudinal MOKE, (c) transverse MOKE. (d) schematic of MOKE setup used in this thesis.

Figure 4-7d shows a schematic of the MOKE apparatus used in this thesis. We pass a laser through a beam expander, after which it is polarized using a Glan-Taylor polarizer and focused upon the sample with a focal spot diameter $\sim 10\mu m$ with a 45° angle of incidence. The reflected light is focused and passed through a second Glan-Taylor polarizer (analyser) such that the transmitted beam is passed to a photodetector (detector 1). When s-polarisation is selected at the polarizer, the rejected beam at the analyzer is parallel to the lab floor when the analyzer is at extinction such that the rejected beam may be captured by a second photodetector to measure background effects. A camera provides optical feedback to align the focal spot onto the sample. The sample is mounted between the poles of an electromagnet providing AC fields. We capture the intensity of the transmitted beam measured using detector 1 and rejected beam using detector 2 as a function of the applied field measured using a gauss meter. The final output represents the average of a user-specified number of cycles of the AC field.

4.4.1. Signal optimization

MOKE performed upon magnetic nanostructures is subject to many challenges regarding signal to noise (SNR) ratio, defined as the ratio of true signal to noise. The most obvious step in addressing this challenge is to increase signal. This may be achieved by increasing laser power, increasing the analyser angle from extinction, and reducing the focal spot size. However, these steps present further challenges.

Firstly, increasing the laser power increases local heating at the focal spot. Our structures are based on polymer scaffolds that readily deform at high laser power. Increasing the analyser angle to improve SNR when interested in longitudinal MOKE introduces features due to transverse MOKE. Finally, by definition of nanostructure, laser

spot size is always an order of magnitude larger than the target structure dimensions and signal from substrate tends to dominate the measurement. The focus of chapter 5 is to eliminate the substrate contribution.

With these constraints placed on improving signal, an alternative approach is to reduce sources of noise. An expression for SNR in MOKE was derived by Allwood et al. [119]:

$$\frac{\text{Signal}}{\text{Noise}} = \frac{R\Delta I}{\left[R^2(I_D + I_S + I_L)^2 + V_J^2\right]^{\frac{1}{2}}} \qquad 4.7$$

Where R is the load resistance of the detector, ΔI is the signal due to MOKE. I_D, I_S, and V_J represent the dark, shot, and Johnson noise in the detector. I_L is the noise within the laser.

At low signal levels, quantization at the analogue to digital converter (ADC) introduces further noise due to finite resolution, where the resolution of an n bit ADC is given by 2^{-n} times the voltage range. These sources of noise may be reduced by using the average of a large number of measurements such that the random noise is cancelled whilst leaving the signal unaffected. However, there is a square root dependence of SNR upon the number of repeats [120], resulting in diminishing returns as the number of repeats increases.

Random noise is evenly distributed across the frequency spectrum, and oversampling may then be employed to enable the use of signal smoothing through the careful use of low-pass filters. MOKE measurements shown in this work were captured with

a minimum sample rate of 10^5 samples per period and the period of the AC fields is no less than 1 second.

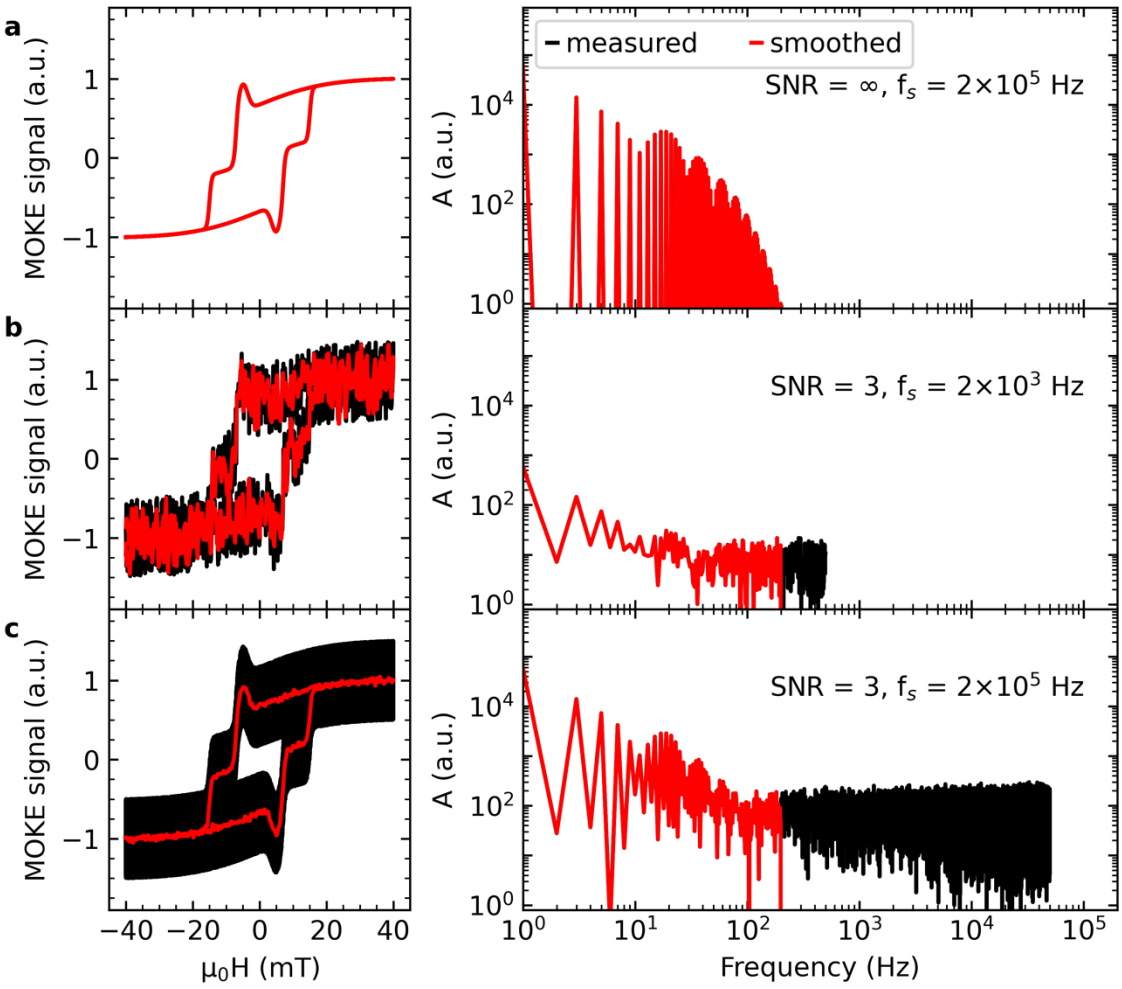

Figure 4-8 (a) artificial hysteresis loop of an arbitrary system. (b) FFT of the artificial hysteresis loop. (c) artificial hysteresis loop resampled with a sample rate of $\mathbf{2 \times 10^3}$ Hz and a quantisation noise source with RMS amplitude of 0.3, yielding an RMS SNR of 3. (d) FFT of (c). (e) artificial hysteresis loop resampled with a sample rate of $\mathbf{2 \times 10^5}$ and random noise source. (f) FFT of (e)

Figure 4-8a shows a contrived hysteresis loop with its associated FFT spectrum. In Figure 4-8b, the AC field applied has a period of 1 second. The Fourier components at $f >$ 200Hz are vanishingly small. We resample the hysteresis loop with a sample rate of 2×10^3Hz whilst adding a random noise source with root-mean-square (RMS) amplitude of 0.3, yielding an RMS SNR of 3 (Figure 4-8c). We apply a sharp low-pass filter with a cut-

off frequency $f_f = 200$ Hz (Figure 4-8d) but poorly recover the detail of the hysteresis loop in Figure 4-8a. Repeating the exercise with a sample rate of 10^5Hz (reflecting our measurement data), recovers the hysteresis loop detail (Figure 4-8e&f). This contrived example offers the advantage of foreknowledge regarding where the signal becomes vanishingly small, and more conservative parameters ($f_f > 500$Hz) are used in this work to prevent the introduction of artefacts or the removal of detail due to filtering.

4.5. Scanning probe microscopy

4.5.1. Atomic force microscopy

Atomic force microscopy (AFM) is a powerful technique for characterizing the topography of a sample [121]. AFM uses a silicon scanning probe with a microscopic cantilever from which a sharp tip emerges. The probe is mounted on a cantilever holder such that it can be secured to a piezo tube, and a laser is projected upon the cantilever's upper surface such that the cantilever deflects the laser towards a photodetector (Figure 4-9). The tip is scanned across the surface of a sample, and the topography deflects the cantilever causing a measurable deflection in the laser.

There exist several modes of operation in AFM, namely contact mode, non-contact mode, and tapping mode, which are characterized by the distance between the tip and the sample surface [122]. Firstly, contact mode places the tip close to the sample surface such that interactions are between the tip and the surface is dominated by the electrostatic repulsion term in the Lennard-Jones potential. In contact mode, the deflection of the cantilever is monitored by the feedback systems, and the voltage across the cantilever is

varied to ensure constant deflection such that the voltage corresponds to the topography of the surface.

In contact mode, the deflection of the cantilever is monitored by the feedback systems, and the voltage across the cantilever is varied to ensure constant deflection such that the voltage corresponds to the topography of the surface. The close contact between the sample and the tip results in damage of softer materials, and contact mode is unsuitable. In non-contact mode, the tip is raised several nanometers (5-15 nm) such that the interaction is dominated by the attractive van der Waals term in the LJ potential. The van der Waals interactions are weak such that the resulting deflections are small, resulting in a weak signal. Therefore, the cantilever oscillates at its resonant frequency, and the LJ potential introduces measurable variations in phase, amplitude, and frequency. Although the increased tip-sample separation greatly reduces the risk of damage to either the sample or the tip, it results in a significant reduction in resolution.

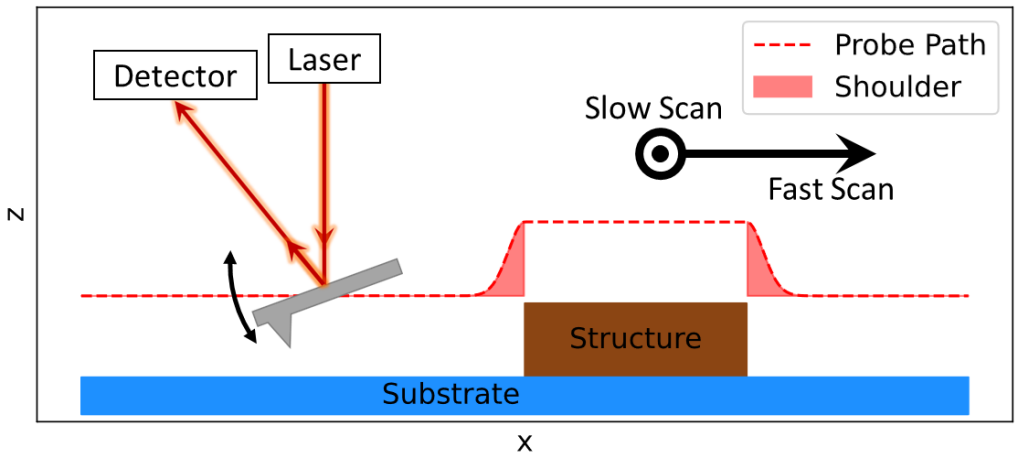

Figure 4-9 Schematic of AFM in tapping mode passing over a sample with probe path and shoulders indicated.

AFM data shown in this work was captured using tapping mode, which compromises between contact and non-contact mode to achieve high resolution with minimal risk of

damage. Like non-contact mode, a driving voltage oscillates the cantilever at the resonant frequency such that the tip briefly contacts the surface of the sample. This contact reduces the oscillation amplitude monitored by the feedback loop. The feedback loop shifts the probe along the z-axis to ensure that oscillation amplitude remains constant; the z-shift then provides topographical information.

The standard operating procedure for AFM is then:

1. Mount cantilever onto cantilever holder
2. Mount cantilever holder onto the piezo tube
3. Identify the z position of the cantilever by focusing the camera by focusing upon the cantilever surface.
4. Align laser to cantilever
5. Align photodetector to deflected laser
6. Tune the system to cantilever resonant frequency
7. Identify z position of the sample by focusing the camera upon the sample surface

When starting the scan, the sample is raised to 1mm below the probe using course movement in the mechanical stage. The automated engage procedure initiates where the piezo tube is lowered, and the feedback system measures the cantilever oscillations. The engage procedure is terminated when the oscillations are perturbed by van der Waals forces from the sample. At this point, the scan starts by tracing the probe along the fast scan axis and repeats the measurement by retracing the probe. Once the retrace is complete, the probe moves a set distance in the perpendicular direction (slow scan-axis) to capture the next line along the fast scan axis.

The capture is optimized by considering the amplitude setpoint, drive amplitude, scan speed, and pixel size along with gain parameters [122]. The amplitude setpoint refers to the amplitude of the cantilever oscillations, and the feedback system operates to keep this target value constant in tapping mode; as such, the amplitude reflects the z-position of the cantilever. The drive amplitude refers to the driving voltage to sustain the oscillation. The end-user optimizes these parameters to sufficiently capture the topography of the sample. Increasing the amplitude setpoint increases the distance between the probe and the sample such that the oscillating tip does not interact with the LJ potential unless high drive amplitudes are used. One may think that reducing the amplitude setpoint and increasing the drive amplitude will yield high-quality data; however, this combination results in the tip making contact with the sample surface. Known as tip-strike, this results in bright-line artefacts in the measurement and may damage both the tip and the sample. The pixel size is determined by the size of the scan area, number of lines, and samples per line. Intuitively, increasing the number of lines and samples per line will increase the resolution of the image, but increasing the number of lines results in longer capture times. One may compensate for the increase in capture time by increasing the scan speed; however, this reduces image quality as the feedback loop may not have sufficient time to adjust the feedback parameters and correctly measure the z-coordinate at a point on the line. The key gain parameters are integral gain and proportional gain describing feedback strength, where low values result in a slow response to topography, and too high a value results in high-frequency artefacts in the scan. There are no standard values for the parameters outlined here, and appropriate values depend on both the nature of the sample and the properties of the probe. The end-user must optimize the parameters in situ by gradually adjusting the amplitude setpoint and drive amplitude until there is good

agreement between the signal detected on the trace and retrace. Then the integral gain must be increased until high-frequency artefacts appear, and the decreased to the highest value where there are longer any artefacts present. This is then repeated for the proportional gain. It should be noted that the parameters are not linearly independent; a change in amplitude set point requires a change in drive amplitude, and a change in drive amplitude may require a change in gain parameters.

AFM is typically useful for mapping the topography of samples with little variation along the z-axis. AFM offers high resolution along z and is therefore very well suited for these tasks. AFM becomes more challenging with more pronounced topographical features such as those seen in this thesis. Pronounced features increase the likelihood of tip strike and shoulders, such as those seen in (Figure 4-9) arising due to interactions with the side walls of the protrusion. AFM remains a powerful technique for characterizing the topography of a sample despite these limitations, especially when coupled with a secondary technique such as electric force microscopy or magnetic force microscopy.

4.5.2. Magnetic force microscopy

Magnetic force microscopy (MFM) may be coupled with AFM to add magnetic information to the topographical maps generated with AFM. A probe with a hard magnetic coating on the upper surface and a soft magnetic coating on the bottom surface may be magnetized to add magnetostatic interactions between the tip and the sample surface. During the capture process, the topography of a sample is mapped using AFM, and after the retrace of the line, the probe traces the measured topography with an offset in z defined by the lift height. At this distance, the probe is no longer sensitive to the LJ potential, and tip-surface interactions are dominated by magnetostatics. A simple DC technique uses the

topography information to keep a constant distance between the sample and the tip; stray fields then introduce deflections. AC techniques oscillate the cantilever, and instead of deflection, the potential results in a change in phase, amplitude, and frequency. The z component of the force gradient ($F_z'(\mathbf{r})$ for a magnetized tip with its apex at position $\mathbf{r}$ is given by the integral [70]

$$F_z'(\mathbf{r}) = \int_{V_{tip}} \mu_0 \mathbf{m}(\mathbf{r}') \cdot \frac{\partial^2 \mathbf{H}(\mathbf{r}+\mathbf{r}')}{\partial z^2} d^3\boldsymbol{r}' \qquad 4.8$$

Where $\mathbf{m}(\mathbf{r}')$ is the magnetization of a volume element $d^3\mathbf{r}'$ in the tip at position $\mathbf{r}'$. This force gradient leads to a phase change in the oscillations proportional to $\partial_Z^2\mathbf{H}$.

The interaction energy between the sample and the tip is given by [123]:

$$E_{int} = -\int_{V_{tip}} \mu_0 \mathbf{M}_{tip} \cdot \mathbf{H}_{sample}\, dV = -\int_{V_{sample}} \mu_0 \mathbf{M}_{sample} \cdot \mathbf{H}_{tip}\, dV \qquad 4.9$$

Where the first integral shows that for some known tip magnetization distribution, sample magnetizations producing identical stray fields cannot be distinguished, conversely, the second integral shows that for some known sample magnetization, tip magnetizations yielding identical stray fields produce identical images. We may then substitute using the scalar potential $\mathbf{H}_{tip} = -\nabla\Phi_{tip}$ and integrate by parts:

$$E_{int} = -\int_{sample} \mu_0 \nabla \cdot \mathbf{M}_{sample} \cdot \Phi_{tip}\, dV - \int_{surface} \mu_0 \mathbf{M} \cdot \hat{\mathbf{n}} \Phi_{tip}\, dS \qquad 4.10$$

Showing two interaction terms corresponding to non-zero divergence of the magnetization $\nabla \cdot \mathbf{M}$, and the interaction of the magnetization with the sample surface $\mathbf{M} \cdot$

$\hat{\mathbf{n}}$. The first term shows that MFM may be approximated by computing the divergence of the magnetization.

Another implication of these expressions is that there exist multiple solutions in the sample magnetization that may yield the measured result. However, we can perform micromagnetic simulations of the imaged structures, and the expected MFM contrast may be computed and compared to MFM measurements, as shown in Figure 4-10. A significant part of this thesis focuses on using micromagnetic simulations and MFM data to identify magnetization states in 3D magnetic nanostructures. The AFM and MFM data shown in this thesis were captured using a Veeco Dimension 3100 SPM system.

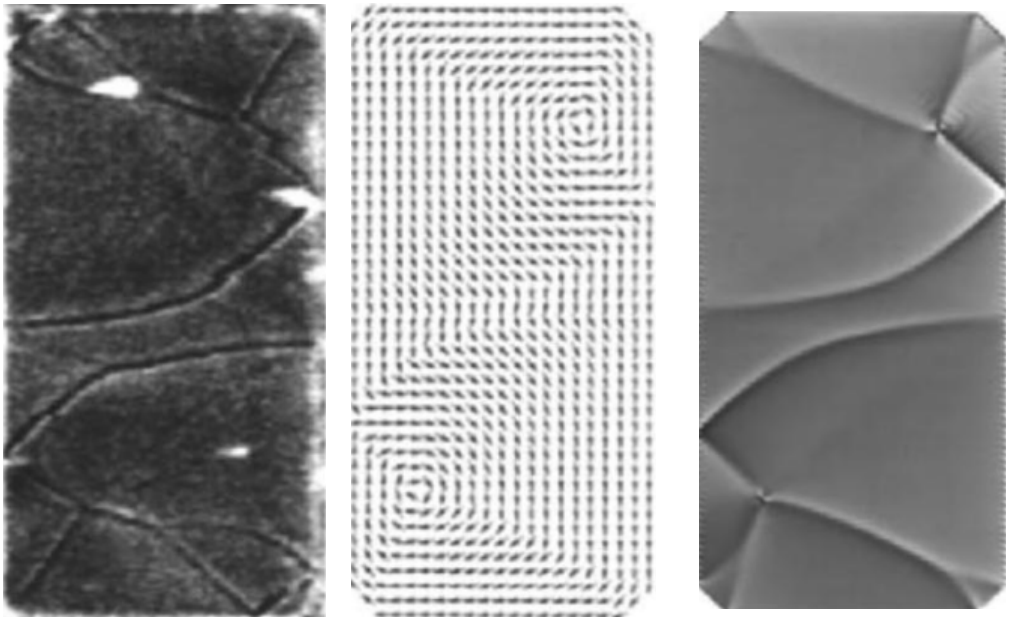

Measured contrast Computed magnetization Computed contrast ($\nabla \cdot \mathbf{M}$)

Figure 4-10 Comparison of simulated magnetization with corresponding computed MFM contrast to contrast measured from a $\mathbf{10 \times 5\ \mu m}$ Permalloy ($\mathbf{Ni_{81}Fe_{19}}$) element with 30nm thickness. [70]

4.6. Scanning Electron Microscopy

This thesis contains a number of images captured using scanning electron microscopy (SEM), which is a high-resolution imaging technique. Optical microscopy is a convenient method for imaging samples, but limitations in resolution render optical microscopy insufficient beyond cursory examination. SEM offers high-resolution imaging that can easily be coupled with energy dispersive x-ray (EDX) analysis for characterizing the elemental composition of materials.

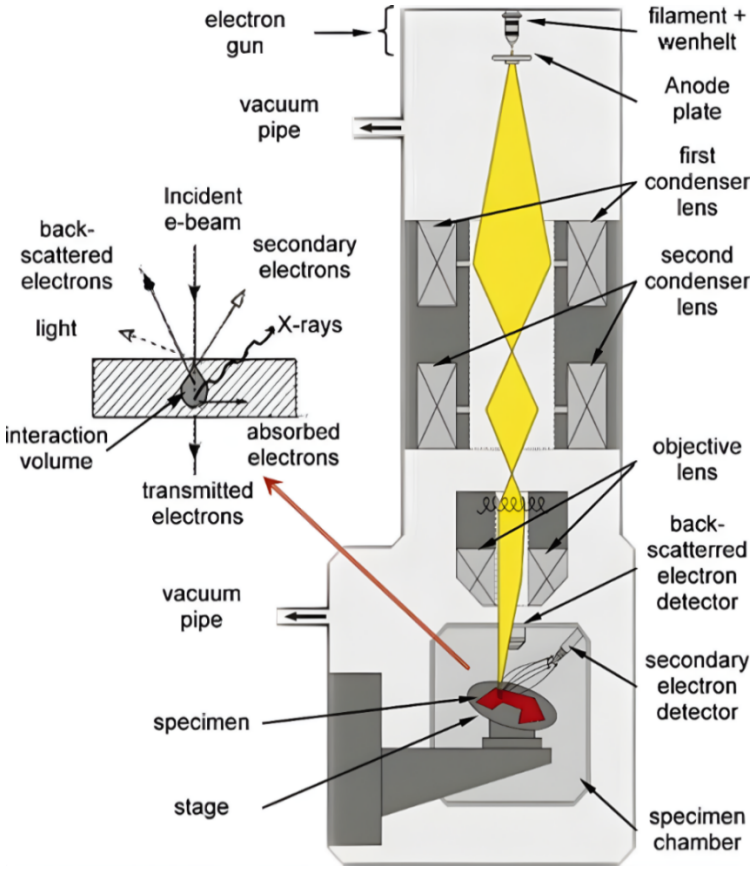

Figure 4-11 Schematic of typical SEM system [124]

SEM relies on focusing an electron beam upon the sample and scanning the focal spot across the field of view. Electrons are generated by an electron gun and accelerated towards the target by an anode plate; focusing is then achieved by a set of condenser lenses (Figure

4-11). The incident electrons are scattered elastically off electrons in the material, producing secondary electrons arriving at the secondary electron detector, and the signal is interpreted by a computer to reproduce an image.

The process also results in the ejection of secondary electrons from the inner shell, resulting in a vacancy that may be filled by a higher energy electron. This results in the emission of x-ray photons with energy equal to the energy difference, which may be exploited in energy dispersive x-ray analysis (EDX). These energies are characteristic of each element and the transition type, with energies pertinent to this work shown in Table 4-1, where K lines refer to a vacancy in the $n = 1$ shell being filled by an electron in the $n = 2$ shell (K_α), or $n = 3$ shell (K_β). And the L lines refer to a vacancy in the $n = 2$ shell being filled by an electron from the $n = 3$ shell (L_α) or $n = 4$ shell (L_β).

Element	$\boldsymbol{K_{\alpha_1}}$ /keV	$\boldsymbol{K_{\beta_1}}$ /keV	$\boldsymbol{L_{\alpha_1}}$ /keV
C	0.277	–	–
O	0.524	–	–
Na	1.040	1.071	–
Si	1.739	1.835	–
Fe	6.403	7.057	0.705
Ni	7.478	8.264	0.851

Table 4-1 characteristic energies of $\boldsymbol{K_{\alpha_1}}$, $\boldsymbol{K_{\beta_1}}$, and $\boldsymbol{L_{\alpha_1}}$ emission lines for elements pertinent to this thesis [125].

It follows that the addition of an x-ray detector to the SEM setup allows the user to measure emission spectra at the focal spot and determine the elemental composition in that region. This is referred to as energy dispersive X-ray (EDX) analysis. By scanning the focal spot of the electron beam, one can capture line profiles and elemental maps of the entire sample.

Despite the high resolution that is achievable with SEM, there are significant challenges to imaging the samples presented in this thesis. Charge build-up on the sample leads to significant imaging artefacts, image drift, and sample damage. Typically, one would ensure that the subject is coated in a conductive material such that all components are grounded, and both charge and heat dissipate. 3D nanostructures in this thesis have vertical side-walls where no material is deposited using line-of-sight deposition and structures are disconnected from the substrate. This is usually addressed by using LOS deposition to deposit thin gold layers with the substrate at an angle from the evaporation direction. However, the lift-off procedures demonstrated in this work render this ineffective such that the alternative is to deposit the gold layers after deposition, which results in masking of the magnetic material and interfering with magnetometry. In these instances, the effects of charging were limited by minimizing exposure times and capturing images at low accelerating voltages. Due to the risk of permanent damage to the structures, all categorization of structures in this thesis was performed before EDX spectroscopy requiring long exposures.

SEM images in this work were captured using a Hitachi SU8230 system, and a Zeiss Sigma HD was used to perform EDX measurements.

4.7. Micromagnetic Simulations

Micromagnetic simulations are a useful tool for understanding the magnetic properties of small structures. There exist a range of standard simulation codes using different methods, available on a commercial or freeware basis. In this work, we use finite

element simulations with nMag [126] and finite-difference simulations with MuMax3 [127].

To perform micromagnetic simulations, we must discretize the simulation geometry using either the finite-difference method (FDM) or the finite-element method (FEM). FDM defines a cuboidal simulation universe in which the simulation geometry is found, and the principal coordinates are discretized such that the simulation geometry is approximated by a series of cuboids in 3D space (Figure 4-12a). FEM discretizes the simulation geometry tetrahedral mesh (Figure 4-12b).

The suitability of each method depends on the simulation geometry and is subject to several considerations, which will be outlined here. FDM discretization yields a structured grid that allows vectorized computations that are intrinsically more efficient in both computational speeds and memory requirements. However, as is apparent in Figure 4-12, FDM yields a poor approximation of curved geometries unless the mesh size is small. Furthermore, the simulation universe is cuboidal such that complex 3D geometries result in a significant number of grid elements with null values still used in computations. In contrast, FEM discretization yields an unstructured grid that requires additional node and connectivity tables resulting in higher memory and computational requirements. Nevertheless, a tetragonal mesh yields a better approximation of curved surfaces with larger mesh sizes, and the simulation geometry defines the simulation universe such that there are no null elements. This work uses micromagnetic simulations performed on nMag, where FEM offers great advantages over FDM in terms of the computational requirements outlined. However, this work also explores large simulation geometries where the

computational requirements are not feasible for FEM discretization, and FDM discretization in MuMax3 becomes favourable.

Micromagnetic simulations solve the Landau-Lifshitz-Gilbert equation (equation 3.76) by performing a time evolution until a convergence condition ($|\partial_t \mathbf{m}| < C$) is reached. MuMax3 offers energy minimization techniques such as the conjugate gradient method with the "minimize" function and the "relax" function, which computes only the damping term of the LLG equation. These energy minimization techniques are significantly faster than time evolutions and useful for computing equilibrium states; however, there is a risk that the system ends up in a saddle point and return incorrect results. As such, energy minimization techniques should only be used to compute small changes in the system [127].

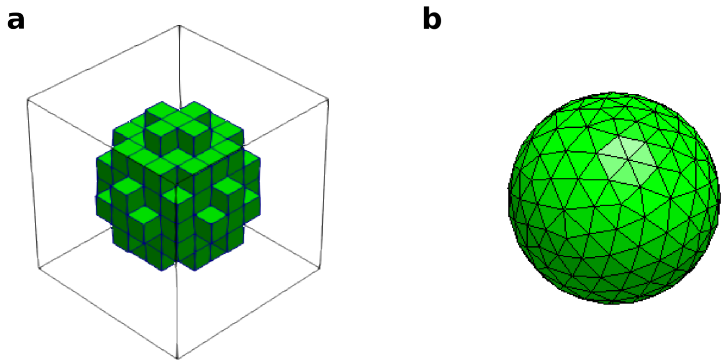

Figure 4-12 spheres with **20nm** radius meshed at **5nm** using (a) finite difference method showing a bounding box indicating the simulation universe, (b) finite element method.

All simulations in this thesis were performed setting material parameters for Permalloy ($Ni_{81}Fe_{19}$) with a saturation magnetization of 0.86×10^6 A m^{-1} (1.08 T), and an exchange stiffness of $A = 13 \times 10^{12}$ J m^{-1}. These parameters yield an exchange length of $\lambda_E \approx 5$ nm, which sets the upper limit of the simulation mesh size. As the energy

minimization methods are not available in nMag, we set the Gilbert damping coefficient to $\alpha = 1$ for investigations into converged states to reduce simulation time. When dynamics are of interest, we set the coefficient to a realistic $\alpha = 0.01$.

5. Simulating Spin Texture and Switching in the Building Blocks of a 3D Artificial Spin-Ice

Frustration arises when all pairwise interactions between the system's constituent parts cannot be satisfied [128] and plays a key role in phenomena such as folding of biological molecules [34], bonding in water ice [33], and disordered ground states [129, 130]. The simplest example of such a system is a set of three antiferromagnetically coupled spins on the corners of an equilateral triangle, as shown in Figure 5-1. Spins μ_1 and μ_2 may orient to minimise the antiferromagnetic interaction, but the third spin can only be arranged to minimise the interaction between either μ_1 or μ_2 leading to two degenerate ground states.

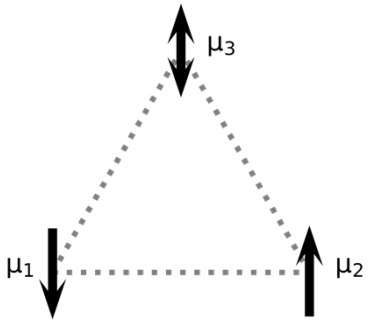

Figure 5-1 model system of three antiferromagnetically coupled spins on the corners of an equilateral triangle where not all pairwise interactions can be satisfied.

In a remarkably simple back-of-the-envelope calculation, Linus Pauling introduced the ice model to account for the observation that the entropy of water ice approaches a finite value as it approaches zero Kelvin. Pauling's model describes oxygen atoms in a water ice crystal as a vertex capable of forming a bond with four adjacent hydrogen atoms where two bonds are either long hydrogen bonds or short covalent bonds. Each hydrogen atom must form one covalent and one hydrogen bond. These constraints result in six possible configurations for each water molecule in the ground state leading to extensive degeneracy at low temperatures [33]. In a 1941 paper, Slater described the arrangements of hydrogen phosphate groups in a potassium diphosphate (KDP) crystal positioned on the corners of tetrahedra, where the crystal field restricts the electric dipole moment of $(H_2PO_4)^-$ groups either towards or away from, the centre of the tetrahedron [103]. Geometric constraints in the KDP crystal restrict the vertex configurations such that two of the dipole moments are directed towards the vertex, and two are directed away from the vertex. With six allowed vertex configurations, Slater drew the analogy to the ice model likening the "in" and "out" orientations to the short and long bonds in Pauling's model, giving rise to the notion of a vertex model describing vertices with four Ising spins directed either towards or away from the vertex. A key difference between Slater's KDP model and Pauling's ice model is that the six configurations in the latter are degenerate, whereas configurations yielding some net polarisation are favoured in the KDP model.

In 1963, Franz Rys explored a two-dimensional square vertex model by drawing arrows on a square planar net yielding the vertex configurations shown in Figure 5-2. In the current nomenclature, vertices showing anti-alignment are referred to as "Type I" vertices, and vertices favouring alignment are referred to as "Type II". The two dimensional

KDP model assigns lower energies to the type-I vertices ($\epsilon_1 = \epsilon_2 > 0$ and $\epsilon_3 = \epsilon_4 = \epsilon_5 = \epsilon_6 = 0$), whereas Rys explored antiferroelectric ordering favouring type-II vertices ($\epsilon_1 = \epsilon_2 = 0$ and $\epsilon_3 = \epsilon_4 = \epsilon_5 = \epsilon_6 > 0$) now known as the Rys F model [102]. Applying this 2D approach, Elliot Lieb developed exact solutions to the ice model [96], Rys F model [95], and the KDP model [94], providing the first exactly solved models in statistical mechanics [93].

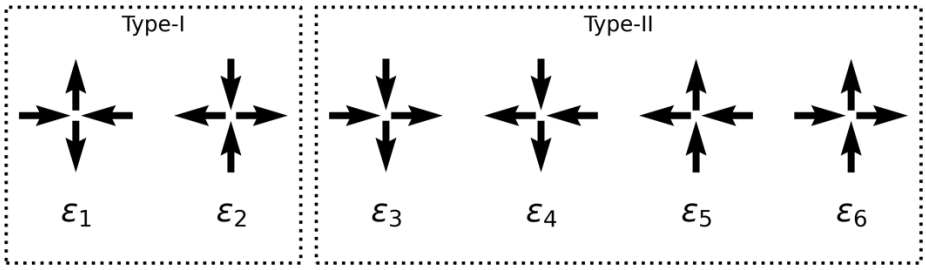

Figure 5-2 arrow representation of the six ice-type vertices in a 2D square lattice. Type-I vertices show antiferromagnetic ordering, whereas Type-II vertices show ferromagnetic ordering and thus carry net polarization.

In 1956, Anderson described a hypothetical lattice with antiferromagnetic spins on corner-sharing tetrahedra where the crystal field, similarly to the electric dipoles in Slater's model, confines the spins to be directed along the local ⟨1,1,1⟩ axis either towards or away from the centre of the tetrahedra. Like Pauling's ice-type model, the six 2-in/2-out vertices are degenerate, but additional 3-in/1-out, 1-in/3-out, 4-in, and 4-out vertex arrangements violating the ice rule are also accessible [131]. Slater ruled these states out in the KDP model due to the restrictions in the possible positions of the hydrogen atoms in the $(H_2PO_4)^-$ groups, but this limitation is not present in the case of Anderson's spin-ice model. When applied to magnetic moments, these ice-rule-violating excitations have a non-zero divergence in the **M** and **H** fields. These excitations act as magnetic monopole-like quasi-particles that propagate through the material and interact via a Coulomb potential [84, 132] akin to the magnetic monopoles described by Dirac in the early 1930s [85].

The subject garnered intense interest upon the discovery that rare-earth titanates such as holmium titanate ($Ho_2Ti_2O_7$) and dysprosium titanate ($Dy_2Ti_2O_7$) exhibit spin ice behaviour with rare-earth ions with non-zero magnetic moments arranged on the corner-sharing tetrahedra in a pyrochlore lattice. These rare earth ions (HO^{3+} or Dy^{3+}) couple via dipolar interactions and ferromagnetic exchange at low temperatures [36, 133]. Heat capacity measurements show a residual entropy in these systems at low temperatures [134], and diffuse neutron scattering shows signatures of magnetic monopole quasiparticles [87].

Although there exist a wide range of techniques by which spin-ice materials may be probed, these are limited to bulk measurements at low temperatures. Wang et al. [37] demonstrated a mesoscopic model system comprising single-domain magnetic nanoislands arranged in a two-dimensional square net where the magnetisation of each wire could be directed either towards or away from a coordination number four vertex. With a demagnetising protocol [135], the two-dimensional artificial spin ice (ASI) could be relaxed into its ground state and the number of each vertex type could be determined using standard in-house measurement techniques such as magnetic force microscopy. The work showed the formation of the ice-rule vertex types and excitations in the form of magnetic monopole-like defects. However, the vertex-type population deviates from what is expected in spin ice materials, as arranging the spins on a two-dimensional surface results in uneven interactions between the spins at the vertices resulting in degeneracy lifting among the ice-type vertices.

Despite this degeneracy lifting between type-I and type-II vertices, ASIs offer a model system to study frustration, with the advantage that interaction energies may be precisely

tuned by varying the wire dimensions or separation at the vertices. Using modern fabrication techniques, it is also trivial to arrange the wires in novel geometries by systematically excluding wires to produce brickwork [136], Shakti [137, 138], and Tetris [139, 140] lattices, or rotating the wires to produce pinwheel lattices [141] as shown in Figure 5-3. The vertices in kagome lattices comprise three wires, with each pair of wires enclosing a 120° angle such that the interaction between each pair of wires is equal. However, there exists no divergence-free vertex configuration, yielding a charge-ordered ground state of alternating $\pm q$ charges and excitations of $\pm 3q$ charges [142].

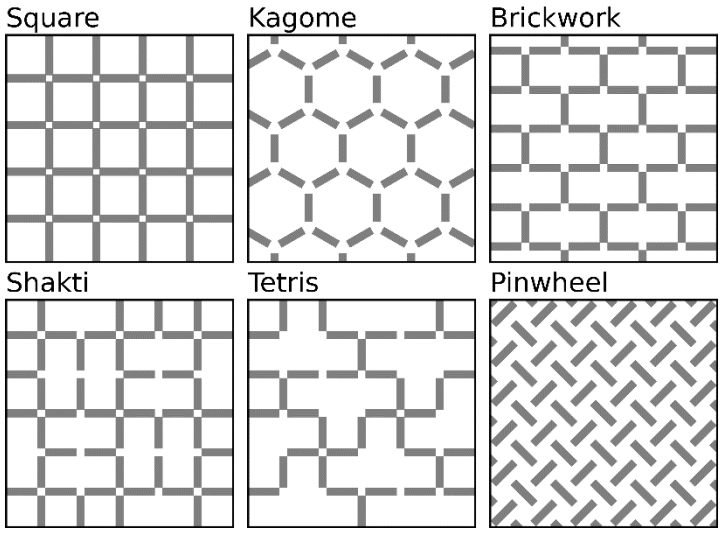

Figure 5-3 Schematic of a selection of 2D frustrated lattices from recent literature covering square [37], Kagome [142], Brickwork [136], Shakti [136, 137], Tetris [139, 140], and Pinwheel [141] lattices.

The degeneracy lifting in square lattices can also be exploited to investigate the properties of the vertex models. For example, vertex-type energy may be tuned by modifying the vertex geometry in a connected square lattice to perturb the micromagnetic texture. With sufficient energy difference between type-I and type-II states, the topological properties of the Rys F-model may be investigated [104, 105].

Even though the result has opened various avenues of research, there remains one significant limitation to using ASI as a model for spin-ice materials: when limited to a 2D system, there is no means to ensure equal interaction between all wires at a coordination four vertex. In a key paper, Perrin et al. [100] divided the wires into horizontal and vertical sublattices. A key factor in the interaction strength is the separation between wires at a vertex which may be tuned by introducing a height offset between the sublattices. This height offset allowed the group to tune the energies of the vertex types to realise phases favouring either antiferromagnetic (type-I) or ferromagnetic (type-II) vertex types. At some critical height, the coulomb phase, where all the ice-type vertices are degenerate, can be realised. This result is particularly interesting for the exploration of the six vertex models and presented a significant step forward for exploring the sixteen-vertex models in spin-ice. However, truly deconfined monopole pairs interact only via a magnetic analogue of Coulomb's law, and the magnetisation of the wires in these systems do not lie along the local ⟨1,1,1⟩ axis resulting in additional energy terms in monopole defects interactions referred to as "string tension". This final limitation can only be overcome by developing a true three-dimensional arrangement of magnetic nanowires where the magnetic moment lies along the local ⟨1,1,1⟩ axis.

Our recent work describes the realisation of a 3D magnetic nanowire lattice comprising magnetic nanowires wires arranged in a connected diamond bond lattice geometry [38] upon which magnetic monopole-like defects and their propagation through the lattice could be measured using standard techniques [39]. This chapter explores the micromagnetic studies performed to support the analysis of the experimental results.

The first step is to determine the suitability of the magnetic nanowires for ASI studies where the wire must function as an "Ising-like" spin. This criterion requires that the wire is single domain at remanence, with the magnetisation either "up" or "down" along the long axis of the wire. The wire must switch between the states with a single sharp transition such that no intermediate states are accessible and retain this behaviour when placed in more complex geometries. We compute the micromagnetic spin textures associated with each vertex type, the associated energies, and surface charge density enabling the identification of vertex types in magnetic force microscopy measurements of the lattices.

Figure 5-4a shows a schematic of these lattices, indicating how these are divided into L1, L2, L3, and L4 sublattices defined by the wire's z-coordinates. Using two-photon lithography, we fabricate a 50μm × 50μm polymer scaffold with a height of five unit cells, upon which a 50nm layer of permalloy ($Ni_{81}Fe_{19}$) layer is deposited using thermal evaporation. The result is a lattice comprising wires with a crescent-shaped cross-section [38]. Figure 5-4b shows an atomic force micrograph of the lattice with the annotated L1, L2, and L3 sublattices in the inset; currently, AFM cannot resolve the L4 sublattice. Figure 5-4c shows a scanning electron micrograph (SEM) of the complete lattice captured at a 45° tilt angle. A high-magnification SEM captured at a 0° tilt angle is shown in Figure 5-4d with annotations indicating the sublattices. Figure 5-4e provides a further intuitive understanding of the lattice structure with a high-magnification image of the top-right corner shown in Figure 5-4a captured at a 45° tilt angle.

We have shown these lattices to be a promising candidate for 3D artificial spin-ice (3DASI) studies with ground state ordering according to the ice rule [38] and extended this by demonstrating magnetic charge propagation upon the lattice [39]. Furthermore, the

study of thermal magnons using Brillouin light scattering spectroscopy shows the propagation of coherent spin waves through the lattices [143]. This chapter considers micromagnetic simulations performed to aid the interpretation of experimental results described in [38, 39] and future work.

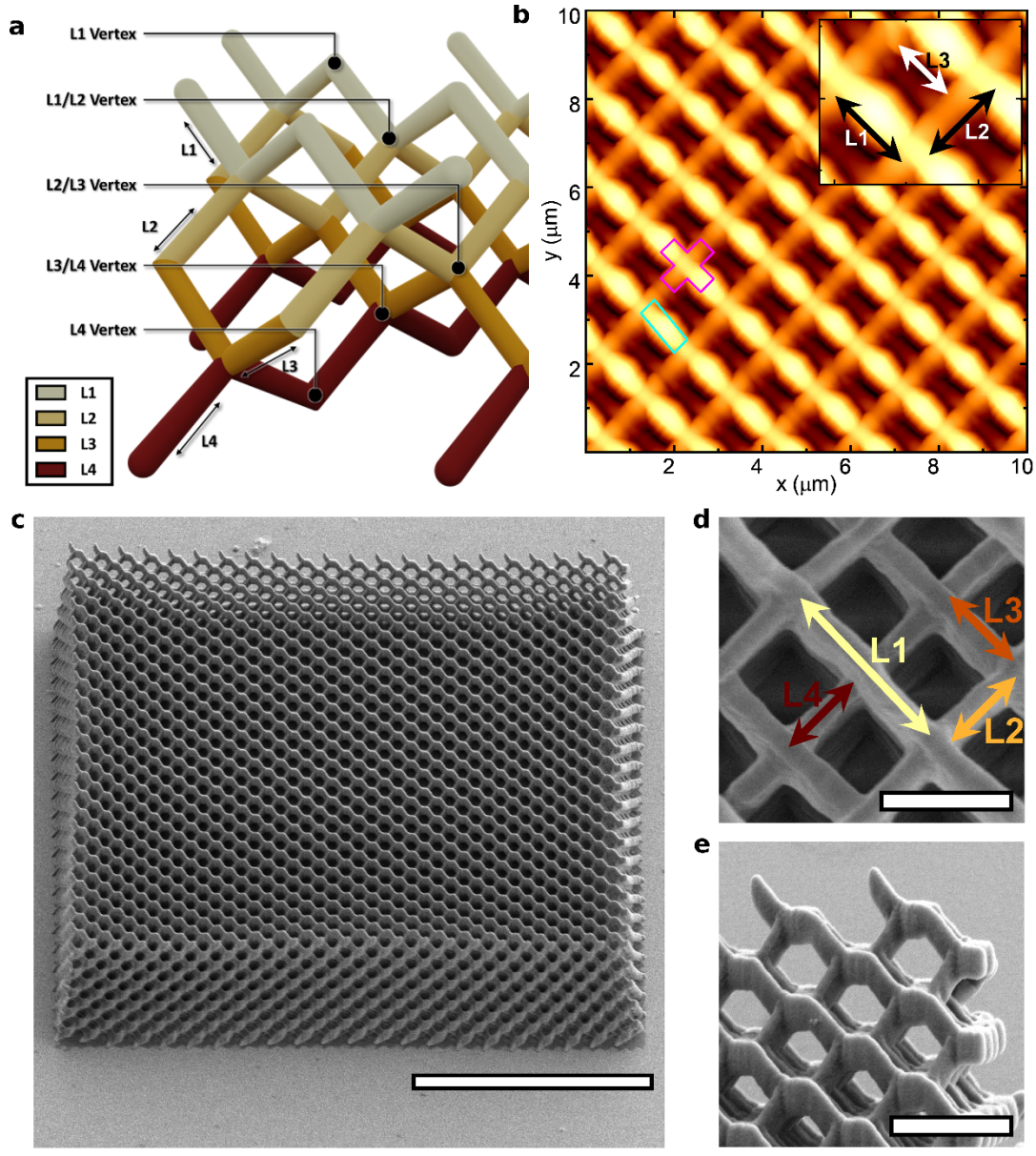

Figure 5-4 (a) Schematic of diamond bond lattice coloured according to sublattices L1, L2, L3, and L4. (b) Atomic force micrograph of a 10μm × 10μm region with L1, L2, and L3 sublattices annotated; L4 currently cannot be resolved using AFM. (c) Scanning electron micrograph (SEM) of an entire lattice at 45° tilt. Scale bare indicates 20μm. (d) High magnification top-down SEM of the lattices with all sublattices annotated. The scale bar indicates 1μm. (e) High magnification SEM of the top-right corner shown in panel (a) taken with a 45-degree tilt. The scale bar indicates 2μm.

Due to computational restraints, it is not feasible to perform simulations on an entire unit cell of the lattice and instead consider different building blocks separately. The schematic shown in Figure 5-4a indicates that the bulk of the lattice comprises coordination-four vertices with coordination-two vertices at the lattice surface. The key to the simulation geometry is the permalloy nanowire cross-section, which is challenging to determine experimentally, and we use geometric arguments to create an idealized geometry. Figure 5-5a shows the cross-section of the IPL-780 scaffold upon which 50nm of permalloy ($Ni_{81}Fe_{19}$) is deposited using line-of-sight thermal evaporation. The voxel shape is ellipsoidal with an approximate lateral feature size of ≈ 160 nm [144]. Thermal evaporation was performed at pressures $< 10^{-6}$ mbar, yielding a mean-free path that is orders of magnitude greater than the source-substrate distance. As a result, we can assume that the evaporant travels in an unimpeded straight line, and we may approximate the deposited layer to follow the upper surface and uniformly thick along the axial direction, as shown in Figure 5-5b.

For simplicity, we approximate the TPL voxel as a cylinder with spherical caps, given that the thickness of any permalloy deposited on the side of the scaffold will be vanishingly thin and below the magnetic dead layer thickness. We remove the sharp edges of the cross-section as the thickness is below the dead-layer thickness. These empirical arguments inform the simulation object geometries shown in Figure 5-5(c-f) showing a single wire, coordination-two vertices, and a coordination-four vertex of a diamond bond lattice where each vertex is at the position of a lattice point. The L1 sublattice comprises an alternating pattern of coordination-four vertices at the L1/L2 junction and the "lower bipod"

coordination-two vertices at the surface termination. The L2 and L3 sublattices consist of coordination-four vertices only at the L2/L3 and L3/L4 junctions.

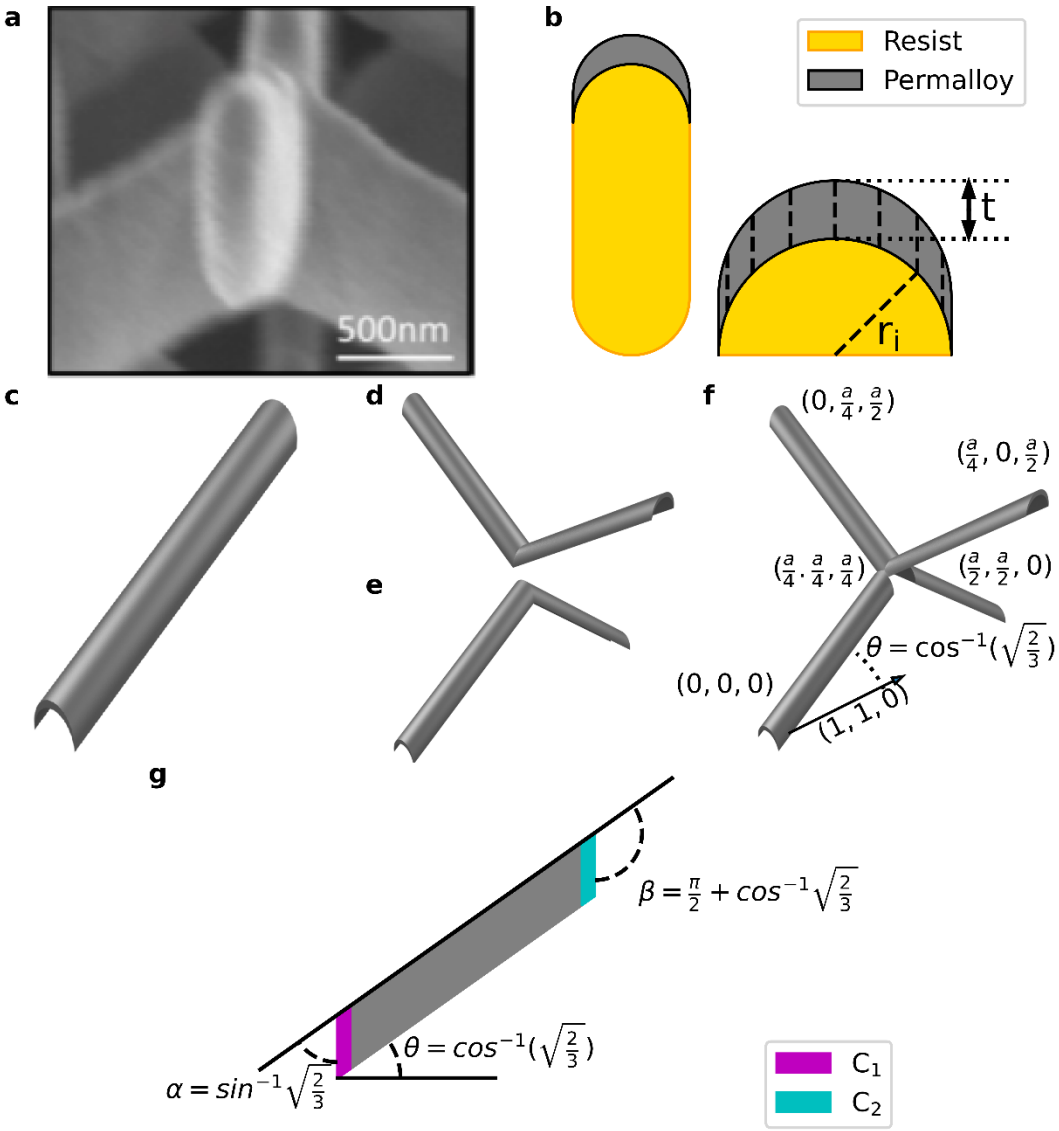

Figure 5-5 (a) SEM of nanowire cross-section in the 3D artificial spin-ice lattice [38]. (b) Schematic showing geometric arguments for determining nanowire cross-section. (c) 3D rendering of a single nanowire. (d) 3D rendering of coordination-two vertex comprising the upper two wires of a tetrapod. (e) 3D rendering of coordination-two vertex comprising the lower two wires of a tetrapod. (f) 3D rendering of the coordination-four vertex with coordinates of features and angle between wires and substrate plane shown. (g) schematic of single wire geometry shown in (d) as seen from the side, illustrating the end caps C_1 and C_2

Each wire's long axis is at an angle of $\theta = \cos^{-1}\sqrt{2/3}$ from the substrate plane. The lattice constant of the experimental system is $a = 2\mu m$ resulting in a nanowire length of 866 nm. We draw attention the caps C_1 and C_2 illustrated in Figure 5-5g, which are not perpendicular to the top and bottom surfaces of the wire.

The maximum mesh spacing is 5nm, below the $Ni_{81}Fe_{19}$ exchange length at $\Delta_d = \sqrt{2A/\mu_0 M_s^2} = 5.29$ nm. Magnetocrystalline anisotropy is assumed to be negligible for $Ni_{82}Fe_{19}$. The Gilbert damping coefficient is set a $\alpha = 1$ for simulations concerning equilibrium states to reduce computational time; a realistic value of $\alpha = 0.01$ is used for simulations requiring time-resolved information.

5.1. Curvature-driven effects in crescent-shaped nanowires

The key to realising a 3D artificial spin ice (3DASI) lattice is that the nanowires are single-domain at remanence and behave as Ising-spins. We can determine these characteristics from a hysteresis loop with fields applied along the long axis projection upon the substrate where two distinct anti-parallel states are seen, separated by an abrupt transition (Figure 3-16). The hard axis hysteresis loop is dominated by coherent rotation (**Error! Reference source not found.**), with the relaxation of the magnetization always along the long axis. In our experimental procedures, the external field is applied parallel to the substrate; this is maintained in simulated protocols. For simplicity in this section, we rotate the single wire geometry by 45° about the z-axis such that the long axis lies along $\cos\sqrt{2/3}\,\hat{\mathbf{i}} + \sin\sqrt{2/3}\;\hat{\mathbf{k}}$.

5.1.1. Demagnetizing components of magnetic nanowires with a crescent-shaped cross-section

Understanding the demagnetization fields in the geometry is beneficial to interpreting further results. However, deriving an analytical expression for the demagnetizing factor in such complex geometries is prohibitively difficult with limited benefit. To contextualize results in this section, we compute the demagnetizing tensor ($\underline{\boldsymbol{N}}$) for the wire by setting the magnetization along the principal axes and taking the ratio of the demagnetizing field and the saturation magnetization (equation 3.64) to yield the outputs shown in Figure 5-6. Along the wire, we consistently observe $\boldsymbol{N_y}$ approaching unity at the thin edges, which confines moments to the x-z plane in this region. The $\boldsymbol{N_x}$ component of the demagnetizing factor at the lower cap ($\mathbf{C_1}$) is maximum at the apex of the inner curve (Figure 5-6a). In contrast, $\boldsymbol{N_x}$ is maximum at the apex of the outer curve in the upper cap ($\mathbf{C_2}$) as shown in Figure 5-6 (c).

The demagnetisation tensor of planar magnetic nanowires with uniform thickness is trivial with the components remaining constant throughout the geometry. These computations indicate a more complicated function, raising the concern that these wires may not function as Ising spins. Ising spins can be in one of two states distinct from each other only by the direction of the magnetic moment [145], modelling an Ising spin using magnetic nanowires then requires symmetry in the demagnetising tensor which is broken by the non-unform thickness of our geometry and the wire ends not being perpendicular to the long axis. This first result raises the question as to whether the differences in states due to this symmetry breaking is significant, or whether an Ising-like approximation holds.

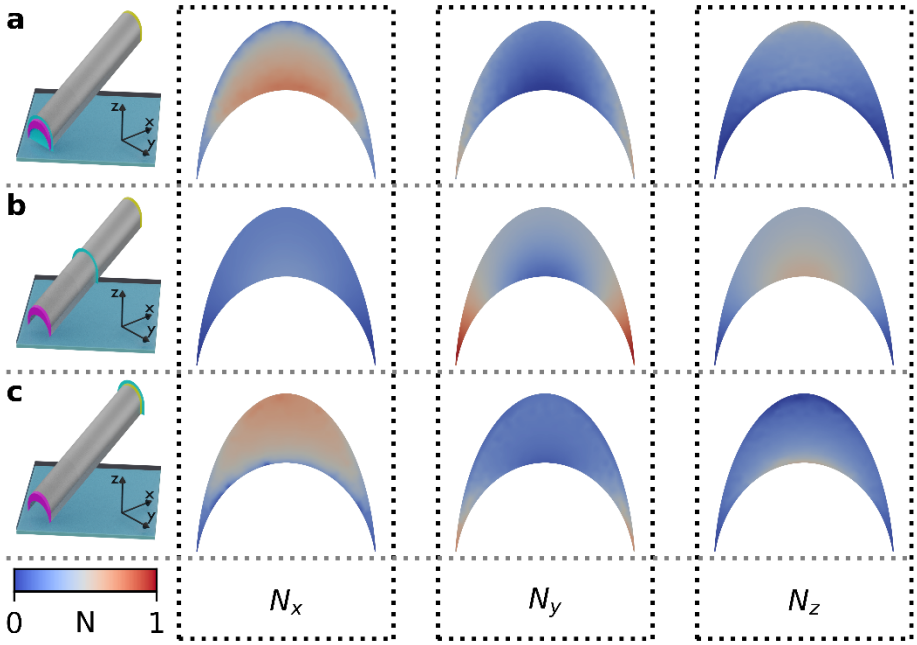

Figure 5-6 computed $\boldsymbol{N_x}$, $\boldsymbol{N_y}$, and $\boldsymbol{N_z}$ components of demagnetization tensor on cross-section of the wire taken (a) bottom cap ($\boldsymbol{C_1}$)of the wire, (b) middle of the wire, (c) top cap ($\boldsymbol{C_2}$) of the wire as indicated by the cyan slice in the diagrams.

5.1.2. Single wire magnetic texture at remanence

The first simulation is a simple relaxation of the single wire. Starting with a random magnetization, we perform a time evolution of the LLG equation until convergence conditions are met to yield the result shown in Figure 5-7. The result shown in Figure 5-7a indicates that the wire is single-domain in the ground state, with magnetization along the extended axis. We note additional interesting textures in the magnetization on the caps of the wire, as shown in Figure 5-7b & Figure 5-7c. The magnetization at the cap C_2 (panel b) is in a crescent state where the magnetization smoothly follows the contours of the cross-section, and we observe some spin canting towards the long axis of the wire. The crescent-shaped texture arises as the moments on the thin edges lie in opposite directions along the z-axis.

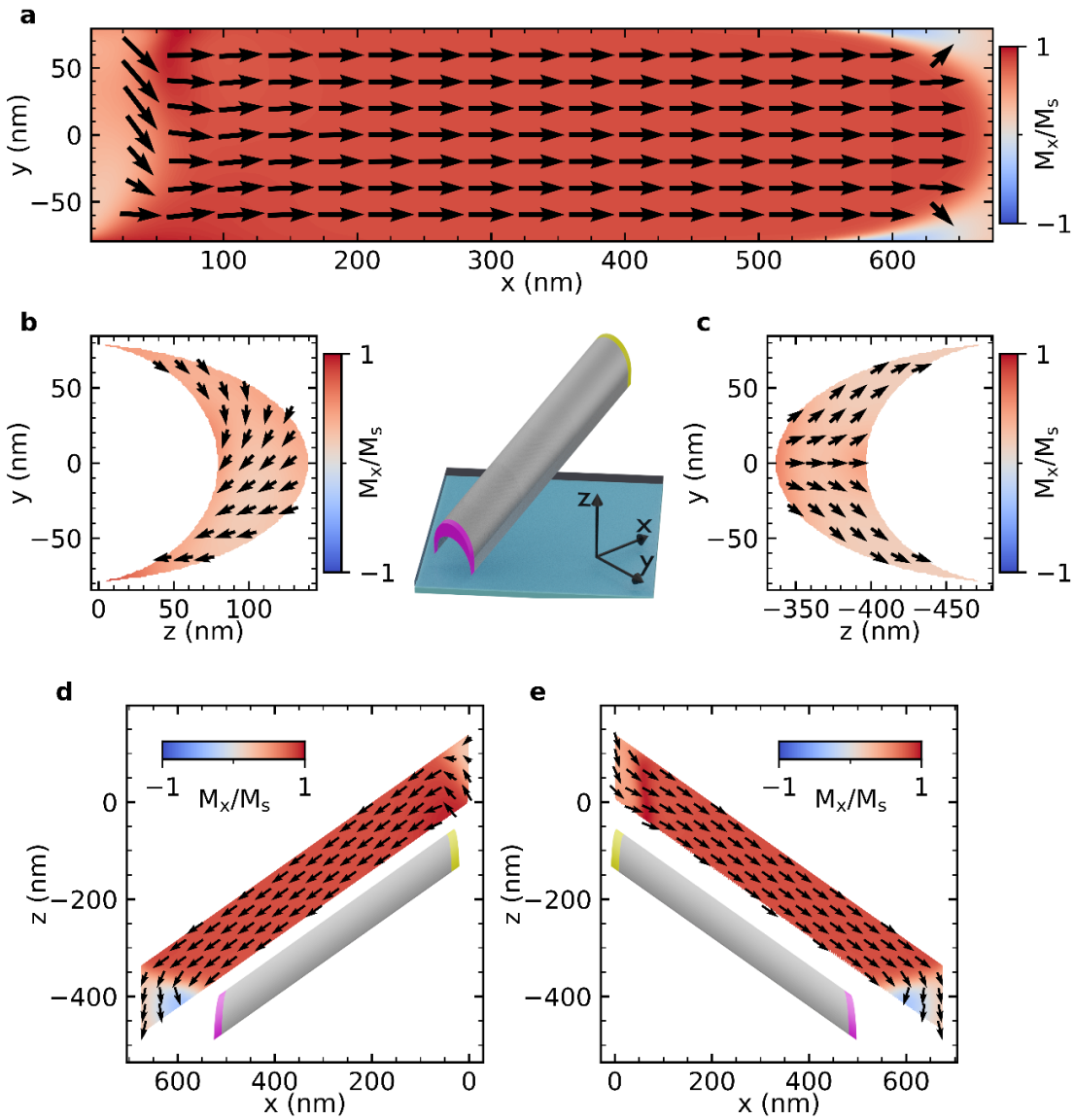

Figure 5-7 Output of relaxation simulation for a single wire. (a) Long-axis magnetization. (b) Magnetization of the upper cap ($\mathbf{C_2}$) indicated with yellow shading on the inset. (c) Magnetization of the lower cap ($\mathbf{C_1}$) indicated with purple shading on the inset. (d, e) side views of wire with orientations indicated in the inset.

The texture upon the bottom cap (C_1) shows a defect reminiscent of a transverse domain wall with the moments at the thin edges in the same direction and topological defects at the centre. The polarity of the defect appears to be determined by the z-component of the magnetization in the bulk of the wire. We refer to this texture as D_1 in the remainder of this work. Previous work performed on transverse domain walls in curved nanowires shows that curvature results in a potential well for head-to-head domain walls

with the core directed away from the centre of curvature and a potential barrier for HH TDW with a core direction towards the centre of curvature. The reverse holds true for TT TDW [24]. It follows that the TDW-like spin texture is likely to be pinned at the C_1 cap which may play a significant role in magnetic reversal.

5.1.3. Domain wall structure in magnetic nanowires with crescent-shaped cross-section

To consider the impact of the novel wire cross-section on the domain wall structure, we relax a domain wall into a 3μm long wire with the crescent-shaped cross-section and a planar nanostrip with an equivalent cross-sectional area. The planar wire then has a width of 292nm and a thickness of 21.5nm. The simulations set the magnetization of the wire ends directed towards the centre, and the magnetization of the central third of the wire is randomized. The moments on the ends of the wire are frozen to allow the domain wall to form when the system is relaxed.

For effective comparison, we transform the results from a cartesian basis to a curvilinear basis, where we define orthogonal basis vectors parallel to the long axis ($\hat{e}_{\parallel}$), tangent to the surface ($\hat{e}_{\dashv}$), and normal to the surface ($\hat{e}_{\perp}$) corresponding to the x, y, and z coordinates in a cartesian basis ($\kappa = 0$) respectively. The different sets of basis vectors are shown in Figure 5-8a. Figure 5-8 (b & c) show the domain wall texture of the crescent wire and the planar equivalent (respectively), and we find striking qualitative differences between the two results with a change in domain wall shape and width.

With thinner edges, one would expect a wider domain wall in the crescent-shaped nanowire due to a reduction in the demagnetising energy. We find that the normal

component of the crescent wire domain wall is non-zero in the circulating region of the VDW in the crescent geometry (Figure 5-8 d) in contrast to the planar case where $M_\perp$ is negligible (Figure 5-8 e), leading to an increase in demagnetising energy.

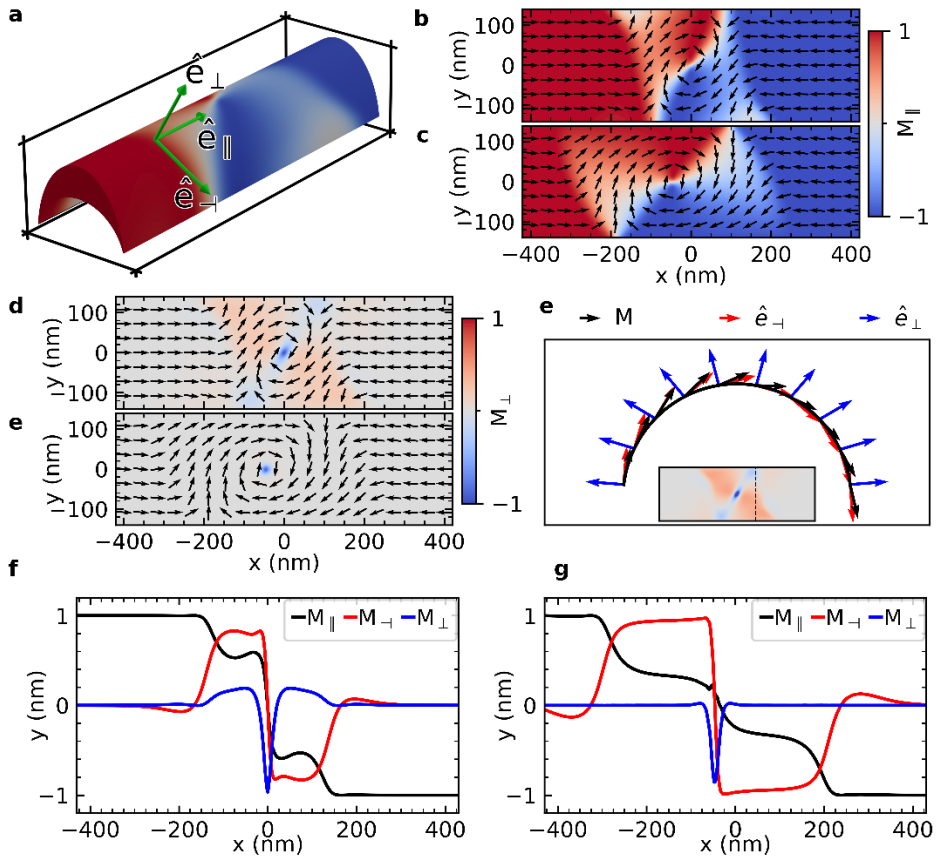

Figure 5-8 (a) CAD rendering of crescent-shaped wire with a vortex domain wall. Annotations show the cartesian basis (black) and the curvilinear basis vectors $\hat{\boldsymbol{e}}_\parallel$, $\hat{\boldsymbol{e}}_\dashv$, and $\hat{\boldsymbol{e}}_\perp$ (green axes). (b) magnetization of a vortex wall in a nanowire with a crescent-shaped cross-section with contrast according to $\boldsymbol{m}_\parallel$. (c) magnetization of a vortex wall in planar equivalent to the crescent wire, contrast according to $\boldsymbol{m}_\parallel$. (d) magnetization of a vortex wall in a nanowire with a crescent-shaped cross-section with contrast according to $\boldsymbol{m}_\perp$. (e) magnetization of a vortex wall in planar equivalent to the crescent wire, contrast according to $\boldsymbol{m}_\perp$. (f) magnetization in a cartesian basis at the upper surface of the crescent wire along a slice perpendicular to the long axis intersection a half antivortex defect. Location of line profile shown in the inset. (g) Line profile of the magnetization through the vortex core along the long axis of the crescent wire. (h) Line profile of magnetization through the vortex core along the long axis of the planar wire. The magnetization in panels g and h are shown on a curvilinear basis with $\boldsymbol{\kappa} = \boldsymbol{0}$ for consistency.

Figure 5-8 f shows a line profile of the magnetization along the upper surface taken perpendicular to the wire axis and intersecting one of the half-antivortex topological

defects as indicated in the inset. The canting towards the surface normal (cyan glyphs) is driven by the curvature driven terms in the exchange energy with wider implications for domain wall structure. Line profiles of the magnetization through the vortex core parallel to the long axis (Figure 5-8 g&h) show the striking difference in domain wall width with the region where $|m_{\parallel}| < 0.95$ has a width of 518 nm for the planar wire, and 282 nm in the crescent wires. The spin canting towards the surface normal increases the demagnetizing energy of the domain wall, resulting in a narrower domain wall to reduce this energy term.

5.2. Magnetic reversal in the building blocks of 3D artificial spin ice

Prior results show the wire to be single-domain at remanence (Figure 5-7a), which satisfies one condition for a magnetic nanowire to be considered Ising-like. Another key criterion is that reversal is that there is a sharp reversal such that there are only two states. Key features of such a reversal is a sharp transition at the coercive field of an easy axis hysteresis loop and a continuous sigmoid function with no hysteresis along the hard axis. We simulate hysteresis loops analogous to measurements performed on our experimental systems: the wire long axes lie at an angle of $\cos^{-1}\sqrt{2/3} \approx 35.264°$ from the substrate. For convenience, the projection of the long axis on the substrate is hereon referred to as the long axis substrate projection (LASP) in the case of the single wire and the coordination-two vertices. We adopt the L1 and L2 sublattice nomenclature for coordination-four vertices where the upper wires lie along L1.

5.2.1. Magnetic reversal of a single wire with crescent-shaped cross-section

Simulated hysteresis loops of single wires reveal a complex reversal mechanism involving both rotation and domain wall motion. Figure 5-9 (a) shows a simulated hysteresis loop with applied field along the long axis projection upon the x-y plane as illustrated in panel b. At remanence, we observe a magnetization nominally identical to the texture shown in Figure 5-7.

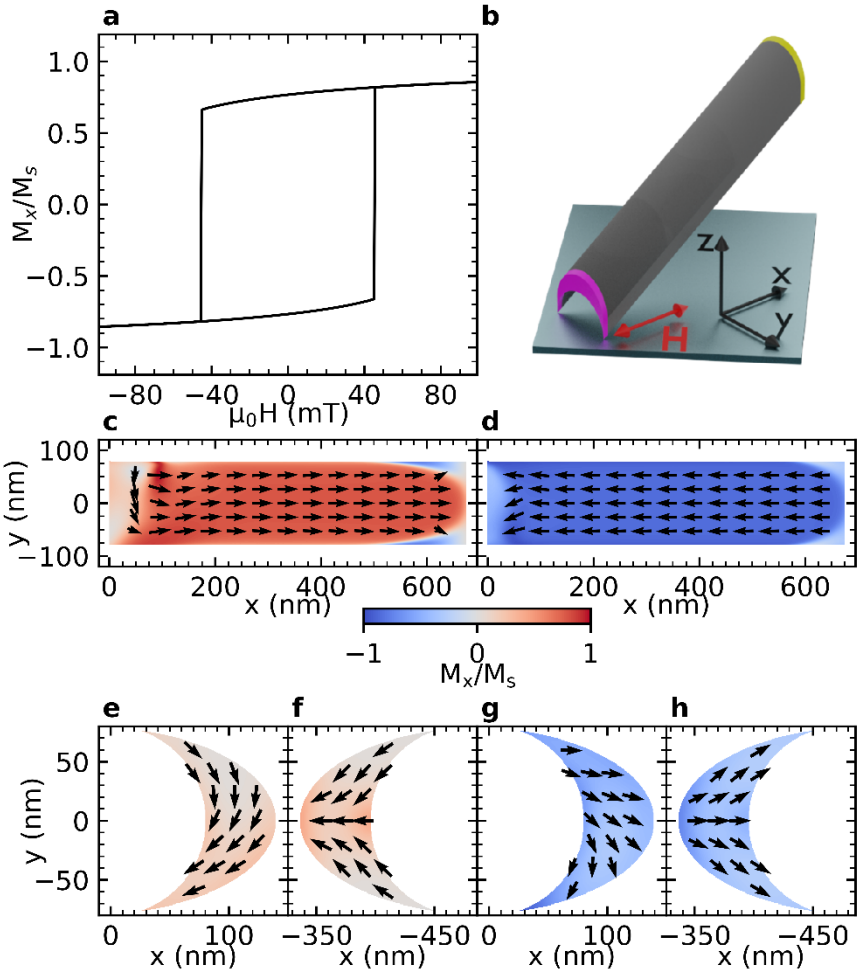

Figure 5-9 (a) Hysteresis loop of a single wire with a crescent-shaped cross-section. The field is applied along the long axis projection upon the substrate (LASP) as indicated by panel b. (c) magnetization of wire before reversal at -45.1 mT (d) magnetization of $\mathbf{C_2}$ (indicated by yellow shading in panel b) before reversal. (e) magnetization of $\mathbf{C_1}$ (indicated by magenta shading in panel b) before reversal. (f) magnetization of wire after reversal, (g) $\mathbf{C_2}$ magnetization after reversal, (h) $\mathbf{C_1}$ magnetization after reversal.

For magnetization purely along the long axis of the wire, the magnetization component along the field direction is expected to be 0.816 M_s, the measured value is 0.767 M_s where the difference of 0.0494 M_s is attributed to the texture at the caps shown in Figure 5-7b and c.

From remanence to just before reversal at -45.1 mT, we see coherent rotation about the y axis at the thin edges of C_1 consistent with expectations from the demagnetizing factor calculations (Figure 5-9a). Near C_2, we see a defect in the magnetization as there is a transition from the crescent edge state to the bulk of the wire (Figure 5-9c). To gain insight into magnetization reversal, we perform time-resolved simulations using the magnetization profile from the instant before the sharp transition and apply a 45.1 mT field to initiate reversal. In contrast to prior simulations showing converged states only, we take snapshots of the reversal. We set the Gilbert damping coefficient to a realistic value of $\alpha = 0.01$.

The reversal does not follow the typical process of domain wall nucleation at the wire edges, followed by DWs propagating towards the centre resulting in annihilation. The magnetization is pinned at the C_1 cap and the defect near C_2 is pushed into the wire slightly (Figure 5-10 a). Here it becomes clear that the texture at C_1 and the defect near C_2 are a half-antivortex and half-vortex pair of topological charges. At 0.3 ns, the C_2 defect becomes a vortex core, and a half-antivortex forms on the edge to conserve topological charge (Figure 5-10 b). The absence of a second half-antivortex near the core prevents propagation, and the core moves perpendicular to the long axis (Figure 5-10 c). At 0.6ns, a VDW forms (Figure 5-10 d) followed by two more at 0.7ns (Figure 5-10 e) and 1 ns (Figure 5-10g). The spin texture prevents the defects from annihilating until 4 half-antivortices

merge to form two antivortex defects at 1.25 ns (Figure 5-10 h) which then enable the vortices to annihilate (Figure 5-10 i).

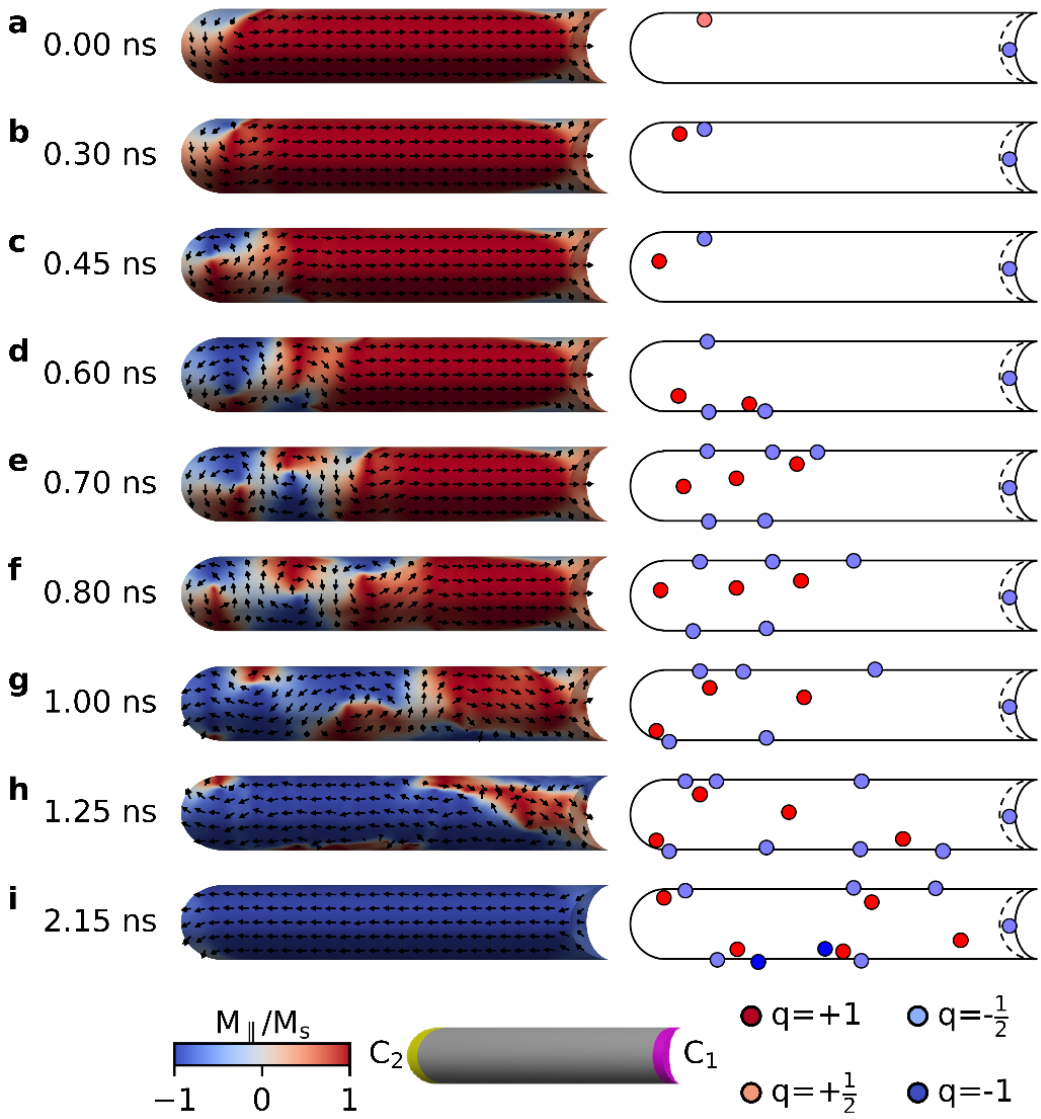

Figure 5-10 Snapshots of reversal in single nanowire with field applied along the LASP. The angle between the long axis and substrate plane is $\boldsymbol{\cos^{-1}\sqrt{2/3} = 35.264°}$. Contrast according to magnetization along long axis. Right-hand side diagrams indicate positions of topological defects with charge $\boldsymbol{q = +1}$ indicating a vortex, and charge $\boldsymbol{q = -1}$ indicating an antivortex.

The crescent-shaped cross-section introduces novel edge states with topological charge, which affect the reversal mechanism. Repeating the same simulation with a Gilbert damping coefficient set to $\alpha = 1$ yields similar results, indicating that the nucleation and

annihilation of the domain walls cannot be attributed to walker breakdown. The distinct edge effects in this geometry also play a significant role in hysteresis loops applied along the wire hard axis, as shown in Figure 5-11 (a). A sigmoid function typical of a hard axis loop where the magnetization reverses via coherent rotation is clearly visible. However, the loop is perturbed by three distinct transitions T_1 at 2.5 mT, T_2 at 32.8 mT, and T_3 at 52.02 mT arising due to edge effects.

Figure 5-11 (c & d) show the magnetization before and after the transition T_1 where we observe C_1 switching from a crescent state to the D_1 state at 2.5 mT. At transition T_2 (Figure 5-11 e&f) we see the crescent shape magnetization of C_2 reversing direction at 32.8 mT. The core of the TDW–like defect in the lower cap is pushed away from its equilibrium position and shows typical TDW behaviour in a curvature-driven potential well. Finally, at 52.02 mT, the TDW-like state at C_1 switches to a crescent state at transition T_3 (Figure 5-11 g&h) to result in a crescent state.

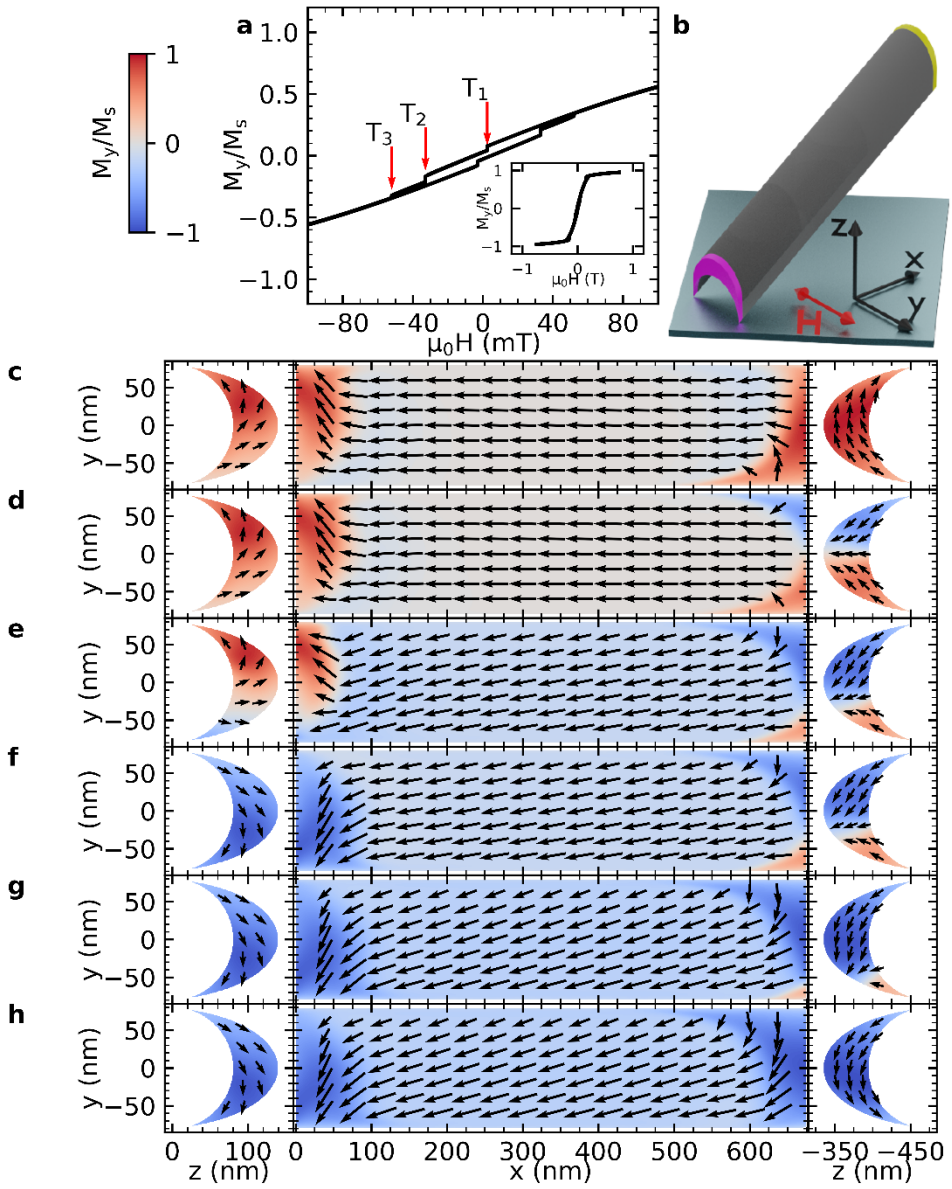

Figure 5-11 (a) Hard-axis hysteresis loop of single wire showing three distinct transitions due to edge state switching. (b) schematic of wire with $\boldsymbol{C_1}$ cap highlighted in magenta, $\boldsymbol{C_2}$ cap highlighted in yellow. (c-h) spin texture of wire before and after the transition $\boldsymbol{T_1}$ (c & d), transition $\boldsymbol{T_2}$ (e & f), and transition $\boldsymbol{T_3}$ (g & h). $\boldsymbol{C_1}$ cap shown on right hand side, top-down view shown in the centre, $\boldsymbol{C_2}$ cap shown on left hand side.

Superficially, these results appear to show that the wires are not Ising-like as the transitions show distinct hysteresis and several discrete states in the hard-axis loops. It should be noted that the transitions are associated with edges that are absent in the experimentally realized 3DASI lattice since there are connected nanowires.

5.2.2. Magnetisation reversal in coordination-two vertices

The surface sublattice L1 comprises wires connected to a coordination-four vertex on one side and a coordination-two vertex on the opposing side. MOKE measurements in the longitudinal geometry, with the projection of the wavevector vector parallel to the projection of L1, appear to be primarily sensitive to the L1 sublattice [144]. Simulations of the upper bipod (Figure 5-5d) and the lower bipod (Figure 5-5e) provide further insight into the energetics and magnetization reversal in these systems.

A simulation of a hysteresis loop with fields applied along the lower bipod LASP yields a relatively square loop with a coercive field of 61.11 mT (Figure 5-12 a). In addition to plotting the magnetization component along the field direction (L_B), we show the component transverse to the field direction (T_A), in the substrate plane, corresponding to the signal one would obtain from transverse MOKE. Applying a field transverse to the LASP yields the hard-axis loop shown in Figure 5-12 b yielding a typical sigmoid shape. There are two distinct transitions in the hard axis loop (L_B) at 8.5 mT and 42.1 mT corresponding to transition T_1 and T_3 in the single wire hard axis loop.

These transitions occur at the edges and correspond to the texture at the C_1 cap switching from a crescent state to the D_1 state at T_1, and a transition from the D_1 state to crescent state at transition T_3.The lower bipod geometry comprises two wires joined at the C_2 cap, and the T_2 transition is absent as a result. The upper bipod geometry has a coercivity of 56.6 mT (Figure 5-12 c). Only the T_2 transition is present at 30.5 mT in the upper bipod hard axis loop (Figure 5-12 d) as the wires are joined at the C_2 cap. Asymmetry in the

demagnetizing tensor and hard-axis reversal of isolated wires reveal more than two well-defined states distinguishable only by the direction of the magnetisation.

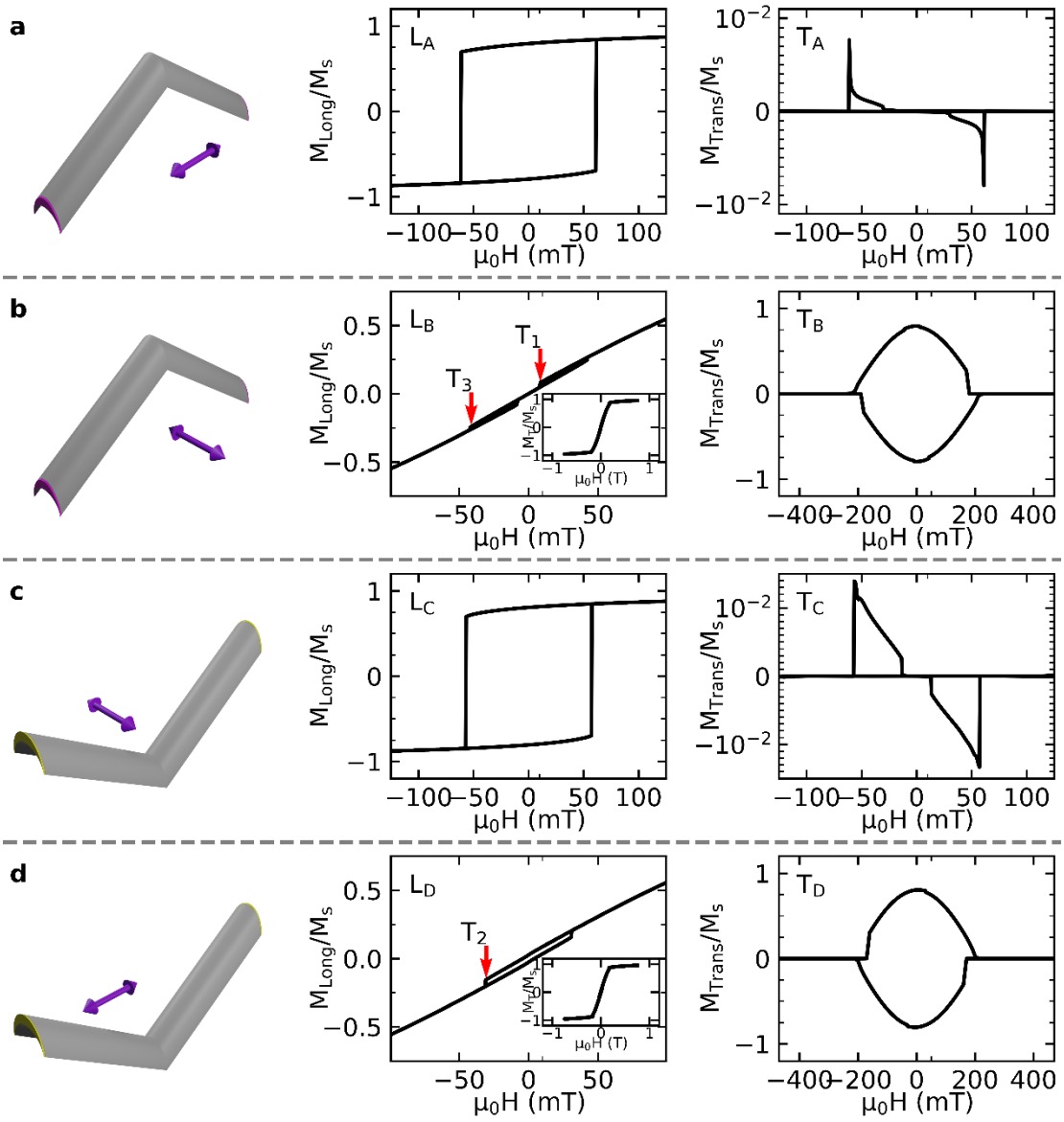

Figure 5-12 Simulated hysteresis loop of bipod geometries showing magnetization component along the field direction ($\mathbf{M_{long}}$) and magnetization perpendicular to the field ($\mathbf{M_{Trans}}$) corresponding to longitudinal and transverse components of signals in MOKE measurements. (a) Field direction along LASP. (b) Field direction perpendicular to the lower bipod LASP. (c) Field direction parallel to the upper bipod LASP. (d) Field direction perpendicular to the upper bipod LASP.

This additional complexity arises due to the varying angles between the end caps and the long axis of the wire. Figure 5-12 shows that placing the wires in more complex

connected geometries removes these caps and we recover the Ising-like behaviour of these nanowires. Symmetry arguments would expect no difference between the upper and lower bipod loops; however, the crescent-shaped cross-section of the wires breaks this symmetry, and we consider the magnetization textures before and after the reversal in LASP loops.

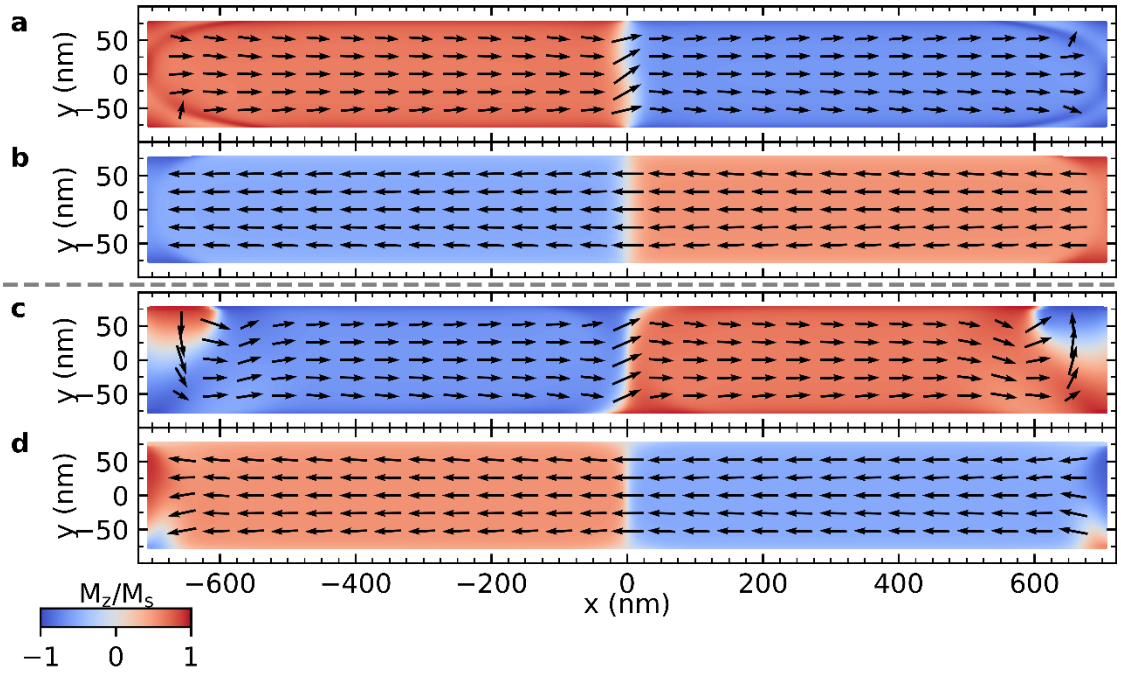

Figure 5-13 Snapshots of key points in simulated hysteresis loops of coordination number two vertices. (a) Lower bipod before reversal. (b) Lower bipod after the reversal. (c) Upper bipod before reversal. (d) Upper bipod after reversal. Contrast according to z-component of magnetization.

The caps of the lower bipod resemble the C_2 caps on the single wire yielding the D_1 defects (Figure 5-13 a), curvature driven exchange pins the defect at the edges leading to a higher coercivity. Half-vortex defects near the C_1 caps on the upper bipod geometry (Figure 5-13 c) provide a nucleation site for domain walls as described in the single wire LASP axis reversal.

5.2.3. Magnetisation reversal in coordination-four vertices

Finally, we simulate hysteresis loops of coordination-four vertices with external fields applied along the L1 sublattice (Figure 5-14 a) with a coercive field of 44 mT and the L2 sublattice (Figure 5-14 b) with a coercive field of 69 mT. These values are consistent with the coercive fields associated with the coordination-two vertices. With an external field applied along L1, reversal is initiated by domain wall nucleation on the C_2 caps found on the upper bipod geometries. Similarly, reversal is initiated by domain wall nucleation on the C_1 caps found on the lower bipod geometries. In both cases, there is a sigmoid shaped background trend that arises from coherent rotation in wires perpendicular to the field direction. We also note the presence of small transitions reminiscent of the T_1, T_2, and T_3 transitions observed in the single wire and bipod hard axis loops.

These results indicate that the coordination-four vertex hysteresis loops are a linear combination of the coordination-two vertex loops. Indeed, the hysteresis loops can be reproduced using a linear combination of the relevant bipod loops. The L1 hysteresis loop is a linear combination of loops L_B and L_C (Figure 5-14 c) and the L2 hysteresis loop is a linear combination of loops L_A and L_D (Figure 5-14 d). This implies that the junction between two sublattices does not result in a correlation between the sublattices; the sublattices are linearly independent.

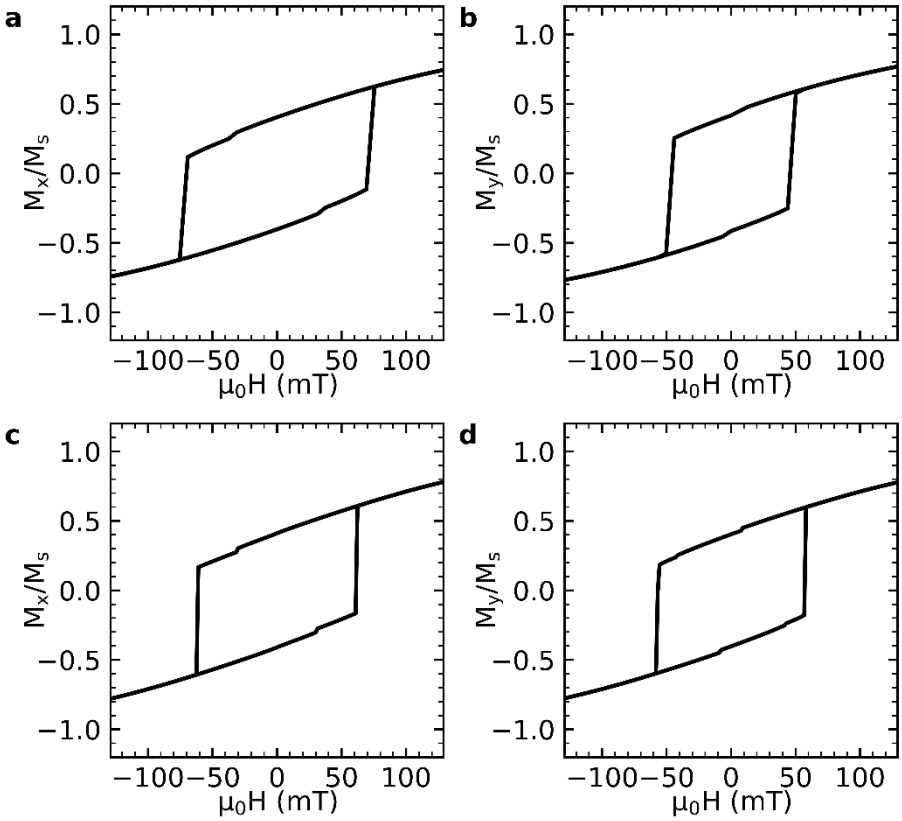

Figure 5-14 Simulated hysteresis loops of coordination-four vertices. (a) external field applied along L1. (b) external field applied along L2. (c) reconstruction of panel (a) using a linear combination of equally-weighted bipod loop $\mathbf{L_B}$ and $\mathbf{L_c}$. (d) reconstruction of panel (b) using a linear combination of equally-weighted bipod loops $\mathbf{L_A}$ and $\mathbf{L_D}$

Using micromagnetic simulations, we have established an understanding of magnetic reversal in the various parts of the nanowire lattice. Careful consideration of the features in the hysteresis loops and which features can be reasonably expected in the physical system enable us to use the simulation results to contextualize experimental results. Standard characterization techniques such as Magnetic Force Microscopy (MFM) and Magnetooptical Kerr Effect (MOKE) magnetometry are typically used on 2D structures. We use the simulation results to gain an understanding of the additional features in these measurements due to the transition from 2D to 3D nano structuring.

Dr Matthew Hunt performed MOKE magnetometry in longitudinal geometry to measure hysteresis in the experimental sample. MOKE measurements were performed

with the incident wavevector at 45° to the substrate, and fields were applied along the projection of the L1 sublattice (Figure 5-15 a).

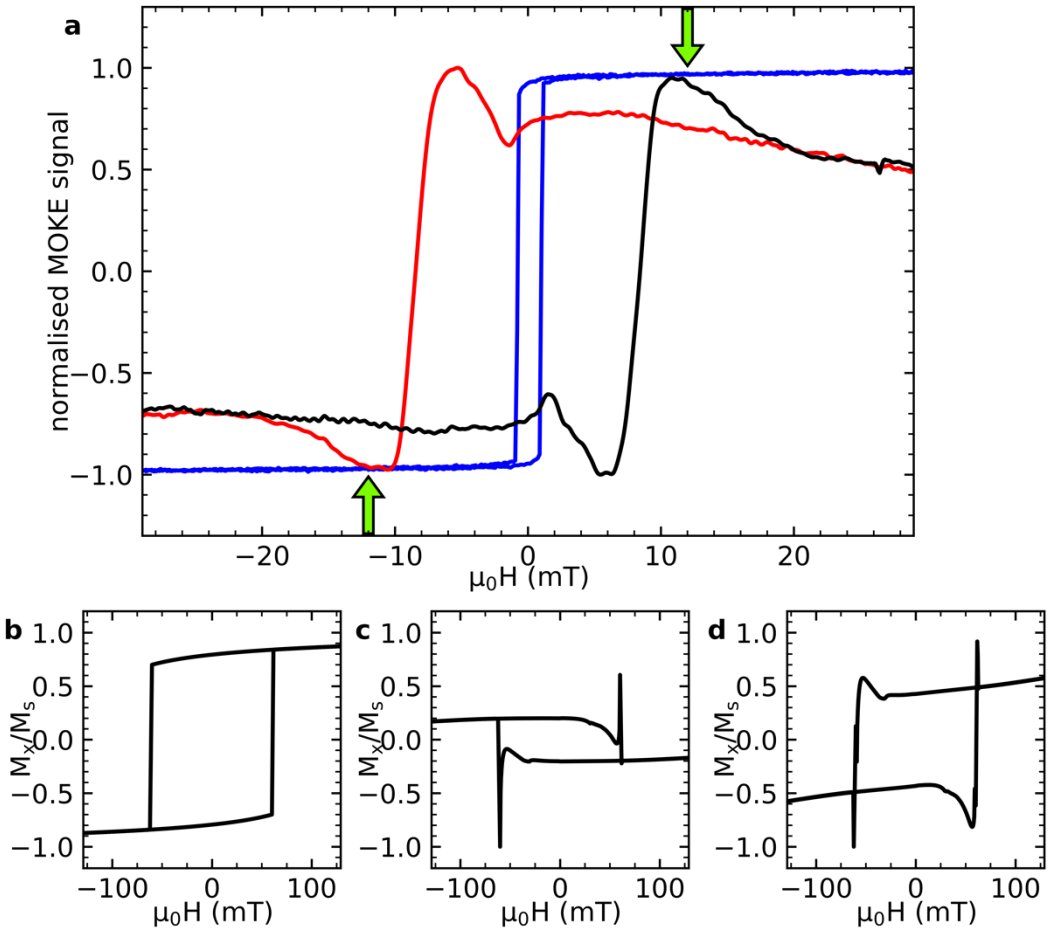

Figure 5-15 (a) Measured hysteresis loop of a 3D magnetic nanowire lattice captured using MOKE magnetometry. For clarity, the loop is separated into the up sweep moving from saturation along the negative direction to the positive direction (black), with the down indicating the reverse (red). Moving the laser focal spot off the lattice yields a typical bulk permalloy hysteresis loop with low coercivity (blue). [38] (b) The longitudinal component of the simulated hysteresis loop of the lower bipod geometry resembles the coordination-two vertices upon the L1 sublattice with the polar component shown in (c). (d) Linear combination of the longitudinal and polar component reproducing the observed lobes in the measurement.

The loop shows a sharp transition at 8.2 mT consistent with reversal via domain wall motion and consistent with the simulation results given that the simulations are performed at 0K. Green arrows indicate lobes near the coercive field; these lobes arise due to the polar MOKE effect and the up sweep (black), and down sweep (red) are plotted separately for

clarity. Moving the laser focal spot away from the structure results in a low coercivity loop (blue) typical of bulk permalloy.

When studying 2D magnetic samples, longitudinal and polar components can be selected by the operator based on which component of the magnetization is to be measured and selecting the incident angle upon the material accordingly (see section 4.4). The measured 3D sample comprises nanowires at an angle of ~35.2° from the substrate, and the incident light is at 45° from the substrate. There exists no experimental means to sufficiently suppress the polar component when performing measurements on these 3D structures. The measurements appear to represent a superposition of the longitudinal and polar signals that cannot be easily separated, and we must refer to micromagnetic simulations to discern the origin of the features in the measured loop.

The key to characterizing the 3DASI is determining to what extent our techniques probe the structure. Simulated loops of the coordination-four vertex show extended tails due to coherent rotation in wires transverse to the applied field. However, these tails are not present in the measured hysteresis loop. We may then conclude that MOKE magnetometry, in this geometry, has limited sensitivity to the magnetization of the L2 sublattice. Given the linear independence of the sublattices, we may consider the coordination-two vertices on the L1 sublattice sufficient, and we interpret the result in light of the upper bipod simulations. For clarity, we show the simulations for the lower bipod hysteresis loop with the longitudinal component L_A (Figure 5-15 b) and the polar component P_A (Figure 5-15 c) where both are normalized. A linear combination is given by $L_A - 2P_A$ (Figure 5-15 d) produces a reasonable first-order approximation in qualitative agreement with the experimental, indicating that MOKE magnetometry is primarily

sensitive to the L1 sublattice and simulations reasonably capture the behaviour of the nanowire lattice.

5.3. Magnetic charge formation and propagation in 3D magnetic nanowire lattices.

Our recent work has demonstrated the formation of magnetic monopole excitations, or magnetic charges, in 3DASI systems [39]. The final section of this chapter explores the micromagnetic simulations performed to support this work and outlines how the results were used to interpret MFM measurements of the 3DASI and informed further Monte Carlo simulations to capture the physics of this system.

5.3.1. Vertex spin textures and energies

A key limitation in square artificial spin ice lattices is the uneven interaction strengths leading to degeneracy lifting in the ice-type vertices (type-I and type-II vertices) as described in the background section. The difference in interaction strength is due to differing separation between the wires that make up the vertex; separation between adjacent wires is smaller than the separation between opposing wires. A 3DASI should overcome this issue to first-order whilst also allowing the possibility to study the impact of broken symmetry upon the surface, with coordination-two vertices on the L1 sublattice.

We compute the various vertex types by setting initial conditions of each wire magnetization either directed towards or away from the vertex and relaxing the system. In prior work, we present these results for1-in/1-out, 2-in, and 2-out states of the coordination-two vertex, and Type-I, Type-II, and type-III vertices of the coordination-four

vertices. Type-IV vertices were omitted as they were out of scope for those works, and simulations relaxed into type-III vertices without introducing artificial pinning [38, 39]. We perform the relaxations by setting magnetization according to the vertex types and adding a region of random magnetization at coordinates where $r < 150$ nm to remove bias during the time evolution of the system. Results to be presented in a later chapter expand the scope and freeze spins where $r > 600$ nm to allow the system to relax into type-IV vertices. Figure 5-16 shows the computed magnetization of the coordination-two vertex in a 2-out state (panel a), 1-in/1-out state (panel b), and a 2-in state (panel c). Contrast is shown according to M_x (i), M_y (ii), M_z (iii), and the surface charge density (iv). The dashed green line indicates the vertex.

In a typical planar system, one would expect the vortex to be located such that one of the half-antivortex defects is pinned at the vertex. However, the 2-in and 2-out states show a vortex domain wall with a core slightly off the vertex with the circulating region at the vertex (Figure 5-16 a & c). The curvature in the cross-section perturbs the domain wall such that there is a significant magnetization component normal to the surface. Additionally, the edges of the wires are thin such that the tangential component of the demagnetization tensor becomes vanishingly small. These factors result in the observed DW position, which minimizes the magnetostatic energy term. We observe a small amount of rotation in the magnetization about the y-axis as the sign of the z-component changes; this yields a small signal in the surface charge density.

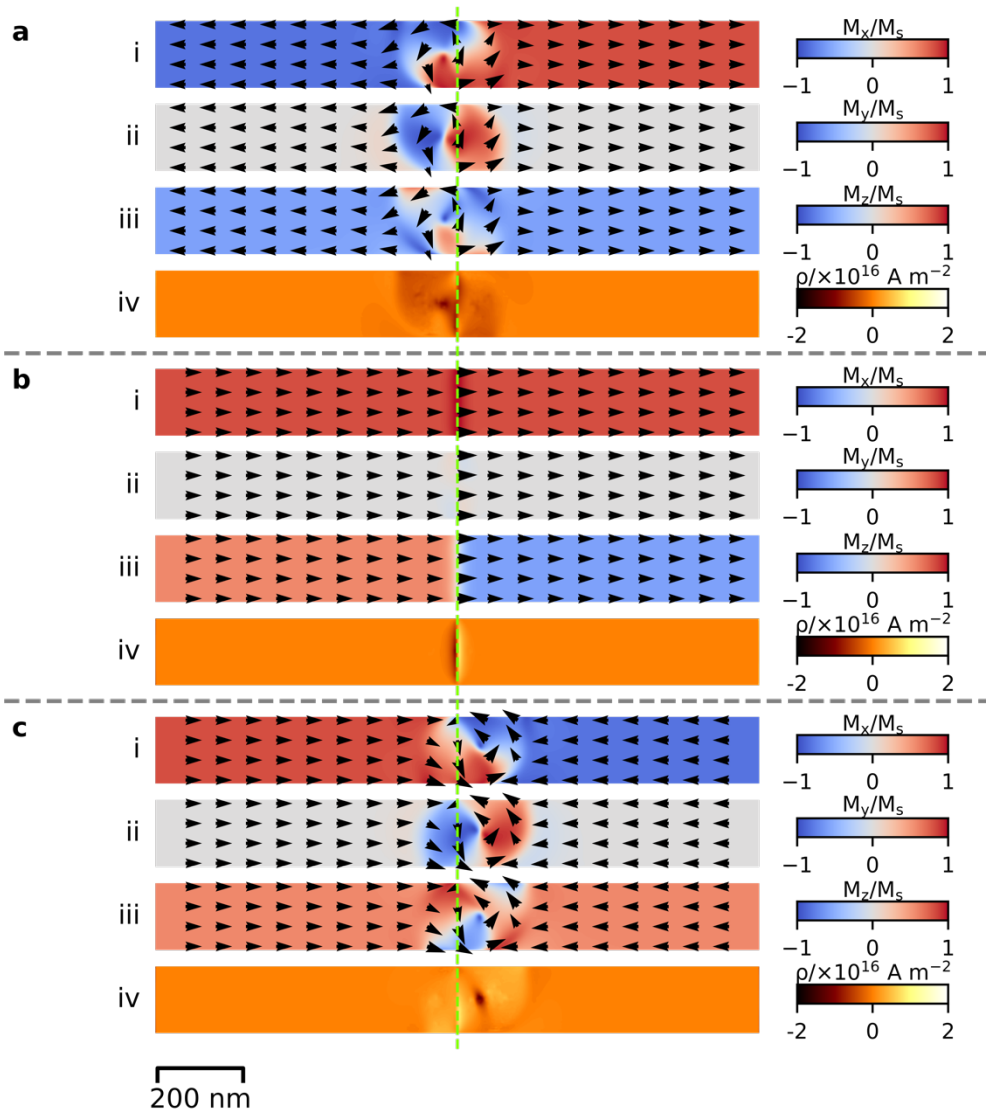

Figure 5-16 Simulated magnetization of coordination-two vertices on the L1 sublattice for (a) 2-out state, (b) 1-in/1-out state, (c) 2-in state. Subplots show $\mathbf{M_x}$ (i), $\mathbf{M_y}$ (ii), $\mathbf{M_z}$ (iii), and surface charge $\boldsymbol{\rho}$ (iv). Dashed green line indicates vertex., glyphs indicate xy component of magnetization.

The presence of a domain wall in the 2-in and 2-out types yields a significant increase in energy, as shown in Table 5-1 with the energy density of the 2-in and 2-out states are 14.225×10^3 J m^{-3} and 14.286×10^3 J m^{-3} respectively, compared to 7.554×10^3J m^{-3} in the 1-in/1-out state.

State	$\mathcal{E}_{demag}\ (\mathbf{J\ m^{-3}})$	$\mathcal{E}_{exch}\ (\mathbf{J\ m^{-3}})$	$\mathcal{E}_{tot}\ (\mathbf{J\ m^{-3}})$
2-out	12.412×10^3	1.812×10^3	14.225×10^3
1-in/1-out	7.255×10^3	0.299×10^3	7.554×10^3
2-in	12.333×10^3	1.953×10^3	14.286×10^3

Table 5-1 Computed energy densities for different coordination-two vertex types on L1 sublattice

Figure 5-17 shows the computed magnetization texture for all coordination-four vertex types and computed energy densities show that degeneracy of the ice-type vertices (Figure 5-17 a&b) is still lifted with an energy density of 10.85×10^3 J m^{-3} for type I vertices, and 10.10×10^3 J m^{-3} for type II vertices. However, this 7% energy difference is smaller compared to prior work on 2D square lattices [97]. In contrast to two-dimensional ASI where, due symmetry, type-III vertices are degenerate, the type-III vertices in our system (Figure 5-17 c) show lower energy configurations when upper wires are aligned, indicating a dominant interaction between wire i and wire iii. We may attribute these energy differences to the cross-section of the wires breaking symmetry, and for convenience, we divide the vertex designations to Type-III a where the upper wires form a 1-in/1-out configuration and Type-III b where the upper wires form a 2-in or 2-out configuration.

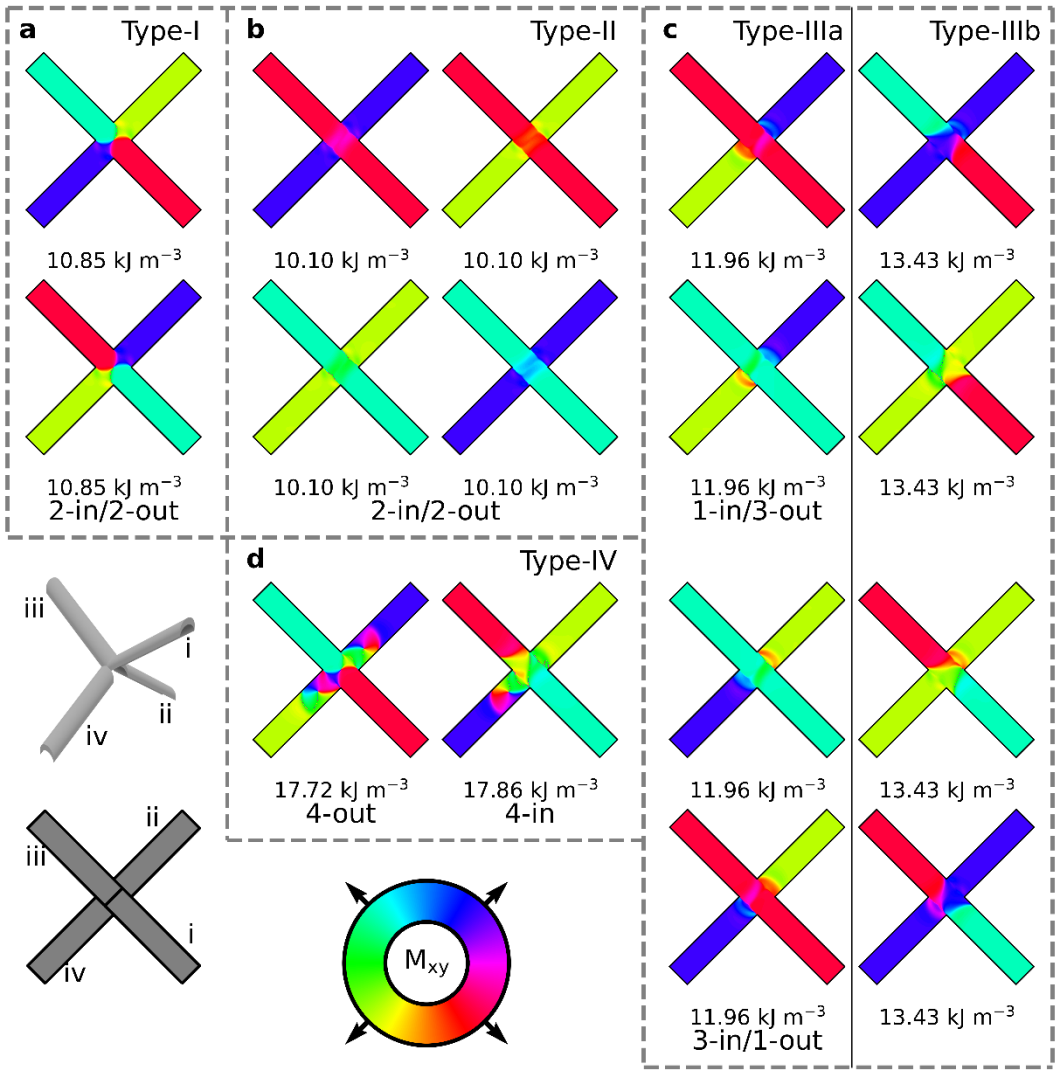

Figure 5-17 Computed in-plane component of magnetization for vertex types on coordination-four vertex with associated energy density. (a) Type-I vertices with opposing magnetization on opposing wires. (b) Type-II vertices with like magnetization on opposing wires. (c) Type-III vertices showing 3-out/1-in and 1-in/3-out states, columns separate Type-III states by energy. (d) Type-IV vertices with 4-in and 4-out states.

Magnetic force microscopy (MFM) is a readily accessible and convenient method to image the magnetic configuration. Sensitive to the second derivative of the stray field with respect to z ($\partial_z^2 H$), the technique is ideal for measuring magnetic charge [142]. Characterization of the magnetization in 2D disconnected lattices is trivial with bright contrast at the poles of each wire, whereas connected wires result in complex textures at the vertex. The expected contrast was modelled by computing the surface charge for Type-I (Figure 5-18 a), Type-II (Figure 5-18 b), Type-III (Figure 5-18 c), Type-IV (Figure 5-18 d) vertices. The contrast is significantly more pronounced on vertices where the upper wire magnetization is anti-aligned. This additional surface charge gives rise to the degeneracy lifting between type-I and type-II vertices and two groups of type-III vertices.

The measured contrast may be compared to the computed contrast and the vertex type assigned according to the closest match. Figure 5-18 (e) shows an example MFM image of a small region of the lattice surface demonstrating the comparison between measured and modelled contrast with a 3-in/1-out state at the L1/L2 vertex and 3-out/1-in states at the adjacent L2/L3 vertices. V-shaped dark contrast on the L2/L3 vertices bears striking similarities to the 1-in/3-out type-IIIb vertices with opposing magnetization in the upper wires of the coordination-four vertex. From the contrast of the coordination-two vertices, the upper wires of the L1/L2 vertex are aligned, which is consistent with the weak bright contrast at the vertex. Considering the previously determined magnetization of the L2 wires, the L1/L2 vertex is a Type-IIIa state is consistent with computed MFM contrast in Figure 5-18 (c).

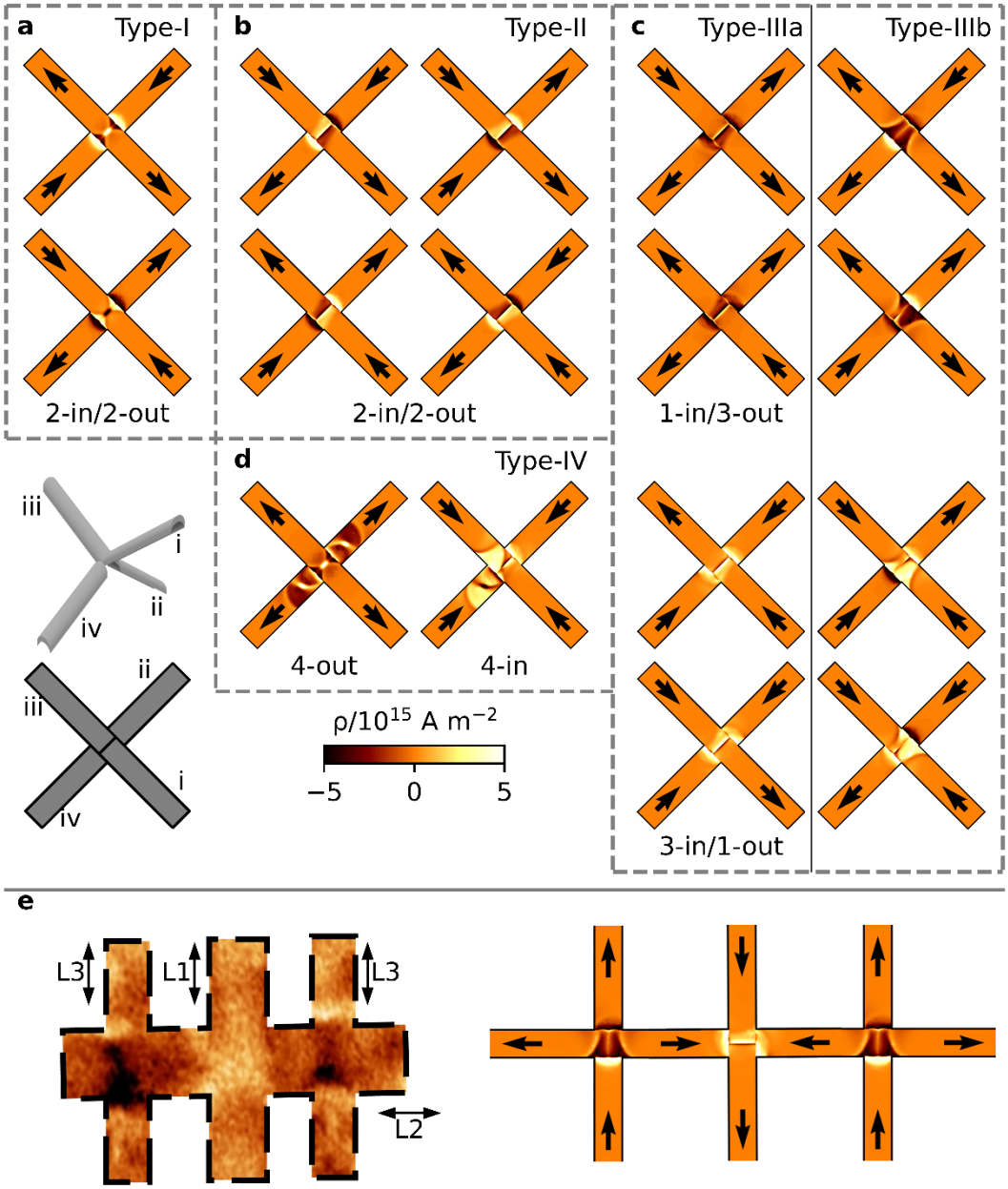

Figure 5-18 Computed surface charge for vertex types on coordination-four vertex. (a) Type-I vertices with opposing magnetization on opposing wires. (b) Type-II vertices with like magnetization on opposing wires. (c) Type-III vertices showing 3-out/1-in and 1-in/3-out states. (d) Type-IV vertices with 4-in and 4-out states. (e) A typical example of vertex identification on an L1/L2 vertex and a pair of L2/L3 vertices by comparison to simulations. MFM image is masked to highlight the structure, sublattices L1, L2, and L3 are annotated.

5.3.2. Vertex potential energy landscape

Precise control of domain wall propagation requires an understanding of the pinning probabilities in the system, and we compute the potential landscape at different symmetry points found in our 3DASI. Starting with a lower bipod geometry representing the coordination-two vertices seen in the L1 sublattice, we relax a domain wall at the vertex in the absence of an external field (Figure 5-19 a). We remove the artificial pinning used in prior simulations. The vortex domain wall is perturbed by the curvature in the wire cross-section to result in the domain wall core being offset slightly from the vertex (Figure 5-19 b). Applying external fields at 0.1mT increments shows depinning fields at $\mu_0 H_x = -2.9$ mT (Figure 5-19 c&d) and $\mu_0 H_x = -2.5$ mT (Figure 5-19 e&f) where the domain wall core offset gives rise to the asymmetry in these field values.

Analysis of the domain wall energies as a function of core position in simulations performed by Dr Andrew May shows that the interaction between the curvature-driven spin canting and the abrupt change in the topography yields a near symmetric, weak potential with a well height of approximately 50 J m^{-3} (Figure 5-19 g). The inset shows magnetostatic and exchange contributions to the potential showing an increase in magnetostatic energy density as the core approaches the vertex, whereas the opposite trend is observed in the exchange energy density. Changes in the magnetostatic and exchange energy are across similar scales (~400 J m^{-3}) with only a small non-linear component to yield the potential well upon summing the contributions.

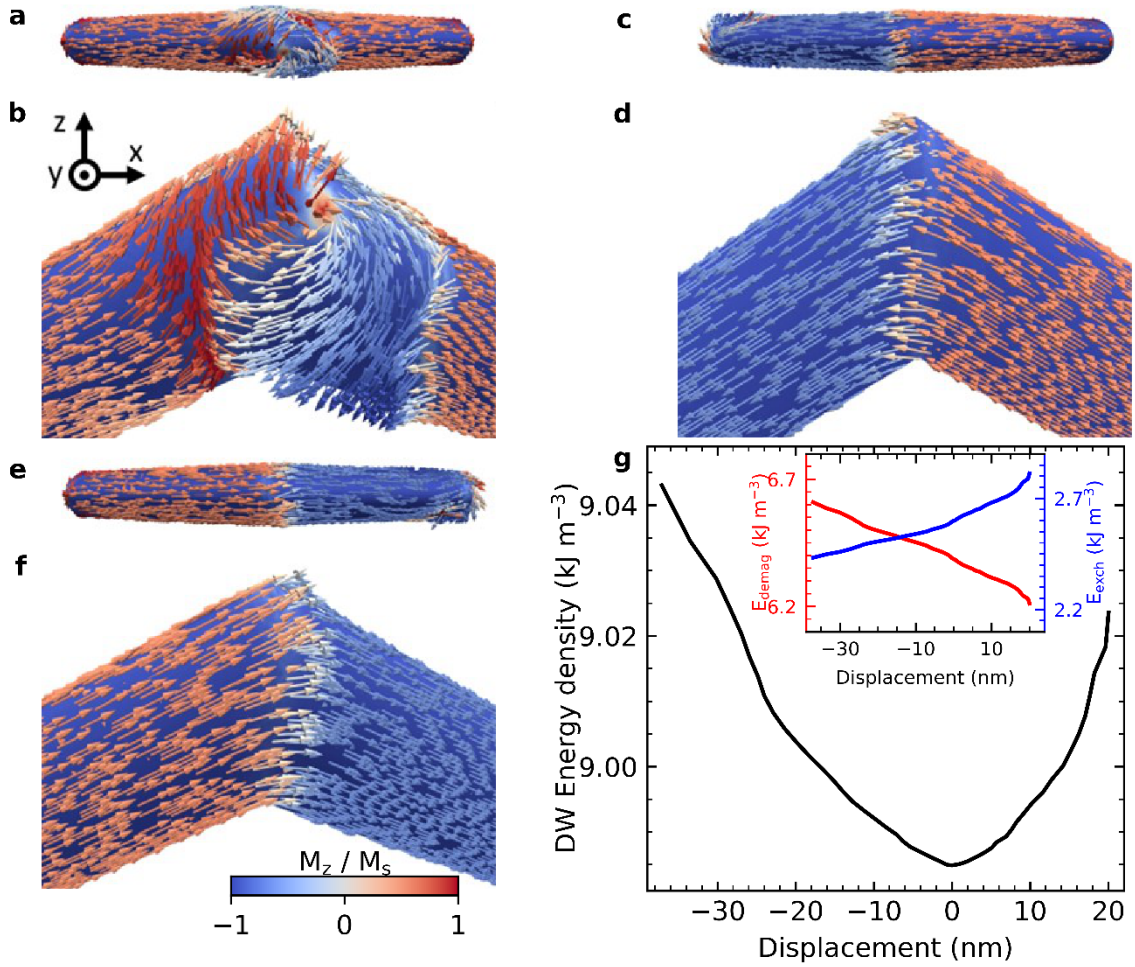

Figure 5-19 Reversal of a coordination-two vertex. (a) initial state with vortex domain wall near the vertex. (b) side view of the domain wall near the vertex. (c) magnetization after applying a 2.9 mT external field in along $-\boldsymbol{x}$ with a side view shown in (d). (e) Magnetization after applying a 2.2 mT field along $+\boldsymbol{x}$ with a side view shown in (f). (g) energy of vortex domain wall as a function of displacement along $\boldsymbol{x}$ from initial position.

We repeat the procedure upon a coordination-two vertex comprising two planar wires with the equivalent cross-sectional area. The vortex domain wall relaxes with one of the half-antivortex edge defects pinned at the vertex (Figure 5-20 a & b), requiring a 9.2 mT external field for the domain wall to move across the vertex and depin to the opposing side (Figure 5-20 c & d). The domain wall depins with a 2.2mT field towards the same side (Figure 5-20 e & f). Computed energy densities as a function of core position show a large variation across ~1kJ m^{-3} in magnetostatic energy as a function of position with a maximum where the DW core is at the vertex (Figure 5-20 g). The variation in the exchange

energy is across a similar scale of ~400 J m^{-3} with a minimum at the vertex. This yields the asymmetry in the potential well where one wall has a height of ~50 J m^{-3} corresponding to the half-antivortex defect depinning like the curved case. The opposite wall height is ~600 J m^{-3} corresponding to the vortex core passing over the vertex with an applied field of 9.2mT.

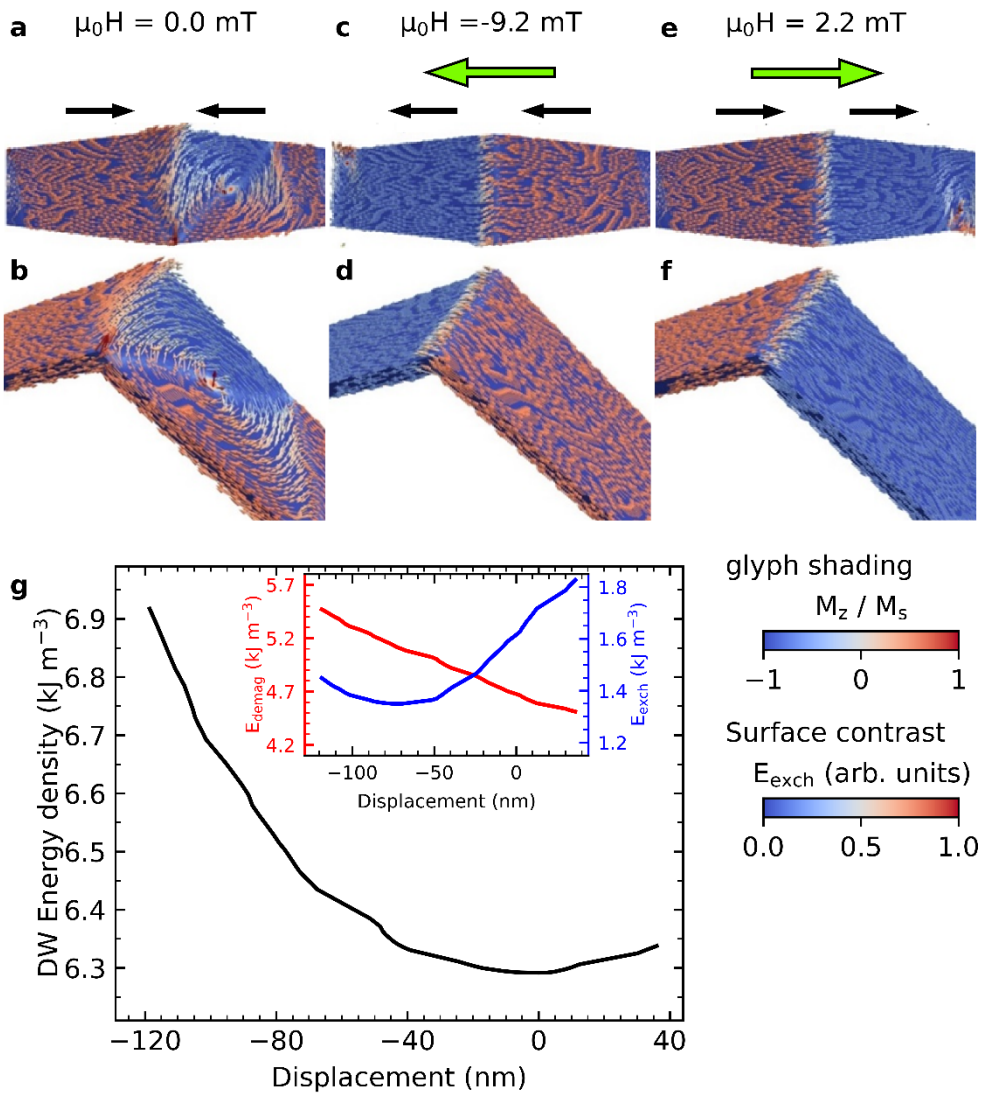

Figure 5-20 Reversal of a coordination-two vertex comprising planar nanostrips with equivalent cross-section. (a) initial state with the angled view presented in (b). Magnetization after applying a 9.2mT external field in $-\boldsymbol{x}$ direction, angled view shown in (d). (e) Magnetization after applying a 2.2 mT external field along $+\boldsymbol{x}$ direction with angled view shown in (f). (g) Energy as a function of domain wall core displacement.

The simulations are performed at T = 0 K, and as such, the depinning fields are expected to be significantly smaller in experiments performed at room temperature. The smaller potential wall heights become negligible at room temperature as thermal fluctuations will yield sufficient energy to overcome the smaller barriers. With consideration of the energies shown in Table 5-1, observing a 2-in or 2-out state of the coordination-two vertices is then unlikely.

After establishing the domain wall potential landscape in the coordination-two vertices of L1, we performed similar procedures upon the coordination-four vertices. We set initial conditions by relaxing the coordination-four vertex into a 3-in/1-out state with the upper wire's magnetization directed towards the vertex (Type III b). Contrary to the simulations yielding the results in Figure 5-17, we do not freeze the magnetization on the edges of the wires, and a vortex domain wall with a +z core direction and clockwise circulation relaxes slightly off the vertex upon one of the lower wires (Figure 5-21 a). As an analogy to applying an external field along the L1 sublattice, we simulate external fields applied along the projection of the upper wires upon the xy plane at 1mT increments to find the domain wall depinning at fields of 40mT in the negative direction (Figure 5-21 b) and 44mT in the positive direction (Figure 5-21 c). Analysis of simulations performed by Dr Andrew May considering the magnetostatic and exchange energy terms as a function domain wall core displacement shows a near symmetric potential well of height $\sim$600 J m^{-3} (Figure 5-21 g), an order of magnitude larger than the coordination-two vertex potential well.

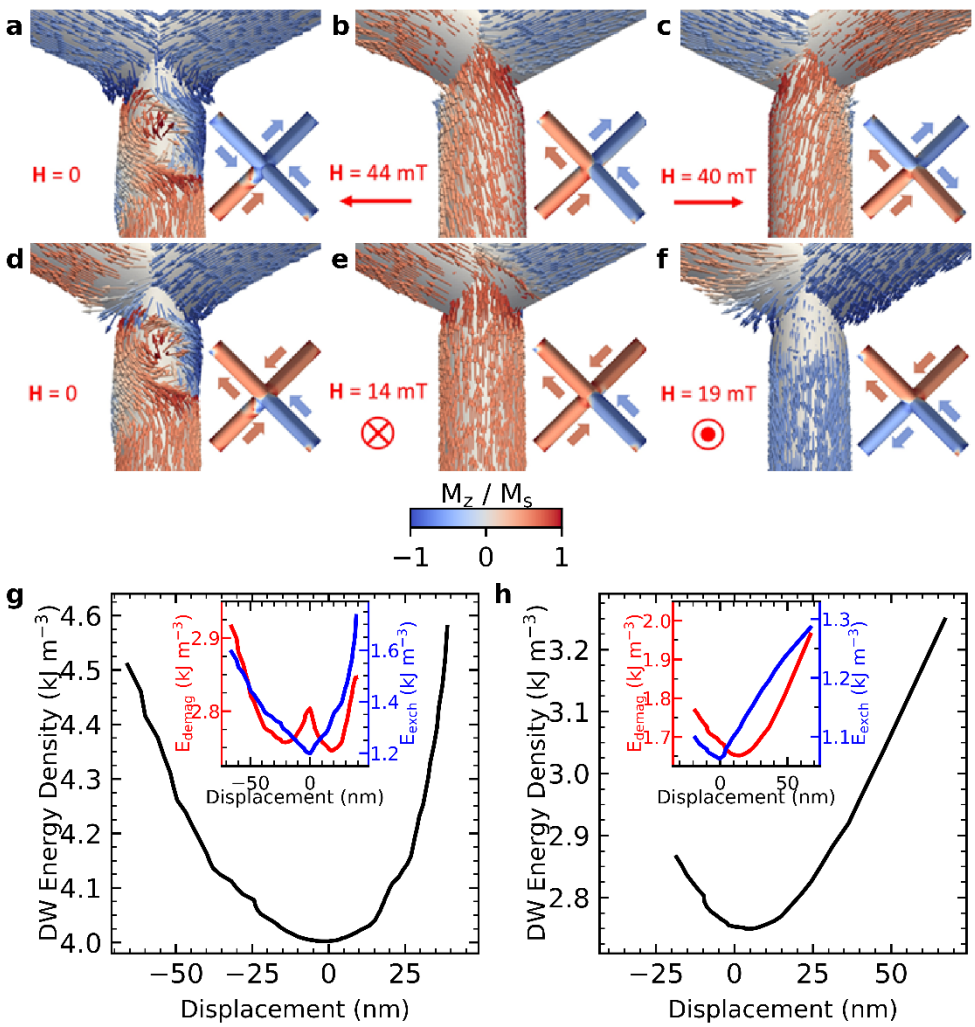

Figure 5-21 (a) Relaxation of a type-IIIb coordination-four vertex with DW forming off the vertex. (b) M after applying a 44mT external field along the negative direction along L1. (c) M after applying a 40mT external field along L1. (d) Relaxation of a type-IIIa coordination-four vertex with DW off the vertex. (e) M after applying -14 mT external field along L2. (f) M after applying 19mT external field along L2. (g) DW energy as a function of displacement with fields applied along L1. (h) DW energy as a function of displacement with fields applied along L2.

Analogous to applying an external field along the L2 sublattice, we simulate external fields applied along the projection of the lower wires upon the xy plane at 1mT increments. The initial configuration is created by relaxing a 3-in/1-out state with the lower wire magnetization directed towards the vertex (Type-III a), yielding a vortex domain wall at the same position as the prior initial conditions (Figure 5-21 d). Depinning occurs at 14 mT in the negative direction (Figure 5-21 e) and 19mT in the positive direction (Figure 5-21 f).

However, the depinning in the negative direction does not result in the opposing wire switching. The domain wall interacts with the topography of the vertex to redistribute the spin texture, and a 46mT field is required to switch the opposing wire.

Analysis of the energy as a function of domain wall core displacement then yields an asymmetric potential well with a wall height of $\sim$400 J m^{-3} in the positive direction, and $\sim$100 J m^{-3} in the negative direction representing the energy barrier for the domain wall to move onto the vertex and redistributing the spin texture.

The potential energy landscapes have thus far been computed for VDW with clockwise circulation; the same procedures for VDW with anticlockwise circulation was repeated. There is a negligible difference between CW and CCW cases for the coordination-two vertex (Figure 5-22 a), its planar equivalent (Figure 5-22 b), and a coordination-four vertex relaxed into a type-IIIb configuration (Figure 5-22 c). For Type-IIIa configurations, the change in circulation yields a decrease in well wall height from $\sim$100 J m^{-3}, to $\sim$20 J m^{-3} in the negative direction (Figure 5-22 d). The cause of the difference is a broken symmetry in the magnetization along L1 in Type-IIIa configurations (Figure 5-24 e). The VDW depins in the negative direction at 7mT compared to 14mT for the CW VDW.

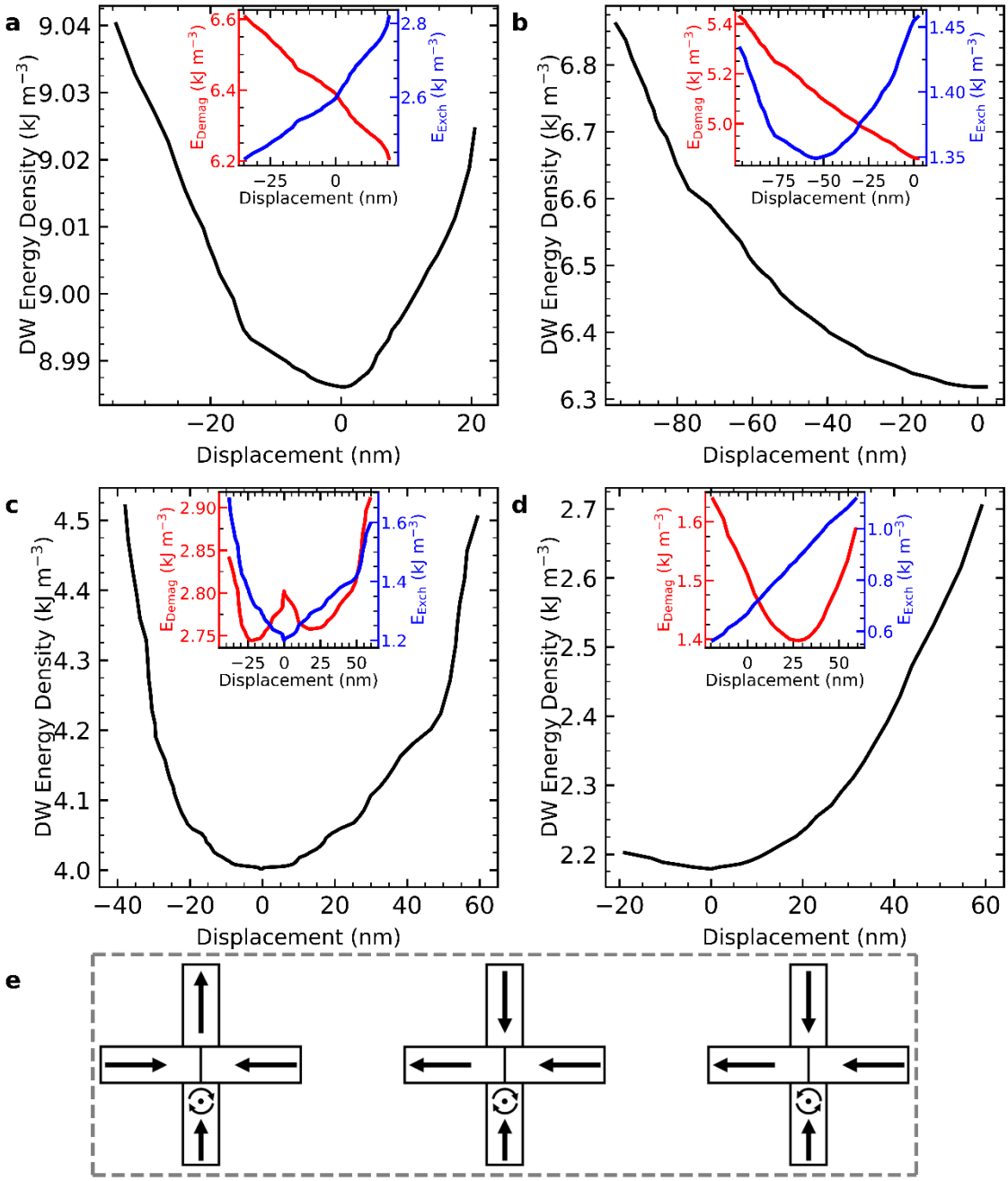

Figure 5-22 Computed domain wall potential energy landscapes using vortex with anticlockwise circulation. (a) the potential landscape for the coordination-two vertex with crescent-shaped cross-section analogous to results shown in Figure 5-19 g. (b) the potential landscape for coordination-two vertex comprising planar equivalent wires analogous to results shown in Figure 5-20 g. (c) domain wall potential as a function of displacement on a coordination-four vertex relaxed into type-IIIb analogous to the results shown in Figure 5-21 g. (d) domain wall potential as a function of displacement on a coordination 3 vertex relaxed into type-IIIa analogous to results shown in Figure 5-21 h. (e) schematic of type IIIb vertex with CW vortex domain wall indicating the symmetry resulting in similar results for CW and CCW VDS. This symmetry is broken in type-IIIa vertex configurations.

5.3.3. Charge propagation in a 3D artificial spin ice lattice

The simulations indicate that domain walls at the coordination-two vertex are energetically unfavourable with a weak pinning potential not sufficient to remain stable at finite temperature. Relaxations of the coordination-four vertex types show that alignment of the upper wires (1-in/1-out state) is energetically favourable, resulting in an energy difference between the ice-rule states (Type-I and Type-II) and between the excited states (Type-IIIa and Type-IIIb). Based on these results, it is reasonable to expect long-range ordering on the L1 sublattice. Injecting a domain wall into the L1 sublattice then yields a type-IIIb vertex as the domain wall is pinned at a coordination-four junction, the periodic pinning potential due to regularly placed coordination-four vertices then allows domain wall motion through the lattice.

Simulated hysteresis loops of coordination-four vertices suggest that the L1 and L2 sublattices are independent; Dr Andrew May performed a series of MFM measurements on the 3DASI at Cardiff University to demonstrate this observation experimentally. We apply a 30mT field along the L1 sublattice, which is sufficient to achieve saturation along the sublattice. Figure 5-23a shows the magnetic force micrograph captured at remanence after applying the saturated field. A coordination-two vertex is highlighted magenta, and a coordination-four is highlighted in red to guide the eye. To further guide the eye, we mask the void regions: bright lobes indicate positive phase, and dark lobes indicate negative phase for our given MFM tip magnetization. We find that the magnetization texture is identical for all coordination-four vertices in the field of view with a magnified view shown in Figure 5-23b, including a schematic of the vertex.

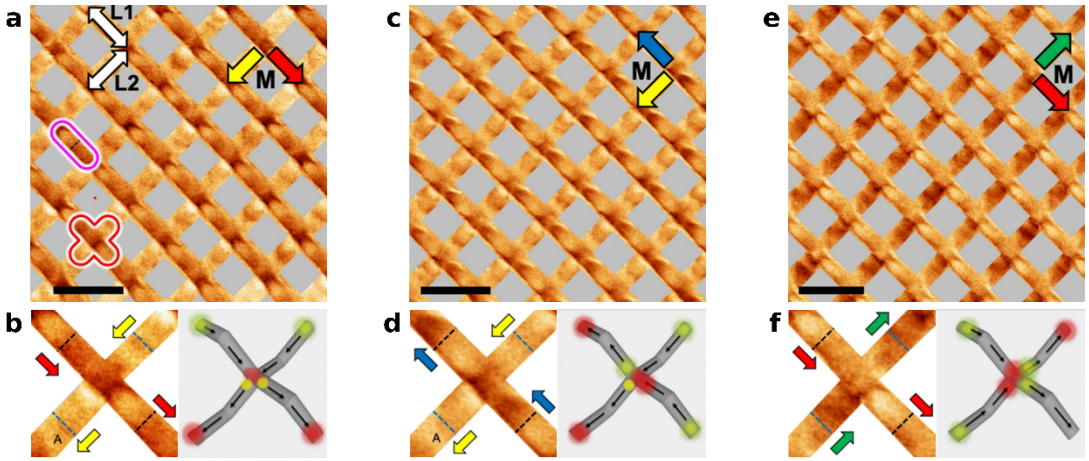

Figure 5-23 Magnetic force micrographs of a 3D magnetic nanowire lattice. (a) Initial condition saturated along L1. (c) lattice after saturating along L1 in an opposing direction to the initial condition. (e) Lattice after saturation along L2 in the opposite direction to L2 magnetization in the initial state. (b, d, f) magnified views of a single coordination-four vertex along with a schematic of a type-II configuration, dashed lines indicate the nearest coordination-two vertex upon L1 and the coordination-four vertex of the L2/L3 junction.

The next step is to apply a saturating field along L1 in the opposing direction resulting in the configuration shown in Figure 5-23c where the L1 magnetization has indeed reversed as shown in the magnified view in Figure 5-23d and its corresponding schematic. The L2 lattice remains unchanged as expected. The system is then returned to the initial state shown in Figure 5-23a, and a saturating field opposing the initial L2 magnetization is applied to produce the configuration shown in Figure 5-23e where the L2 sublattice has indeed switched without affecting the L1 sublattice. A magnified view of a single coordination-four vertex is shown in Figure 5-23f with the accompanying schematic. These results establish the linear independence of the sublattices for fields applied along their substrate projections, consistent with computational results.

Injecting domain walls in the sublattices leads to Type-III vertex states, and we use computed MFM contrast to determine if the monopole states can be identified and tracked. We saturate the 3DASI and apply 0.25mT field increments in opposing directions along L1 (Figure 5-24 a-e) and L2 (Figure 5-24 f-j). The images were captured at remanence.

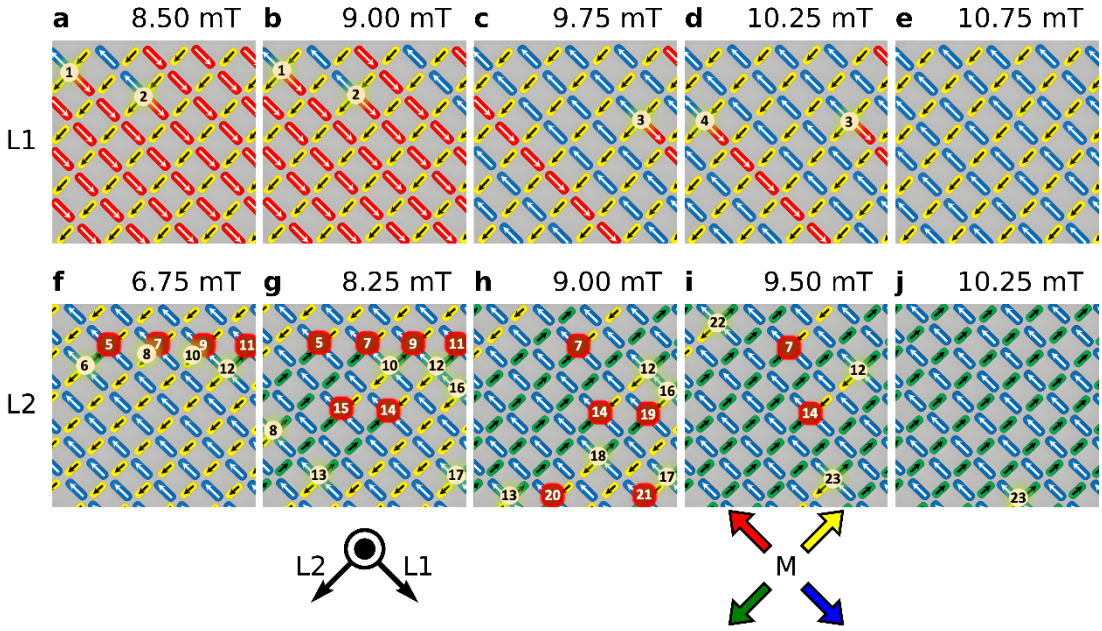

Figure 5-24 (a-e) Schematics of magnetization in 3DASI after fields applied along the substrate projection of the L1 sublattice. Islands on the L1 sublattice represent the surface coordination-two vertices, and islands on the L2 sublattice represent the upper wires of the coordination-four vertices at L2/L3 junctions. (f-j) schematics of magnetization after fields are applied along the L2 sublattice projection upon the substrate.

At 8.5 mT along L1, two monopoles with $-2q$ at L1/L2 junctions (Figure 5-24 a). Further field increments lead to additional chains of wires switching, and a third $-2q$ monopole is visible at 9.75 mT (Figure 5-24 c) along with a fourth at 10.25 mT (Figure 5-24 d). After a 10.75 mT field, L1 has entirely switched within the imaged region (Figure 5-24 e). One would expect corresponding $+2q$ forming on the lattices but following the chains of switched wires indicates that these charges are outside of the field of view. The L2 sublattice comprises only coordination-four vertices alternating between L1/L2 junctions and L2/L3 junctions, yielding a greater number of pinning events. After a 6.75 mT field along L2 (Figure 5-24 f), there are four $\pm 2q$ monopole pairs with 5, 6, 7, 8, 11, and 12 pinned at an L1/L2 junction and monopoles 8 and 10 pinned at an L2/L3 junction. Further field increments lead to the creation of further monopoles (monopoles 12-18) whilst others move along the L2 sublattice and leave the field of view or appear to annihilate (e.g. There

is a striking difference between monopole formation upon L1 and L2, with a small number of uncorrelated monopoles appearing when fields are applied along L1. There is a net charge in the observed area, but we would expect a neutral charge across the entire lattice. A large number of correlated monopoles arise with fields applied along the L2 sublattice projection upon the substrate resulting in charge neutrality being maintained within the field of view. This difference is attributed to the energy difference between monopole excitations upon the coordination-two and coordination-four vertices, where the monopole energy is a factor of three larger in the coordination-two vertices. Although micromagnetic simulations provide insight on individual vertices and aid the identification of vertex types, simulating full lattices to capture the observed behaviour is not feasible. The computed vertex type energies inform Monte Carlo (MC) simulations using a compass needle model performed by Michael Saccone at Los Alamos National Laboratories, where a surface energetics factor α_{ij} is introduced to account for the energy difference and represents the ratio of coordination-two excitation energy to coordination-four excitation energy. MC simulations using α_{ij}=1, $\alpha_{ij} = 3.2$ (as observed in micromagnetic simulations), and $\alpha_{ij} = 6.4$ were performed. The MC method models the lattice as a set of compass needles with a uniform linear magnetic moment that relaxes the system in a Coulomb potential. The full method is detailed in [39]. Setting the surface energetics factor to $\alpha_{ij} = 1$ with a field applied along the projection of L1 yielded a large number of excitations upon L1 with short Dirac string in contrast to the experimental results. Setting the $\alpha_{ij} = 3.2$ as indicated by micromagnetic simulations yielded a monopole density consistent with experimental results, but Dirac string significantly shorter. Increasing the surface energetics factor to $\alpha_{ij} = 6.4$ yielded results with excitations and Dirac string lengths consistent with measurements (Figure 5-25).

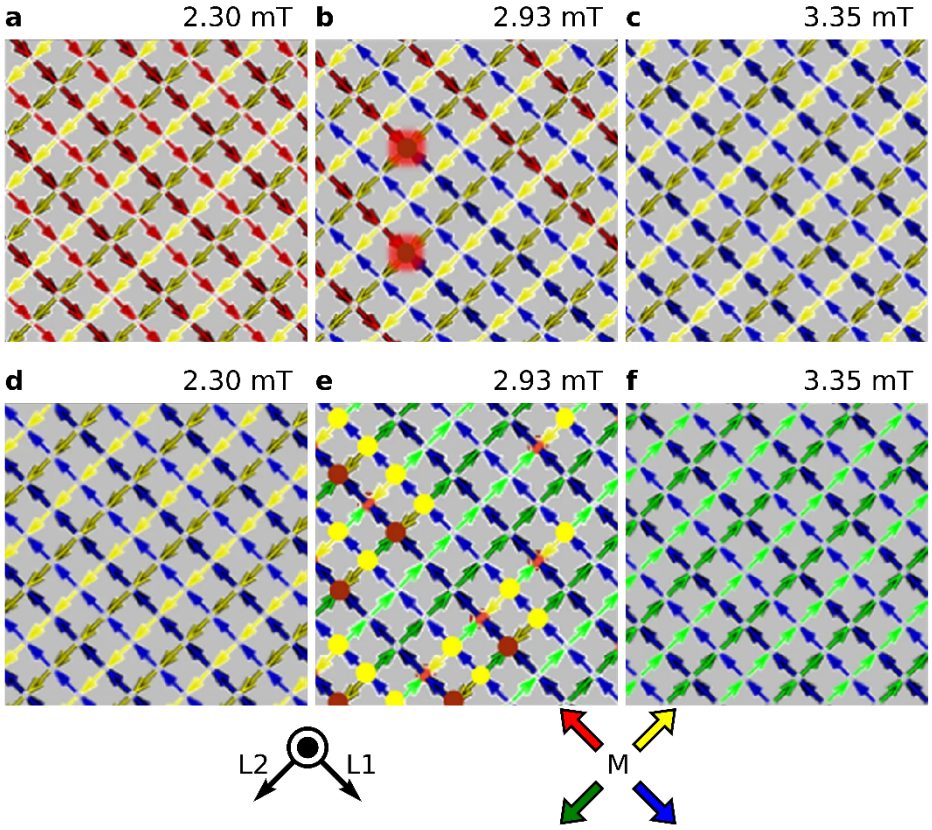

Figure 5-25 Monte Carlo simulations reproducing the results shown in Figure 5-24. (a-c) fields applied along the projection of the L1 sublattice. (d-f) fields applied along the L2 sublattice.

The striking discrepancy between the required surface energetics factor and the value indicated by micromagnetic simulations arises from the differences in approach. The compass needles in MC simulations are disconnected; this results in the methods treating interactions at the vertex differently. Magnetic charge is evenly distributed across the compass needle, whereas it is concentrated at the vertex in micromagnetic simulations.

A final point is the consideration of the chemical potential (μ), referring to the energy required to nucleate monopole excitations. This may be computed by the difference between two adjacent nanowire junctions in oppositely charged excited states and two adjacent junctions in an ice-rule state. The effective potential may be used to quantify the extent to which monopoles remain closely correlated and is defined as $\mu^* = \mu/u$ where $u =$

$\mu_0 Q^2/4\pi a$ and a is the lattice spacing. When this value approaches half the Madelung constant ($M_C/2 = 0.819$ for diamond lattices), a charge crystal becomes energetically favourable and a possible state during field-driven dynamics.

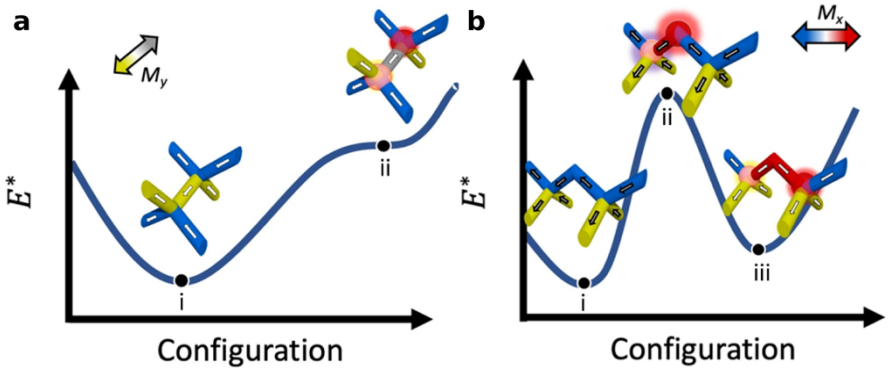

Figure 5-26 (a) Energy for monopole nucleation upon the L2 sublattice comprising adjacent coordination-four vertices. The schematic depicts a single nucleation event from a pair of ice-rule states (i) to a monopole antimonopole pair (ii). (b) Energy for monopole nucleation upon the L1 sublattice comprising pairs of coordination-four vertices separated by a coordination-two vertex. Starting at the ice-rule states (i), a nucleation event yields a high energy intermediate state with one of the monopoles upon the coordination-two vertex (ii), a further flip reduces the energy state with a monopole-antimonopole pair separated by the coordination-two vertex wires (iii).

The effective chemical potential associated with a single spin-flip yielding a monopole-antimonopole pair in adjacent coordination-four vertices (Figure 5-26a) within the dipolar model was evaluated at $\mu^* = 1.03$. The energies of excited states in coordination-two vertices restrict monopole-antimonopole pairs upon the surface termination; however, this state must be surpassed to produce a charge pair on two coordination-four vertices separated by a coordination-two vertex (Figure 5-26b). The effective energy of the intermediate state is determined to be $E^*_{int} = 5.16$. Less favourable Coulomb interactions for monopoles across the L1 coordination-2 vertex result in an effective chemical potential of $\mu^* = 1.22$. The combination of the energy barrier of the intermediate state and the larger effective chemical potential of the final state results in a

larger number of uncorrelated monopoles upon L1, as shown in both experimental results and MC simulations.

5.4. Summary

Interest in artificial spin-ice has rapidly expanded over the past two decades; not only as a means to study magnetic monopole defects, but also as model systems for ground state ordering in the exactly solved vertex models in statistical mechanics. Until recently, artificial spin-ices have been restricted to two-dimensional systems incapable of fully capturing monopole dynamics due to degeneracy lifting among the ice-type vertices. The realisation of a three-dimensional artificial spin-ice presents a major step forward for the community by placing moments along their local ⟨1,1,1⟩ axes. This chapter explores micromagnetic simulations used to characterise the building blocks of the 3D nanowire lattices and contextualise measurements of the experimental system.

Switching and charge propagation in a connected nanowire lattice occurs through domain wall motion, our fabrication method yields a novel crescent-shaped cross-section with non-uniform thickness, and we performed simple relaxations to determine the impact of this cross-section upon domain wall structure. We find that the resultant domain wall structure is perturbed with an out-of-plane component in the circulating region, resulting in increased magnetostatic energy and a subsequent narrowing of the domain wall when compared to the planar equivalent.

A contrived example of an isolated wire with a crescent-shaped cross-section and angled end caps shows behaviour which is not entirely Ising-like; the complex end caps introduce edge defects resulting in more than two states on a hard-axis hysteresis loop.

However, this is an artifact of using an idealised isolated nanowire, and the Ising-like behaviour is recovered when the wires are placed in more complex geometries reflective of the vertices found in the experimental system.

We simulate hysteresis loops of the coordination-two and coordination-four vertices found in the lattice to determine whether the switching behaviour of the lattices is comparable to simulation results. MOKE measurements of the hysteresis loop reveal a square loop with distinct lobes near the switching field. We can attribute some of the features in the measured loop to effects of permalloy film upon the substrate, but we find that the remaining features are not well captured in micromagnetic simulations of coordination-four vertices; simulations of coordination-four vertices show a significant amount of coherent rotation not observed in the MOKE measurements. The MOKE measurements appear to be primarily sensitive to the magnetisation of the L1 sublattice, and it is reasonable to consider the 'lower bipod' geometry found in this layer. Indeed, the features found in physical measurements may be reproduced from the lower bipod simulations. However, this exercise reveals that longitudinal and polar components of MOKE cannot entirely be suppressed when performing MOKE measurements upon 3DASI.

To complete the simulations, we model the sixteen vertex types of coordination-two vertices and the excited states upon the coordination-two vertices. Computed surface charge density enables the identification of different vertex types measured in the experimental system using magnetic force microscopy, aiding with experiments demonstrating magnetic charge formation and propagation through the lattices. Most interesting are the computed energy densities of the vertex types. Consideration of these

energetics informed the parameters for Monte-Carlo simulations of the lattices accurately capturing charge formation and propagation in the lattices.

One would expect degeneracy of the ice-type vertices to be recovered in a three-dimensional system. However, we find that our crescent-shaped cross-section breaks the symmetries and, although smaller than reported in other works, there is an energy difference between the type-I and type-II vertices. In contrast to 2DASI, we also find some degeneracy lifting among the type-III vertices due to our cross-section where a 1-in/1-out state upon the upper wires of the coordination-four vertex is favoured. Finally, we find the energy of a q=±2 charge upon a surface coordination-two vertex is a factor of three higher than an equivalent charge upon the coordination-four vertices. Not only is the domain wall energy upon the lower bipod high, the pinning potential is also very weak. These energies suggest that long-range ordering upon the L1 sublattices is favourable, and any charge that forms upon the surface quickly moves down to the lower layers.

Monte-Carlo simulations also enabled the effective chemical potential to quantify the extent to which the charges remain closely correlated. We find an effective chemical potential of μ^*=1.03, close to half the Madelung constant of diamond lattices (M_c/2=0.819) where a charge-ordered state becomes favourable and is predicted to be achievable using field-driven dynamics.

Although these first attempts at fabricating a 3DASI do not entirely recover degeneracy among the ice-type vertices and introduce additional degeneracy lifting among the type-III vertices, the work presented in this chapter presents a significant step forward. Using a variety of 3D nanostructuring techniques along with different metallisation methods, it should be possible to recover the symmetries required to recover degeneracy.

However, the observed degeneracy lifting may also be exploited and tailored to manipulate the energy landscape and realise physical systems to directly visualise three-dimensional iterations of the Rys-F and KDP vertex models, and explore field-driven demagnetisation protocols to realise magnetic charge crystal states.

6. Fabrication of Isolated 3D Magnetic Nanostructures Using Sacrificial Layers and Two-Photon Lithography

6.1. Introduction to domain wall conduits

The notion of manipulating magnetism as a means of recording data traces back to the 1870s with the proposal of using magnetisation of a wire to record sound [146]. Exploiting magnetism has become the dominant approach to data storage, with technologies such as hard disk drives being well-established and magnetic random access memory recently reaching maturity. The observation of spin-polarised current injection [147] and giant magnetoresistance [148, 149] in the 1980s heralded the introduction of spintronics; the use of spin rather than, or in addition to, charge in logic [150-152] and sensing [153, 154] devices.

Spintronics within the magnetism community primarily focuses on magnetic nanostructures, where shape anisotropy or uniaxial magnetocrystalline anisotropy are exploited to force an easy magnetisation axis. With a single easy axis, the magnetisation may point ‘up’ or ‘down’ to represent a 1 or a 0. Applying magnetic fields or spin-polarised

currents mobilises domain walls, such that these magnetic domains may be moved through a conduit. With negligible magnetocrystalline anisotropy, permalloy ($Ni_{81}Fe_{19}$) nanowires form excellent domain wall conduits [155] as the demagnetising energy terms ensure the magnetisation of magnetic domains is aligned with the long axis of the wire.

As the past decades have shown, magnetic nanowires in complex arrangements may be used to perform logic operations as an alternative to traditional complementary metal-oxide semiconductor (CMOS) elements [156]. Research efforts have seen the realisation of NOT [157-159], AND [160], and NOR [161] gates sufficient to perform all logic operations when combined, with later efforts demonstrating single reconfigurable devices capable of functioning as AND, NAND, OR, and NOR gates [162].

The best-known example of a domain wall conduit-based device is magnetic racetrack memory, which exploits the orientation of domains along the wire to encode data. External fields or spin-polarised currents move the domain walls along the wire such that the domain orientation may be measured using giant magnetoresistance, and manipulated using perpendicular spin currents [6]. Perhaps the most promising aspect of the concept is that, in principle, the wires may be arranged in a 3D volume rather than a 2-dimensional surface like current technologies. Although conceptually simple, and a recent promising experimental realisation appearing in the literature notwithstanding [26], realising a 3D magnetic racetrack memory device presents significant challenges.

6.1.1. Controlled domain wall motion in magnetic nanowires

Any domain wall conduit for technological applications must enable controlled domain wall motion regardless of the number of dimensions; the operator must be able to

move domain walls between well-defined positions. This is achieved by trapping (pinning) domain walls by locally altering the domain wall potential through modulations in the conduit geometry or through magnetostatic interactions with other nearby objects.

Ono et al presented the first example of geometric pinning through the introduction of artificial defects in a conduit [163, 164]. Briefly after this result, Yokoyama et al [32] presented direct imaging of domain wall pinning in permalloy nanowires with varying widths and two 'necks' where the wire width is reduced along the length as shown in Figure 6-1a. With the width of the second neck (farthest away from the injection pad) set at 0.2 times the wire width (W), the width of the first neck was changed from 0.2W to 0.8W to control the pinning potential. A small field parallel to the wire long axis injects a domain wall which pins at the first neck, a subsequent larger field is required to move the domain wall from the first neck to the second where the domain wall position could be measured using Kerr microscopy Figure 6-1(b-d). The depinning field increased with decreasing neck width, however, there appears to be a limit of the absolute neck width, below which the depinning field does not change Figure 6-1e. In this regime, the depinning field represents the nucleation field required to form a second domain wall after the defect.

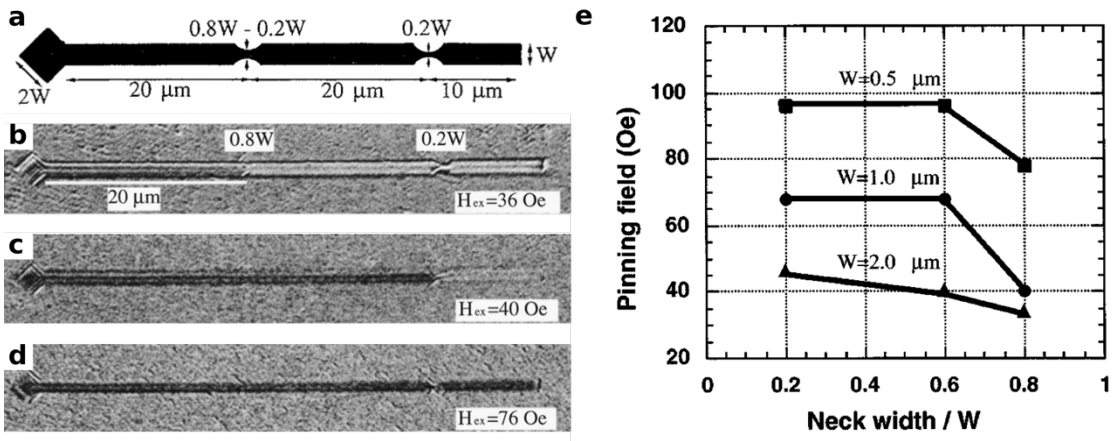

Figure 6-1 (a) Schematic of wires with necks and nucleation pad presented by Yokoyama et al., with neck widths ranging of 0.2W, 0.4W, and 0.8W. where W is the wire width. (b-d) Change in domain patterns for the 1μm widths wire after application of varying fields. Images obtained using Kerr microscopy. Domain wall depinning field as a function of neck width and wire width. All figures from [165].

Shortly after the work presented by Yokoyama et al, Himeno et al [166] presented 500nm wide magnetic nanowires consisting of a $Ni_{81}Fe_{19}$ (5 nm)/Cu (20nm)/$Ni_{81}Fe_{19}$ (20 nm) tri-layer with a neck along the wire. A schematic of the experimental configuration is shown in Figure 6-2a. DWs were injected through local field pulses at the wire ends by passing currents through a copper wire and applying a uniform field parallel to the wire long axis for DW propagation. Changes in the magnetisation were measured as a change in resistance across the wire. With this approach, a large number of measurements could be taken to determine the probability of pinning as a function of neck width with both the mean and the width of the probability density function decreasing with increasing neck width (Figure 6-2 b & c).

Parallel to the work performed by Himeno, Kläui et al demonstrated DW pinning using triangular notches in a permalloy nanowire ring and showed that these notches functioned as an attractive potential well for head-to-head transverse domain walls [167]. In later work, the group demonstrated that these triangular notches present potential

barriers for vortex domain walls. Specifically, the constriction presented a repulsive barrier for the VDW core, but a potential well for the half-antivortex elements of the VDW [168].

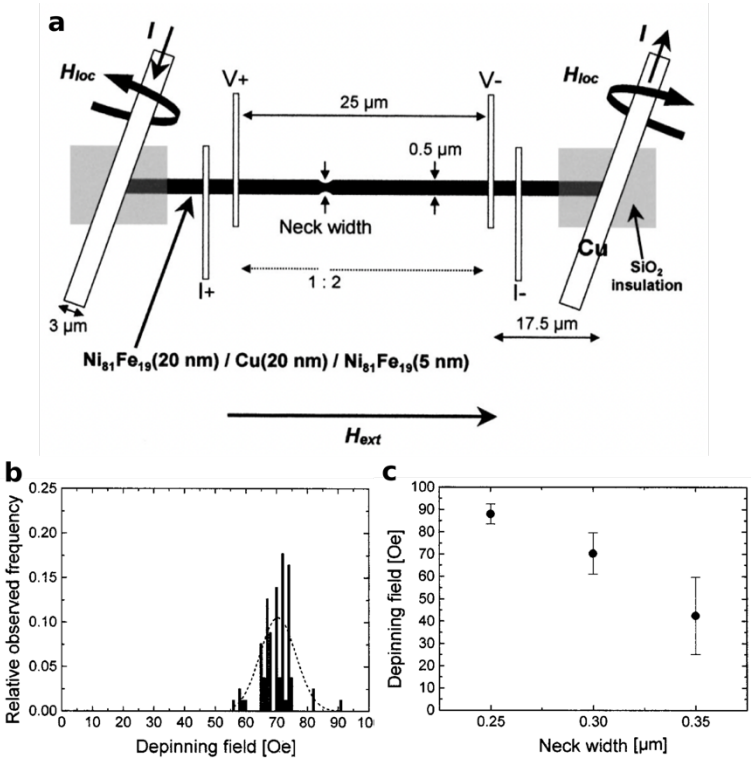

Figure 6-2 (a) schematic illustration of the sample presented in [166]. Black part is the NiFe (5nm)/Cu(20 nm)/NiFe(20 nm) trilayer magnetic nanowire with a along the wire. Domain walls are injected using fields produced by passing currents through the Cu wires, external field pulses parallel to the wire propagate the domain wall. A four-point probe is indicated for resistance measurements. (b) Depinning field distribution for the sample with a 0.3μm wide neck, dotted line indicates Gaussian best fit. (c) mean depinning field as a function of neck width, error bars indicate full width at half maximum.

Micromagnetic simulations show the pinning mechanism may be attributed to a reduction in the stray field; the half-integer topological charges at the wire edges yield a large stray field which is minimised by reducing the width of these regions. Reducing the width of a VDW core does little to reduce stray field but comes at a high cost in exchange energy such that the constriction in the nanowire presents a potential barrier for the components with integer winding number.

Subsequent work has focused on exploiting domain wall types in wires with triangular notches in early memory device concepts [19], and exploring notch shape effects on the pinning potential [20]. In their 2008 paper proposing a magnetic racetrack memory device, Parkin et al used regularly spaced triangular notches to introduce well-defined locations for domain walls such that magnetic domains may be reliably moved along the wire [6].

Pinning through the introduction of artificial defects has been demonstrated to be an effective means for controlling domain wall motion, and the past decades have seen the exploration of various alternative pinning mechanisms such as exchange bias-driven pinning [27], locally perturbing magnetic properties of via ion implantation [169, 170] or local metal diffusion [171].

One factor to consider in the development of domain wall conduit devices, is that demand for density will require conduits to be closely spaced. O'Brien et al demonstrated that magnetostatic interactions between domain walls in adjacent wires yield significant pinning potentials at small separations [30]. This result indicates potential limitations in the realisation of domain wall devices arising from crosstalk due to interacting domain walls in adjacent wires. Nonetheless, this potential problem also presented an opportunity to explore the use of stray fields from nearby devices to introduce and tailor pinning potentials. The same group explored the use of magnetised stubs near the conduit creating either a potential well or a potential barrier for transverse domain walls dependent on the direction of the TDW core with respect to the stub magnetisation [31].

The final pinning mechanism pertinent to this work is achieved through the addition of curvature. Lewis et al produced curved domain wall conduits with varying radii of

curvature [24] to find varying pinning potentials depending on the transverse domain wall chirality. Head-to-head domain walls with the core pointing away from the centre of curvature and tail-to-tail TDW with the core pointing towards the centre of curvature experience potential well, whereas opposing chirality yields a potential barrier. Micromagnetic simulations of head-to-head domain walls with opposite chirality reveal that the potentials can be explained by considering surface charge in the two scenarios as discussed in section 3.2.10. The magnitude of the potential wells and barriers is proportional to the radius of curvature, an observation that has led theoretical exploration of curvature-driven effects in micromagnetism [25, 74, 172] resulting in the burgeoning field of curvilinear magnetism.

6.1.2. Controlled domain wall injection

One notable detail in the investigations of artificial pinning is that the pinning fields are typically smaller than the fields required to inject a domain wall into a simple wire. The typical reversal process of a single wire also involves nucleation of a domain wall simultaneously at both ends of the wire, followed by the propagation of the domain walls at the centre of the wire where these annihilate. Schrefl et al demonstrated that breaking the wire symmetry by tailoring the wire ends yields different nucleation fields [173], which may be exploited to control domain wall injection. The injection field is reduced by reducing the demagnetising factor associated with the external field axis. In the investigations into pinning potentials previously discussed, this has been achieved by adding low aspect ratio nucleation pads at the end of the wire [19, 20, 165], or adding high aspect ratio segments with the long axis perpendicular to the applied fields [24, 30, 31].

Field-driven domain wall injection is most convenient in research settings focusing on single conduits, and is therefore the chosen method in this work. However, it must be noted that field-driven domain wall injection is not favourable in practical devices due to difficulties in limiting applied fields to single nanowires, affecting neighbouring structures [174]. An alternative injection method is to use local Oersted fields such as those shown in Figure 6-2a by passing currents through perpendicular wires [166]. However, the power requirements and additional space requirements render these unsuitable for commercial devices. Domain wall nucleation using spin-transfer torque (STT) requires lower currents and less space, which are key factors to the scalability [175]. Domain wall injection via STT is well-established through in-line injection [176], magnetic tunnel junctions/spin valve stacks [177], with the latter being the favoured approach in current commercially available MRAM devices [178].

6.1.3. The challenge of creating three-dimensional magnetic nanowires

As explored in the prior sections, methods for controlled domain wall injection and motion in domain wall conduits are well-established. The most significant challenge in realising a three-dimensional domain wall device is fabricating nanowires in an arbitrary three-dimensional geometry and subsequently characterising these wires.

Perhaps the most ambitious attempt at producing 3D magnetic nanowires functioning as a magnetic racetrack memory device was demonstrated by Gu et al [26]. The group used typical 2D fabrication methods to pattern a 2D racetrack upon a water-soluble $Sr_3Al_2O_6$ (SAO) layer which can be lifted off and transferred onto another substrate with large out-of-plane protrusions. With the nanowires resting to follow the topography of the second substrate, a 3D racetrack is produced.

Our recent published works demonstrate the feasibility of producing complex 3D magnetic nanostructures [38, 39, 144] using two-photon lithography and line-of-sight deposition. Due to the relative ease of fabricating large and complex structures, work on 3D nanomagnetism using two-photon lithography has primarily focused on the study of frustrated systems [60, 62]. However, work on magnetic nanowires produced using TPL is starting to emerge demonstrating the fabrication of cylindrical nanowires [44], and isolated magnetic nanowires [179] which are the subject of this chapter.

The past decade has seen intense research effort exploring direct-write methods for 3D magnetic nanostructure fabrication as discussed in chapter 2. Two-photon lithography (TPL) has shown itself to be an effective means for producing complex 3D magnetic nanostructures such as frustrated nanowire lattices [38, 39, 60, 62, 144]. However, the metallisation of structures created using negative-tone photoresists is achieved via thermal evaporation, resulting in magnetic material on the substrate. The problem associated with the sheet film is two-fold. Firstly, for 3D nanostructures close to the substrate, there will be an unwanted magnetostatic interaction that may perturb the spin texture. Secondly, when carrying out magnetometry, the signal from the sheet film may mask subtle features due to the nanostructure. The lattices presented in chapter 5 included several unit cells below the functional layer such that the separation between this layer and the substrate minimises magnetostatic interactions. The extent of the structures in the substrate plane was also sufficient to minimise, although not eliminate, signal from the substrate during MOKE measurements. These challenges become more pronounced with studies of isolated domain wall conduits where the target area is orders of magnitude smaller than the focal

spot in techniques such as MOKE, and substrate signal dominates signal from target structures.

Focused electron beam-induced deposition (FEBID) is a promising technique for magnetic nanowire fabrication [40-43] with lateral feature sizes to the order of a few nm [45]. There are still limitations in the range of available precursors and their associated functional materials. The deposits from FEBD often have a reduced purity, ranging between 60 – 90%. To address this issue, FEBD may be used to produce non-magnetic scaffolds upon which magnetic material may be deposited. This approach, like combining TPL and LOS deposition, results in magnetic material on the substrate. Sanz-Hernández et al. [41] created nanowire scaffolds at an angle from the substrate using FEBID upon which a Permalloy film was deposited. Using a dark-field MOKE technique, the group could separate magnetometry of the wires from that arising from the substate. Dark-field MOKE techniques are helpful for simple geometries, but their benefits are more questionable for more complex nanostructures. Adding additional redundant layers below the functional top layer of the 3DASI presents challenges in more advanced techniques such as XMCD and STXM, where X-ray penetration depth is critical. For the above reasons, it is desirable to remove the substrate film entirely.

6.1.4. The use of sacrificial layers to achieve selective deposition

The use of sacrificial layers is well-established in micromachining and semiconductor fabrication. The additional material may provide anchor points to support suspended structures such as cantilevers [180] and suspended beams [181] through fabrication. Semiconductor device fabrication regularly employs materials such as PMMA, positive photoresists, or inorganic materials such as silicate (SiO_2), titanium, and aluminium, which

are patterned such that regions are selectively masked during processing. Key to sacrificial layer techniques is identifying suitable materials and solvents for the lift-off procedure. The ideal process uses materials that remain intact during the fabrication process until the lift-off procedure, and the lift-off procedure should only affect the sacrificial layer to ensure the desired structures remain intact.

Aqueous hydrofluoric acid (HF) is a common reagent that removes inorganic materials. However, its poor selectivity and extreme toxicity render the reagent inconvenient and hazardous to the user [182]. Several HF free methods exist using acids and oxidants, but these only address safety concerns regarding HF and still suffer poor selectivity [182]. Some methods use PMMA or positive photoresists, which are commonly removed using reactive ion etching [183], acetone[184], or thermal degradation[185].

Introducing a sacrificial layer in the TPL fabrication process would enable the removal of substrate film and improve TPL with LOS deposition as a platform for research into 3D magnetic nanostructuring. However, none of the aforementioned materials are compatible with the fabrication process; either the chemicals required for lift-off equally lift off the desired polymer scaffold, or the developer chemicals used in TPL remove the sacrificial layer before samples are ready for deposition.

Linder et al. [186] identified PAA as a candidate sacrificial layer for surface micromachining as the substance is water-soluble but insoluble to acetone, IPA, and PGMEA. PAA. Spin-coating PAA upon a substrate is a straightforward process where the layer thickness is easily controlled with PAA concentration and rotation speeds. Superficially, using PAA as a sacrificial layer is then a near-ideal candidate for nanostructuring using two-photon lithography. This chapter explores Poly(Acrylic Acid)

(PAA) as a sacrificial layer compatible with TPL and demonstrates its utility in 3D nanostructure fabrication. We expand the negative-tone resist TPL fabrication protocol outlined in chapter 4.1 to include spin-coating of a PAA layer upon the substrate, nanostructuring the PAA using laser ablation, and a lift-off procedure after the deposition of magnetic materials. We perform optical magnetometry upon a range of nanostructures and present energy dispersive X-ray (EDX) analysis indicating the procedure's success.

6.2. Developing a method incorporating sacrificial layers in 3D magnetic nanostructuring using two-photon lithography

In the fabrication process initially proposed, negative-tone photoresist (IPL-780) is drop-cast upon a cleaned glass coverslip (Figure 6-3 a), struts are written using the standard TPL procedure outlined in chapter 4 (Figure 6-3 b) and unexposed resist is removed using a PGMEA developer (Figure 6-3 c). After development, a ~100 nm layer of PAA is deposited using a spin coater at 4000 rpm for 60 seconds (Figure 6-3d). Once the PAA has been deposited, more IPL-780 is drop-cast upon the structure, and the samples are mounted back into the TPL system (Figure 6-3 e) to write the structures upon the struts (Figure 6-3 f). After development (Figure 6-3 g), a thin film of permalloy is deposited using thermal evaporation (Figure 6-3 h) followed by a lift-off procedure to remove the background film (Figure 6-3 i).

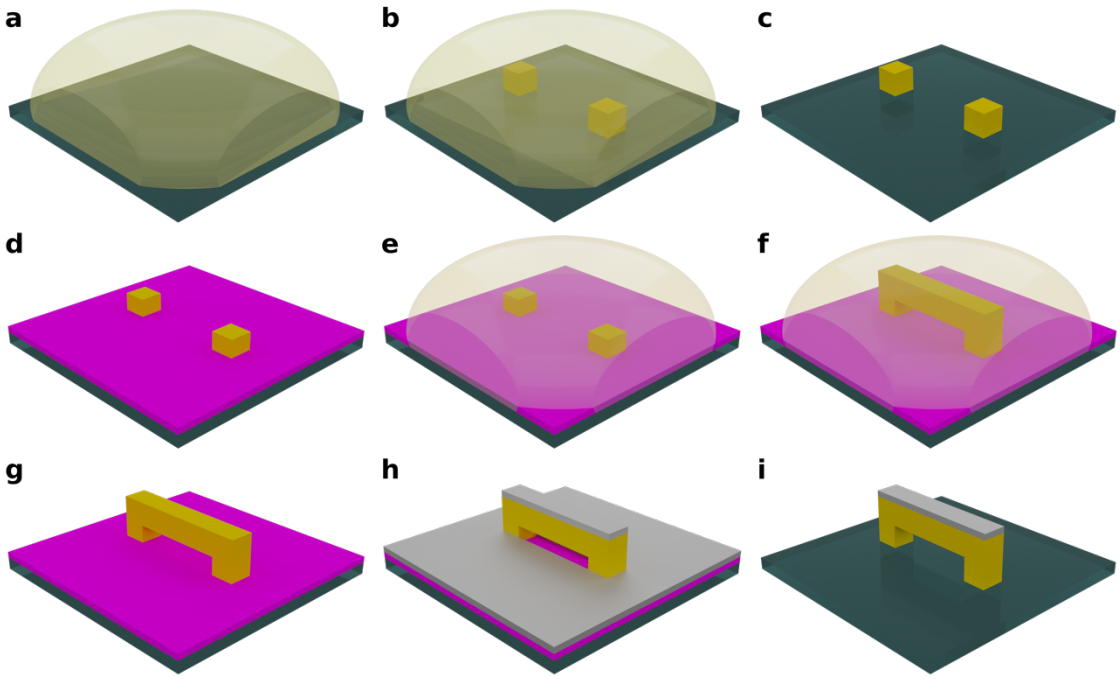

Figure 6-3 Initial proposed fabrication process using a PAA sacrificial layer. (a-c) struts for the desired geometry written using a standard TPL process. (d) a PAA layer is spin-coated upon the substrate. (e-g) the remainder of the structure is written and developed. (h) the functional material is evaporated onto the sample, and (i) the sacrificial layer is lifted off in a water bath.

Initial work by Myléne Carouel shows this process to be unsuitable as adhesion of the struts to the substrate is insufficient during the spin coating process resulting in their removal. PAA can be ablated with femtosecond laser exposure at high intensities, and this presents a promising opportunity to address challenges in the prior process. The proposed method starts with cleaning a glass coverslip in a 20-minute ultrasonic acetone bath followed by a 20-minute ultrasonic IPA bath. A thin PAA layer is spin-coated onto the substrate using an aqueous PAA solution (5% w/v) (Figure 6-4 b). Index-matched immersion oil is drop-cast on the opposite side of the coverslip, and the substrate is mounted in the TPL system. Using high-intensity femtosecond laser pulses, the PAA layer is then ablated to expose the glass substrate at the anchor points of the desired structure (Figure 6-4 c). After ablation, the negative photoresist (IPL-780) is drop-cast onto the substrate (Figure 6-4 d), and the desired structure is written into the ablated regions

(Figure 6-4 e). Unexposed resist is washed away in a 20-minute PGMEA bath followed by an IPA bath and dried carefully using compressed air (Figure 6-4 f). A thin film of permalloy ($Ni_{81}Fe_{19}$) is then deposited using thermal evaporation with pressures not exceeding 10^{-6} mbar (Figure 6-4 g) and lift-off of the substrate film is performed by placing the sample in a DI water bath (Figure 6-4 h).

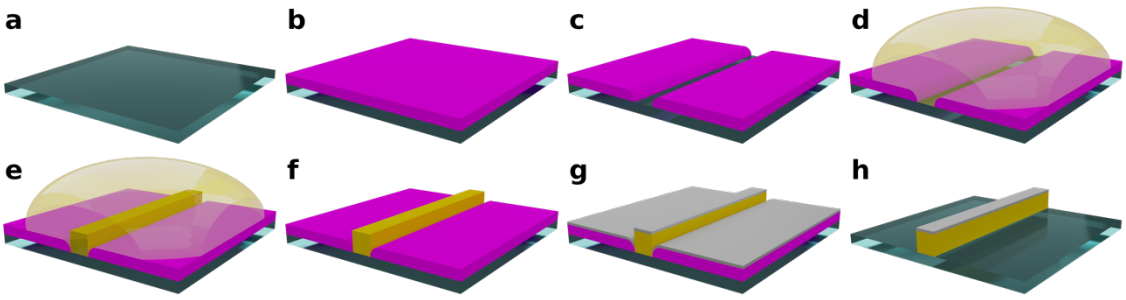

Figure 6-4 Schematic of fabrication process using a PAA sacrificial layer. (a) Use of a clean (glass or ITO covered glass), (b) a thin layer of PAA is spin-coated upon the substrate. (c) the projection of the geometry is ablated into the PAA layer to expose the substrate, and (d) IPL-780 is drop-cast upon the slide. (e) The desired geometry is written into the ablated track and (f) placed in a developer. (g) the functional material is evaporated upon the sample, and (h) the PAA layer is lifted off in a water bath.

Linder et al. [186] measured PAA layer thickness as a function of spin-coater speed and PAA concentration of the initial solution to find a 110nm thickness with a 5% (w/v) solution after spin coating at 4000 rpm. After spin-coating a PAA layer according to these parameters, we explore ablation with varying laser power and scan speed. A series of lines were scanned through the PAA layer, whereby the laser power and scan speed were varied.

Atomic force microscopy (AFM) was then used to inspect any ablation associated with the laser scan, as shown in Figure 6-5. AFM measurements of tracks ablated at 50mW and a scan speed of 0.2 mm s^{-1}, 50mW at 0.4 mm s^{-1} , 70mW at 0.4 mm s^{-1}, and 70mW at 0.8 mm s^{-1} are shown in Figure 6-5(a-d). There is a strong dependence on laser power and scan speed in the ablation width and depth, requiring high laser power coupled with slow

scan speeds to achieve uniform ablation. Using AFM data, we measure the RMS roughness of the PAA layers using unexposed regions (as illustrated in Figure 6-5e, blue square) and characterize the ablated trenches using line profiles perpendicular to the trench (as shown in Figure 6-5e, red line).

The RMS roughness of the unexposed PAA layer measured at the region marked with a blue square in Figure 6-5e is (1.166 ± 0.414) nm (Figure 6-5h), where the standard deviation gives the uncertainty. Profiles are obtained for the trenches with a typical example shown in Figure 6-5g, where a shoulder on the trench walls suggests the redeposition of ablated material. We use the profiles to measure the trench depth (Figure 6-5h) and full width at half maximum (FWHM) (Figure 6-5i).

There is a logarithmic dependence of trench depth upon laser power with a distinct ablation threshold at lower power (Figure 6-5h) consistent with equation 4.1. At higher intensities, trench depth saturates as the lateral feature size exceeds the PAA film thickness of 110 nm. There exists an approximately linear dependence of channel width upon laser power (Figure 6-5i). These results indicate that compromises are in order during nanofabrication; high laser powers result in consistent tracks exposing the substrate but large lateral feature sizes, leaving much of the substrate exposed when smaller structures are written into the trench.

We select lower laser powers for ablation to recover sufficiently small feature sizes. The ablation geometry is defined as the projection of the TPL geometry upon the substrate, and we stack layers of the ablation geometry to ensure ablation through the entire thickness of the PAA layer. We repeat each layer five times to ensure even ablation before

moving down. Repeating each layer also removes material that has been ablated but redeposited inside the trenches.

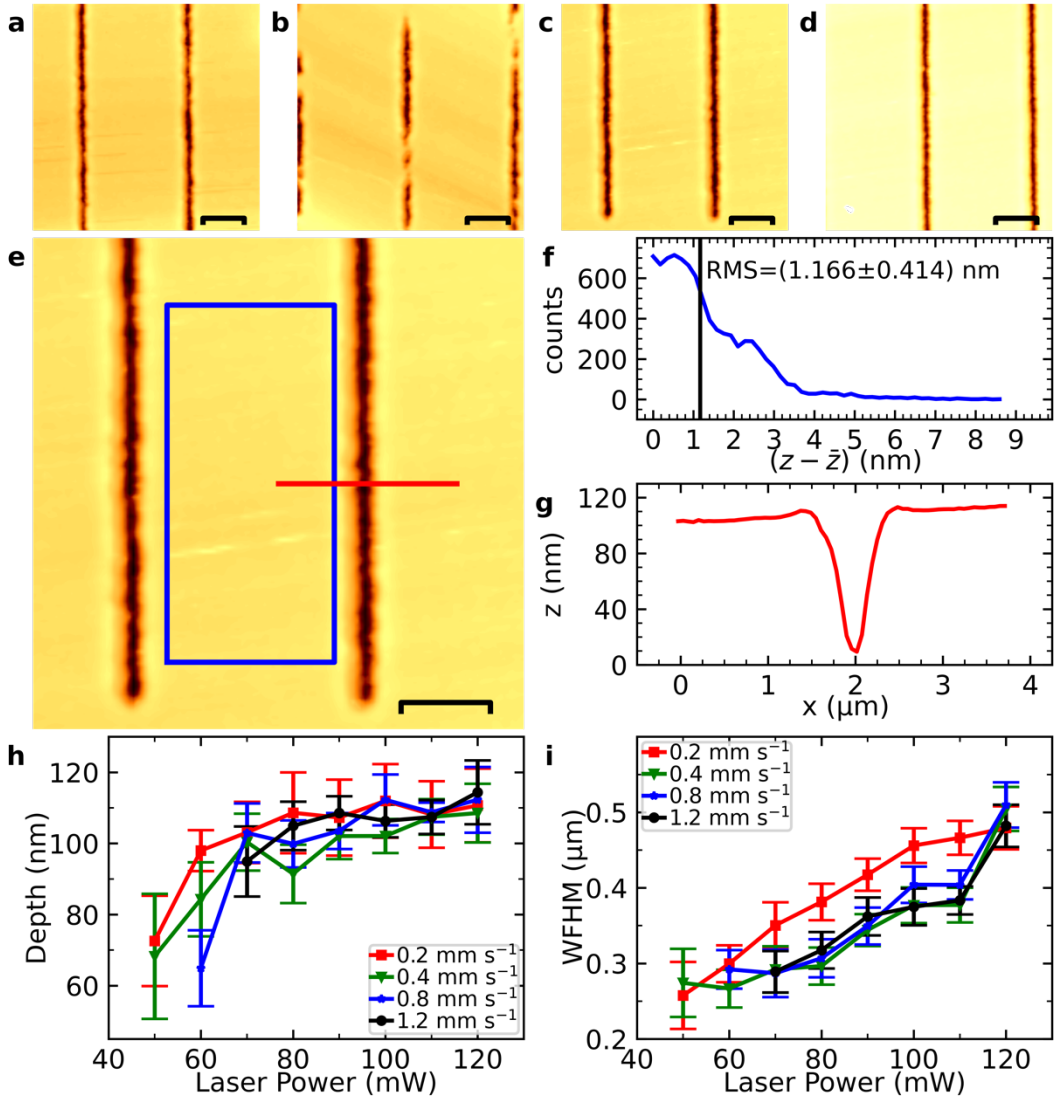

Figure 6-5 (a-d) Ablated tracks in PAA layer with parameters (a) 50 mW, 0.2 mm s^{-1}. (b) 50 mW, and 0.4 mm s^{-1}, (c) 70 mW and 0.4 mm s^{-1} (d) 70 mW and 0.8 mm s^{-1}. (e) illustrative set of ablation tracks in PAA, indicating regions for roughness measurement and line profiles. Scale bars for a-e indicate 2 μm (f) roughness measurement of PAA layer spin-coated upon the substrate at 4000 rpm with an initial concentration of 5% (w/v). (g) illustrative line profile of PAA trench captured perpendicular to the trench direction. (h) PAA trench depth after a single exposure. (i) PAA trench width after a single exposure

To test the feasibility of this method, we start with the simplest possible geometry, a single nanowire written into a trench. The process requires precise alignment of the TPL geometry to the PAA geometry, and we encounter a new challenge; the glass coverslips,

PAA, and uncured IPL-780 have similar refractive indices ($n_{glass} \approx 1.5$, $n_{PAA} = 1.508$, and $n_{IPL} \approx 1.485$) resulting in negligible contrast on the Nanoscribe optical microscope used for visual feedback needed during alignment. We selected glass with a 50nm indium tin oxide (ITO) layer with a refractive index of $n_{ITO} \approx 1.858$ as an alternative substrate, and the improved contrast enabled alignment. AFM measurements of a trench show that ablation at a low dose (60 mW, 0.8 mm s^{-1}) and five repetitions per layer, result in uniform trenches (Figure 6-6a & b) to which we can reasonably align the TPL geometry to the trench (Figure 6-6 c & d).

When successful, the lift-off procedure results in intact nanostructure scaffolds with the functional material deposited upon the scaffold, with negligible material remaining on the substrate. Lift-off may fail due to damage to the nanostructures. This may be due to insufficient ablation such that the TPL structures are not anchored to the substrate or that adhesion of the TPL structures to the substrate is inadequate due to the high surface tension of water. Any significant movement of the sample in the water bath may strip the structures from the substrate.

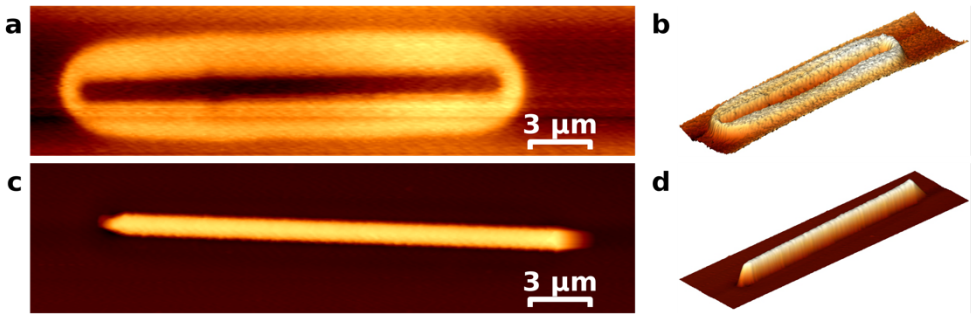

Figure 6-6 (a) Atomic force micrograph of trench ablated into PAA layer, (b) 3D rendering of (a). (c) Atomic force micrograph of wire before lift-off written into the ablated trench using two-photon lithography. (d) 3D rendering of (c).

To determine any potential impacts from surface tension, an experiment was performed whereby sets of nanowire scaffolds (80μm × 1μm × 3μm) were written using TPL without a PAA sacrificial layer (Figure 6-7a), and the sample was placed in a water bath as if lifting off. The sample is subsequently removed from the water and dried using compressed air. After the mock lift-off process, the wires are dislodged and removed from their location (Figure 6-7 b), indicating that water surface tension is too high for nanostructures to remain stable during lift-off. The damage likely occurs while removing the sample from the water bath and drying it using compressed air. We create another set of nanowires (Figure 6-7 c) and repeat the mock lift-off procedure with the additional step of slowly displacing the water with IPA to reduce the surface tension and reduce damage during removal and drying. Using this method, the wires remain intact and in place (Figure 6-7 d). Finally, we repeat our improved procedure on a set of wires written into trenches ablated into a PAA sacrificial layer (Figure 6-7 e). The wires remain intact during lift-off, indicating that the structures are well aligned to the trenches and anchored to the substrate (Figure 6-7 f).

Another condition for lift-off failure is the functional material not lifting off sufficiently. The failure may result from the ablated region being too large or insufficient alignment, exposing the substrate to anchor the deposited film. However, optical microscopy images also reveal halo-like patterns around nanostructures, indicating a change in the properties of the PAA layer. We suspect PAA is cross-linking with itself, reducing its solubility in water.

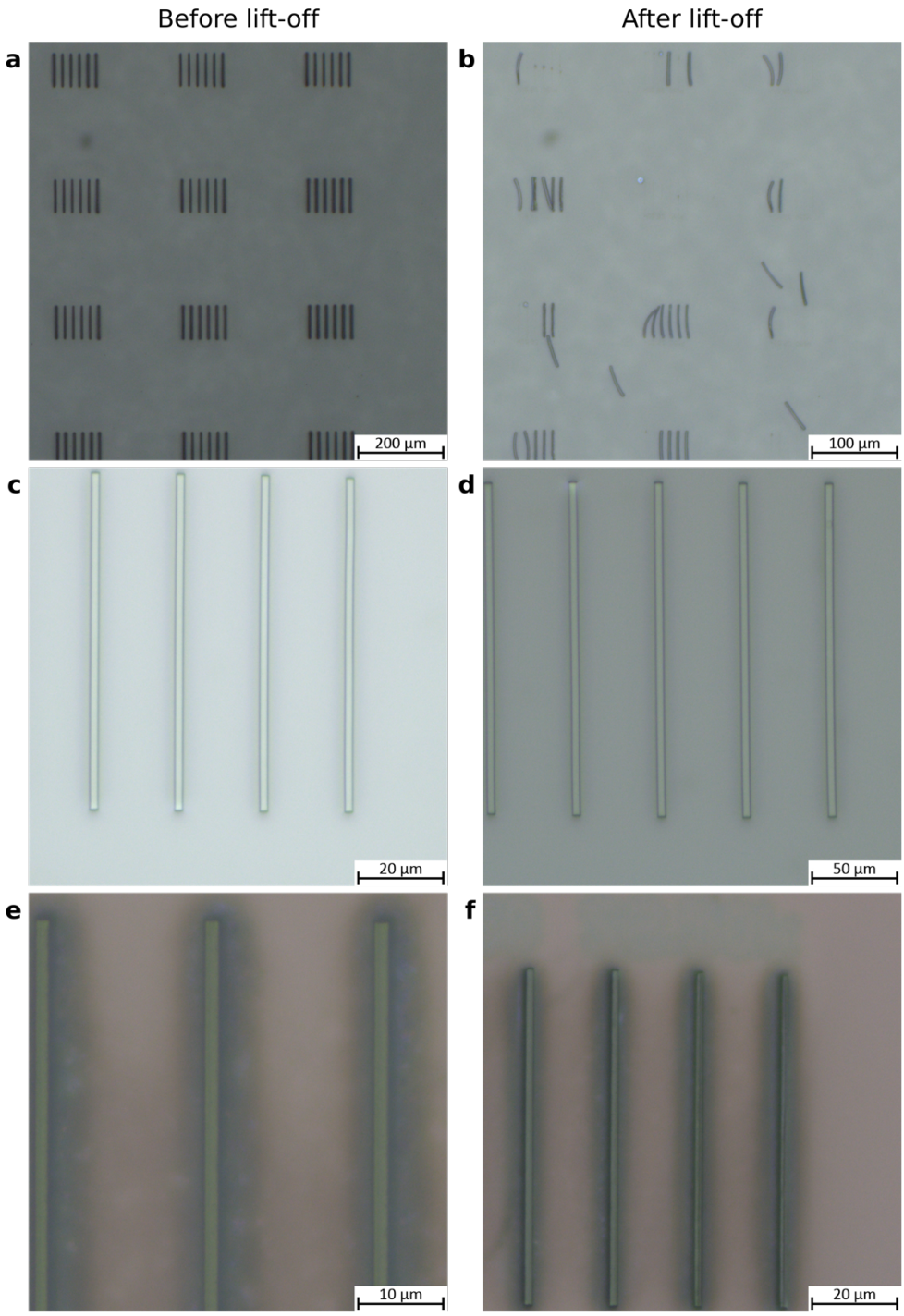

Figure 6-7 Test of lift-off procedure. (a) Nanowire scaffolds are written onto the substrate, (b) nanowire scaffolds after DI water bath. (c) the second set of nanowire scaffolds written onto the substrate, (d) nanowire scaffolds after DI water bath where the water is slowly displaced with IPA. (e) Nanowire scaffolds were written into trenches ablated into PAA (f) nanowire scaffolds after DI water bath with IPA displacement.

The lift-off procedure was performed after depositing a 25nm Permalloy layer using thermal evaporation with evaporation pressures not exceeding 10^{-6} mbar, and subsequently place the sample in a DI water bath for 24 hours. After lift-off, a significant amount of permalloy remains anchored to the sample (Figure 6-8 a). This anchoring may be due to improper alignment of the TPL structures or cross-linking of PAA. The Carboxylic Acid (COOH) functional group of PAA reacts with aqueous sodium hydroxide (NaOH) to produce water-soluble Sodium Polyacrylate, which may improve the dissolution of the cross-linked PAA [187]. We replace the DI water bath with aqueous NaOH (0.5 mol l^{-1}) and repeat the procedure on samples where the halo-like patterns are visible around the nanostructures (Figure 6-8 b). After a 24-hour DI water bath, some halos are still visible using optical microscopy (Figure 6-8 c). The halos are not present after a five-minute $NaOH_{aq}$ bath, although there is clear evidence of residue upon the substrate. A further concern is the separation required between structures and the impact on the lift-off procedure. We perform the final test using a set of rectangular nanoislands of varying aspect ratios with 10 μm separation (Figure 6-8 e) where no permalloy is visible near the cluster of islands. For all nine devices, permalloy is visible between the islands in only three cases. Once again, there is clear evidence of residue with a significant build-up between the islands. SEM images show the residue upon the nanoislands, indicating formation during the lift-off procedure. This residue is likely remnant NaOH from the lift-off procedure, and displacing the aqueous sodium hydroxide before displacing with IPA should prevent the deposition of NaOH.

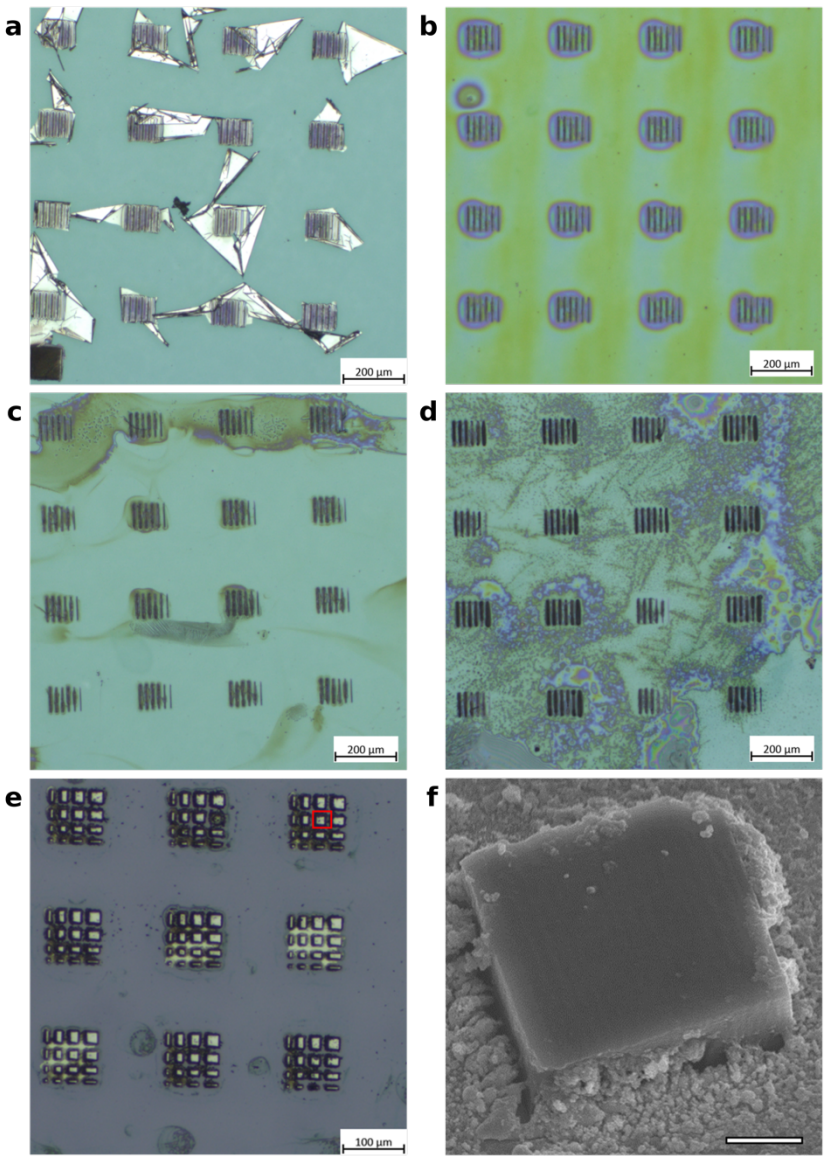

Figure 6-8 Lift-off tests using water and aqueous sodium hydroxide. (a) lift-off after a 24-hour DI water bath with significant permalloy remaining on the substrate. (b) optical micrograph of nanowires in PAA trenches before deposition, showing halo-like patterns around the structures. (c) halo-like structures are still visible after a 24-hour DI water bath. (d) no halo-like structures visible after five-minute $\mathbf{NaOH_{aq}}$ bath. (e) Array of nanoislands with varying aspect ratios after lift-off. Permalloy appears to have been removed in six of nine cases. The red square indicates the structure shown in SEM. (f) SEM of square nanoisland showing clear powdery residue on top of the structure, indicating deposition during lift-off.

A method to fabricate isolated magnetic nanowires using TPL, LOS deposition, and sacrificial layers is now established as follows:

1. Clean substrate (Glass or ITO coated glass) in a 20-minute ultrasonic acetone bath followed by a 20-minute ultrasonic IPA bath.
2. Spin-coat 5% (w/t) solution of PAA at 4000 rpm
3. Drop-cast immersion oil on the non-PAA side of the substrate
4. Ablate substrate projection of geometry upon the substrate
5. Drop-cast IPL780 upon the sample, write TPL geometry
6. 20-minute PGMEA bath, followed by a 20-minute IPA bath, dry with compressed air.
7. Evaporate permalloy using thermal evaporation
8. NaOH(aq, 0.5 mol l^{-1}) bath until permalloy has lifted off
9. Displace NaOH solution with DI water.
10. Displace DI water with IPA, dry sample using compressed air.

With these adjustments to the initially conceived technique, we produced a set of wires suspended 3μm above the substrate (Figure 6-9a). The optical micrograph shows a dark region around the wire on the substrate, yet the colour is inconsistent with permalloy. We suspect this may be damage to the ITO layer on the substrate from ablation or NaOH contamination from the lift-off procedure. EDX measurements should indicate the nature of this dark region. We measure the wire length at 80μm and a width of 440nm (Figure 6-9b). An easy axis hysteresis loop captured using MOKE magnetometry (Figure 6-9c) shows a coercive field of ~8 mT, and we capture a sigmoid curve along the hard axis (Figure

6-9d). Both MOKE loops were captured at an incident angle of 45° in s-polarization with an analyzer angle at 2° from extinction.

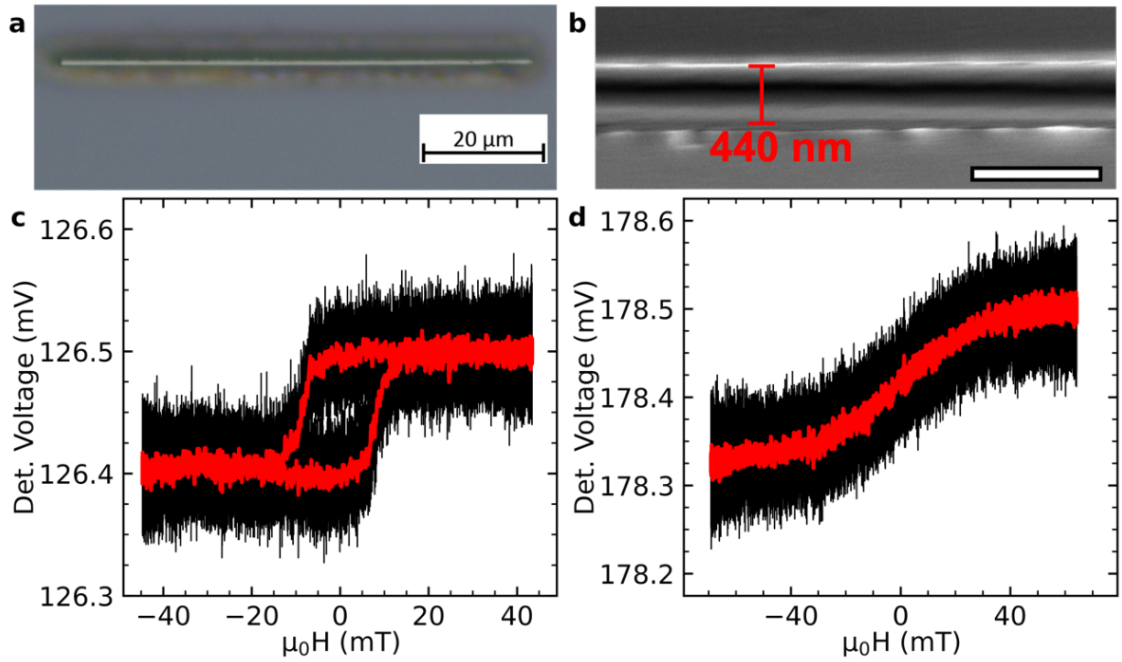

Figure 6-9 (a) optical micrograph of single wire after lift-off procedure. (b) the width measurement of wire was performed on top-down SEM of wire. Scale bar indicates 1 µm (c) Easy axis hysteresis loop with sharp transition at ~**8 mT**. (d) Hard axis hysteresis loop of wire.

A key challenge in MOKE magnetometry upon nanostructures is the signal to noise ratio (SNR). SNR is typically optimized by maximizing the incident laser power and careful alignment of the optics; one may also adjust the SNR by optimizing the analyzer angle, though it should be noted that in p-polarized light, the transverse effect may become more prominent. Polymer thermal conductivity is typically low, risking structural deformation at high laser power.

6.3. Fabricating simple isolated domain-wall conduits using a sacrificial layer

After establishing the suitability of the methods, a series of devices was created to explore a proof of concept for PAA sacrificial layers in the fabrication of complex 3D magnetic nanostructures such as 3D artificial spin-ice lattices and magnetic racetrack memory devices. We create 100μm long magnetic nanowires raised 2.5 μm above the substrate with varying nanowire widths. Since 300nm wide wires could be fabricated reliably, these form the basis of the single nanowire geometries with a schematic of the simplest case shown in Figure 6-10a. A 25 nm layer of permalloy was deposited using thermal evaporation.

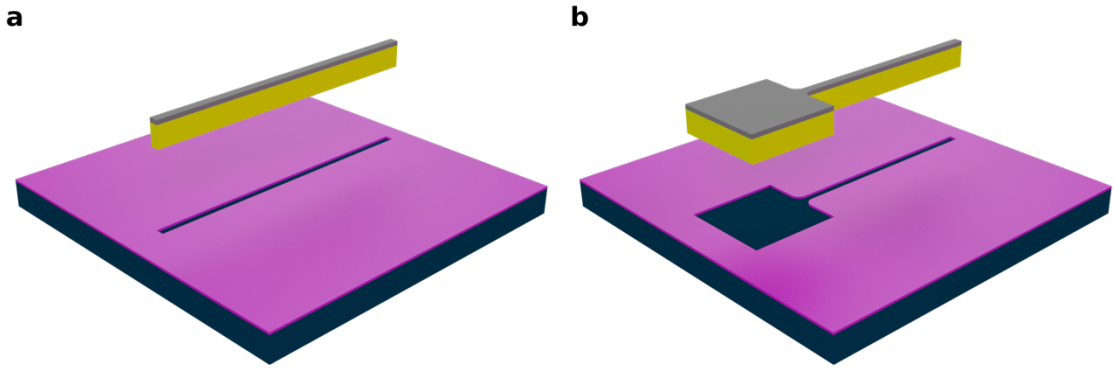

Figure 6-10 Schematics of devices fabricated in this section. In the schematic, the device is offset along z to show the ablation geometry upon the substrate. (a) single wire comprising a cuboidal scaffold upon which permalloy is deposited. (b) unperturbed wire with nucleation pad.

The domain wall nucleation field in high aspect ratio wires is likely too high for racetrack-like devices, and the symmetry means domain walls likely nucleate from both ends of the wire. Previous attempts used the injection of domain walls from the substrate, but we note that the unstructured film reduces the reproducibility of the nucleation, and the film has been removed in this case. Hence, well-established science from 2D nanowire

studies is utilised. A larger low aspect ratio geometric shape can be harnessed to reproducibly inject domain walls into the wire at low fields, well below the nucleation field of the lone wire. A 20μm × 20μm nucleation pad was added to the wire with a tapered region to form a smooth transition between pad and wire (Figure 6-10b). Before moving onto magnetometry, we next sought to demonstrate the success of the sacrificial layer approach via elemental mapping.

6.1. Validation of lift-off procedure

SEM imaging of magnetic nanostructures on polymer scaffolds is challenging; non-conducting polymer results in the magnetic coating being disconnected from the substrate to yield significant charging, resulting in artefacts and drift in the image. A thin layer of gold deposited at an angle to connect the wires to the substrate is typically sufficient to address charging. However, we can only deposit gold after the lift-off procedure, which masks the magnetic material and is therefore sub-optimal for EDX analysis. The alternative is to operate at low accelerating voltages to minimize charging and drift, sacrificing SNR. We measured the X-ray fluorescence spectra focusing on an arbitrary position on the nucleation pad (Figure 6-11, position i) and the substrate (Figure 6-11, position ii) at 10kV, with a repeat at 15kV at different positions (Figure 6-11, position iii & iv). In both cases, we can resolve both the K and L series emission lines of nickel and iron in measurements upon the nucleation pad and no detectable signal upon the substrate.

We still find some drift at 10kV, but this does not present an issue when measuring the spectra at individual points due to short exposure time. However, the drift is sufficient to impact the efficacy of elemental mapping. We minimize drift by imaging at 5kV, although

this comes at the cost of not measuring the K series emission lines. Fortunately, the point spectra in Figure 6 11 show sufficient signal at the lower energy L series emission lines.

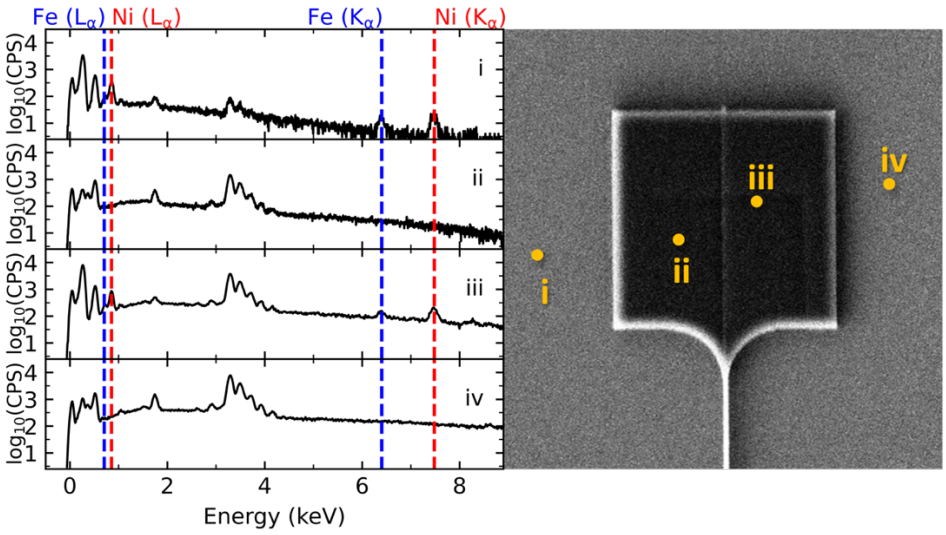

Figure 6-11 EDX emission spectra captured using a 10 kV beam current on the nucleation pad (i) and the substrate (ii) and captured using a 15kV beam current on the nucleation pad (iii) and the substrate (iv).

We may use the spectra to determine the permalloy composition and ensure the ratio of nickel to iron is sufficient to hold the assumption of negligible magnetocrystalline anisotropy. Controlling for the bremsstrahlung background in spectrum iii, a least-squares fitting of a function comprising two Gaussian peaks with equal width centred at 0.705 keV (iron) and 0.851 keV (nickel) allows the determination of the composition (Figure 6-12). After controlling for background signal, the measured peak sizes are (165.07 ± 26.49) cps and (675.13 ± 14.29) cps for iron and nickel, respectively. These measurements yield an iron fraction of (0.196 ± 0.025), consistent with $Ni_{81}Fe_{19}$.

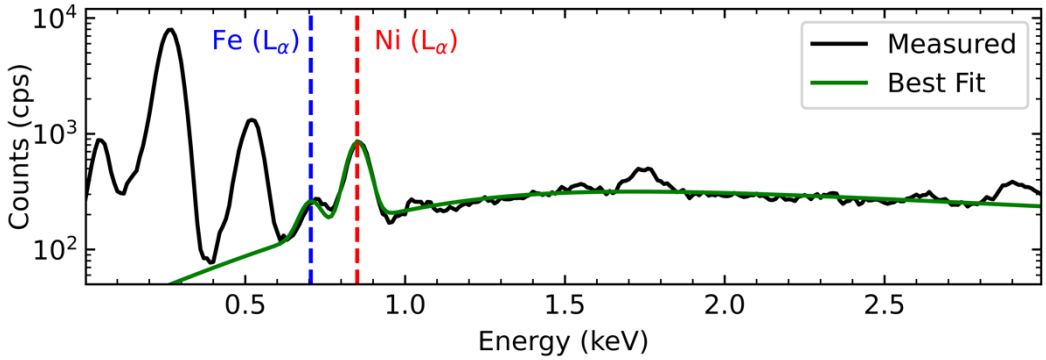

Figure 6-12 EDX emission spectrum measured on the nucleation pad with least squares fitting of nickel and iron $\mathbf{L_\alpha}$ lines after controlling for background.

To confirm the feasibility of using a 5kV beam voltage, we measure a line profile starting on the nucleation pad and moving onto the substrate (Figure 6-13). We see a sharp transition in the counts at the L_α (0.705 keV) emission line for iron (blue) and the L_α (0.851 keV) emission line for nickel (red) at the edge of the nucleation pad. Spectra taken on the nucleation pad (magenta) show clear peaks centred on the relevant emission lines, whereas spectra taken on the substrate (cyan) lack these peaks.

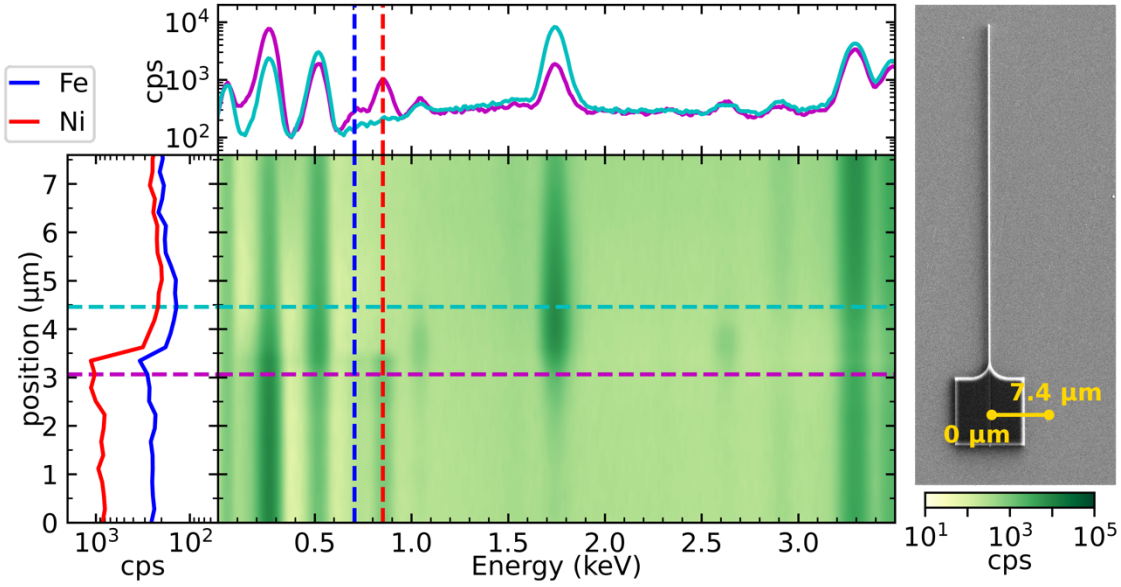

Figure 6-13 EDX line scan starting on the nucleation pad and ending on the substrate. With the approximate location indicated on the SEM inset. The top panel shows slices of the spectrum taken at positions indicated by the corresponding coloured line in the spectrogram. The left panel indicates counts at the $\boldsymbol{L_\alpha}$ emission lines for iron (blue) and nickel (red) as a function of position.

We perform further line scans perpendicular to the wire, showing Ni and Fe emission lines only on the wire, with none on the substrate detected within the noise floor of the detector. (Figure 6-14a). Finally, we perform a line scan parallel to the wire long-axis, moving off the end of the wire (Figure 6-14b). In all cases, there are clear L_α peaks for iron and nickel upon the device and no signal above the background upon the substrate.

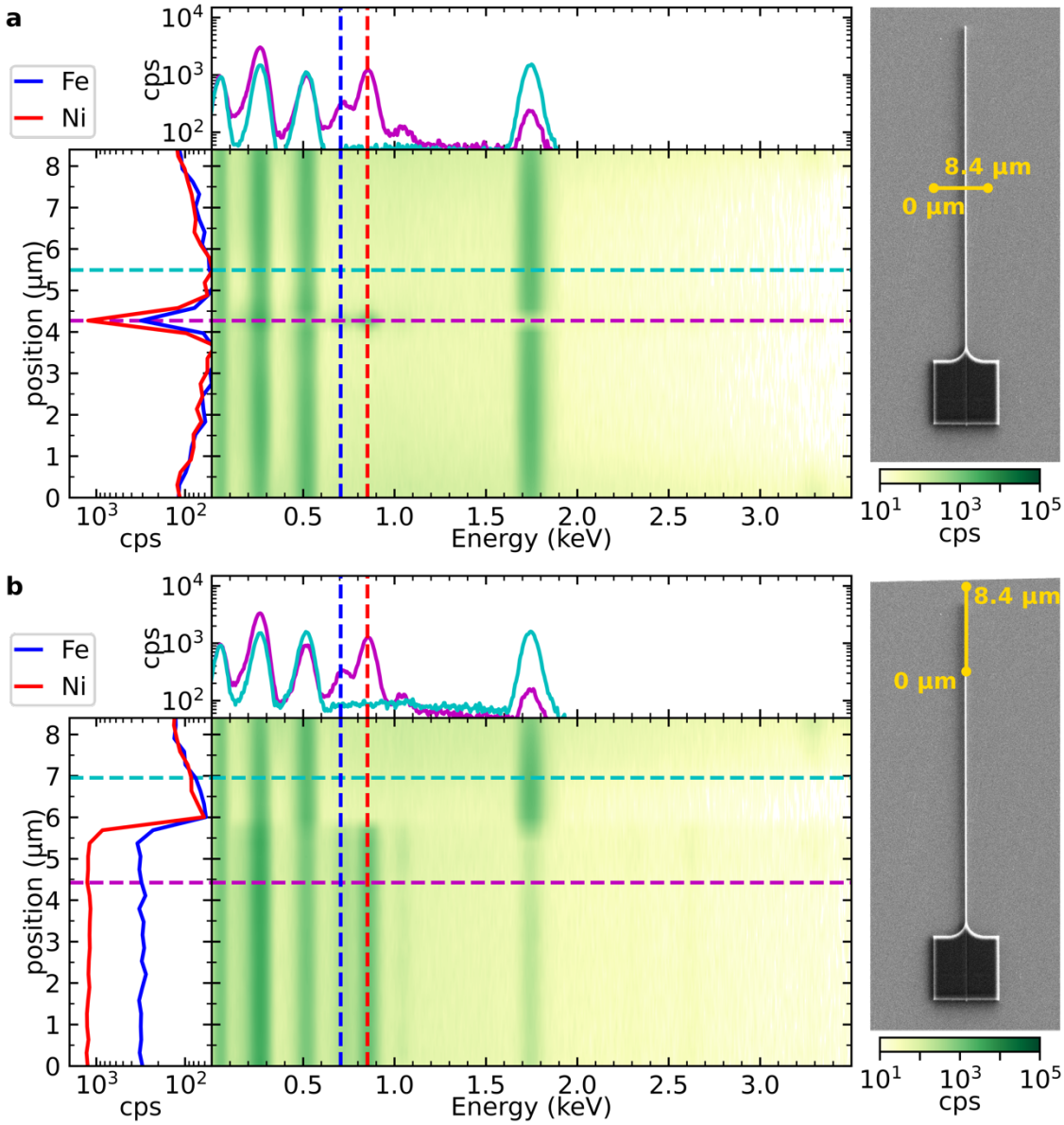

Figure 6-14 (a) EDX line scan starting on substrate moving across the wire perpendicular to the wire's long axis. (b) EDX line scan starts on the substrate, moves along the wire length, and ends on the wire. The SEM inset shows the positions of the scans. In both figures, the top panel shows slices of the spectrum taken at positions indicated by the corresponding coloured line in the spectrogram. The left panel indicates counts at the $\boldsymbol{L_\alpha}$ emission lines for iron (blue) and nickel (red) as a function of position.

The data consistently show other peaks at 0.277keV, 0.524 keV, and 1.739 keV corresponding to the K_α lines of carbon, oxygen, and silicon (respectively). The chemical composition of IPL-780 has been estimated at 3.0 wt% Hydrogen, 24.9 wt% oxygen, 0.8 wt% nitrogen, and 71.2 wt% carbon [188], giving rise to the peaks at these energies upon the structure. SEM systems are inherently subject to carbon contamination [189] such that carbon is detected on the substrate. The measured substrate is ITO covered glass, giving rise to the oxygen and silicon peaks on the substrate, where the latter is masked by the nanostructure.

These results indicate the complete removal of permalloy from the substrate. However, the view angle of the line scans is insufficient to determine the presence of permalloy upon the side walls of the structures. Elemental maps shown in Figure 6-15 were captured with a 45° tilt and reduced beam voltage to 5kV to minimise drift. A further reduction in drift was achieved by only measuring regions in the image selected with a free-form selection tool.

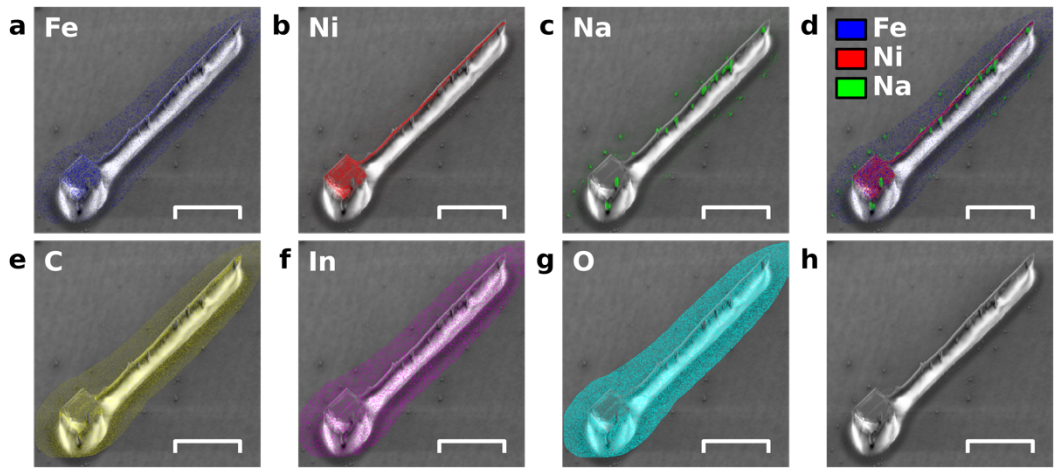

Figure 6-15 EDX Elemental maps showing deposition of (a) iron, (b) nickel, (c) sodium (d) composite of iron, nickel and sodium. (e) carbon, (f) indium, and (g) oxygen. (h) SEM of the mapped region. Scale bars indicate 20 μm.

At 5kV, only the L series lines of Fe and Ni are accessible; with inherently lower count rates and a low concentration, the elemental map of iron shows a faint signal above the noise floor on top of the structures (Figure 6-15a). With a fourfold increase in concentration, the nickel map clearly shows the material deposited on top of the structures with none present on the sides (Figure 6-15b). However, we observe gaps in the coating that match with bright spots on the sodium map (Figure 6-15c & d). As previously discussed, it is then likely that these deposits arise from the lift-off procedure, depositing on top of the NiFe layer. We note that sodium hydroxide is not known to affect the magnetic properties of the material.

6.2. Domain wall injection, propagation, and pinning

With confidence in the lift-off procedure, MOKE magnetometry experiments were performed upon wires of increasing complexity. Domain wall pinning is key to the function of a domain wall conduit; as such, additional wires with an out-of-plane protrusion were fabricated to introduce a pinning potential (Figure 6-16).

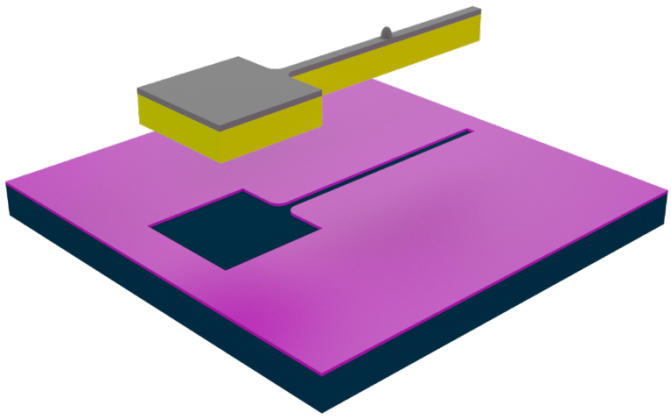

Figure 6-16 (a) Schematic of the nanowire with nucleation pad and ellipsoidal defect. The device in the schematic is offset in z to show ablation geometry.

Data from the simple wire geometry reveals a square loop with an abrupt transition indicative of domain wall motion occurring at 9.9 mT (Figure 6-17a) as one would expect from previous studies into high aspect ratio permalloy nanowires [190]. Positioning the focal spot upon the nucleation pad of the unperturbed wire yields a rounded loop with a coercivity of 0.56 mT (Figure 6-17b) and ~0.97 mT when the focal spot is upon the wire (Figure 6-17c). Introducing a nucleation pad reduces the switching field by an order of magnitude, thus demonstrating effective domain wall injection. The squareness of the loop at this position indicates that injection is highly repeatable.

The measurement upon the nucleation pad produced a rounded hysteresis loop with a sharp transition at 0.46 mT (Figure 6-17d), and an injection field at 1.63 mT was measured by positioning the focal spot between the nucleation pad and the perturbation in the centre of the wire (Figure 6-17e). Moving the focal spot beyond the perturbation yields a switching field of 3.00mT (Figure 6-17f), an approximate factor of 2 increase. Moving the laser spot slightly off the structure yields no detectable signal after 2000 repeats (Figure 6-17 g-h) indiscating an absence of magnetic material in these regions. The switching field measured beyond the defect is unlikely to be caused by domain wall nucleation on the free end of the wire, given the 9.9mT nucleation field measured on the free wire.

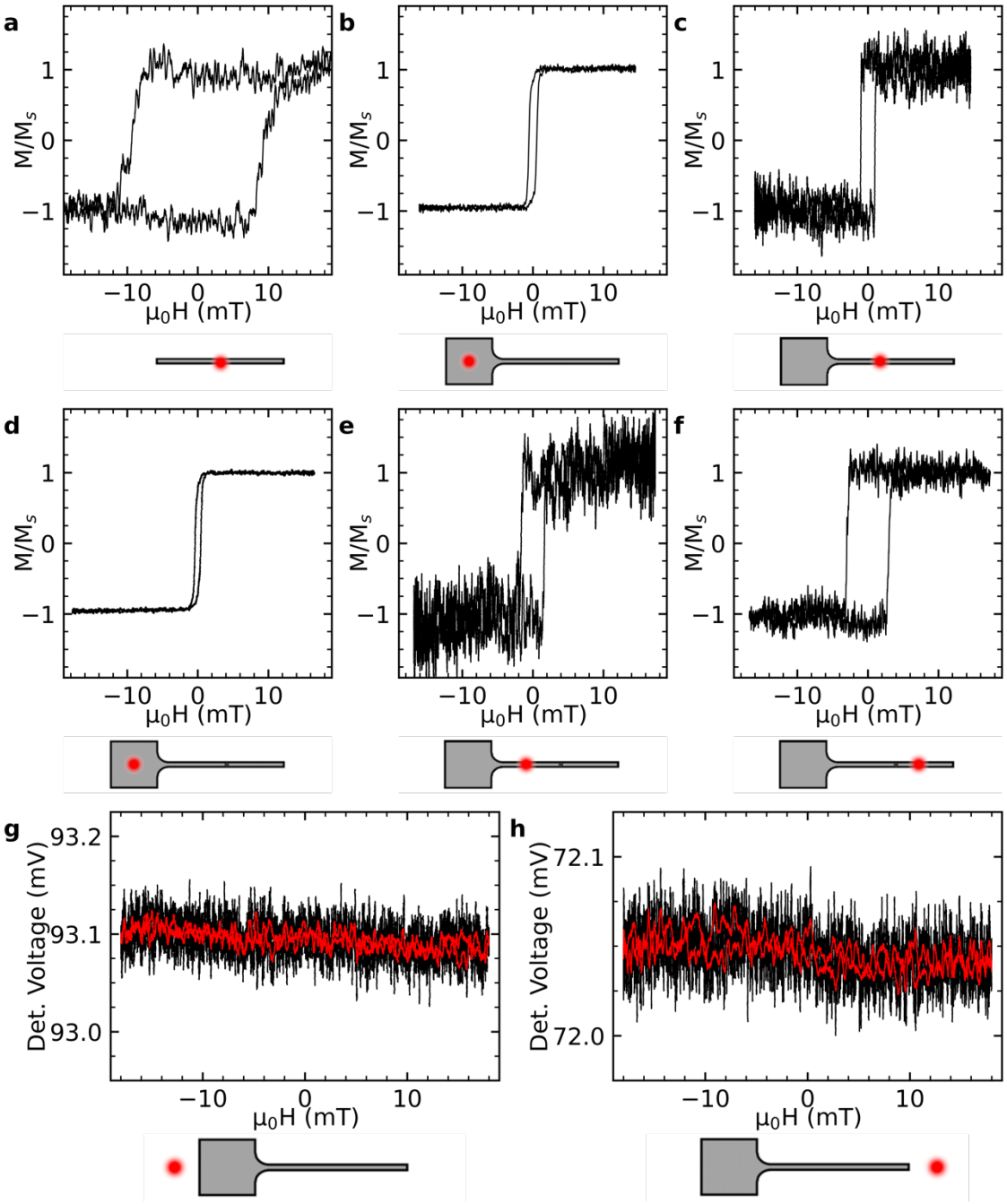

Figure 6-17 (a) MOKE measurement of hysteresis loop obtained from the simple nanowire. (b) Loop of complex wire nucleation pad. (c) Measured hysteresis loop of complex wire. (d) Measured hysteresis loop of complex wire with perturbation. Measured on the nucleation pad. (e) on the wire between the perturbation and the nucleation pad. (f) measured on the wire after the perturbation. (g&h) Measurements with focal spot off the structure.

These results show promise for the concepts such as magnetic racetrack memory devices where controlled domain wall injection and motion are required in 3D geometries to realize its promises. Although the MOKE data suggest that the 3D nanostructured defect

may be producing pinning, identification of the pinning mechanism requires a detailed nanoscale knowledge of how NiFe coats the defect geometry. Figure 6-18 shows that from some angles, the defect appears to have vertical sidewalls. This was difficult to confirm due to charging limiting the quality of images, and prolonged exposure to the electron beam led to the deformation of the defect. Such sidewalls may yield a discontinuity in the NiFe wire, which may also yield the measured magnetometry. In the near future, the research group will be optimizing such defects to ensure no vertical sidewalls. With this in mind, it was decided to carry out modelling, assuming the future target experimental geometry, in order to understand the pinning mechanism.

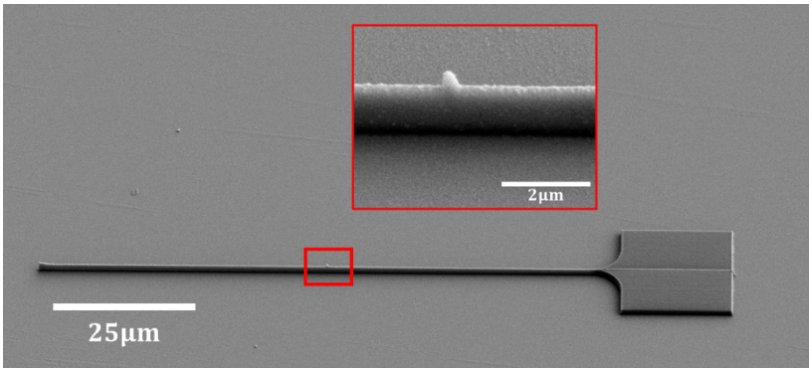

Figure 6-18 SEM of the nanowire with nucleation pad and ellipsoidal perturbation captured at **45**° tilt with high magnification image of perturbation in the inset showing near-vertical sidewalls on the perturbation.

Similar to the wire geometry definition in chapter 4, the simulation object is defined in terms of the written TPL scaffold with the top surface extruded along z according to the deposition thickness. The extrusion region then represents the magnetic material, and therefore the simulation object shown in Figure 6-19. The base scaffold cross-section is defined as a 300nm wide strip with rounded edges reflecting the ellipsoidal voxel shape of the TPL system. The scaffold cross-section is extruded to create a 4µm nanowire. At the perturbation site, we introduce a half ellipsoid with a lateral feature size of 250nm,

protruding 250nm from the surface. We use typical material parameters for Permalloy ($Ni_{81}Fe_{19}$) with $M_s = 0.86 \times 10^6\ A\,m^{-1}$ and an exchange stiffness of $13 \times 10^{-12}\ J\,m^{-1}$ yielding an exchange length of 5.29 nm. The simulation reflects only a small wire section and removes surface charges on the wire ends to simulate an infinitely long wire.

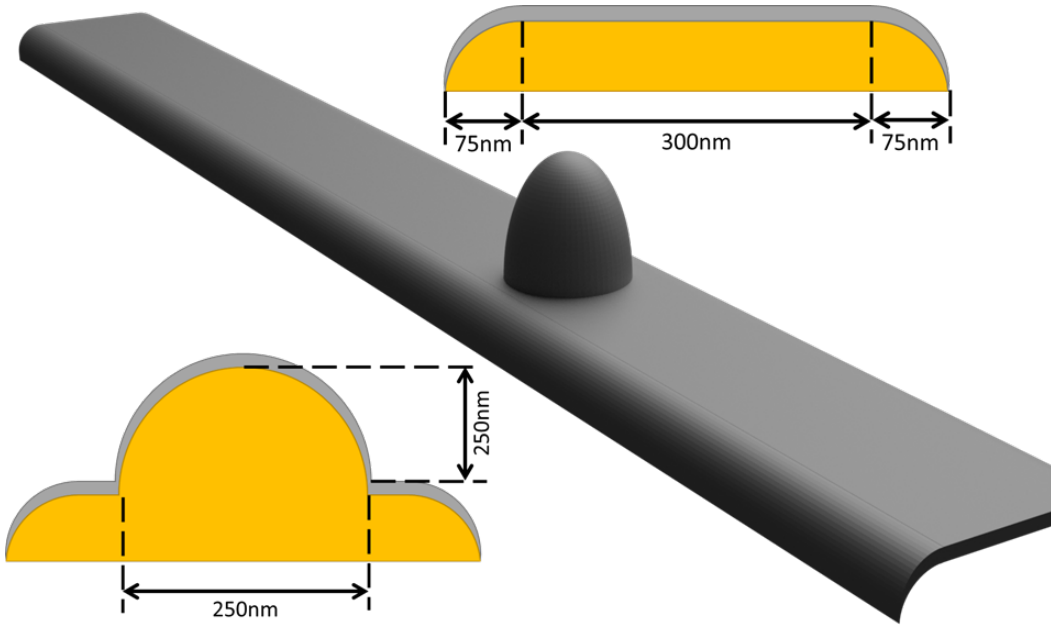

Figure 6-19 CAD rendering of simulation object with cross-sections.

Typically, finite element simulations are preferable for geometries where curvature is a factor, as unstructured grids can better approximate curved surfaces. However, the required simulation geometry results in unfeasible memory requirements and computation times. GPU acceleration could address the computational time, but the vRAM is limited in even the most advanced GPUs. Finite difference simulations employ structured grids with significantly smaller memory requirements. The simulations were performed using MuMax3 on a pair of Nvidia Tesla v100 GPUs with a combined 64GB vRAM enabling the geometry to be meshed at 3 nm; below the ~5.29 nm exchange length of permalloy and sufficient to approximate curved surfaces.

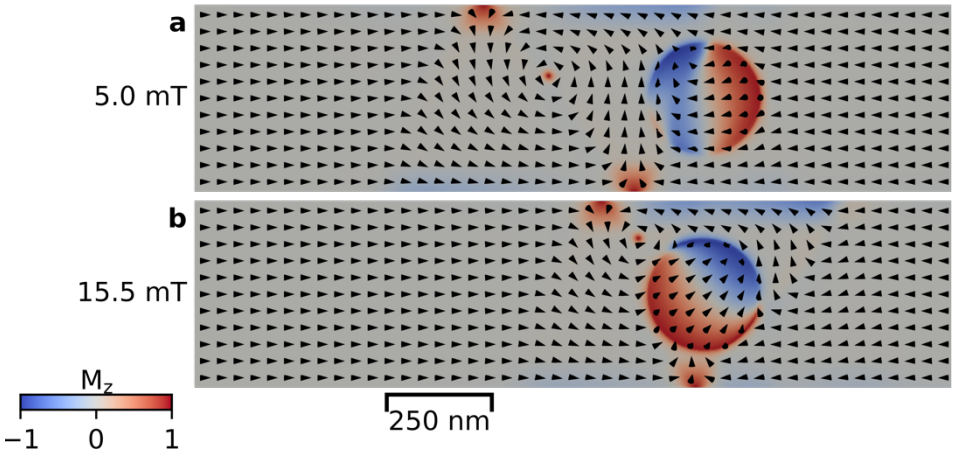

Figure 6-20 Converged states computed using finite difference micromagnetic simulations of the perturbed region of the nanowires. (a) a vortex domain wall meeting the perturbation after applying a 5mT external field. (b) magnetic texture at 15.5 mT, before depinning.

We relax a vortex domain wall with $+z$ polarity and anti-clockwise circulation at the start of the wire and apply a 5 mT field to push the vortex wall towards the perturbation (Figure 6-20a). With increasing field steps, the vortex core follows a path around the perturbation until 15.5 mT (Figure 6-20b), after which the domain wall depins.

We simulate domain wall depinning by taking the converged state at 15.5 mT (Figure 6-21a), setting the Gilbert damping constant to $\alpha = 0.01$ and performing a time evolution with an external field of 16 mT. At 0.3 ns, a strained texture forms on the edge of the perturbation opposite to the vortex core (Figure 6-21b), which resolves as the domain wall fragments through the formation of a vortex-antivortex pair at 0.45 ns (Figure 6-21c), the initial vortex core moves onto the perturbation at 0.65 ns (Figure 6-21d), and across the perturbation (Figure 6-21e) until 2.35 ns (Figure 6-21f). The vortex core leaves the perturbation at 2.60 ns (Figure 6-21g).

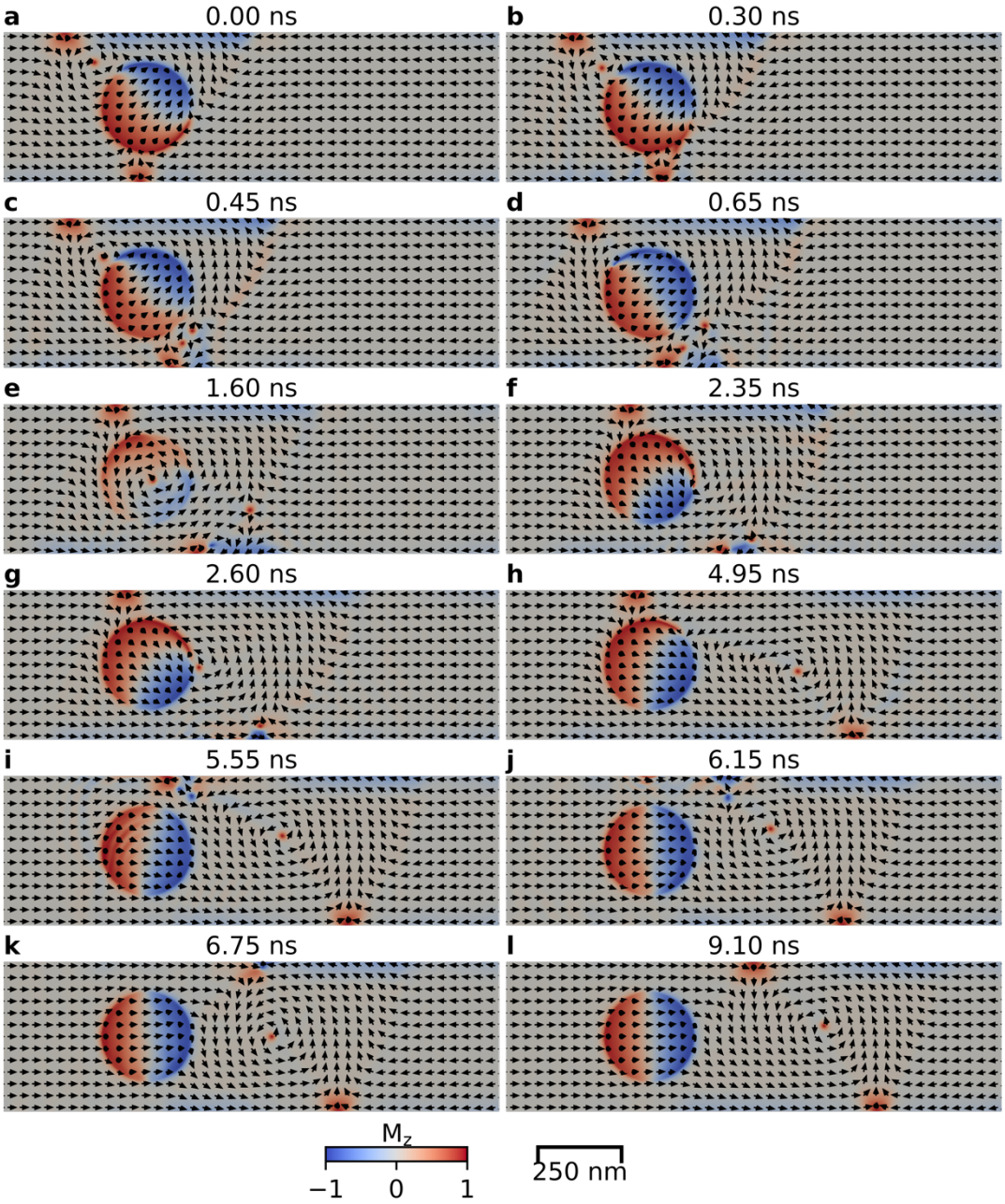

Figure 6-21 Snapshots of simulated domain wall depinning at an out-of-plane perturbation on a magnetic nanowire.

A surprising result is that the second vortex core and the half anti-vortex edge defect annihilate to leave a half-vortex edge defect. The fragmented domain wall then consists of a vortex-antivortex pair and a half-vortex-antivortex pair of edge defects. The upper edge defect remains pinned while the others move along the wire until 4.95ns (Figure 6-21h), when the antivortex core and the bottom half-vortex combine to yield a half-antivortex

edge defect and restore the typical configuration of a vortex wall. However, the upper edge defect remains between the perturbation and the edge until 5.55ns, where another instance of fragmentation occurs with the nucleation of a vortex-antivortex pair at the upper edge defect (Figure 6-21i). The new vortex core and the top half antivortex edge defect combine at 6.15 ns (Figure 6-21j), and the new half-vortex edge defect and the antivortex core move along the wire until the topological defects combine at 6.75ns (Figure 6-21k). At 9.1 ns (Figure 6-21l), the vortex domain wall structure is restored, and the domain wall depins.

6.3. Optical magnetometry on magnetic nanowire lattices fabricated using PAA sacrificial layers

After demonstrating the proof of principle, we apply the method to produce a 3D ASI geometry with a wire length of 1μm and permalloy deposition thickness of 25nm (Figure 6-22a). A key challenge in 3DASI systems is to separate switching occurring in different sublattices at different depths. The projection of the sublattices on the substrate is orthogonal, enabling MOKE magnetometry to study depth-dependent switching in the L1 and L2 sublattices. Three MOKE effects corresponding to different magnetization components must be considered. Firstly, the longitudinal component introduces a polarization rotation in the reflected light proportional to the magnetization component parallel to the projection of the incident wavevector upon the substrate. The transverse component is associated with a change in intensity of the reflected light proportional to the magnetization component perpendicular to the incident plane. And the polar component introduces a polarization rotation in reflected light proportional to the magnetization component parallel to the surface normal. We define our coordinate axes such that these components correspond to M_x, M_y, and M_z respectively. In our experimental geometry, the

incident wavevector is at 45 degrees to the substrate such that we can expect polar signal in addition to longitudinal and transverse components (Figure 6-22b). Longitudinal and polar components are associated with the rotation of the polarization. Sensitivity to these components may be suppressed by increasing the analyzer angle to 90°, whereas the transverse component can be completely suppressed by using s-polarized light. It then follows that the transverse component may be isolated using p-polarized light at large analyzer angles.

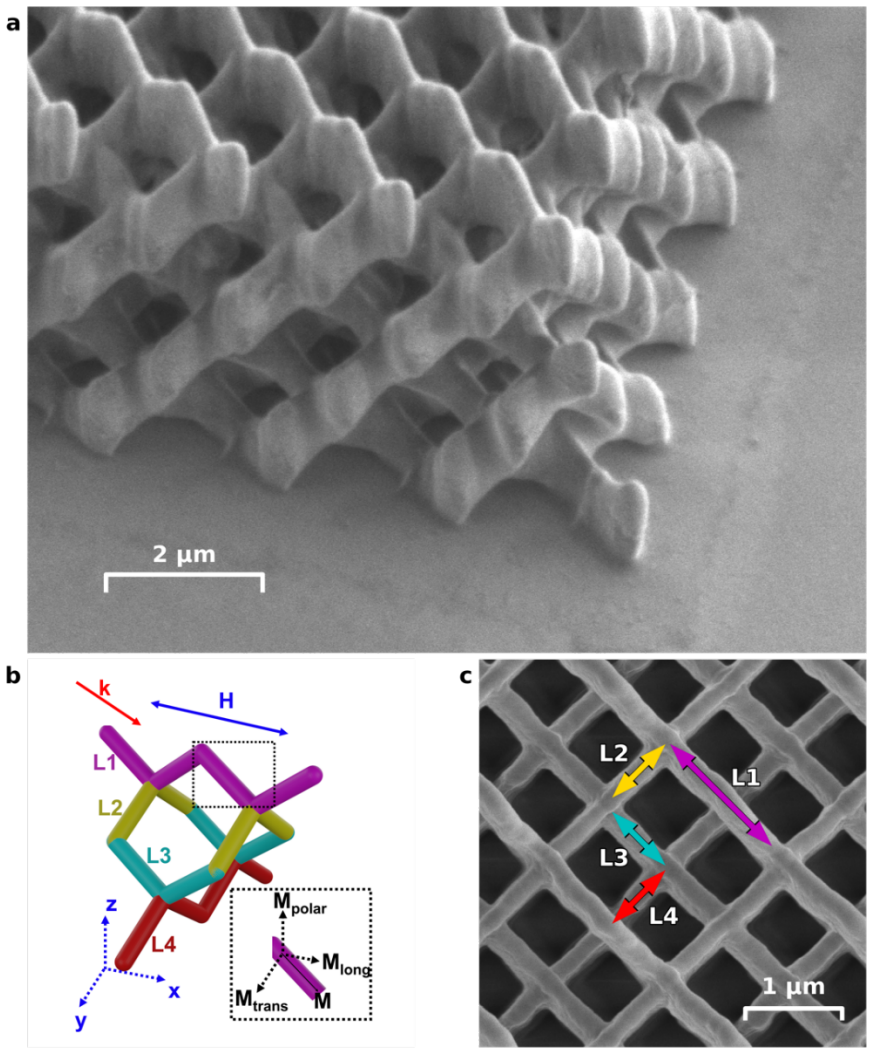

Figure 6-22 (a) SEM micrograph of 3DASI corner captured at 45° tilt. (b) Schematic of experimental MOKE geometry with 3ASI. A unit cell of 3DASI is shown, with different sub-lattices depicted. The laser with wavevector k makes an angle of 45 degrees with respect to the substrate and with projection along L1 as depicted. (c) top-down SEM of 3DASI with sublattices annotated.

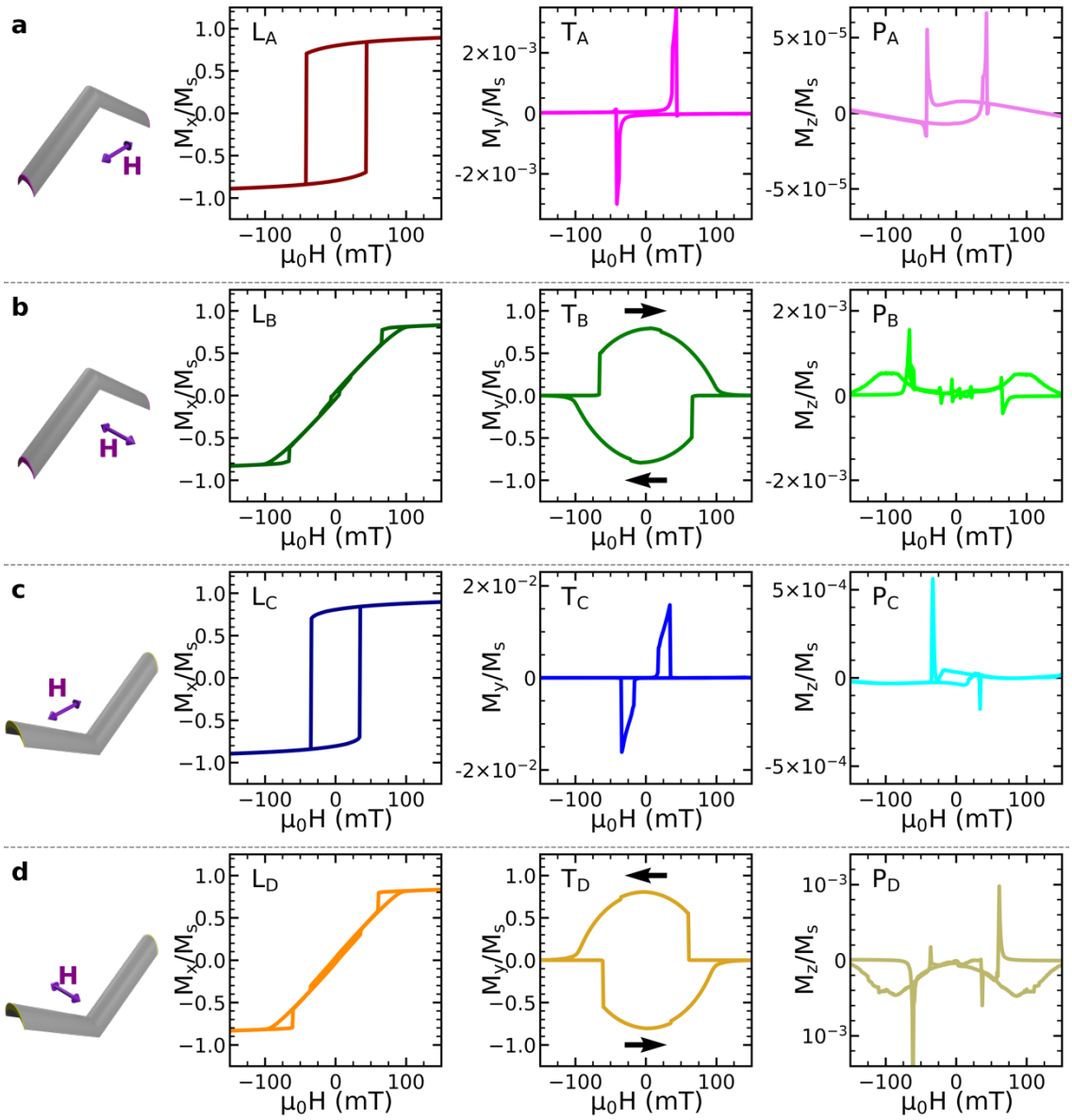

Figure 6-23 simulated hysteresis loops of the bipod geometries. Loops are labelled using the format $\mathbf{X_Y}$ where **X** denotes the longitudinal (L), Transverse (T), or polar (P) component. **Y** denotes (a) loop with fields applied along the lower bipod long axis projection, (b) hard axis loop of the lower bipod, (c) loop with fields applied to the upper bipod long axis projection, and (d) hard axis loop of the upper bipod. Black arrows on $\mathbf{T_B}$ and $\mathbf{T_D}$ indicate direction of the loop.

Chapter 5 demonstrates that magnetic reversal in the lattice may be modelled as a linear combination of reversals in bipod (coordination two) geometries, and MOKE is not equally sensitive to the different sublattices. As such, finite element simulations of bipod structures in the experimental field geometries are best suited to aid understanding of the features in the MOKE loops. We consider the lower bipod geometry found at the coordination two vertices with fields applied along the LASP (Figure 6-23a) and perpendicular to the LASP (Figure 6-23b), as well as the upper bipod geometry with fields applied parallel (Figure 6-23c) and perpendicular (Figure 6-23d) to the LASP. We label each loop as longitudinal (L), transverse (T), or polar (P) with subscripts A and B representing the field applied parallel and perpendicular to the lower bipod LASP of the substrate, respectively, and C and D representing the field applied parallel and perpendicular to the upper bipod LASP. The longitudinal loops are consistent with those seen in chapter 5, with coherent rotation from saturation to the coercive field at 43 mT for $L_A$and 34 mT for L_C. Before the switch, there are peaks in the transverse magnetization which appear to originate from the vertex area before the nucleation of a domain wall.

At remanence (Figure 6-24a), there is some slight canting towards the edges at the apex to avoid the sharp change in the direction of the surface. With increasing fields (Figure 6-24 b-d), the magnetization rotates towards the transverse direction until the reversal at ~43 mT.

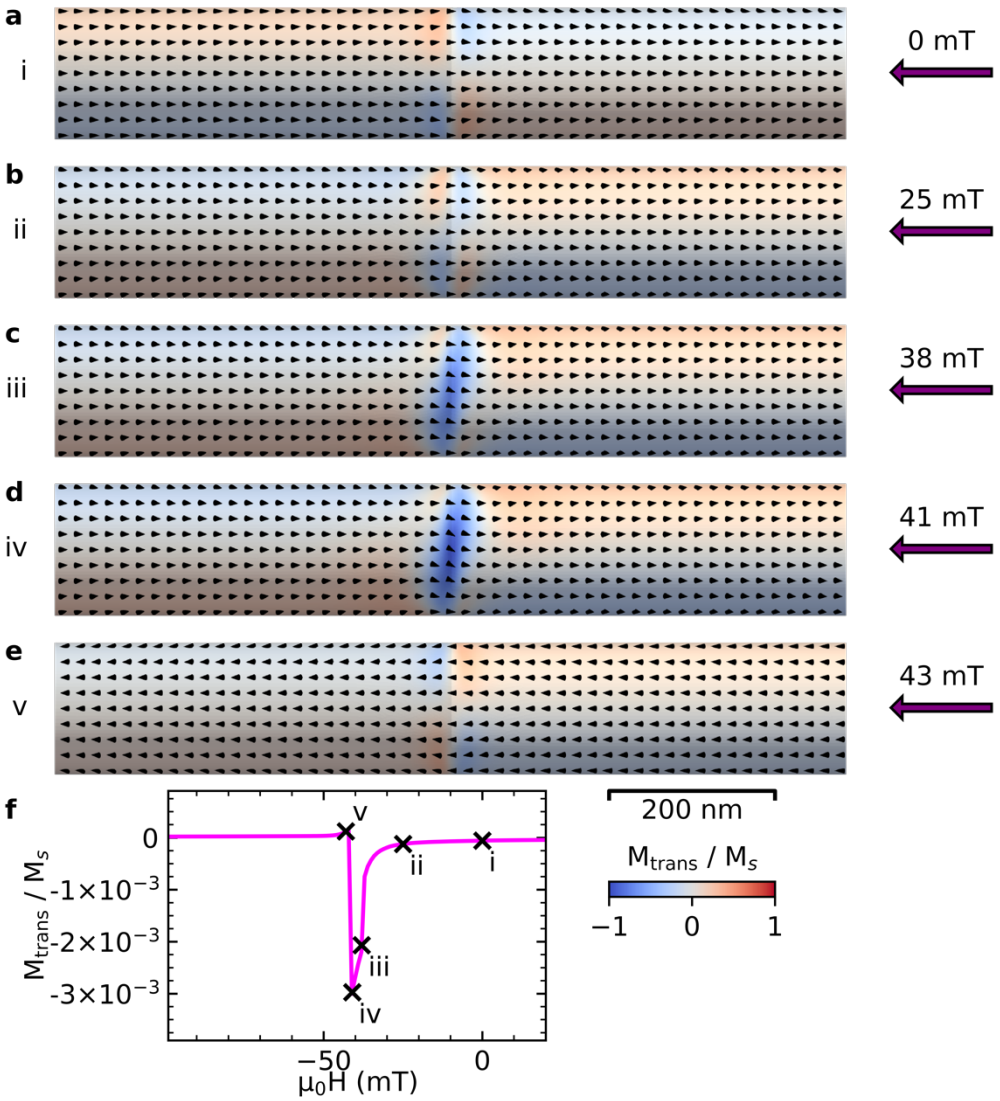

Figure 6-24 Transverse magnetization at the apex of lower bipod geometry with fields applied along the LASP. Contrast ranges from $-\mathbf{0.5M_s}$ to $\mathbf{0.5M_s}$ to enhance subtle features. (a-e) equilibrium states with external fields indicated and labelled i-v corresponding to annotations on (f). (f) The peak of the transverse hysteresis loops with the key states annotated.

The simulations of hysteresis loops with fields applied perpendicular to the LASP (T_B and T_D) show a sharp transition in the magnetization at 66mT and 60mT in T_B and T_D (respectively) which occur, somewhat counterintuitively, between saturation and remanence. Black arrows indicate the direction of the hysteresis loop, and Table 6-1 summarizes the energy terms in the lower bipod transition. The magnetization textures before and after this switch in the lower bipod geometry indicate that the sudden transition

is a result of competition between the demagnetizing energy and Zeeman energy terms. As a result, the magnetization follows the surface of the wire with negligible magnetization along the wire long axis at 66mT (Figure 6-25a).

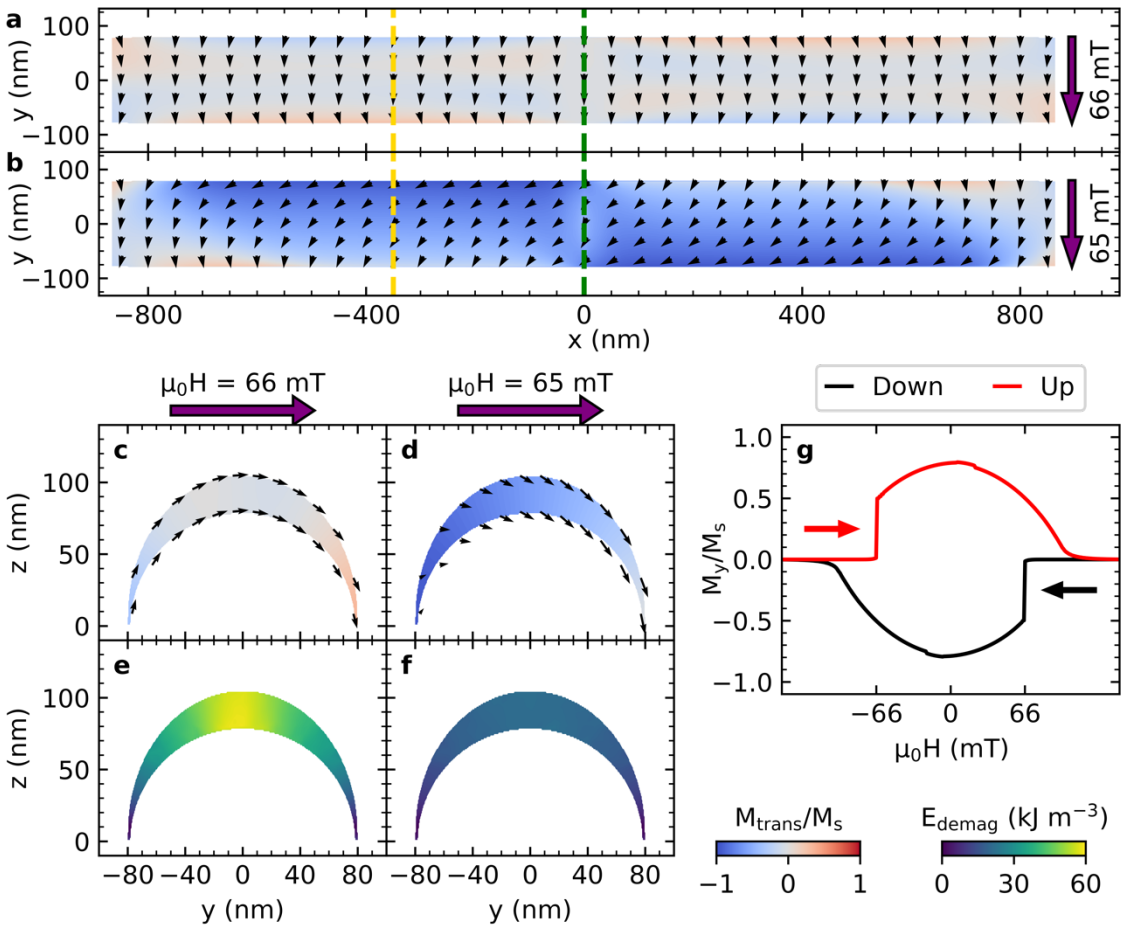

Figure 6-25 (a) Top-down view of the Magnetization texture of lower bipod geometry before transition at 66mT. (b) magnetization texture of lower bipod geometry after transition at 65mT. (c) cross-section of lower bipod taken at the yellow dashed line, showing surface magnetization before the switch at 66mT. (d) cross-section after the switch, at 65mT. Contrast is according to the transverse component of the magnetization (projection of long axis upon the substrate in this instance). (e) Demagnetization energy density associated with (c). (f) Demagnetization energy associated with (d). (g) Hysteresis loop $\mathbf{T_B}$ with up sweep and down sweep separated.

After the transition (Figure 6-25b), the spins have rotated towards the local long axis of the wire. A cross-section of the wire taken at the location indicated by the yellow dashed line (Figure 6-25 c&d) shows the longitudinal and polar components of the magnetization with contrast according to the transverse component. Before the transition, the

magnetization follows the contours of the curved surface; however, there is a high demagnetization energy density associated with this state (Figure 6-25e) as the external field and the curvature in the surface result in spin canting towards the surface normal. At 65 mT, this texture is energetically unfavourable, and moments rotate towards the local long axis to reduce demagnetization energy.

μ_0H (mT)	$\mathcal{E}_d$ (J m^{-3})	$\mathcal{E}_{exch}$(J m^{-3})	$\mathcal{E}_z$ (J m^{-3})	$\mathcal{E}_{tot}$(J m^{-3})
66	28.507×10^3	2.143×10^3	-44.096×10^3	-13.445×10^3
65	17.812×10^3	1.271×10^3	-34.020×10^3	-14.937×10^3
Change	-10.695×10^3	-0.872×10^3	10.076×10^3	-1.492×10^3

Table 6-1 Summary of energy terms in the transition seen in the $\mathbf{T_B}$ hysteresis loop.

The result appears counter-intuitive as the Zeeman energy term is proportional to $-\mathbf{M} \cdot \mathbf{H}_{ext}$, and one would typically associate a large sharp transition in a hysteresis loop with the minimization of Zeeman energy; not a significant increase in this term. Table 6-1 summarizes the energy density terms in this transition, indicating that the minimization of demagnetization and exchange energy terms result in a net decrease in energy.

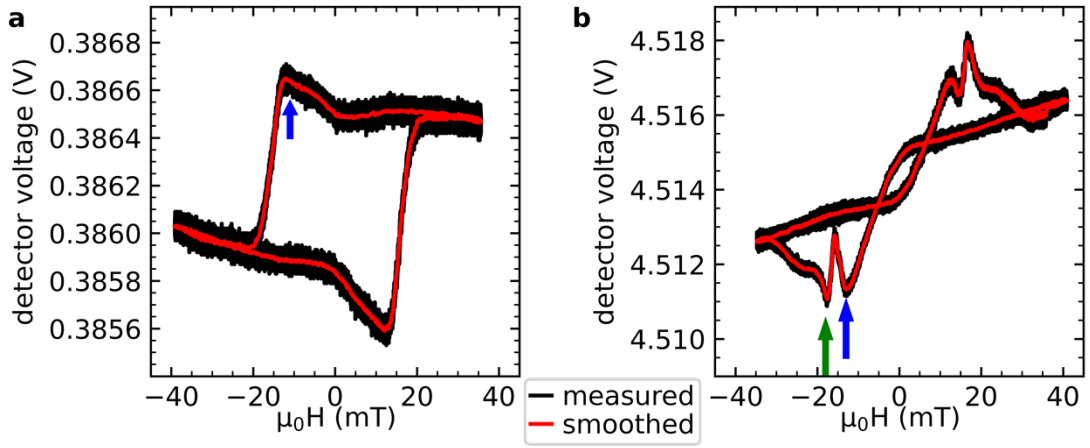

Figure 6-26 magnetic hysteresis loop of lattices with fields applied along the L1 sublattice substrate projection captured in s-polarization. (a) captured with analyser **2**° from extinction. (b) captured with analyzer **90**° from extinction.

A MOKE loop with applied field along the L1 sublattice projection upon the substrate was measured using s-polarized light with the analyzer angle at 2° from extinction and shows a sharp transition at $H_c \approx 15$ mT (Figure 6-26a), and a non-linear background likely due to coherent rotation in L2. A peak at ~13 mT (blue arrow) is indicative of a component other than longitudinal MOKE. s-polarized light suppresses the transverse component and opening the analyzer to 90° from extinction suppresses the longitudinal and polar components. It follows that s-polarized light with large analyzer angles should not yield any signal. However, measurements in this configuration still show a clear signal due to magnetization reversal (Figure 6-26b) with distinct peaks at ~13 mT (blue arrow) and ~18 mT (Green arrow). We attribute the presence of transverse MOKE when using s-polarized light to a slight imperfection in the alignment of the polarizer.

The introduction of a second detector measuring the intensity of the beam rejected at the analyzer allows the measurement of the features due to transverse MOKE in s-polarization should there be any. Detector 1 voltage primarily shows a longitudinal signal from L1 with a coercive field of 14mT and some rounding from rotation in L2 (Figure 6-27a). The peaks at 12 mT are no longer present in the transmitted signal, likely due to subtle differences in the experimental configuration. However, these peaks are still clearly present in the rejected signal (Figure 6-27b, magenta arrows). P-polarized light is sensitive to transverse MOKE, and at small analyzer angles, we measure a square loop with a coercive field at 14mT (Figure 6-27c), consistent with the s-polarization measurements. Our experimental geometry prohibits using a second detector in p-polarization as the beam is rejected vertically; instead of measuring the rejected signal, we repeat the measurement with an open analyzer to capture transverse MOKE. In this measurement (Figure 6-27d),

we find depressions in the signal at 13mT (magenta arrows) corresponding to the observed peaks in Figure 6-27b. However, there is a background that cannot be easily explained in terms of the simulation results in Figure 6-23. The transitions in T_B and T_D occur before remanence. In contrast, measurements show the rotation initiating at larger fields with a sharp transition at ~30mT after remanence (Green arrow), and the signal appears to change sign. Suspecting a slight offset in the sample rotation, we repeat the simulations with a 5° rotation in the simulation geometry (Figure 6-27e-h), and we recover the features seen in the measurements.

The ~13mT peaks and depressions in the measurements correspond to the peaks at 30 mT int T_A (Figure 6-27f) and the transition at 33mT (green arrow) corresponds to the 68mT transition in simulation T_B. The ratio between fields of the simulated transition and the peak is ~2.2, in close agreement with the ratio between the fields associated with the measured transition and the peak at ~2.3. There is a marked difference between the transverse signal captured using s and p-polarization; only transverse features from the L1 sublattice are visible in s-polarization, and features from both L1 and L2 are visible in p-polarization.

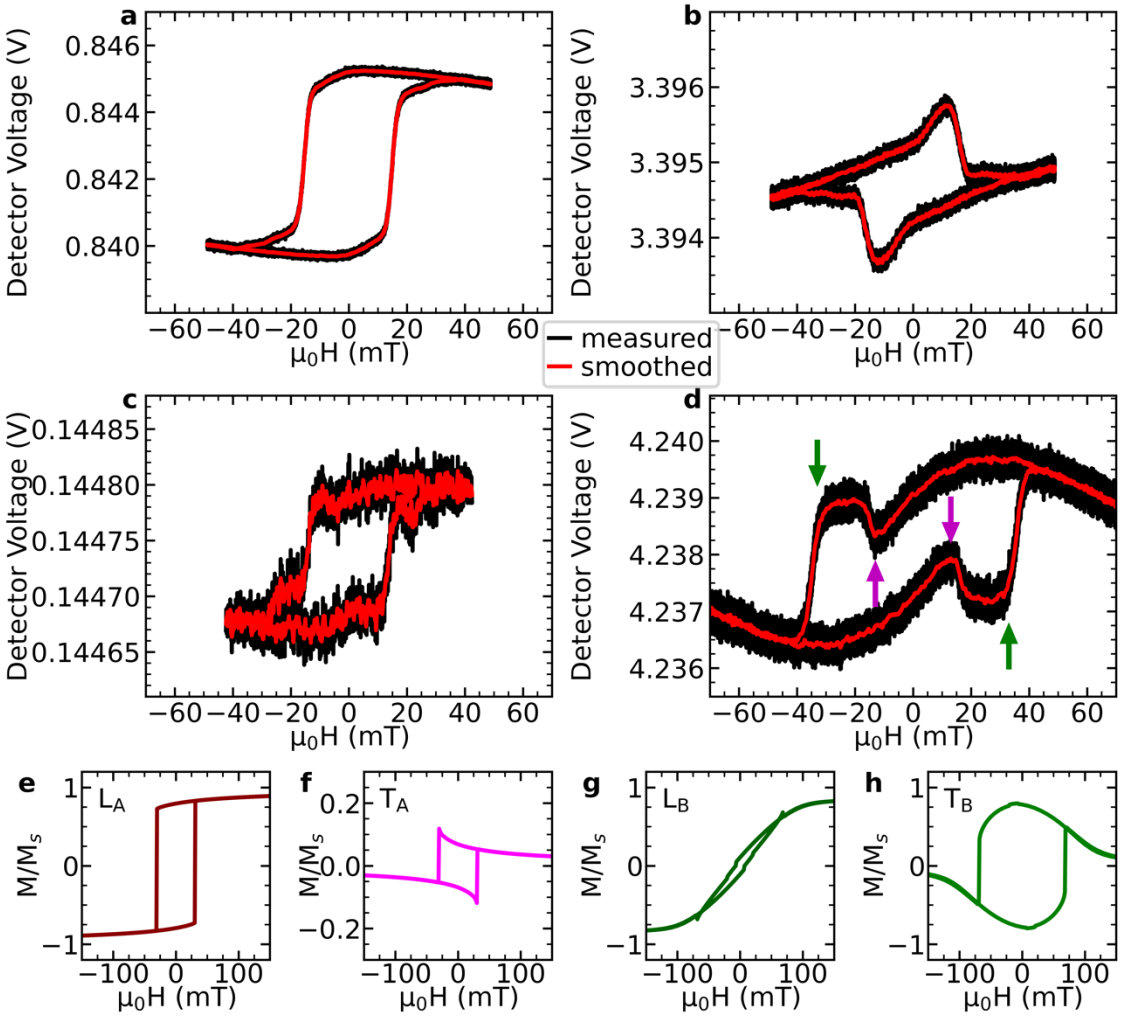

Figure 6-27 MOKE measurements performed on the lattice, with fields applied along the substrate projection of the L1 sublattice. (a) detector 1 voltage measuring the transmitted signal with an analyzer angle at **2**° in s-polarization. (b) detector 2 voltage measuring rejected signal associated with (a). (c) detector 1 voltage with a **2**° analyzer angle in p-polarization. (d) detector 2 voltage with a **90**° analyzer angle in p-polarization. (e-h) simulated hysteresis loops of the lower bipod geometry rotated 5 degrees about z. (e) longitudinal component of LASP loop, (f) transverse component of LASP loop. (g) longitudinal component of hard axis loop, (h) transverse component of hard axis loop.

Hysteresis loops measured using s-polarized light with varying sample orientations with respect to the applied field yield varying transverse signals in the second detector. Starting at the initial orientation with the L1 substrate projection aligned with the external field (Figure 6-28a), we find that the signal deviates by a fraction of $\sim 6.1 \times 10^{-4}$ from the mean. This decreases to $\sim 1.6 \times 10^{-4}$ when rotating the sample by 20° (Figure 6-28b). With

L1 at a 45° angle from the external field, the transverse signal becomes vanishingly small (Figure 6-28c), and increases to $\sim 2.2 \times 10^{-4}$ at 65° (Figure 6-28d), and 1.8×10^{-4} at 90° (Figure 6-28e). These measurements are summarized in Table 6-2

Angle	Deviation from mean
0°	6.1×10^{-4}
20°	1.6×10^{-4}
45°	5.1×10^{-5}
65°	2.3×10^{-4}
90°	1.8×10^{-4}

Table 6-2 Deviation from the signal mean of the rejected beam in MOKE hysteresis loops presented in Figure 6-28.

These results present an interesting challenge. Using s-polarized light, the transverse component should be entirely suppressed, yet the measurements are clearly sensitive to a transverse component. Upon first glance, it seems that the apparent transverse features arise due to slight misalignment in the polarizer such that there is some p-polarized component in the incident light. However, there is also a striking difference between the features captured using s and p polarized light at large analyzer angles.

Regardless of this challenge, these measurements show that we can combine MOKE magnetometry and micromagnetic simulations to obtain switching information from the individual sublattices through careful consideration of the experimental geometry.

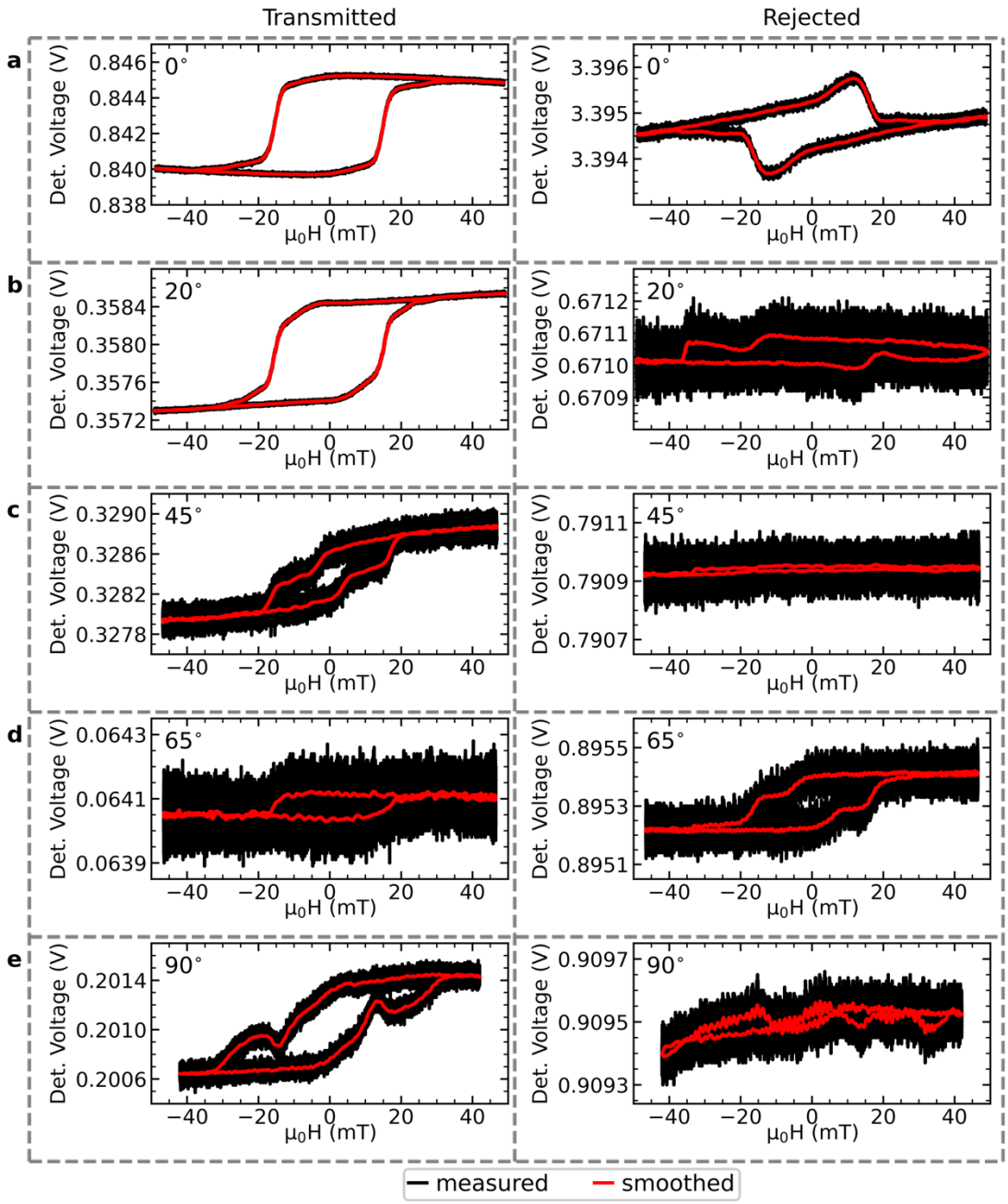

Figure 6-28 Transmitted and rejected MOKE signal in s-polarisation for varying sample rotations. (a) at **0°** (field applied along L1 sublattice substrate projection, also shown in Figure 6-27 and repeated here for convenience), (b) **20°** sample rotation, (c) **45°** rotation, (d) **65°** rotation, and (e) **90°** rotation (field applied along L2 sublattice substrate projection).

6.4. Summary

Two-photon lithography is a promising 3D magnetic nanostructure fabrication technique, as demonstrated in prior work [17, 18, 38, 44, 191]. One of the challenges that

have thus far limited the application is the inability to deposit functional materials selectively, resulting in significant substrate contamination. MOKE magnetometry upon magnetic nanowires above substrate film is primarily sensitive to switching in the film, rendering the technique ineffective. Careful design considerations may reduce dipolar interactions between the substrate film and the functional components of the nanostructures by increasing the separation between the two. However, these requirements create limitations in the feasibility of certain nanostructure designs.

The removal of substrate film with standard photolithography techniques is well-established with two-step photolithography employing sacrificial layers to remove substrate film. However, the available photoresists for two-step lithography are incompatible with the solvents used in two-photon lithography. This chapter identifies poly(acrylic acid) (PAA) as a suitable candidate for a sacrificial layer as it is unaffected by TPL solvents but swells in water. A thin layer of PAA can be spin-coated upon the substrate, and the PAA layer is ablated to expose the substrate such that desired nanostructures can be written into the exposed region. After development, the functional material may be cast upon the sample, and lifting off the PAA layer removes substrate film to leave the functional material only on the desired structures. EDX measurements show that the fabrication method effectively removes substrate film, achieving the desired objective. Without substrate contamination, we effectively characterized an isolated magnetic nanowire with a nucleation pad and demonstrated controlled domain wall injection in a magnetic nanowire suspended 3μm above the substrate. We measure square hysteresis loops using MOKE magnetometry and find a coercive field of ~9 mT on isolated magnetic nanowires without a nucleation pad. When moving to a wire with a 20 μm x 20 μm, we measure a

coercivity of ∼0.5 mT on the nucleation pad, and an injection field of ∼1 mT. These values are consistent with the extensive literature detailing investigations into similar systems [119, 151, 160, 192, 193] indicating that the lift-off procedure has no adverse effect on the magnetic properties of the material. This proof-of-principle can be easily extended to arbitrary 3D geometries not limited to magnetism; there exists an increasing interest in 3D nanostructuring among communities focusing on areas such as photonics and superconductivity where selective deposition is key to progress.

One challenge in magnetic racetrack memory devices is the ability to move domain walls through the wire controllably; we introduced an out-of-plane perturbation in the wire to create a domain wall pinning site. MOKE measurements indeed show three distinct switching fields across the wire with a coercivity of ∼0.5 mT on the nucleation pad, an injection field at ∼1.6 mT, and a depinning field at the perturbation of ∼3 mT. However, SEM images of the perturbation cast doubt on whether these results can indeed be attributed to the pinning mechanism indicated by FDM simulations; the sides of the perturbation are near vertical, and it is reasonable to suggest that this results in discontinuous coverage of permalloy. The observed pinning is then due to an effective hole in the wire.

Applying the technique to the fabrication of 3DASI allowed the control for substrate film and builds greater confidence in the origin of the features seen in hysteresis loops. We demonstrate that MOKE can be used in combination with micromagnetic simulations to obtain switching information from separate sublattices. This could be further refined in order to study thermal ordering in 3DASI systems.

7. Discussion, conclusions, and further work

3D nanomagnetism has been subject to keen interest within the magnetism community, and the first realisations of 3D magnetic nanostructures present significant opportunities in both fundamental and applied research [17, 41, 44, 57, 60, 194]. Chapter 5 uses micromagnetic simulations to explore the magnetic behaviour of the first 3-dimensional artificial spin ice lattice, which was fabricated using two-photon lithography and line-of-sight deposition [38]. From a phenomenological model, we determined that the magnetic nanowires fabricated with this method have crescent-shaped cross-sections with non-uniform thickness. Not only is the fabrication of a 3DASI novel, but wires with these properties also have thus far not been explored.

Key questions arise in determining the suitability of these lattices as a platform for studying 3D artificial spin ice. A core requirement for an artificial spin ice lattice is that each wire must be Ising-like, where the magnetisation may lie parallel or antiparallel along an easy axis with no intermediate states such that the magnetisation may be described using an Ising variable $\sigma = \pm 1$. Superficially, it appears that this condition is not met as hysteresis loops with fields along the hard axis reveal subtle but distinct plateaus that may be

interpreted as stable states. These plateaus arise from topological defects forming at the ends of the wires and show interesting behaviour as the magnetisation of these defects interacts with the complex geometry at the edges of the wire. Although interesting, we note that these simulation objects are highly contrived representations of the wires in the experimental system; the simulation objects represent isolated wires with sharp edges which are not present in the experimental system. Indeed, when the wires are combined into geometries more representative of the experimental lattices, the edge states disappear, and Ising-like behaviour is recovered.

The novel cross-section has several impacts on the behaviour and energetics of coordination-two and coordination-four vertices within the lattice. First is the size and shape of domain walls in these wires. With narrow edges, the magnetostatic energy associated with the edge defects of a vortex wall is reduced. One would expect this to yield a broadening of the domain wall to reduce exchange energy terms by minimising the angle between adjacent spins. However, the curved surface introduces out-of-plane magnetisation in the circulating region and magnetostatic energy is reduced by narrowing the wire. In calculations of the domain wall potential at the apex of a coordination-two vertex, we find that the perturbation to the domain wall structure results in a weak pinning potential with implications for magnetic behaviour at the surfaces of the lattices.

The second impact of the crescent-shaped cross-section is found in the energies of the coordination-four vertex types. A key restriction in 2-dimensional artificial spin-ice is degeneracy lifting among the ice-type vertices in a square ice [37]. Although beneficial in the study of the Rys-F and KDP vertex models [106], this limitation prevents the realisation of true deconfined magnetic monopole defects. The origin of this degeneracy lifting is a

broken symmetry in the ice-type vertices where type-I and type-II vertices are distinguishable; extending to a 3-dimensional system restores this symmetry. The energy calculations of coordination-four vertices in our system show that this symmetry is not restored due to the cross-section of our wires. Although smaller than previously reported in 2D systems [97], the degeneracy lifting remains. We also find additional degeneracy lifting among the type-III vertices which has not been reported in 2D systems. The cross-section of the wires results in a distinction between the 'upper' and 'lower' wires in a coordination-four vertex, where an alignment of the upper wire magnetisation is preferred. This gives rise to the observed degeneracy-lifting among the ice-type vertices and the type-III vertices.

There is one more striking result in the energy calculations showing that the energy of a 2-in or a 2-out excitation yielding a $Q = \pm 2$ charge upon the coordination two vertices is a factor of ≈ 3 higher than the energy associated with a $Q = \pm 2$ charge (type-III state) upon the coordination four vertex. The energies associated with the vertex types are determined by the magnetisation textures at the vertex, the versatility of TPL enables the vertex geometry to be perturbed such that these energies may be tuned. This approach has already been established in 2D systems to select energies described by either the KDP or Rys-F models [106], and could be explored in our systems to realise these in three dimensions or to recover degeneracy. Another approach, which presents a greater challenge from a design perspective, is to create a disconnected system where the magnetisation texture at the vertex is no longer a factor.

The computational requirements of finite-element modelling are intensive, and the calculations presented in this work are at the limits of current computational capacity. As

such, we used the micromagnetic simulations' results to inform the Monte-Carlo simulation parameters to capture the full lattice's behaviour. We demonstrate this by modelling the charge propagation experiment outlined in section 5.3.3 and outlined in [39]. With the validity established, there are additional implications to consider:

1. A magnetic charge forming upon a coordination-two vertex is highly energetic
2. Magnetic charges at coordination-two vertices are weakly pinned.
3. The cross-section of the wire favours alignment of the upper wires in a coordination-four vertex – favouring large magnetic domains upon the L1 sublattice.

Monte Carlo simulations accounting for the energetics yield an effective potential of the magnetic monopole defects at $\mu^* = 1.03$, close to half the Madelung constant $M_c/2 = 0.819$ of diamond lattices. When $2\mu^* \approx M_c$, one may expect the formation of a highly correlated charge-ordered system, or charge crystal, yet to be realised in a 3D artificial spin-ice system. This presents a clear future direction for exploring parameters such as wire length, width, and thickness to realise such a state.

The reduction of feature size achieved with TPL [63-65] enables the fabrication of nanowire lattices with blocking temperatures close to, or below room temperatures. 2D and 2.5D thermally active ASI has been studied recently [195, 196], but is yet to be extended to 3DASI. Studying such a system will be challenging with the techniques shown in this thesis and will rely on modern synchrotron techniques such as scanning transmission x-ray microscopy. Here, the presence of magnetic material upon the substrate becomes particularly challenging as the substrate signal dominates in measurements. Further challenges arise as magnetostatic interactions between the substrate and the functional

components may affect the system's behaviour. The lattices described in chapter 5 are designed such that there is sufficient separation between the substrate and the functional components of the structure by including redundant layers that are shadowed by the top unit cell during deposition. Although these additional layers reduce the magnetostatic interactions, x-ray absorption by these layers severely impacts the feasibility of such techniques.

Removing the substrate film is a key step to advancing research into 3D magnetic nanostructures using two-photon lithography; in addition to enabling a wider range of measurement techniques for 3D artificial spin-ice lattices, selective deposition enables the investigation of isolated magnetic nanowires using optical magnetometry. Chapter 6 describes the development of a novel fabrication method incorporating a sacrificial layer compatible with the TPL process. The use of sacrificial layers is already a well-established and ubiquitous approach to achieving selective deposition; however, the materials are incompatible with the TPL development process. Using laser ablation, water-soluble poly(acrylic acid) can be removed from target regions to expose the substrate unto which the desired nanostructure may be anchored. A key advantage to this approach is that ablation is achieved by using the same system as the TPL step; the sample is mounted onto the sample holder after spin-coating a PAA layer, and drop-casting photoresist onto the sample after ablation does not require the sample to be removed from the holder.

The implementation of sacrificial layers in TPL nanostructuring is absent in the literature. Although using sacrificial stencil masks has been explored [66], this approach would be prohibitively difficult for 3D nanostructures. In this work, we show that laser ablation may be used to selectively remove the PAA layer to expose the substrate providing

anchor points for the TPL writing stage. To establish the feasibility of our approach for magnetism, we fabricated well-understood permalloy nanowires of (length: 80 μm, width: 300 nm, and thickness 25nm) and characterised these using EDX and MOKE magnetometry.

EDX measurements clearly show the success of the lift-off procedure. EDX spectra indicate that the deposited permalloy has the expected composition ($Ni_{81}Fe_{19}$) within error, and we measure no permalloy upon the substrate near the wire. Elemental maps captured at 45-degree tilt show no permalloy deposited upon the sides of the scaffolds.

Hysteresis loops of an isolated magnetic nanowire reveal a square loop indicative of a single transition via domain wall motion, we measured a coercive field of 9.9 mT consistent with values reported elsewhere [190]. MOKE magnetometry with the laser spot at several different locations on the substrate near the wire shows no detectable signal indicating magnetic material. We introduce a 20 μm x 20 μm nucleation pad to the wire and measure the nucleation pad coercivity at 0.56 mT consistent with thin film permalloy deposited using thermal evaporation [197], and a reversal in the wire at 0.97 mT. Finally, we introduce an out-of-plane defect at the centre of the wire and we measure a nucleation field of 0.46 mT, and an injection field of 1.63 mT. The differences in the nucleation and injection fields are likely due to subtle variations at the joint between the nucleation pad and the wire. We measure a depinning field of 3.00 mT demonstrating the ability to control domain wall position.

Micromagnetic simulations of the pinning mechanism reveal a complex reversal mechanism where transient topological defects after the perturbation are required to enable the vortex domain wall core to move down the wire. However, SEM images of the perturbation create uncertainty as to whether the observed pinning is due to the processes

seen in the simulations; the sides of the perturbation in the physical system appear near vertical, suggesting the observed pinning may be due to simple discontinuities in the wire.

Uncertainty regarding the specific pinning mechanism notwithstanding, we have demonstrated the feasibility of using PAA as a sacrificial layer in 3D magnetic nanostructuring with two-photon lithography. This work opens opportunities to explore the impact of out-of-plane perturbations on domain wall pinning potentials and the fabrication of 3D domain wall conduits such as 3D magnetic racetrack memory devices.

We applied the sacrificial layer technique to produce a complex magnetic nanowire lattice similar to the subject of chapter 5 and remove spurious signals due to substrate film. Initial optical magnetometry measurements revealed an additional challenge in performing MOKE measurements of 3D magnetic nanostructures: the topography of the sample results in mixing of the transverse, longitudinal, and polar MOKE modes leading to numerous features in hysteresis loops. Using micromagnetic simulations, we were able to identify the source of various features observed in the measurements and gain insight into depth-dependent magnetic switching in the lattice.

In closing, the work presented in this thesis provides insight into the first experimentally realised 3D artificial spin-ice lattices and builds a foundational part of future research in these types of systems. The new fabrication methods presented in chapter 6 enable further investigation into 3DASI using a variety of techniques previously inaccessible due to substrate film, and open new avenues for exploring 3D magnetic domain wall conduits.

8. References

[1] R. Wood, "Future hard disk drive systems," *Journal of Magnetism and Magnetic Materials,* vol. 321, no. 6, pp. 555-561, 2009/03/01/ 2009, doi: https://doi.org/10.1016/j.jmmm.2008.07.027.

[2] H. J. Richter, "Density limits imposed by the microstructure of magnetic recording media," *Journal of Magnetism and Magnetic Materials,* vol. 321, no. 6, pp. 467-476, 2009/03/01/ 2009, doi: https://doi.org/10.1016/j.jmmm.2008.04.161.

[3] S. Sankar, M. Shaw, and K. Vaid, "Impact of temperature on hard disk drive reliability in large datacenters," in *2011 IEEE/IFIP 41st International Conference on Dependable Systems & Networks (DSN)*, 27-30 June 2011 2011, pp. 530-537, doi: 10.1109/DSN.2011.5958265.

[4] M. Dayarathna, Y. Wen, and R. Fan, "Data Center Energy Consumption Modeling: A Survey," *IEEE Communications Surveys & Tutorials,* vol. 18, no. 1, pp. 732-794, 2016, doi: 10.1109/COMST.2015.2481183.

[5] A. S. G. Andrae and T. Edler, "On Global Electricity Usage of Communication Technology: Trends to 2030," *Challenges,* vol. 6, no. 1, 2015, doi: 10.3390/challe6010117.

[6] S. Parkin, M. Hayashi, and L. Thomas, "Magnetic Domain-Wall Racetrack Memory," *Science,* vol. 320, no. 5873, pp. 190-194, 2008/04/11 2008, doi: 10.1126/science.1145799.

[7] N. L. Schryer and L. R. Walker, "The motion of 180° domain walls in uniform dc magnetic fields," *Journal of Applied Physics,* vol. 45, no. 12, pp. 5406-5421, 1974/12/01 1974, doi: 10.1063/1.1663252.

[8] W. Döring, "Über die Trägheit der Wände zwischen Weißschen Bezirken," vol. 3, no. 7, pp. 373-379, 1948, doi: doi:10.1515/zna-1948-0701.

[9] A. Mougin, M. Cormier, J. P. Adam, P. J. Metaxas, and J. Ferré, "Domain wall mobility, stability and Walker breakdown in magnetic nanowires," *Europhysics Letters (EPL),* vol. 78, no. 5, p. 57007, 2007/05/31 2007, doi: 10.1209/0295-5075/78/57007.

[10] M. Yan, A. Kákay, S. Gliga, and R. Hertel, "Beating the Walker Limit with Massless Domain Walls in Cylindrical Nanowires," *Physical Review Letters,*

vol. 104, no. 5, p. 057201, 02/01/ 2010, doi: 10.1103/PhysRevLett.104.057201.

[11] M. Yan, C. Andreas, A. Kákay, F. García-Sánchez, and R. Hertel, "Fast domain wall dynamics in magnetic nanotubes: Suppression of Walker breakdown and Cherenkov-like spin wave emission," *Applied Physics Letters,* vol. 99, no. 12, p. 122505, 2011/09/19 2011, doi: 10.1063/1.3643037.

[12] J. Askey, M. Hunt, W. Langbein, and S. Ladak, "Asymmetric dual Bloch point domain walls in cylindrical magnetic nanowires," *APL Materials,* vol. 10, no. 7, p. 071105, 2022/07/01 2022, doi: 10.1063/5.0089291.

[13] C. Bran *et al.*, "Direct observation of transverse and vortex metastable magnetic domains in cylindrical nanowires," *Physical Review B,* vol. 96, no. 12, p. 125415, 09/11/ 2017, doi: 10.1103/PhysRevB.96.125415.

[14] E. M. Palmero, C. Bran, R. P. del Real, and M. Vázquez, "Vortex domain wall propagation in periodically modulated diameter FeCoCu nanowire as determined by the magneto-optical Kerr effect," *Nanotechnology,* vol. 26, no. 46, p. 461001, 2015/10/26 2015, doi: 10.1088/0957-4484/26/46/461001.

[15] J. García *et al.*, "Template-assisted Co–Ni alloys and multisegmented nanowires with tuned magnetic anisotropy," *physica status solidi (a),* https://doi.org/10.1002/pssa.201300731 vol. 211, no. 5, pp. 1041-1047, 2014/05/01 2014, doi: https://doi.org/10.1002/pssa.201300731.

[16] F. Abreu Araujo and L. Piraux, "Spin-transfer-torque driven vortex dynamics in electrodeposited nanowire spin-valves," *Spin,* vol. 7, no. 1, p. 1740007, 2017, doi: 10.1142/S2010324717400070.

[17] G. Williams *et al.*, "Two-photon lithography for 3D magnetic nanostructure fabrication," *Nano Research,* vol. 11, no. 2, pp. 845-854, 2018/02/01 2018, doi: 10.1007/s12274-017-1694-0.

[18] J. Askey, M. O. Hunt, W. Langbein, and S. Ladak, "Use of Two-Photon Lithography with a Negative Resist and Processing to Realise Cylindrical Magnetic Nanowires," *Nanomaterials,* vol. 10, no. 3, 2020, doi: 10.3390/nano10030429.

[19] D. Atkinson, D. S. Eastwood, and L. K. Bogart, "Controlling domain wall pinning in planar nanowires by selecting domain wall type and its application in a memory concept," *Applied Physics Letters,* vol. 92, no. 2, p. 022510, 2008/01/14 2008, doi: 10.1063/1.2832771.

[20] L. K. Bogart, D. S. Eastwood, and D. Atkinson, "The effect of geometrical confinement and chirality on domain wall pinning behavior in planar nanowires," *Journal of Applied Physics,* vol. 104, no. 3, p. 033904, 2008/08/01 2008, doi: 10.1063/1.2961313.

[21] L. K. Bogart, D. Atkinson, K. O'Shea, D. McGrouther, and S. McVitie, "Dependence of domain wall pinning potential landscapes on domain wall chirality and pinning site geometry in planar nanowires," *Physical Review B,* vol. 79, no. 5, p. 054414, 02/11/ 2009, doi: 10.1103/PhysRevB.79.054414.

[22] M. Hayashi, L. Thomas, R. Moriya, C. Rettner, and S. P. Parkin Stuart, "Current-Controlled Magnetic Domain-Wall Nanowire Shift Register," *Science,* vol. 320, no. 5873, pp. 209-211, 2008/04/11 2008, doi: 10.1126/science.1154587.

[23] S. Parkin and S.-H. Yang, "Memory on the racetrack," *Nature Nanotechnology,* vol. 10, no. 3, pp. 195-198, 2015/03/01 2015, doi: 10.1038/nnano.2015.41.

[24] E. R. Lewis *et al.*, "Magnetic domain wall pinning by a curved conduit," *Applied Physics Letters,* vol. 95, no. 15, p. 152505, 2009/10/12 2009, doi: 10.1063/1.3246154.

[25] K. V. Yershov, V. P. Kravchuk, D. D. Sheka, and Y. Gaididei, "Curvature-induced domain wall pinning," *Physical Review B,* vol. 92, no. 10, p. 104412, 09/14/ 2015, doi: 10.1103/PhysRevB.92.104412.

[26] K. Gu *et al.*, "Three-dimensional racetrack memory devices designed from freestanding magnetic heterostructures," *Nature Nanotechnology,* 2022/09/22 2022, doi: 10.1038/s41565-022-01213-1.

[27] I. Polenciuc *et al.*, "Domain wall pinning for racetrack memory using exchange bias," *Applied Physics Letters,* vol. 105, no. 16, p. 162406, 2014/10/20 2014, doi: 10.1063/1.4899134.

[28] C. Bran, J. A. Fernandez-Roldan, R. P. del Real, A. Asenjo, O. Chubykalo-Fesenko, and M. Vazquez, "Magnetic Configurations in Modulated Cylindrical Nanowires," *Nanomaterials*, vol. 11, no. 3, doi: 10.3390/nano11030600.

[29] Ó. Iglesias-Freire *et al.*, "Spin configuration in isolated FeCoCu nanowires modulated in diameter," *Nanotechnology,* vol. 26, no. 39, p. 395702, 2015/09/11 2015, doi: 10.1088/0957-4484/26/39/395702.

[30] L. O'Brien *et al.*, "Near-Field Interaction between Domain Walls in Adjacent Permalloy Nanowires," *Physical Review Letters,* vol. 103, no. 7, p. 077206, 08/14/ 2009, doi: 10.1103/PhysRevLett.103.077206.

[31] L. O'Brien *et al.*, "Tunable Remote Pinning of Domain Walls in Magnetic Nanowires," *Physical Review Letters,* vol. 106, no. 8, p. 087204, 02/24/ 2011, doi: 10.1103/PhysRevLett.106.087204.

[32] T. J. Hayward *et al.*, "Pinning induced by inter-domain wall interactions in planar magnetic nanowires," *Applied Physics Letters,* vol. 96, no. 5, p. 052502, 2010/02/01 2010, doi: 10.1063/1.3275752.

[33] L. Pauling, "The Structure and Entropy of Ice and of Other Crystals with Some Randomness of Atomic Arrangement," *Journal of the American Chemical Society,* vol. 57, no. 12, pp. 2680-2684, 1935/12/01 1935, doi: 10.1021/ja01315a102.

[34] D. U. Ferreiro, E. A. Komives, and P. G. Wolynes, "Frustration in biomolecules," (in eng), *Q Rev Biophys,* vol. 47, no. 4, pp. 285-363, 2014, doi: 10.1017/S0033583514000092.

[35] L. Pustil'nik, "Solar flare phenomena as phase transition caused by frustration of current percolation," *Astrophysics and Space Science,* vol. 264, no. 1, pp. 171-182, 1998.

[36] M. J. Harris, S. T. Bramwell, D. F. McMorrow, T. Zeiske, and K. W. Godfrey, "Geometrical Frustration in the Ferromagnetic Pyrochlore Ho2Ti2O7," *Physical Review Letters,* vol. 79, no. 13, pp. 2554-2557, 09/29/ 1997, doi: 10.1103/PhysRevLett.79.2554.

[37] R. F. Wang *et al.*, "Artificial 'spin ice' in a geometrically frustrated lattice of nanoscale ferromagnetic islands," *Nature,* vol. 439, no. 7074, pp. 303-306, 2006/01/01 2006, doi: 10.1038/nature04447.

[38] A. May, M. Hunt, A. Van Den Berg, A. Hejazi, and S. Ladak, "Realisation of a frustrated 3D magnetic nanowire lattice," *Communications Physics,* vol. 2, no. 1, p. 13, 2019/02/01 2019, doi: 10.1038/s42005-018-0104-6.

[39] A. May, M. Saccone, A. van den Berg, J. Askey, M. Hunt, and S. Ladak, "Magnetic charge propagation upon a 3D artificial spin-ice," *Nature Communications,* vol. 12, no. 1, p. 3217, 2021/05/28 2021, doi: 10.1038/s41467-021-23480-7.

[40] M. Huth, F. Porrati, and O. V. Dobrovolskiy, "Focused electron beam induced deposition meets materials science," *Microelectronic Engineering,* vol. 185-186, pp. 9-28, 2018/01/05/ 2018, doi: https://doi.org/10.1016/j.mee.2017.10.012.

[41] D. Sanz-Hernández *et al.*, "Fabrication of Scaffold-Based 3D Magnetic Nanowires for Domain Wall Applications," *Nanomaterials,* vol. 8, no. 7, 2018, doi: 10.3390/nano8070483.

[42] I. Utke, P. Hoffmann, and J. Melngailis, "Gas-assisted focused electron beam and ion beam processing and fabrication," *Journal of Vacuum Science & Technology B: Microelectronics and Nanometer Structures Processing, Measurement, and Phenomena,* vol. 26, no. 4, pp. 1197-1276, 2008/07/01 2008, doi: 10.1116/1.2955728.

[43] W. F. van Dorp and C. W. Hagen, "A critical literature review of focused electron beam induced deposition," *Journal of Applied Physics,* vol. 104, no. 8, p. 081301, 2008/10/15 2008, doi: 10.1063/1.2977587.

[44] M. Hunt *et al.*, "Harnessing Multi-Photon Absorption to Produce Three-Dimensional Magnetic Structures at the Nanoscale," *Materials,* vol. 13, no. 3, 2020, doi: 10.3390/ma13030761.

[45] W. F. van Dorp, B. van Someren, C. W. Hagen, P. Kruit, and P. A. Crozier, "Approaching the Resolution Limit of Nanometer-Scale Electron Beam-Induced Deposition," *Nano Letters,* vol. 5, no. 7, pp. 1303-1307, 2005/07/01 2005, doi: 10.1021/nl050522i.

[46] O. V. Dobrovolskiy *et al.*, "Complex-Shaped 3D Nanoarchitectures for Magnetism and Superconductivity," in *Curvilinear Micromagnetism: From Fundamentals to Applications*, D. Makarov and D. D. Sheka Eds. Cham: Springer International Publishing, 2022, pp. 215-268.

[47] M. K. I. Al Mamoori *et al.*, "Magnetic Characterization of Direct-Write Free-Form Building Blocks for Artificial Magnetic 3D Lattices," *Materials*, vol. 11, no. 2, doi: 10.3390/ma11020289.

[48] L. Keller *et al.*, "Direct-write of free-form building blocks for artificial magnetic 3D lattices," *Scientific Reports,* vol. 8, no. 1, p. 6160, 2018/04/18 2018, doi: 10.1038/s41598-018-24431-x.

[49] R. Córdoba, D. S. Han, and B. Koopmans, "Manipulating the switching in modulated iron nanowires grown by focused electron beam induced deposition," *Microelectronic Engineering,* vol. 153, pp. 60-65, 2016/03/05/ 2016, doi: https://doi.org/10.1016/j.mee.2016.01.032.

[50] R. Lavrijsen *et al.*, "Fe:O:C grown by focused-electron-beam-induced deposition: magnetic and electric properties," *Nanotechnology,* vol. 22, no. 2, p. 025302, 2010/12/07 2011, doi: 10.1088/0957-4484/22/2/025302.

[51] L. Serrano-Ramón *et al.*, "Ultrasmall Functional Ferromagnetic Nanostructures Grown by Focused Electron-Beam-Induced Deposition," *ACS Nano,* vol. 5, no. 10, pp. 7781-7787, 2011/10/25 2011, doi: 10.1021/nn201517r.

[52] R. Córdoba, J. Sesé, J. M. De Teresa, and M. R. Ibarra, "High-purity cobalt nanostructures grown by focused-electron-beam-induced deposition at low current," *Microelectronic Engineering,* vol. 87, no. 5, pp. 1550-1553, 2010/05/01/ 2010, doi: https://doi.org/10.1016/j.mee.2009.11.027.

[53] J. Pablo-Navarro, C. Magén, and J. M. de Teresa, "Purified and Crystalline Three-Dimensional Electron-Beam-Induced Deposits: The Successful Case of Cobalt for High-Performance Magnetic Nanowires," *ACS Applied Nano Materials,* vol. 1, no. 1, pp. 38-46, 2018/01/26 2018, doi: 10.1021/acsanm.7b00016.

[54] R. Córdoba *et al.*, "Functional nickel-based deposits synthesized by focused beam induced processing," *Nanotechnology,* vol. 27, no. 6, p. 065303, 2016/01/13 2016, doi: 10.1088/0957-4484/27/6/065303.

[55] A. Perentes, G. Sinicco, G. Boero, B. Dwir, and P. Hoffmann, "Focused electron beam induced deposition of nickel," *Journal of Vacuum Science & Technology B: Microelectronics and Nanometer Structures Processing, Measurement, and Phenomena,* vol. 25, no. 6, pp. 2228-2232, 2007/11/01 2007, doi: 10.1116/1.2794071.

[56] D. Sanz-Hernández, R. F. Hamans, J.-W. Liao, A. Welbourne, R. Lavrijsen, and A. Fernández-Pacheco, "Fabrication, Detection, and Operation of a Three-Dimensional Nanomagnetic Conduit," *ACS Nano,* vol. 11, no. 11, pp. 11066-11073, 2017/11/28 2017, doi: 10.1021/acsnano.7b05105.

[57] J. Hinum-Wagner, D. Kuhness, G. Kothleitner, R. Winkler, and H. Plank, "FEBID 3D-Nanoprinting at Low Substrate Temperatures: Pushing the Speed While Keeping the Quality," *Nanomaterials*, vol. 11, no. 6, doi: 10.3390/nano11061527.

[58] M. Luitz *et al.*, "High Resolution Patterning of an Organic–Inorganic Photoresin for the Fabrication of Platinum Microstructures," *Advanced Materials,* https://doi.org/10.1002/adma.202101992 vol. 33, no. 37, p. 2101992, 2021/09/01 2021, doi: https://doi.org/10.1002/adma.202101992.

[59] J. T. Fourkas, "Chapter 1.3 - Fundamentals of Two-Photon Fabrication," in *Three-Dimensional Microfabrication Using Two-photon Polymerization*, T. Baldacchini Ed. Oxford: William Andrew Publishing, 2016, pp. 45-61.

[60] C. Donnelly *et al.*, "Element-Specific X-Ray Phase Tomography of 3D Structures at the Nanoscale," *Physical Review Letters,* vol. 114, no. 11, p. 115501, 03/16/ 2015, doi: 10.1103/PhysRevLett.114.115501.

[61] P. Pip, C. Donnelly, M. Döbeli, C. Gunderson, L. J. Heyderman, and L. Philippe, "Electroless Deposition of Ni–Fe Alloys on Scaffolds for 3D Nanomagnetism," *Small,* https://doi.org/10.1002/smll.202004099 vol. 16, no. 44, p. 2004099, 2020/11/01 2020, doi: https://doi.org/10.1002/smll.202004099.

[62] P. Pip *et al.*, "X-ray imaging of the magnetic configuration of a three-dimensional artificial spin ice building block," *APL Materials,* vol. 10, no. 10, p. 101101, 2022/10/01 2022, doi: 10.1063/5.0101797.

[63] G. Seniutinas, A. Weber, C. Padeste, I. Sakellari, M. Farsari, and C. David, "Beyond 100 nm resolution in 3D laser lithography — Post processing solutions," *Microelectronic Engineering,* vol. 191, pp. 25-31, 2018/05/05/ 2018, doi: https://doi.org/10.1016/j.mee.2018.01.018.

[64] P. Mueller, M. Thiel, and M. Wegener, "3D direct laser writing using a 405nm diode laser," *Opt. Lett.,* vol. 39, no. 24, pp. 6847-6850, 2014/12/15 2014, doi: 10.1364/OL.39.006847.

[65] R. Wollhofen, J. Katzmann, C. Hrelescu, J. Jacak, and T. A. Klar, "120 nm resolution and 55 nm structure size in STED-lithography," *Opt. Express,* vol. 21, no. 9, pp. 10831-10840, 2013/05/06 2013, doi: 10.1364/OE.21.010831.

[66] S. Puce *et al.*, "3D-microfabrication by two-photon polymerization of an integrated sacrificial stencil mask," *Micro and Nano Engineering,* vol. 2, pp. 70-75, 2019/03/01/ 2019, doi: https://doi.org/10.1016/j.mne.2019.01.004.

[67] J. Walker, D. Halliday, and R. Resnick, *Halliday & Resnick principles of physics*, Tenth edition, International student version. ed. (Halliday and Resnick Principles of physics). Singapore: Wiley, 2014.

[68] W. Gerlach and O. Stern, "Der experimentelle Nachweis der Richtungsquantelung im Magnetfeld," *Zeitschrift für Physik,* vol. 9, no. 1, pp. 349-352, 1922/12/01 1922, doi: 10.1007/BF01326983.

[69] G. E. Uhlenbeck and S. Goudsmit, "Spinning Electrons and the Structure of Spectra," *Nature,* vol. 117, no. 2938, pp. 264-265, 1926/02/01 1926, doi: 10.1038/117264a0.

[70] K. M. Krishnan, *Fundamentals and applications of magnetic materials*, First edition. ed. Oxford, United Kingdom: Oxford University Press, 2016.

[71] L. F. Yin *et al.*, "Magnetocrystalline Anisotropy in Permalloy Revisited," *Physical Review Letters,* vol. 97, no. 6, p. 067203, 08/09/ 2006, doi: 10.1103/PhysRevLett.97.067203.

[72] A. Aharoni, *Introduction to the theory of ferromagnetism* (International series of monographs on physics ; 93). Oxford: Clarendon Press, 1996.

[73] J. A. Osborn, "Demagnetizing Factors of the General Ellipsoid," *Physical Review,* vol. 67, no. 11-12, pp. 351-357, 06/01/ 1945, doi: 10.1103/PhysRev.67.351.

[74] D. D. Sheka, V. P. Kravchuk, and Y. Gaididei, "Curvature effects in statics and dynamics of low dimensional magnets," *Journal of Physics A: Mathematical and Theoretical,* vol. 48, no. 12, p. 125202, 2015/03/02 2015, doi: 10.1088/1751-8113/48/12/125202.

[75] A. Hubert and R. Schäfer, *Magnetic domains : the analysis of magnetic microstructures*. Berlin ;: Springer, 1998.

[76] Y. Nakatani, A. Thiaville, and J. Miltat, "Head-to-head domain walls in soft nano-strips: a refined phase diagram," *Journal of Magnetism and Magnetic Materials,* vol. 290-291, pp. 750-753, 2005/04/01/ 2005, doi: https://doi.org/10.1016/j.jmmm.2004.11.355.

[77] S. Jamet, N. Rougemaille, J. C. Toussaint, and O. Fruchart, "25 - Head-to-head domain walls in one-dimensional nanostructures: An extended phase

diagram ranging from strips to cylindrical wires," in *Magnetic Nano- and Microwires*, M. Vázquez Ed.: Woodhead Publishing, 2015, pp. 783-811.

[78] C. A. Ferguson, D. A. MacLaren, and S. McVitie, "Metastable magnetic domain walls in cylindrical nanowires," *Journal of Magnetism and Magnetic Materials,* vol. 381, pp. 457-462, 2015/05/01/ 2015, doi: https://doi.org/10.1016/j.jmmm.2015.01.027.

[79] G. Bertotti, I. D. Mayergoyz, and C. Serpico, *Nonlinear magnetization dynamics in nanosystems [electronic resource] / Giorgio Bertotti, Isaak D. Mayergoyz, Claudio Serpico* (Elsevier series in electromagnetism). Amsterdam ;: Elsevier, 2009.

[80] M. Lakshmanan, "The fascinating world of the Landau–Lifshitz–Gilbert equation: an overview," *Philosophical Transactions of the Royal Society A: Mathematical, Physical and Engineering Sciences,* vol. 369, no. 1939, pp. 1280-1300, 2011/03/28 2011, doi: 10.1098/rsta.2010.0319.

[81] L. Berger, "Motion of a magnetic domain wall traversed by fast‐rising current pulses," *Journal of Applied Physics,* vol. 71, no. 6, pp. 2721-2726, 1992/03/15 1992, doi: 10.1063/1.351045.

[82] E. Salhi and L. Berger, "Current‐induced displacements and precession of a Bloch wall in Ni‐Fe thin films," *Journal of Applied Physics,* vol. 73, no. 10, pp. 6405-6407, 1993/05/15 1993, doi: 10.1063/1.352611.

[83] S. P. Parkin Stuart, M. Hayashi, and L. Thomas, "Magnetic Domain-Wall Racetrack Memory," *Science,* vol. 320, no. 5873, pp. 190-194, 2008/04/11 2008, doi: 10.1126/science.1145799.

[84] C. Castelnovo, R. Moessner, and S. L. Sondhi, "Magnetic monopoles in spin ice," *Nature,* vol. 451, no. 7174, pp. 42-45, 2008/01/01 2008, doi: 10.1038/nature06433.

[85] P. A. M. Dirac, "Quantised singularities in the electromagnetic field," *Proceedings of the Royal Society of London. Series A, Containing Papers of a Mathematical and Physical Character,* vol. 133, no. 821, pp. 60-72, 1931/09/01 1931, doi: 10.1098/rspa.1931.0130.

[86] L. D. C. Jaubert and P. C. W. Holdsworth, "Signature of magnetic monopole and Dirac string dynamics in spin ice," *Nature Physics,* vol. 5, no. 4, pp. 258-261, 2009/04/01 2009, doi: 10.1038/nphys1227.

[87] D. J. P. Morris *et al.*, "Dirac Strings and Magnetic Monopoles in the Spin Ice Dy2Ti2O7," *Science,* vol. 326, no. 5951, p. 411, 2009, doi: 10.1126/science.1178868.

[88] E. Ising, "Beitrag zur Theorie des Ferromagnetismus," *Zeitschrift für Physik,* vol. 31, no. 1, pp. 253-258, 1925/02/01 1925, doi: 10.1007/BF02980577.

[89] H. E. Stanley, *Phase transitions and critical phenomena*.

[90] D. Sherrington and S. Kirkpatrick, "Solvable Model of a Spin-Glass," *Physical Review Letters,* vol. 35, no. 26, pp. 1792-1796, 12/29/ 1975, doi: 10.1103/PhysRevLett.35.1792.

[91] K. Binder, "Kinetic ising model study of phase separation in binary alloys," *Zeitschrift für Physik,* vol. 267, no. 4, pp. 313-322, 1974/08/01 1974, doi: 10.1007/BF01669454.

[92] S. Efthymiou, M. J. S. Beach, and R. G. Melko, "Super-resolving the Ising model with convolutional neural networks," *Physical Review B,* vol. 99, no. 7, p. 075113, 02/06/ 2019, doi: 10.1103/PhysRevB.99.075113.

[93] R. J. Baxter, *Exactly solved models in statistical mechanics*. Elsevier, 2016.

[94] E. H. Lieb, "Exact Solution of the Two-Dimensional Slater KDP Model of a Ferroelectric," *Physical Review Letters,* vol. 19, no. 3, pp. 108-110, 07/17/ 1967, doi: 10.1103/PhysRevLett.19.108.

[95] E. H. Lieb, "Exact Solution of the Problem of the Entropy of Two-Dimensional Ice," *Physical Review Letters,* vol. 18, no. 17, pp. 692-694, 04/24/ 1967, doi: 10.1103/PhysRevLett.18.692.

[96] E. H. Lieb, "Residual Entropy of Square Ice," *Physical Review,* vol. 162, no. 1, pp. 162-172, 10/05/ 1967, doi: 10.1103/PhysRev.162.162.

[97] J. M. Porro, A. Bedoya-Pinto, A. Berger, and P. Vavassori, "Exploring thermally induced states in square artificial spin-ice arrays," *New Journal of Physics,* vol. 15, no. 5, p. 055012, 2013/05/16 2013, doi: 10.1088/1367-2630/15/5/055012.

[98] L. A. Mól, R. L. Silva, R. C. Silva, A. R. Pereira, W. A. Moura-Melo, and B. V. Costa, "Magnetic monopole and string excitations in two-dimensional spin ice," *Journal of Applied Physics,* vol. 106, no. 6, p. 063913, 2009/09/15 2009, doi: 10.1063/1.3224870.

[99] G. Möller and R. Moessner, "Magnetic multipole analysis of kagome and artificial spin-ice dipolar arrays," *Physical Review B,* vol. 80, no. 14, p. 140409, 10/22/ 2009, doi: 10.1103/PhysRevB.80.140409.

[100] Y. Perrin, B. Canals, and N. Rougemaille, "Extensive degeneracy, Coulomb phase and magnetic monopoles in artificial square ice," *Nature,* vol. 540, no. 7633, pp. 410-413, 2016/12/01 2016, doi: 10.1038/nature20155.

[101] L. A. S. Mól, W. A. Moura-Melo, and A. R. Pereira, "Conditions for free magnetic monopoles in nanoscale square arrays of dipolar spin ice," *Physical Review B,* vol. 82, no. 5, p. 054434, 08/30/ 2010, doi: 10.1103/PhysRevB.82.054434.

[102] F. Rys, "Über ein zweidimensionales klassisches Konfigurationsmodell," in *Helvetica Physica Acta*, 1963, vol. 36, no. 5: BIRKHAUSER VERLAG AG VIADUKSTRASSE 40-44, PO BOX 133, CH-4010 BASEL, SWITZERLAND, pp. 537-&.

[103] J. C. Slater, "Theory of the Transition in KH2PO4," *The Journal of Chemical Physics,* vol. 9, no. 1, pp. 16-33, 1941/01/01 1941, doi: 10.1063/1.1750821.

[104] C. Nisoli, "Topological order of the Rys F-model and its breakdown in realistic square spin ice: Topological sectors of Faraday loops," *Europhysics Letters,* vol. 132, no. 4, p. 47005, 2020/11/01 2020, doi: 10.1209/0295-5075/132/47005.

[105] D. M. Arroo and S. T. Bramwell, "Experimental measures of topological sector fluctuations in the F-model," *Physical Review B,* vol. 102, no. 21, p. 214427, 12/22/ 2020, doi: 10.1103/PhysRevB.102.214427.

[106] V. Schánilec *et al.*, "Approaching the Topological Low-Energy Physics of the F Model in a Two-Dimensional Magnetic Lattice," *Physical Review Letters,* vol. 129, no. 2, p. 027202, 07/07/ 2022, doi: 10.1103/PhysRevLett.129.027202.

[107] Y. Fang and Y. He, "Resolution technology of lithography machine," *Journal of Physics: Conference Series,* vol. 2221, no. 1, p. 012041, 2022/05/01 2022, doi: 10.1088/1742-6596/2221/1/012041.

[108] W. Hu, K. Sarveswaran, M. Lieberman, and G. H. Bernstein, "Sub-10 nm electron beam lithography using cold development of poly(methylmethacrylate)," *Journal of Vacuum Science & Technology B: Microelectronics and Nanometer Structures Processing, Measurement, and Phenomena,* vol. 22, no. 4, pp. 1711-1716, 2004/07/01 2004, doi: 10.1116/1.1763897.

[109] J. Fischer, "Three-dimensional optical lithography beyond the diffraction limit," 2012.

[110] S. Ravi-Kumar, B. Lies, H. Lyu, and H. Qin, "Laser Ablation of Polymers: A Review," *Procedia Manufacturing,* vol. 34, pp. 316-327, 2019/01/01 2019, doi: https://doi.org/10.1016/j.promfg.2019.06.155.

[111] R. Srinivasan, B. Braren, K. G. Casey, and M. Yeh, "Ultrafast imaging of ultraviolet laser ablation and etching of polymethylmethacrylate," *Applied Physics Letters,* vol. 55, no. 26, pp. 2790-2791, 1989/12/25 1989, doi: 10.1063/1.101910.

[112] M. D. Shirk and P. A. Molian, "A review of ultrashort pulsed laser ablation of materials," *Journal of Laser Applications,* vol. 10, no. 1, pp. 18-28, 1998/02/01 1998, doi: 10.2351/1.521827.

[113] S. R. Cain, F. C. Burns, C. E. Otis, and B. Braren, "Photothermal description of polymer ablation: Absorption behavior and degradation time scales," *Journal*

of Applied Physics, vol. 72, no. 11, pp. 5172-5178, 1992/12/01 1992, doi: 10.1063/1.351997.

[114] H. Schmidt, J. Ihlemann, B. Wolff-Rottke, K. Luther, and J. Troe, "Ultraviolet laser ablation of polymers: spot size, pulse duration, and plume attenuation effects explained," *Journal of Applied Physics,* vol. 83, no. 10, pp. 5458-5468, 1998/05/15 1998, doi: 10.1063/1.367377.

[115] F. C. Burns and S. R. Cain, "The effect of pulse repetition rate on laser ablation of polyimide and polymethylmethacrylate-based polymers," *Journal of Physics D: Applied Physics,* vol. 29, no. 5, pp. 1349-1355, 1996/05/14 1996, doi: 10.1088/0022-3727/29/5/034.

[116] H. Sato and S. Nishio, "Polymer laser photochemistry, ablation, reconstruction, and polymerization," *Journal of Photochemistry and Photobiology C: Photochemistry Reviews,* vol. 2, no. 2, pp. 139-152, 2001/12/13 2001, doi: https://doi.org/10.1016/S1389-5567(01)00015-6.

[117] P. C. Gasson, "Materials Sciences and Engineering – Eighth edition. W. D. Callister and D. G. Rethwisch John Wiley and Sons, The Atrium, Southern Gate, Chichester, West Sussex, PO19 8SQ, UK. 2010. 968pp. Illustrated. £47.99. ISBN 978-0-470-50586-1," *Aeronautical journal,* vol. 115, no. 1168, pp. 388-389, 2011, doi: 10.1017/S0001924000005947.

[118] M. Albrecht *et al.*, "Magnetic multilayers on nanospheres," *Nature Materials,* vol. 4, no. 3, pp. 203-206, 2005/03/01 2005, doi: 10.1038/nmat1324.

[119] D. A. Allwood, G. Xiong, M. D. Cooke, and R. P. Cowburn, "Magneto-optical Kerr effect analysis of magnetic nanostructures," *Journal of Physics D: Applied Physics,* vol. 36, no. 18, pp. 2175-2182, 2003/09/04 2003, doi: 10.1088/0022-3727/36/18/001.

[120] R. Bhargava and I. W. Levin, "Effective Time Averaging of Multiplexed Measurements: A Critical Analysis," *Analytical Chemistry,* vol. 74, no. 6, pp. 1429-1435, 2002/03/01 2002, doi: 10.1021/ac011153n.

[121] G. Binnig, C. F. Quate, and C. Gerber, "Atomic Force Microscope," *Physical Review Letters,* vol. 56, no. 9, pp. 930-933, 03/03/ 1986, doi: 10.1103/PhysRevLett.56.930.

[122] V. instruments. "Dimension 3100 Manual." https://www.scu.edu/media/school-of-engineering/photos/cns/Dimension3100D-Manual.pdf (accessed.

[123] C. D. Wright and E. W. Hill, "Reciprocity in magnetic force microscopy," *Applied Physics Letters,* vol. 67, no. 3, pp. 433-435, 1995/07/17 1995, doi: 10.1063/1.114623.

[124] M. A. Sutton, N. Li, D. C. Joy, A. P. Reynolds, and X. Li, "Scanning Electron Microscopy for Quantitative Small and Large Deformation Measurements

Part I: SEM Imaging at Magnifications from 200 to 10,000," *Experimental Mechanics,* vol. 47, no. 6, pp. 775-787, 2007/12/01 2007, doi: 10.1007/s11340-007-9042-z.

[125] R. D. Deslattes, E. G. Kessler, P. Indelicato, and E. Lindroth, "X-ray transition energies-new comprehensive evaluation," *AIP Conference Proceedings,* vol. 434, no. 1, pp. 89-104, 1998/07/08 1998, doi: 10.1063/1.56172.

[126] T. Fischbacher, M. Franchin, G. Bordignon, and H. Fangohr, "A Systematic Approach to Multiphysics Extensions of Finite-Element-Based Micromagnetic Simulations: Nmag," *IEEE Transactions on Magnetics,* vol. 43, no. 6, pp. 2896-2898, 2007, doi: 10.1109/TMAG.2007.893843.

[127] A. Vansteenkiste, J. Leliaert, M. Dvornik, M. Helsen, F. Garcia-Sanchez, and B. Van Waeyenberge, "The design and verification of MuMax3," *AIP Advances,* vol. 4, no. 10, p. 107133, 2014/10/01 2014, doi: 10.1063/1.4899186.

[128] S. T. Bramwell and M. J. P. Gingras, "Spin Ice State in Frustrated Magnetic Pyrochlore Materials," *Science,* vol. 294, no. 5546, pp. 1495-1501, 2001/11/16 2001, doi: 10.1126/science.1064761.

[129] L. Pauling, "The Nature of the Chemical Bond. II. The One-Electron Bond and the Three-Electron Bond," *Journal of the American Chemical Society,* vol. 53, no. 9, pp. 3225-3237, 1931/09/01 1931, doi: 10.1021/ja01360a004.

[130] W. F. Giauque and J. W. Stout, "The Entropy of Water and the Third Law of Thermodynamics. The Heat Capacity of Ice from 15 to 273°K," *Journal of the American Chemical Society,* vol. 58, no. 7, pp. 1144-1150, 1936/07/01 1936, doi: 10.1021/ja01298a023.

[131] P. W. Anderson, "Ordering and Antiferromagnetism in Ferrites," *Physical Review,* vol. 102, no. 4, pp. 1008-1013, 05/15/ 1956, doi: 10.1103/PhysRev.102.1008.

[132] S. R. Giblin, S. T. Bramwell, P. C. W. Holdsworth, D. Prabhakaran, and I. Terry, "Creation and measurement of long-lived magnetic monopole currents in spin ice," *Nature Physics,* vol. 7, no. 3, pp. 252-258, 2011/03/01 2011, doi: 10.1038/nphys1896.

[133] S. T. Bramwell and M. J. Harris, "Frustration in Ising-type spin models on the pyrochlore lattice," *Journal of Physics: Condensed Matter,* vol. 10, no. 14, p. L215, 1998/04/13 1998, doi: 10.1088/0953-8984/10/14/002.

[134] A. P. Ramirez, A. Hayashi, R. J. Cava, R. Siddharthan, and B. S. Shastry, "Zero-point entropy in 'spin ice'," *Nature,* vol. 399, no. 6734, pp. 333-335, 1999/05/01 1999, doi: 10.1038/20619.

[135] R. F. Wang *et al.*, "Demagnetization protocols for frustrated interacting nanomagnet arrays," *Journal of Applied Physics,* vol. 101, no. 9, p. 09J104, 2007/05/01 2007, doi: 10.1063/1.2712528.

[136] J. Li *et al.*, "Comparing artificial frustrated magnets by tuning the symmetry of nanoscale permalloy arrays," *Physical Review B,* vol. 81, no. 9, p. 092406, 03/29/ 2010, doi: 10.1103/PhysRevB.81.092406.

[137] G.-W. Chern, M. J. Morrison, and C. Nisoli, "Degeneracy and Criticality from Emergent Frustration in Artificial Spin Ice," *Physical Review Letters,* vol. 111, no. 17, p. 177201, 10/22/ 2013, doi: 10.1103/PhysRevLett.111.177201.

[138] M. J. Morrison, T. R. Nelson, and C. Nisoli, "Unhappy vertices in artificial spin ice: new degeneracies from vertex frustration," *New Journal of Physics,* vol. 15, no. 4, p. 045009, 2013/04/16 2013, doi: 10.1088/1367-2630/15/4/045009.

[139] H. Saglam *et al.*, "Entropy-driven order in an array of nanomagnets," *Nature Physics,* vol. 18, no. 6, pp. 706-712, 2022/06/01 2022, doi: 10.1038/s41567-022-01555-6.

[140] Y. Lao *et al.*, "Classical topological order in the kinetics of artificial spin ice," *Nature Physics,* vol. 14, no. 7, pp. 723-727, 2018/07/01 2018, doi: 10.1038/s41567-018-0077-0.

[141] R. Macêdo, G. M. Macauley, F. S. Nascimento, and R. L. Stamps, "Apparent ferromagnetism in the pinwheel artificial spin ice," *Physical Review B,* vol. 98, no. 1, p. 014437, 07/31/ 2018, doi: 10.1103/PhysRevB.98.014437.

[142] S. Ladak, D. E. Read, G. K. Perkins, L. F. Cohen, and W. R. Branford, "Direct observation of magnetic monopole defects in an artificial spin-ice system," *Nature Physics,* vol. 6, no. 5, pp. 359-363, 2010/05/01 2010, doi: 10.1038/nphys1628.

[143] S. Sahoo, A. May, A. van Den Berg, A. K. Mondal, S. Ladak, and A. Barman, "Observation of Coherent Spin Waves in a Three-Dimensional Artificial Spin Ice Structure," *Nano Letters,* vol. 21, no. 11, pp. 4629-4635, 2021/06/09 2021, doi: 10.1021/acs.nanolett.1c00650.

[144] A. May, "Realising 3D Artificial Spin-Ice Systems Using Two-Photon Lithography and Line-Of-Sight Deposition," School of Physics and Astronomy, Cardiff University, 2020. [Online]. Available: http://orca.cardiff.ac.uk/id/eprint/141913

[145] D. Ruelle, "Statistical Mechanics: A Short Treatise Statistical Mechanics: A Short Treatise , Giovanni Gallavotti , Springer-Verlag, New York, 1999. $68.00 (339 pp.) ISBN 3-540-64883-6," *Physics today,* vol. 54, no. 5, pp. 63-63, 2001, doi: 10.1063/1.1381111.

[146] R. Jean-Michel, "Recording History," in *Recording and Voice Processing, Volume 1: History and Generalities*: Wiley, 2021, pp. 1-43.

[147] M. Johnson and R. H. Silsbee, "Interfacial charge-spin coupling: Injection and detection of spin magnetization in metals," *Physical Review Letters,* vol. 55, no. 17, pp. 1790-1793, 10/21/ 1985, doi: 10.1103/PhysRevLett.55.1790.

[148] M. N. Baibich *et al.*, "Giant Magnetoresistance of (001)Fe/(001)Cr Magnetic Superlattices," *Physical Review Letters,* vol. 61, no. 21, pp. 2472-2475, 11/21/ 1988, doi: 10.1103/PhysRevLett.61.2472.

[149] G. Binasch, P. Grünberg, F. Saurenbach, and W. Zinn, "Enhanced magnetoresistance in layered magnetic structures with antiferromagnetic interlayer exchange," *Physical Review B,* vol. 39, no. 7, pp. 4828-4830, 03/01/ 1989, doi: 10.1103/PhysRevB.39.4828.

[150] S. Matsunaga *et al.*, "Fabrication of a Nonvolatile Full Adder Based on Logic-in-Memory Architecture Using Magnetic Tunnel Junctions," *Applied Physics Express,* vol. 1, no. 9, p. 091301, 2008/08/22 2008, doi: 10.1143/APEX.1.091301.

[151] D. A. Allwood, G. Xiong, C. Faulkner, D. Atkinson, D. Petit, and R. Cowburn, "Magnetic domain-wall logic," *science,* vol. 309, no. 5741, pp. 1688-1692, 2005.

[152] S. Jun, "Logic devices and circuits based on giant magnetoresistance," *IEEE Transactions on Magnetics,* vol. 33, no. 6, pp. 4492-4497, 1997, doi: 10.1109/20.649887.

[153] S. Parkin, J. Xin, C. Kaiser, A. Panchula, K. Roche, and M. Samant, "Magnetically engineered spintronic sensors and memory," *Proceedings of the IEEE,* vol. 91, no. 5, pp. 661-680, 2003, doi: 10.1109/JPROC.2003.811807.

[154] B. Dieny, V. S. Speriosu, S. S. P. Parkin, B. A. Gurney, D. R. Wilhoit, and D. Mauri, "Giant magnetoresistive in soft ferromagnetic multilayers," *Physical Review B,* vol. 43, no. 1, pp. 1297-1300, 01/01/ 1991, doi: 10.1103/PhysRevB.43.1297.

[155] R. D. McMichael and M. J. Donahue, " Head to head domain wall structures in thin magnetic strips," *IEEE Trans. Magn.,* vol. 33, p. 4167, 1997, doi: 10.1109/20.619698.

[156] G. A. Prinz, "Magnetoelectronics," *Science,* vol. 282, no. 5394, pp. 1660-1663, 1998/11/27 1998, doi: 10.1126/science.282.5394.1660.

[157] D. A. Allwood, G. Xiong, M. D. Cooke, C. C. Faulkner, D. Atkinson, and R. P. Cowburn, "Characterization of submicrometer ferromagnetic NOT gates," *Journal of Applied Physics,* vol. 95, no. 12, pp. 8264-8270, 2004/06/15 2004, doi: 10.1063/1.1751236.

[158] D. A. Allwood *et al.*, "Submicrometer Ferromagnetic NOT Gate and Shift Register," *Science,* vol. 296, no. 5575, pp. 2003-2006, 2002, doi: doi:10.1126/science.1070595.

[159] P. Xu, K. Xia, C. Gu, L. Tang, H. Yang, and J. Li, "An all-metallic logic gate based on current-driven domain wall motion," *Nature Nanotechnology,* vol. 3, no. 2, pp. 97-100, 2008/02/01 2008, doi: 10.1038/nnano.2008.1.

[160] C. C. Faulkner, D. A. Allwood, M. D. Cooke, X. Gang, D. Atkinson, and R. P. Cowburn, "Controlled switching of ferromagnetic wire junctions by domain wall injection," *IEEE Transactions on Magnetics,* vol. 39, no. 5, pp. 2860-2862, 2003, doi: 10.1109/TMAG.2003.816247.

[161] R. Anisul Haque, M. Yamamoto, R. Nakatani, and Y. Endo, "Magnetic logic gate for binary computing," *Science and Technology of Advanced Materials,* vol. 5, no. 1-2, pp. 79-82, 2004/01/01 2004, doi: 10.1016/j.stam.2003.09.015.

[162] C. Murapaka, P. Sethi, S. Goolaup, and W. S. Lew, "Reconfigurable logic via gate controlled domain wall trajectory in magnetic network structure," *Scientific Reports,* vol. 6, no. 1, p. 20130, 2016/02/03 2016, doi: 10.1038/srep20130.

[163] T. Ono, H. Miyajima, K. Shigeto, K. Mibu, N. Hosoito, and T. Shinjo, "Propagation of a Magnetic Domain Wall in a Submicrometer Magnetic Wire," *Science,* vol. 284, no. 5413, pp. 468-470, 1999/04/16 1999, doi: 10.1126/science.284.5413.468.

[164] T. Ono, H. Miyajima, K. Shigeto, and T. Shinjo, "Magnetization reversal in submicron magnetic wire studied by using giant magnetoresistance effect," *Applied Physics Letters,* vol. 72, no. 9, pp. 1116-1117, 1998/03/02 1998, doi: 10.1063/1.120941.

[165] Y. Yokoyama *et al.*, "Kerr microscopy observations of magnetization process in microfabricated ferromagnetic wires," *Journal of Applied Physics,* vol. 87, no. 9, pp. 5618-5620, 2000/05/01 2000, doi: 10.1063/1.372469.

[166] A. Himeno, T. Ono, S. Nasu, K. Shigeto, K. Mibu, and T. Shinjo, "Dynamics of a magnetic domain wall in magnetic wires with an artificial neck," *Journal of Applied Physics,* vol. 93, no. 10, pp. 8430-8432, 2003/05/15 2003, doi: 10.1063/1.1556980.

[167] M. Kläui, C. A. F. Vaz, J. A. C. Bland, W. Wernsdorfer, G. Faini, and E. Cambril, "Domain wall pinning and controlled magnetic switching in narrow ferromagnetic ring structures with notches (invited)," *Journal of Applied Physics,* vol. 93, no. 10, pp. 7885-7890, 2003/05/15 2003, doi: 10.1063/1.1557758.

[168] M. Kläui *et al.*, "Domain wall behaviour at constrictions in ferromagnetic ring structures," *Physica B: Condensed Matter,* vol. 343, no. 1, pp. 343-349, 2004/01/01/ 2004, doi: https://doi.org/10.1016/j.physb.2003.08.067.

[169] D. Kumar, S. Gupta, T. Jin, R. Nongjai, K. Asokan, and S. N. Piramanayagam, "Modification of Structural and Magnetic Properties of Masked Co–Pt Films

Induced by High-Energy Ion Implantation," *IEEE Magnetics Letters,* vol. 9, pp. 1-5, 2018, doi: 10.1109/LMAG.2017.2768324.

[170] D. Kumar, S. Gupta, T. Jin, R. Nongjai, K. Asokan, and S. N. Piramanayagam, "Tailoring the structural and magnetic properties of masked CoPt thin films using ion implantation," *AIP Advances,* vol. 8, no. 5, p. 056504, 2018/05/01 2017, doi: 10.1063/1.5007767.

[171] T. L. Jin *et al.*, "Tuning magnetic properties for domain wall pinning via localized metal diffusion," *Scientific Reports,* vol. 7, no. 1, p. 16208, 2017/11/24 2017, doi: 10.1038/s41598-017-16335-z.

[172] R. Streubel *et al.*, "Magnetism in curved geometries," *Journal of Physics D: Applied Physics,* vol. 49, no. 36, p. 363001, 2016/08/17 2016, doi: 10.1088/0022-3727/49/36/363001.

[173] T. Schrefl, J. Fidler, K. J. Kirk, and J. N. Chapman, "Domain structures and switching mechanisms in patterned magnetic elements," *Journal of Magnetism and Magnetic Materials,* vol. 175, no. 1, pp. 193-204, 1997/11/01/ 1997, doi: https://doi.org/10.1016/S0304-8853(97)00156-X.

[174] D. Kumar *et al.*, "Domain wall memory: Physics, materials, and devices," *Physics Reports,* vol. 958, pp. 1-35, 2022/05/05/ 2022, doi: https://doi.org/10.1016/j.physrep.2022.02.001.

[175] R. Sbiaa and S. N. Piramanayagam, "Multi-level domain wall memory in constricted magnetic nanowires," *Applied Physics A,* vol. 114, no. 4, pp. 1347-1351, 2014/03/01 2014, doi: 10.1007/s00339-013-7979-6.

[176] T. Phung *et al.*, "Highly Efficient In-Line Magnetic Domain Wall Injector," *Nano Letters,* vol. 15, no. 2, pp. 835-841, 2015/02/11 2015, doi: 10.1021/nl503391k.

[177] J. A. Katine, F. J. Albert, R. A. Buhrman, E. B. Myers, and D. C. Ralph, "Current-Driven Magnetization Reversal and Spin-Wave Excitations in Co $/$Cu $/$Co Pillars," *Physical Review Letters,* vol. 84, no. 14, pp. 3149-3152, 04/03/ 2000, doi: 10.1103/PhysRevLett.84.3149.

[178] R. C. Sousa and I. L. Prejbeanu, "Non-volatile magnetic random access memories (MRAM)," *Comptes Rendus Physique,* vol. 6, no. 9, pp. 1013-1021, 2005/11/01/ 2005, doi: https://doi.org/10.1016/j.crhy.2005.10.007.

[179] A. van den Berg, M. Caruel, M. Hunt, and S. Ladak, "Combining two-photon lithography with laser ablation of sacrificial layers: A route to isolated 3D magnetic nanostructures," *Nano Research,* 2022/07/30 2022, doi: 10.1007/s12274-022-4649-z.

[180] N. V. Lavrik, M. J. Sepaniak, and P. G. Datskos, "Cantilever transducers as a platform for chemical and biological sensors," *Review of Scientific*

Instruments, vol. 75, no. 7, pp. 2229-2253, 2004/07/01 2004, doi: 10.1063/1.1763252.

[181] N. Ferrell, J. Woodard, and D. Hansford, "Fabrication of polymer microstructures for MEMS: sacrificial layer micromolding and patterned substrate micromolding," *Biomedical Microdevices,* vol. 9, no. 6, pp. 815-821, 2007/12/01 2007, doi: 10.1007/s10544-007-9094-y.

[182] J. Korvink, J. Korvink, and O. Paul, *MEMS A Practical Guide to Design, Analysis and Applications*. Burlington: Elsevier Science, 2005.

[183] A. Bagolini, L. Pakula, T. L. M. Scholtes, H. T. M. Pham, P. J. French, and P. M. Sarro, "Polyimide sacrificial layer and novel materials for post-processing surface micromachining," *Journal of Micromechanics and Microengineering,* vol. 12, no. 4, pp. 385-389, 2002/06/14 2002, doi: 10.1088/0960-1317/12/4/306.

[184] K. Walsh, J. Norville, and T. Yu-Chong, "Photoresist as a sacrificial layer by dissolution in acetone," in *Technical Digest. MEMS 2001. 14th IEEE International Conference on Micro Electro Mechanical Systems (Cat. No.01CH37090)*, 25-25 Jan. 2001 2001, pp. 114-117, doi: 10.1109/MEMSYS.2001.906492.

[185] Y. Kwang-Seok and Y. Euisik, "Microfabrication of 3-dimensional photoresist structures using selective patterning and development on two types of specific resists and its application to microfluidic components," in *17th IEEE International Conference on Micro Electro Mechanical Systems. Maastricht MEMS 2004 Technical Digest*, 25-29 Jan. 2004 2004, pp. 757-760, doi: 10.1109/MEMS.2004.1290695.

[186] V. Linder, B. D. Gates, D. Ryan, B. A. Parviz, and G. M. Whitesides, "Water-Soluble Sacrificial Layers for Surface Micromachining," *Small,* https://doi.org/10.1002/smll.200400159 vol. 1, no. 7, pp. 730-736, 2005/07/01 2005, doi: https://doi.org/10.1002/smll.200400159.

[187] J. Clayden, *Organic chemistry*. Oxford ;: Oxford University Press, 2001.

[188] U. T. Sanli *et al.*, "3D Nanoprinted Plastic Kinoform X-Ray Optics," *Advanced Materials,* https://doi.org/10.1002/adma.201802503 vol. 30, no. 36, p. 1802503, 2018/09/01 2018, doi: https://doi.org/10.1002/adma.201802503.

[189] P. Hirsch, M. Kässens, M. Püttmann, and L. Reimer, "Contamination in a scanning electron microscope and the influence of specimen cooling," *Scanning,* https://doi.org/10.1002/sca.4950160207 vol. 16, no. 2, pp. 101-110, 1994/03/01 1994, doi: https://doi.org/10.1002/sca.4950160207.

[190] W. C. Uhlig and J. Shi, "Systematic study of the magnetization reversal in patterned Co and NiFe Nanolines," *Appl. Phys. Lett.,* vol. 84, p. 759, 2004.

[191] M. Hunt, "Optical Magnetometry and Micromagnetic Simulations of Three-Dimensional Magnetic Nanostructures," School of Physics and Astronomy, Cardiff University, 2017.

[192] D. A. Allwood, G. Xiong, and R. P. Cowburn, "Domain wall diodes in ferromagnetic planar nanowires," *Applied Physics Letters,* vol. 85, no. 14, pp. 2848-2850, 2004/10/04 2004, doi: 10.1063/1.1802388.

[193] D. Atkinson, D. A. Allwood, G. Xiong, M. D. Cooke, C. C. Faulkner, and R. P. Cowburn, "Magnetic domain-wall dynamics in a submicrometre ferromagnetic structure," *Nature Materials,* vol. 2, no. 2, pp. 85-87, 2003/02/01 2003, doi: 10.1038/nmat803.

[194] S. Ladak, A. Fernández-Pacheco, and P. Fischer, "Science and technology of 3D magnetic nanostructures," *APL Materials,* vol. 10, no. 12, p. 120401, 2022, doi: 10.1063/5.0136801.

[195] V. Kapaklis *et al.*, "Thermal fluctuations in artificial spin ice," *Nature Nanotechnology,* vol. 9, no. 7, pp. 514-519, 2014/07/01 2014, doi: 10.1038/nnano.2014.104.

[196] A. Farhan *et al.*, "Emergent magnetic monopole dynamics in macroscopically degenerate artificial spin ice," *Science Advances,* vol. 5, no. 2, p. eaav6380, doi: 10.1126/sciadv.aav6380.

[197] S. Lamrani *et al.*, "Microstructure investigation and magnetic study of permalloy thin films grown by thermal evaporation," *The European Physical Journal Applied Physics,* vol. 74, no. 3, p. 30302, 2016.